X-Ray Powder Diffraction as a Non-Destructive Tool for Characterising Laser Wakefield Betatron Radiation



Gavin Cheung

Linacre College, Oxford

Thesis submitted in fulfilment of the requirements for the degree of

Doctor of Philosophy at the University of Oxford

Hilary Term, 2018

Abstract

Laser wakefield accelerators provide a relatively simple means of generating bright X-rays beams which are useful across many fields and industries. To achieve this, a sufficiently powerful laser is required and just a few centimetres of gas. In contrast, other bright X-ray sources, such as synchrotrons, require significantly more infrastructure and can span many hundreds of metres.

This thesis looks at a novel diagnostic technique based on X-ray diffraction from a powder in order to characterise X-ray beams with large shot-to-shot variations. The mechanics behind the method, named XCERP diffraction, are presented and the results of simulations are provided as a proof of principle study. XCERP diffraction is shown to be able to retrieve details of the energy spectrum and the beam divergence in a single shot without prior knowledge of the spectral shape.

A campaign at the Centre for Advanced Laser Applications in Munich focused on the first experimental demonstration of XCERP diffraction. The results reveal that an increased level of radiation shielding was required as a source of ionising radiation was found to be present whenever an electron beam was generated. This source of radiation is thought to have obscured potential X-ray diffraction.

An investigation of the unknown radiation source was performed using Geant4. From simulations of the CALA target chamber, it was found that the CCD of interest would have been subjected to both bremsstrahlung radiation and stray electrons when an electron beam is steered into a steel floor. Further simulations show potential methods of reducing the flux of particles reaching the CCD.

Finally, the designs of an electron spectrometer and filter array are described in detail to measure properties of the electron bunches and betatron radiation produced during an experimental campaign at the Astra Gemini laser facility.

Acknowledgements

I would like to first and foremost thank my supervisor, Prof. Simon Hooker, for giving me this opportunity as well as all his guidance, patience and understanding throughout my D.Phil. Everyone in the Hooker group and the our close relatives (Dr. Laura Corner, Prof. Roman Walczak) has made my working life so enjoyable. Special shout-outs to the cheerleaders who made my RAL experiences that bit more bearable. James, Chris #1, Zak, Rob and Jimmy—thanks for putting up with my pedantry on experiment. I've had many a good time with you all.

Many, many thanks to Prof. Dr. Stefan Karsch for allowing me to use the laser system at CALA in Garching, Germany. I would also like to thank Stefan's team—especially Hao Ding, Max Gilljohann, Johannes Götzfried, Tobias Heider, Matthias Heigoldt, Sabine Schindler and Johannes Wenz—for their assistance in not only running the experiment whilst I was in Germany, but also after I had left! I would not have been able to finish without your efforts. Special thanks to Johannes who put up with my many, many, many e-mails... you just happened to be the 'go to' guy.

Thanks to David McGonegle, Shamim Patel and Matthew Suggit who have all helped me at some point with my diffraction related problems. Also thanks to many others from the physics department, including Tom, Paul, Naren, Elliot and others.

I would like to thank all of the wonderful people at Linacre and beyond. In no particular order, thanks to Laura, Stephen, Tom, Hannah, Glenn, Frances, Symon, Cara, Pete, Karrar, James, Ollie, Salam, Ivey, Rosie, Sam, Isabel, Neven, Ricardo, Carryn, Janaki, Charlie,... the list goes on.

Role of the Author

Much of the theory presented in Chapter 2 can be found in [1–3]. Calculations of the effective volume for the geometries following the Bragg-Brentano geometry were performed independently, but are based on the method set out in [1, 3]. The generalised geometry set out in Section 2.6.3 was developed by the author.

The idea for using diffraction to measure betatron radiation was first suggested by Simon Hooker during the author's first year of the DPhil programme. This initially led to a dead end as no useful information could be retrieved from the collection of overlapping Debye-Scherrer rings. The author took inspiration from [4] to incorporate single photon counting as a solution to distinguishing first order diffraction of a ray of wavelength λ and second order diffraction of a ray of wavelength $\lambda/2$. From this, the author developed the theoretical framework of XCERP diffraction and implemented it into MATLAB which led the method of retrieving the spectrum and divergence of an arbitrary beam.

The Astra Gemini experiment was run by members of the Hooker research group. The author acted as Deputy Target Area Operator during this campaign. The capillaries used during the experiment were machined by Rob Shalloo (Oxford). Operation of the discharge circuitry was mainly done by Anthony Dyson, but delegated this task to other members after training. Many of the LABVIEW codes used were written by the author, with the exception of a few which were adapted by the author. The gas control code used was adapted by Chris Thornton and then Rob Shalloo. The burden of data taking was shared by all members of the team, with the author primarily driving the control code. The Andor Basic scripts used for capturing the betatron radiation, spectrometer images and Lanex screens were all based on a script written by Stuart Mangles (ICL) and adapted by the author. The coding and testing of the particle tracking algorithm used in the energy calibration of the electron spectrometer for an arbitrary geometry was performed by the author. The magnets and Lanex screens were borrowed during

the experiment. Analysis of the electron spectrometer data was also implemented and performed by the author. Measurements of the Lanex positions taken by the author were cross-checked with those by Laura Corner. The design of the Ross filters (and all iterations of the design thereof) and subsequent analysis is the author's own work.

The experiment at CALA was performed by the author with Simon Hooker and the Karsch research group (LMU). The laser setup for each day was performed entirely by members of Stefan Karsch's group. The author dealt with the CCD used to measure XCERP diffraction for the most part, including adding the lead shielding and operating it during runs. The control code was managed by Max Gilljohann (LMU). A number of data runs were performed by the Karsch group alone after the author had returned back to the UK. Many of the physical measurements were taken by Johannes Goetzfried (LMU). The event identification algorithm was designed and coded by the author as was the majority of the analysis relating to the XCERP diffraction CCD. The electron charge and energy calibration was provided by Hao Ding (LMU).

The installation of GEANT4 was aided by Roman Walczak (Oxford) and Giles Barr (Oxford). Simulation of the CALA experiment was a gradual process due to the steep learning curve of GEANT4. A number of code examples were found in the code repository to serve as tutorials. Analysis of the simulations were performed by the author.

List of Publications

Cheung, G. and Hooker, S. M. **X-ray characterization by energy-resolved powder diffraction**. Phys. Rev. Accel. Beams 19, 82801 (2016).

Cowley, J., Thornton, C., Arran, C., Shalloo, R. J., Corner, L., Cheung, G., Gregory, C. D., Mangles, S. P. D., Matlis, N. H., Symes, D. R., Walczak, R., Hooker, S. M. **Excitation and Control of Plasma Wakefields by Multiple Laser Pulses**. Phys. Rev. Lett. 119, (2017).

Shalloo, R. J., Corner, L., Arran, C., Cowley, J., Cheung, G., Thornton, C., Walczak, R and Hooker, S. M. **Generation of laser pulse trains for tests of multi-pulse laser wakefield acceleration**. Nucl. Instruments Methods Phys. Res. Sect. A Accel. Spectrometers, Detect. Assoc. Equip. 829, (2016).

Ding, H., Döpp, A., Gilljohann, M., Götzfried, J., Schindler, S., Wildgruber, L., Cheung, G., Hooker, S. M. and Karsch, S. **Nonlinear plasma wavelength scalings in a laser wakefield accelerator**. Phy. Rev. Lett. (Submitted).

Contents

List of Figures **xi**

List of Tables **xii**

1 Introduction **1**
1.1 Bright X-ray sources and their applications . . . 1
1.1.1 A brief history of traditional bright light sources . . . 2
1.1.2 Generation of bright radiation . . . 2
1.2 Laser wakefield acceleration as a source of bright radiation . . . 3
1.2.1 Electron acceleration . . . 4
1.2.2 Radiation generation . . . 5
1.2.3 Methods for characterising betatron radiation . . . 6
1.3 Theory of betatron radiation . . . 7
1.4 Outline of the thesis . . . 9

2 Theory of X-Ray Diffraction **11**
2.1 Introduction . . . 11
2.2 Scattering from a Single Electron . . . 11
2.3 Scattering from an Atom . . . 13
2.4 Scattering from a Crystal . . . 14
2.4.1 Bragg law . . . 14
2.4.2 Structure factor . . . 15
2.4.3 Multiple unit cells . . . 16
2.4.4 Debye-Waller factor . . . 17
2.5 Scattering from a Powder . . . 17
2.5.1 Multiplicity . . . 18
2.5.2 Lorentz-polarisation factor . . . 18
2.6 Effective Volume . . . 19
2.6.1 X-ray diffraction in reflection mode . . . 21
2.6.2 X-ray diffraction in transmission mode . . . 25
2.6.3 General X-ray diffraction . . . 26
2.7 Reflectivity Calculation . . . 27
2.8 Summary . . . 28

3 X-Ray Characterisation by Energy-Resolved Powder Diffraction 29
3.1 Introduction . . . 29
3.2 Concept of XCERP Diffraction . . . 30
3.3 Theory of XCERP Diffraction . . . 31
3.4 MATLAB Implementation . . . 33
3.4.1 Markov chain Monte Carlo sampling . . . 33
3.4.2 Ray tracing . . . 35
3.4.3 Material considerations . . . 36
3.4.4 Reflectivity calculation . . . 38
3.4.5 Scaling of rays . . . 39
3.4.6 Beam generation . . . 40
3.5 Simulation examples . . . 41
3.5.1 Spectrum retrieval . . . 41
3.5.2 Divergence retrieval . . . 45
3.5.3 Polarisation effects . . . 51
3.6 Discussion . . . 51
3.7 Summary . . . 55

4 Astra Gemini Experiment 57
4.1 Introduction . . . 57
4.2 Experimental Setup . . . 59
4.3 Electron Energy Measurement . . . 62
4.3.1 Theory . . . 63
4.3.2 Comparison of code with theory . . . 64
4.3.3 Simulations using Gemini parameters . . . 65
4.3.4 Application to the Gemini experiment . . . 69
4.3.5 Limitations of the model . . . 75
4.4 Betatron Radiation Measurement . . . 76
4.4.1 Theory . . . 76
4.4.2 Filter wheel design . . . 78
4.4.3 Methods . . . 81
4.4.4 Example betatron spectrum retrieval . . . 88
4.5 Experimental Results . . . 90
4.6 Discussion . . . 96
4.7 Summary . . . 101

5 CALA Experiment 102
5.1 Introduction . . . 102
5.2 Experimental Setup . . . 102
5.3 CCD Operation . . . 104
5.3.1 Basic overview . . . 104
5.3.2 Sources of noise . . . 105
5.3.3 Energy conversion . . . 106
5.4 Noise Analysis Methods . . . 107
5.4.1 Background removal . . . 112
5.5 Event Recognition Algorithm . . . 115

5.5.1 Particle signatures . . . 115
5.5.2 Algorithm description . . . 116
5.6 Experimental Results . . . 119
5.6.1 Reducing background radiation . . . 121
5.6.2 Data selection . . . 124
5.7 Discussion . . . 129
5.8 Summary . . . 135

6 Geant4 Simulations **136**
6.1 Introduction . . . 136
6.2 Modelling the Geometry . . . 137
6.2.1 Target area . . . 139
6.2.2 Vacuum chamber . . . 139
6.2.3 Electron spectrometer . . . 140
6.2.4 X-ray camera and shielding . . . 140
6.3 Modelling Physical Processes . . . 141
6.3.1 Tracking of particles . . . 141
6.3.2 Physics list . . . 142
6.3.3 Step size . . . 142
6.3.4 Cut in range . . . 143
6.4 Particle Generation . . . 145
6.5 Particle Detection . . . 146
6.6 Comparison to Experiment . . . 148
6.7 Estimation of Detected Particles . . . 154
6.7.1 Simulation calculations . . . 160
6.8 Improvements to the Shielding . . . 161
6.8.1 Additional aluminium shield . . . 162
6.8.2 Adding plastic layer . . . 162
6.8.3 Increasing lead shielding . . . 164
6.8.4 Discussion . . . 168
6.9 Validation Checks . . . 168
6.10 Summary . . . 170

7 Conclusion **173**
7.1 Outlook . . . 175

References **177**

List of Figures

2.1 Simple derivation of the Bragg law. 15
2.2 Fraction of plane normals contributing to diffraction from a powder. . . 20
2.3 Geometries used in the calculation of the effective volume for X-ray diffraction in reflection mode. 22
2.4 Geometries used in the calculation of the effective volume for X-ray diffraction in transmission mode. 24

3.1 Geometry of an XCERP diffraction measurement. 32
3.2 Scatter plot of photons driffracted by powdered silicon. 36
3.3 Energy spectrum of betatron radiation using MCMC sampling. 42
3.4 Comparison of the incident and retrieved spectra for diffraction by powdered silicon. 44
3.5 Plots of radial distance as a function of photon energy. 46
3.6 Distribution of diffracted photons. 48
3.7 Demonstration of retrieved energy-dependent divergence with XCERP diffraction. 49
3.8 Comparison of angularaly-resolved spectrum retrieved by XCERP diffraction. 50
3.9 Comparison of the diffraction patterns for different beam polarisations. 52
3.10 Comparison of the incident and retrieved spectra for diffraction by powdered silicon including the effects of quantum efficiency. 55

4.1 CAD drawing of target chamber at the Astra Gemini facility 59
4.2 Plot of electron trajectory in the yz-plane for an energy of 5 GeV. . . . 65
4.3 Plot of electron displacement as a function of time. 66
4.4 Magnetic flux density of permanent magnets in units of teslas. 66
4.5 Simulation of electron trajectories between 10 MeV to 3 GeV. 67
4.6 Energy calibrations for Lanex screens with a change in screen position. 68
4.7 Energy calibrations for Lanex screens with a change in electron pointing. 68
4.8 Image of Lanex screen with projection of lines of equal electron energy. 70
4.9 Example of photoluminescence of low energy Lanex screen due to a LWFA-produced electron beam. 72
4.10 Example of electron energy spectrum as measured by the low energy Lanex screen. 72
4.11 Mass attenuation coefficient of aluminium, iron and cobalt. 77
4.12 Transmittance for balanced filters as a function of photon energy. . . . 78
4.13 Transmittance differnce for balanced Ross pairs. 81

4.14 Transmittance difference for quasi-balanced Ross pairs. 82
4.15 Image of a filter wheel fabricated by the Target Fabrication group in the Central Laser Facility. 82
4.16 Image of filter wheel illuminated by betatron radiation. 85
4.17 Comparison of the effective transmittance difference of chromium and titanium. 86
4.18 Comparison of experimentally measured CCD counts through various filters with modelled CCD counts. 88
4.19 Energy spectral density for betatron radiation using Ross pairs. 89
4.20 Charge measurement on the low energy Lanex screen after processing for Run 69. 91
4.21 Plot of the 25%, 50% and 75% cut-off energy on the low energy Lanex screen for Run 69. 92
4.22 Electron divergence measurement on the low energy Lanex screen for run 69. 92
4.23 Example of beam whose transverse position varies with energy. 93
4.24 Standard deviation of the centres of a Gaussian fit to energy cross sections of the electron spectrum on the low energy Lanex screen for run 69. . . 94
4.25 Example of streak-like electron beam. 94
4.26 Best fit betatron radiation critical energy for run 69. 95
4.27 Best fit betatron radiation scaling factor for run 69. 95
4.28 Plot of best fit betatron radiation critical energy as a function of the 50% cut-off electron energy. 96
4.29 Plot of best fit betatron radiation critical energy as a function of the 90% cut-off electron energy. 97
4.30 Plot of best fit betatron radiation critical energy as a function of electron beam divergence. 98
4.31 Plot of best fit betatron radiation scaling factor as a function of the 50% cut-off electron energy. 98
4.32 Plot of best fit betatron radiation scaling factor as a function of the 90% cut-off electron energy. 99
4.33 Plot of best fit betatron radiation scaling factor as a function of the electron beam charge. 100

5.1 Schematic of XCERP diffraction setup at the Centre for Advanced Laser Applications. 103
5.2 Example dark image of the Andor DO432-BN-DD at −30 °C. 108
5.3 Mean CCD counts along pixel columns for a set of dark images at −30 °C. 109
5.4 Example dark image at −40 °C, 100 ms exposure time and 1 µs/pixel readout speed. 109
5.5 Mean CCD counts along pixel columns for a set of dark images at −40 °C. 110
5.6 Example dark image at −50 °C, 100 ms exposure time and 1 µs/pixel readout speed. 110
5.7 Mean CCD counts along pixel columns for a set of dark images at −50 °C. 111
5.8 Mean pixel value of 100 consecutive images after subtraction of the average image. 111

5.9 Standard deviation of each pixel across 100 consecutive dark images. . 112
5.10 Example image after novel background subtraction at −50 °C. 114
5.11 Example image after novel background subtraction at −30 °C 114
5.12 Example of a subimage of a single data image at two different colour scales. 116
5.13 Example of a subimage of a single data image at two different colour scales after background subtraction. 117
5.14 Example of binary mask. 118
5.15 Events classified by shape and size. 118
5.16 Example of processed data image, containing only X-ray events. 119
5.17 Plot of quantum efficiency and transmittance for the Andor DO432-BN-DD. 120
5.18 Example raw data image with minimal shielding. 121
5.19 Example raw data image with additional lead shielding 122
5.20 Example raw data image with additional lead shielding and increased distance from interaction point. 123
5.21 Histograms of Figure 5.18, 5.19 and 5.20. 124
5.22 Electron spectrometer images for consecutive shots showing unstable electron beam production. 125
5.23 Electron spectrometer images for similar shots. 126
5.24 Sample section of an image of X-ray events after processing. Each event shown may originally have been a multiple pixel event. 127
5.25 Histogram of X-ray energies for different events. 128
5.26 Map of pixel location to angle in degrees. 129
5.27 Histogram of X-ray events binned against energy and angle. 130
5.28 Retrieved X-ray spectra for all event types. 131
5.29 Histogram of X-ray events binned against energy and angle for 5 reference shots. 131
5.30 Histogram of X-ray events binned against energy and angle for 5 powder shots. 132
5.31 Difference in histogram of X-ray events for 5 powder shots and 5 reference shots binned against energy and angle. 133
5.32 Simulated scatter plot of angle from powder centre to detector as a function of photon energy. 134

6.1 Example of GEANT4 geometry with 5 incident electrons. 138
6.2 Comparison of electron energy spectrum used in GEANT4 and as measured in experiment. 147
6.3 GEANT4 simulation of 10^5 electrons. 149
6.4 Comparison of energy spectra of scored particles from GEANT4 simulations. 151
6.5 GEANT4 simulation of 10^6 initial electrons. 152
6.6 GEANT4 simulation of 10^5 initial electrons and no aluminium or lead shielding. 153
6.7 Comparison of energy spectra of scored particles from GEANT4 simulations. 154
6.8 Differential cross section as a function of polar angle and scattered photon energy. 157
6.9 Difference of path length remaining L_{rem} and range R of an electron plotted against electron energy. 159

6.10 GEANT4 simulation of 10^6 initial electrons with an additional 30 µm aluminium shield. 163
6.11 Comparison of energy spectra of scored particles from GEANT4 simulations of 10^6 initial electrons with and without a 30 µm layer of aluminium 163
6.12 GEANT4 simulation of 10^6 initial electrons with a 25 mm plastic layer covering the aluminium breadboard and an additional 30 µm aluminium shield. 165
6.13 Comparison of energy spectra of scored particles from GEANT4 simulations. 165
6.14 GEANT4 simulation of 10^6 initial electrons with increased lead shielding from 5 mm to 10 mm and an additional 30 µm aluminium shield. 166
6.15 GEANT4 simulation of 10^6 initial electrons with increased lead shielding from a 5 mm layer extending to the chamber floor to a 50 mm cube surrounding the aluminium cube, and an additional 30 µm aluminium shield. 167
6.16 Comparison of energy spectra of scored particles from GEANT4 simulations of 10^6 initial electrons with 5 mm thick, 10 mm and 50 mm lead shielding and an additional 30 µm aluminium shield. 167
6.17 GEANT4 simulation of 10^6 initial electrons with electron spectrometer positioned ~ 2 m upstream from the scorer. 169
6.18 Comparison of energy spectra of scored particles from GEANT4 simulations at different distances. 169
6.19 Comparison of energy spectra of scored particles from GEANT4 simulations of 10^5 initial electrons with various combinations of step size and cut in range. 170

List of Tables

6.1 Production thresholds of photons and electron for aluminium and lead using various range in cuts 145
6.2 Table of cross sections σ, mass attenuation coefficients μ and probability of Compton scattering, for various photon energies. 160

Chapter 1

Introduction

1.1 Bright X-ray sources and their applications

It would not be an overstatement to say that the discovery of X-rays [5] has revolutionised our understanding of the world. The application of X-rays span across many areas of science, industry and medicine. Examples include structural analysis of materials via X-ray diffraction, non-destructive testing of machined components and radiotherapy. Over the last few decades, there have been many impressive developments in X-ray generation, resulting in brighter, shorter duration beams and at shorter wavelengths [6]. This has opened up a plethora of possibilities. For instance, in traditional X-ray crystallography, structure determination is inferred from a diffraction pattern produced by constructive interference from a crystalline material. With the advent of bright, ultrashort (on the femtosecond timescale) X-ray beams, a temporal and 3D 'snapshot' of a single particle, such as a virus can be captured in its native environment [7]. The short pulse duration also allows for investigation of ultrafast phenomena such as chemical reactions.

1.1.1 A brief history of traditional bright light sources

There are many facilities around the world capable of producing radiation with high brilliance. This was made possible after four generations of development in synchrotron radiation, starting with the so-called first generation light sources that were primarily used for high energy physics studies. The production of radiation was initially considered to be a parasitic by-product of the synchrotron accelerators, but the second generation sources were built as dedicated light sources [8]. The current workhorse for bright sources of radiation are the third and fourth generation light sources, which use 'insertion devices' placed in straight sections of the beamline to generate the high brilliance beams from the circulating electron bunches. The insertion devices house a periodic magnetic field which cause the injected electrons to 'wobble' as they propagate through the structure, thereby generating synchrotron radiation. The devices are also known as *undulators* or *wigglers*, depending on the size of the undulations. Fourth generation light sources are very similar to third generation sources, but further improves on various properties of the radiation.

1.1.2 Generation of bright radiation

Before being steered into insertion devices or used in some other beamline application, the particle beams are generated and accelerated to high energies in an accelerator that is either linear or circular. A common scheme for reaching GeV level electron beams is to use a radio frequency linear accelerator (RF linac) which uses alternating electric fields in a chain of cavities, synchronised such that an electron bunch will have traversed the length of each cavity before the sign of the electric field flips, leading to the bunch always being accelerated in the same direction.

The undulators and wigglers themselves are conceptionally simple devices, consisting of arrays of magnets arranged with alternating poles such that any charged particle travelling in the vicinity experiences a continuously varying and periodic magnetic field.

This field causes the energetic particle to bend and radiate into a narrow cone in the forward direction. There are, of course, a number of technical challenges associated with this. For example, in order to contain the magnetic field in the desired region, permanent magnets can be arranged in what is known as a Halbach array whereby the magnetic field is significantly reduced on one side of the array while being enhanced on the opposite side [9, 10].

The rise of fourth generation light sources stems from free electron lasers (FELs) which operate similarly to undulators, but additionally uses a phenomenon whereby the electrons interact with the combined field of the magnetic structure and its self-made radiation in a positive feedback loop to produce bright, coherent radiation [11].

1.2 Laser wakefield acceleration as a source of bright radiation

Although third and fourth generation light sources are widely used, an alternative approach for both the acceleration of electrons and the production of bright radiation has been gaining ever increasing attention—plasma wakefield acceleration. In this scheme, the accelerating field comes from the displacement of background electrons in an underdense plasma, leaving behind a volume of positively charged plasma ions. This space-charge separation creates a strong electrostatic field, known as a *wakefield*, which can be used to accelerate either an externally injected bunch of particles or plasma electrons trapped through some mechanism.

A prominent advantage of plasma wakefield acceleration is its ability to sustain much higher electric fields, on the order of 100 GV/m. These field strengths are huge compared to those typically found in RF linacs which are inherently limited by electrical breakdown of the cavity walls, leading to fields less than 100 MV/m [12]. Consequently, a huge reduction in the accelerating length can be achieved for a given desired beam energy, which may lead to reduced costs, infrastructure and manpower required for operation.

For comparison, the Diamond Light Source in Oxfordshire is a third generation light source over 500 m long (circumference) and produces 3 GeV electron beams. Contrasting with this, an energy of 4.2 GeV can be achieved over a mere 9 cm using a laser wakefield accelerator [13]. Of course, it must be said that this would not be possible without a state-of-the-art laser system, which can be very expensive and also has a size of order 10s of metres. The repetition rate and reliability of lasers would also require improvement in order to compete directly with current third generation light sources.

1.2.1 Electron acceleration

There are several methods to displace the electrons, or more accurately, to excite plasma waves. The method of interest for this thesis is laser wakefield acceleration (LWFA) whereby an ultrashort high-intensity laser pulse is tightly focused into a plasma; charged particles in the vicinity of the high electric field experience a force, called the *ponderomotive force*, which scales as the gradient of the intensity.

After the laser propagates past a point in the plasma, the background electrons stream back to their initial positions due to the space charge separation, but overshoot due to their momentum, resulting in a longitudinal wave with frequency ω_p. In the co-moving frame of the laser pulse, the wakefield structure appears static as the wave propagates with phase velocity equal to the laser group velocity. Hence, charged particles which are 'trapped' in the wakefield can be accelerated close to the speed of light.

The idea of using a wakefield (resulting from the interaction of an underdense plasma with a strong laser pulse of duration shorter than the plasma frequency) for particle acceleration was first suggested by Tajima and Dawson in their seminal paper [14]. Previous laser systems were not capable of such short pulse durations, and required an alternative route to driving the wakefield. Two such instances are the self-modulated laser wakefield accelerator (SM-LWFA) [15, 16]—based on instabilities in a single long pulse—and the plasma beat wave accelerator (PBWA) [17] which uses two co-propagating

pulses whose frequencies differ by the plasma frequency. With the advent of *chirped pulse amplification* (CPA) [18], in which a laser pulse is stretched and chirped using gratings, amplified and then compressed again, ultrashort durations on the scale of the plasma frequency could be produced, allowing the LWFA field to flourish.

Typically, the charge obtained in a laser-plasma generated electron beam is of the order of picocoulombs to a few nanocoulombs. First reports of the generation of quasi-monoenergetic beams took place in 2004 [19–21], with the current highest electron beam energy coming in at 4.2 GeV [13].

1.2.2 Radiation generation

Two main approaches of producing radiation from LWFAs exist. Not covered in any length in this work is the generation of secondary radiation outside of the laser-plasma interaction, using the electron beam produced by the laser wakefield accelerator to seed some other interaction, like Thomson scattering [22, 23], synchrotron radiation generation in an undulator [24–26] or 'lasing' in a FEL [27].

The other route essentially comes 'for free' since electromagnetic radiation is emitted during any process in which charged particles are accelerated. In the case of LWFAs, this radiation can be very pronounced. The primary cause of this radiation is the motion of particles as they are accelerated in the wakefield in the direction *transverse* to the laser pulse propagation. The simplest method of initiating this motion is to inject the particles away from the laser axis; the electric field acts to focus (or defocus) the injected particles, resulting in the particles performing an undulating motion and emitting *betatron radiation* in the process. In practice, off-axis injection often occurs naturally, so most LWFAs also emit significant amounts of betatron radiation. An alternate condition to allow the emission of betatron radiation is to inject the electrons with a large initial transverse momentum.

This radiation has a number of useful properties, such as small source size (on the

order of a few microns) which makes it ideal for applications requiring good spatial coherence, such as phase contrast imaging [28, 29]. In these applications, detailed images of objects can be produced which would normally be transparent. On the other hand, the brightness and tuneability of betatron radiation lends itself to imaging relatively opaque materials, since harder X-rays can be generated with an increase in laser power. An excellent example is the tomographic reconstruction of a bone sample [30].

1.2.3 Methods for characterising betatron radiation

In many applications of betatron radiation, it is necessary or helpful to characterise the radiation source. Useful parameters to measure include: the source size, the spectrum and the brightness. These measurements are complicated by the fact that in many cases, the properties of the betatron source fluctuate significantly from shot to shot, reflecting jitter in the parameters of the electron beam.

A number of different techniques have been developed by various authors to characterise the betatron radiation produced in a laser wakefield accelerator. For example, penumbral imaging of a knife-edge can be used to measure the betatron source size whereby the X-ray beam is partially obstructed by the edge and the Fresnel diffraction measured using an X-ray charge-coupled device (CCD) [28, 31–33].

By recording the transmission through arrays of filters, the betatron spectrum can be estimated [30, 33–35]. The spectrum can also be measured by scanning a single-crystal X-ray monochromator [36], which yields a time-averaged spectrum, or in a single shot by photon counting [37, 38].

Measurement of the betatron radiation can also provide a way to probe details of the acceleration process. Albert et al. use the total flux of X-rays recorded and the energy spectrum of the electron beam to identify the betatron oscillation amplitude and electron energy before acceleration using a fit to their simulation model [36]. In another study, a direct measurement of the electron orbits during acceleration could be identified

from the betatron radiation spatial profile [39]. When long dielectric capillaries are used, *dephasing* (where the electron bunch outruns the acceleration region of the wakefield) can potentially be identified by looking for bremsstrahlung radiation due to electrons hitting the capillary walls [40].

1.3 Theory of betatron radiation

A brief outline of the key betatron radiation theory is given here [41]. For an electron performing betatron oscillations of amplitude r_β in a plasma focusing channel, the betatron frequency is given by

$$\omega_\beta = \frac{\omega_\mathrm{p}}{\sqrt{2\gamma}}, \tag{1.1}$$

where γ is the Lorentz factor and $\omega_\mathrm{p} = [n_\mathrm{e} e^2/(m_\mathrm{e}\epsilon_0)]^{1/2}$ is the plasma frequency.

The power radiated by the electron over a single betatron period $\bar{P}_s$ is given by [41]

$$\bar{P}_s \simeq r_\mathrm{e} m_\mathrm{e} c^3 \gamma_{z0}^2 k_\beta^2 a_\beta^2/3, \tag{1.2}$$

where $r_\mathrm{e} = (4\pi\epsilon_0)^{-1}(e^2/m_\mathrm{e}/c^2)$ is the classical electron radius, m_e is the mass of an electron, $a_\beta = \gamma_{z0} k_\beta r_\beta$ is the betatron strength parameter and $k_\beta = k_p/\sqrt{2\gamma_{z0}}$ is the betatron wave number. Hence,

$$\begin{aligned} \bar{P}_s &\propto \gamma_{z0}^4 k_\beta^4 r_\beta^2 \\ &\propto \gamma_{z0}^2 r_\beta^2. \end{aligned} \tag{1.3}$$

The total energy radiated by a single electron W_s is found from the product of $\bar{P}_s$, the time it takes to travel a single period $\lambda_\beta/c = 2\pi/(ck_\beta)$ and the number of betatron

periods N_β

$$W_s \simeq (2\pi/3) r_\mathrm{e} m_\mathrm{e} c^2 \gamma_{z0}^2 k_\beta a_\beta^2 N_\beta, \tag{1.4}$$

$$\propto \gamma_{z0}^4 k_\beta^3 r_\beta^2 N_\beta,$$

$$\propto \gamma_{z0}^{5/2} r_\beta^2 N_\beta. \tag{1.5}$$

In the asymptotic limit where $a_\beta \gg 1$, i.e. continuous, wiggler-like radiation, the spectrum in the plane of betatron oscillation is given by

$$\frac{\mathrm{d}^2 I}{\mathrm{d}\omega\,\mathrm{d}\Omega} \simeq N_\beta \frac{3e^2}{2\pi^2 \epsilon_0 c} \frac{\gamma_{z0}^2 \xi^2}{1+\gamma_{z0}^2\theta^2} \left[\left(\frac{\gamma_{z0}^2\theta^2}{1+\gamma_{z0}^2\theta^2} \right) \mathcal{K}_{1/3}^2(\xi) + \mathcal{K}_{2/3}^2(\xi) \right], \tag{1.6}$$

where θ is the angle away from axis, $\mathcal{K}_m$ is the modified Bessel function of the second kind and

$$\xi = \frac{\omega}{\omega_\mathrm{c}} \left(1+\gamma^2\theta^2\right)^{3/2}. \tag{1.7}$$

The critical frequency is the frequency above which little radiation is emitted and is given by

$$\omega_\mathrm{c} = 3 a_\beta \gamma^2 \omega_\beta. \tag{1.8}$$

This definition follows that of [41, 42]. The emission in the plane of oscillation is confined to a cone of angle $\Theta \sim a_\beta/\gamma_{z0}$. Integrating (1.6) over all frequencies gives

$$\frac{\mathrm{d}I}{\mathrm{d}\Omega} \simeq \omega_\mathrm{c} N_\beta \frac{7e^2}{96\,\pi\epsilon_0 c} \frac{\gamma_{z0}^2}{(1+\gamma_{z0}^2\theta^2)^{5/2}} \left[1 + \frac{5}{7} \left(\frac{\gamma_{z0}^2\theta^2}{1+\gamma_{z0}^2\theta^2} \right) \right]. \tag{1.9}$$

It is worth noting that the formulae above are based on electron motion in a channel. When considering betatron radiation from a LWFA, where the electrons are longitudinally accelerated to high energies, the motion of the electrons would be expected to evolve

over the course of the beam acceleration, thereby changing the spectral characteristics of the X-ray emission. Indeed, as the electrons gain energy, their relativistic mass causes the betatron frequency to decrease as well as the oscillation amplitude. However, since there is a strong dependence on the radiated power with the electron energy, the majority of betatron radiation is emitted in the last few oscillations when the electrons are most energetic, and the radiation characteristics are well-described by applying the final electron parameters to the expressions above.

1.4 Outline of the thesis

Laser wakefield accelerators are an interesting, and increasingly important light source, producing betatron radiation which have a number of useful applications. The main objective of this work is to investigate the feasibility of a new method for characterising betatron radiation non-destructively, and in a single shot. This method makes use of a camera operating in a 'single photon' mode to measure X-ray diffraction from a powder of known structure.

Chapter 2: The basic theory pertaining to powder diffraction is presented here. The main result is an expression which allows calculation of the probability of diffraction for a photon of given energy and is used in later chapters.

Chapter 3: The novel technique for measuring betatron radiation is described in detail here. The method allows an angularly-resolved energy spectrum to be obtained using a CCD. Simulations are shown which demonstrate the principal behind the technique. The XCERP diffraction concept and the contents of this chapter was published as an editors' suggestion [43].

Chapter 4: An experimental campaign which took place at the Astra Gemini facility is introduced in this chapter. Two of the diagnostics which the author designed are described and some results of the experiment are presented.

Chapter 5: The implementation of the novel technique, described in Chapter 3, for

an experiment at the Ludwig-Maximilians-Universität is presented. The outcomes of the experiment are discussed.

Chapter 6: Simulations of the experimental setup from Chapter 5 were performed on GEANT4 to investigate sources of radiation other than diffraction. Improvements to the setup are discussed.

Chapter 7: A summary of the work presented in the preceding chapters is given here. The directions for future work are laid out here.

Chapter 2

Theory of X-Ray Diffraction

2.1 Introduction

The phenomenon of X-ray diffraction simply put is the term for the scattering of short wavelength electromagnetic waves by the atoms in the substance which the waves are incident on. For crystals, the periodic nature of the atoms result in a fixed phase relation between scattering sites thus giving rise to strong constructive interference in certain directions. Only the electrons in the atoms of a material are considered in X-ray diffraction as they are many orders of magnitude less massive than the positively charged nuclei, and so are accelerated—and hence radiate—much more strongly in response to the electric field of incident electromagnetic radiation.

This section describes some of the basic theory involved in the extensive field of X-ray diffraction. Much of what is described below can be found in [1–3].

2.2 Scattering from a Single Electron

First, we consider a simple electromagnetic plane wave with angular frequency ω incident on a free electron. The classical result is that the electron re-radiates a portion of the incident EM wave as Thompson scattered radiation. For an *unpolarised* X-ray beam

with initial (time-averaged) intensity $I_0 = (c/\mu_0)B_0^2/2 = c\epsilon_0 E_0^2/2$, where E_0 (B_0) is the peak electric (magnetic) field, the scattered intensity I_e from a *single electron* is given by the well known *Thomson formula* [3], which in SI units is

$$\begin{aligned} I_\mathrm{e} &= I_0 \left(\frac{e^2}{4\pi\varepsilon_0 m_\mathrm{e} c^2 R}\right)^2 \left(\frac{1+\cos^2 2\theta}{2}\right), \\ I_\mathrm{e} &= I_0 \left(\frac{r_\mathrm{e}}{R}\right)^2 \left(\frac{1+\cos^2 2\theta}{2}\right), \\ I_\mathrm{e} &\approx 7.94 \times 10^{-30}\,\mathrm{m}^2 \left(\frac{I_0}{R^2}\right)\left(\frac{1+\cos^2 2\theta}{2}\right), \end{aligned} \tag{2.1}$$

where 2θ is the angle between the direction of propagation of the incident beam and that of the scattered beam, R is the distance from the electron to the point of observation, and r_e is the classical electron radius. The factor of 10^{-30} may seem to imply that virtually no radiation would be scattered, however even in a few milligrams of material, there are some 10^{20} electrons which can contribute to scattering.

The term in brackets containing θ is a polarisation factor which can take on different forms for different polarisations of the incident beam. The polarisation factors for some common polarisations are:

(i) $\dfrac{1+\cos^2 2\theta}{2}$, for unpolarised light as above;

(ii) $\cos^2 2\theta$, for light polarised in the plane of the incident and scattering directions;

(iii) 1, for light polarised perpendicular to the plane of the incident and scattering directions;

(iv) $\dfrac{1}{2}\left[1+\cos^2 2\theta + p\sin^2 2\theta\right]$, for a more general polarisation state where p is the degree of polarisation and ranges from $p=-1$ (equivalent to case (ii)), through $p=0$ (equivalent to case (i)), up to $p=1$ (equivalent to case (iii)).

2.3 Scattering from an Atom

In an atom, radiation is scattered from the bound electrons and so is dependent on the electronic charge distribution in the atom. The *atomic scattering factor* f describes the efficiency of diffraction from the bound electrons into a given direction. It is given by the ratio of the amplitude of the wave coherently scattered by the bound electrons to the amplitude of the wave scattered by a single free electron. The factor accounts for the phase relation between the bound electrons and is in general a complex number, so the intensity of the diffracted wave will be proportional to $|f|^2$. Hence,

$$I_{\text{coh}} = I_0 \, |f|^2 \left(\frac{r_{\text{e}}}{R}\right)^2 \left(\frac{1 + \cos^2 2\theta}{2}\right). \tag{2.2}$$

As the deflection angle θ approaches zero, the waves from each electron in the atom become more in phase with each other and f increases, up to the maximal value of the atomic number Z (since this is the number of bound electrons) in the case of forward scattering when $\theta = 0$. Similarly, as the wavelength of incident radiation increases, the relative path difference between scattered waves decreases, leading to less destructive interference and the factor $f \to Z$.

The atomic scattering factor can be calculated by summing the scattering from each of the N_{e} electrons in the atom, $f = \sum_{n=1}^{N_{\text{e}}} f_{\text{e},n}$. Here, f_{e} is the *scattering factor* which is a measure of the scattering efficiency and is given by the ratio of the amplitude of unmodified scattering from a single electron in a given element to that of classical theory, where unmodified scattering refers to scattering for which the wavelength remains unchanged.

The modified scattering from an electron is $i_{\text{e}} = 1 - f_{\text{e}}^2$. The modified scattering factor per atom is thus $i = \sum_{n=1}^{N_{\text{e}}} i_{\text{e},n} = \sum_{n=1}^{N_{\text{e}}} (1 - f_{\text{e},n}^2) = Z - \sum_{n=1}^{N_{\text{e}}} f_{\text{e},n}^2$ and relates to the proportion of radiation which is scattered incoherently. This *Compton modified radiation* is incoherent due to the increase in radiation wavelength and also the absence

of a fixed phase relation between incident and scattered wave. It is shown in [44–46] the sum of the modified and unmodified scattering of an electron in an atom for a given direction yields the same classical result for Thomson scattering of a free electron. In other words, as the unmodified scattering decreases, due to, say, increasing θ, the level of modified scattering increases to keep the overall level of scattering constant.

Explicit calculation of the atomic scattering factor is not required as they can be taken from precompiled tables [47] which have previously been calculated using the relativistic Hartree-Fock equations as set out in [48].

2.4 Scattering from a Crystal

2.4.1 Bragg law

In a single crystal where there is a well-known relation in the positions of atomic sites, the superposition of waves scattered from adjacent planes lead to constructive and destructive interference. A simple relation can be found which satisfies the condition for constructive interference from these planes by considering the path of two rays as shown in Figure 2.1. Constructive interference occurs when the path difference ABC is some integer multiple m of the wavelength of the rays λ. This leads to the famous Bragg law:

$$m\lambda = 2\, d_{hkl}\, \sin\theta_{\mathrm{B}}, \tag{2.3}$$

where d_{hkl} is the interplanar spacing between between the $\{hkl\}$ set of planes and m is known as the order of diffraction, with $m = 1, 2, 3, \ldots$. For a cubic crystal with lattice constant a_0, the interplanar spacing is $d_{hkl} = a_0/\sqrt{h^2 + k^2 + l^2}$. Finally, θ_{B} is the angle between the diffracting set of planes and the diffracted ray, commonly referred to as the *Bragg angle*.

Note that m can be omitted from (2.3) since m-th order diffraction from the

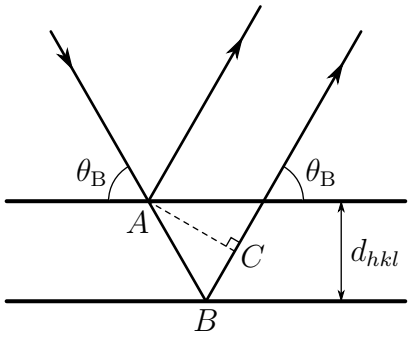


Figure 2.1: Simple derivation of the Bragg law.

$\{h, k, l\}$ set of planes with spacing d can be regarded as first order diffraction from the $\{mh, mk, ml\}$ set of planes with spacing $d' = d/m$ [3].

2.4.2 Structure factor

Recalling from Section 2.3, the intensity scattered from a single atom is given by (2.2). For a structure containing multiple atoms, the total EM field scattered is equal to the sum of the scattered fields from each atomic site. The expression for the diffracted intensity from a crystal depends not only on the atomic scattering factors of the individual atoms in the unit cell, but also some term which accounts for the phase difference in the reflected radiation from different atomic sites. These two parts form the *structure factor* F_{hkl} and is given by

$$F_{hkl} = \sum_{n=1}^{N_{\text{atom}}} f_n \exp\left[2\pi \mathrm{i}\left(hu_n + kv_n + lw_n\right)\right], \tag{2.4}$$

where N_{atom} is the total number of atoms of in the unit cell. The position vector of the n-th atom can be written in terms of the *primitive translation vectors* $\mathbf{a}_1$, $\mathbf{a}_2$ and $\mathbf{a}_3$ (also known as the *crystallographic axes*), giving

$$\mathbf{r}_n = u_n\mathbf{a}_1 + v_n\mathbf{a}_2 + w_n\mathbf{a}_3, \tag{2.5}$$

where u, v and w are the *fractional* coordinates of the atom in the unit cell.

The structure factor can often be simplified such as in the case of a monatomic face-centred cubic crystal where: $F_{hkl} = 4f$ when h, k and l are all even or all odd; and $F_{hkl} = 0$ when h, k and l have mixed parity. These simplifications occur due to destructive interference between the atoms in the unit cell.

2.4.3 Multiple unit cells

The structure factor accounts for the phase relation of atoms in a unit cell. However, there is also a phase relation between neighbouring unit cells. A derivation can be found in [1], but the main result is the width of a diffraction line decreases as the number of unit cells in the crystal increases. The function describing this is of the form

$$y_i = \frac{\sin^2 N_i\, x_i}{\sin^2 x_i}, \tag{2.6}$$

where $x_i = \frac{1}{2}\Delta\mathbf{k} \cdot \mathbf{a}_i$ and N_i is the number of unit cells in the crystal along the direction of the crystal axis $\mathbf{a}_i$. The quantity $\Delta\mathbf{k}$ is the difference in wave vectors of the incident and reflected wave. The maximum of the function is found when x_i is a multiple integer of π, corresponding to the Bragg condition being satisfied.

Closely related to the primitive translation vectors $\mathbf{a_i}$, which describe the length of the unit cell along the direction of the crystal axes, are the *reciprocal lattice vectors* b_i, which are perpendicular the crystal planes and form the basis for reciprocal space. By expressing $\Delta\mathbf{k}$ in terms of reciprocal lattice vectors and integrating (2.6) over the volume in reciprocal space containing all reciprocal vectors which contribute to diffraction in a given direction, it can be found that the total energy diffracted is proportional to $R^2\lambda^3 N/v$, where R is the distance to the point of observation, λ is the X-ray wavelength, $N = \prod_i N_i$ is the total number of unit cells in the crystal and v is the volume of each unit cell.

2.4.4 Debye-Waller factor

Another modification to the intensity of X-ray diffraction is the effect of thermal vibrations, causing small deviations from the ideal fractional coordinates u, v and w mentioned above, and is referred to as the *Debye-Waller factor*, or *Debye temperature factor*. The result of this is to perturb the fixed phase relationship between atomic sites in the crystal and hence reduce the intensity of Bragg peaks in favour of increasing the overall background level. The intensity factor giving rise to the reduction is commonly of the form $\exp[-2W(T)]$, where $W(T)$ is a function which can be calculated from the average displacement of an atom, which varies with temperature T.

The explicit calculation of the factor is highly non-trivial, requiring many approximations, such as assuming constant volume with increasing temperature (contrasting with the more typical physical scenario of constant pressure). The situation is exacerbated if the crystal is composed of multiple elements. A comprehensive discussion of the Debye-Waller factor can be found in [2].

An analytical model for the factor is derived in [49] and is stated here for reference.

$$\exp(-2W) = \exp\left[-2B\left(\frac{\sin\theta}{\lambda}\right)^2\right], \tag{2.7}$$

where B is dependent on the material and the temperature. Physically, B is directly proportional to the mean-square displacement of an atom in the direction normal to the plane of diffraction.

2.5 Scattering from a Powder

The diffraction of X-rays is commonly studied using materials which are in a single-crystal form, resulting in well-defined and bright *Laue spots*, when the Bragg condition (2.3) is met—more formally, it is the 3-dimensional analogy of the Bragg law, the *Laue equations* which determine this.

An alternative setup is to use powdered material in which there are many randomly oriented crystallites. As a result, there will always be a number of crystallites which satisfy the Laue equations, but since there is no correlation between these crystallites, diffracted rays will be projected into a cone with opening full-angle $2(2\theta)$, forming circular rings—Debye-Scherrer rings—on a plane detector.

2.5.1 Multiplicity

In an ideal powder, reflections from equivalent planes contribute to the same diffraction signal. The number of equivalent planes depends on the symmetry properties of the lattice. For instance, in a simple cubic crystal system, the (100) plane would contribute to the same signal as the $(\bar{1}00)$, (010), $(0\bar{1}0)$, (001) and $(00\bar{1})$ planes, leading to a *multiplicity* of 6 for this family of reflections. The multiplicity term for the family of planes $\{hkl\}$ is represented by M_{hkl}. Note that the usual notation of a bar (e.g. $\bar{x}$) is used to represent the negative integer value in the planes mentioned above. This factor is not present for diffraction from a crystal since each of these planes result in Laue spots which are spatially separated on a detector for a fixed orientation of the crystal.

2.5.2 Lorentz-polarisation factor

From Section 2.2 it is commented that the polarisation of the incident radiation plays a role in the intensity diffracted. The *Lorentz-polarisation factor* accounts for both the effects of polarisation and the diffraction geometry for a given crystal orientation relative to the ingoing and outgoing beams.

For all cases of diffraction, there is an intrinsic finite width to the signal (c.f. (2.6)), regardless of the incident beam divergence. This implies there is a small range of angles through which diffraction can occur and so an *integrated intensity* is often implied as the measurable quantity. In the case of single crystal diffraction, it is experimentally measured by rotation of the sample about the axis which is normal to the plane of

the incident and reflected beam, followed by integration of the diffracted signal. The same precession is not required for the powder method since the domains are randomly orientated. In other words, all possible angles are covered without rotating the sample. Hence, the equivalent integrated intensity in powder diffraction is calculated from just the integration of the powder signal.

By considering the path difference of rays incident on different atoms in a plane, the range of angles which contribute to a single diffraction line is calculated when the condition for destructive interference is met. Using this argument, it can be shown that the range varies as $1/\sin\theta$, which in turn determines the integrated intensity. The width of the diffraction line can be found by applying the same interference above, but for scattering from consecutive parallel planes. This leads to the *Scherrer equation* [1] which varies as $1/\cos\theta$. Hence the combined effect gives rise to the geometrical factor of $1/(\sin\theta\cos\theta) \propto 1/\sin 2\theta$.

There is a further correction for powder diffraction which can be visualised by considering the normal vectors of all planes in the powder, forming a uniform distribution of points on a sphere. The range of angles which contribute to diffraction for a given hkl combination lies in an annular strip of width $\Delta\theta$ as depicted in Figure 2.2. Hence, the total fraction of correctly oriented planes is equal to the area of the strip divided by the area of the sphere, which turns out to be proportional to $\cos\theta$. Therefore, the final Lorentz-polarisation factor (down to some constant C) for a powdered material is

$$LP = C\,\frac{1+\cos^2 2\theta}{\sin\theta}. \tag{2.8}$$

2.6 Effective Volume

The intensity of the diffracted beam increases as a larger volume of the material is irradiated, i.e. when more crystal planes contribute to the diffraction process. However,

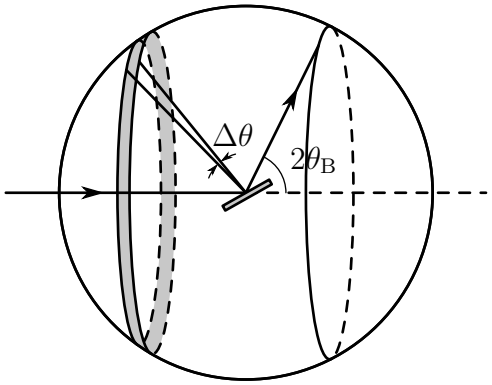


Figure 2.2: Fraction of plane normals contributing to diffraction from a powder.

at the same time, this reflected beam is subject to attenuation as it traverses the sample. For a homogeneous material, the intensity of the X-ray beam I decreases with increasing distance through the material x.

$$\begin{aligned} -\frac{dI}{I} &= \mu \, \mathrm{d}x, \\ \Rightarrow I(x) &= I_0 \, \exp\left[-\left(\frac{\mu}{\rho}\right)\rho \, x\right], \end{aligned} \tag{2.9}$$

where ρ is the material density, I_0 is the intensity at $x = 0$ and (μ/ρ) is the mass attenuation coefficient. This latter quantity is dependent on the material and varies with photon energy. It is worth pointing out that for a powder material, the density ρ outside the round brackets should be replaced with the density of the powder ρ' and is related to the density of the material in bulk form ρ by the *packing factor* $f = \rho'/\rho$. The mass attenuation coefficient is always expressed using the bulk density ρ.

The two competing effects of attenuation and increased diffraction as the beam penetrates further into the material depend on the geometry, which is discussed below for the two different modes of diffraction: *reflection*, where the diffraction signal of interest is on the same side of the sample as the incident beam; and *transmission*, where

the observed diffraction is on the side of the sample from which the incident beam exits the material. The factor which represents these two effects will be referred to as the *effective volume* V [1]. Note that the effective volume relates to the number of unit cells in the sample N (c.f. Section 2.4.3) via $N = V/v$, recalling v is the volume of the unit cell.

The effective volume was independently calculated for a number of different geometries as shown below, but can be found in literature in an equivalent form [50].

2.6.1 X-ray diffraction in reflection mode

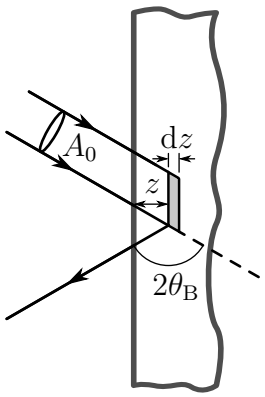
Symmetric back reflection from an infinite slab

A common configuration for X-ray diffraction in reflection mode is for the angle of incidence and angle of reflection to be equal (see Figure 2.3(a)). The crystal plane from which the beam diffracts is parallel to the target surface, meaning the incident and reflected beam both form an angle θ_B (from (2.3)) with the plane of the surface. This configuration is known as the Bragg-Brentano geometry [51]. The material is often assumed to be infinitely thick as it results in an effective volume which remains constant irrespective of angle.

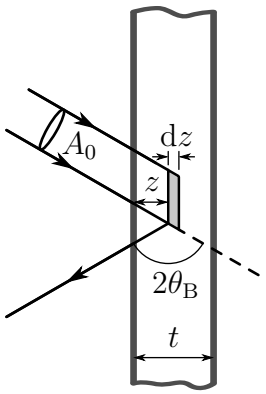
Given an incident beam of cross-sectional area A_0, the total path length l taken by a ray which has diffracted from a volume element $\mathrm{d}V = A_0\ \mathrm{d}z/\sin\theta_\mathrm{B}$ some distance z from the surface, can be calculated as

$$l(z) = 2\left(\frac{z}{\sin\theta_\mathrm{B}}\right). \tag{2.10}$$

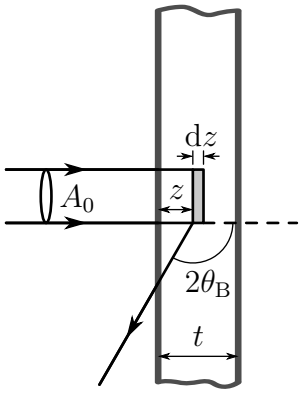
The effective volume can then be calculated by integrating the attenuation term from



(a) Symmetric incident and reflected beam in reflection mode (infinite thickness).



(b) Symmetric incident and reflected beam in reflection mode (finite thickness).



(c) Asymmetric incident and reflected beam in reflection mode.

Figure 2.3: Geometries used in the calculation of the effective volume for X-ray diffraction in reflection mode.

(2.9) over all volume elements

$$V = \iiint_V \exp\left[-\mu l(z)\right] \mathrm{d}V. \tag{2.11}$$

Note, the linear absorption coefficient μ should be replaced with an *effective* absorption coefficient $\mu' = \mu f$ when dealing with a powder.

For the case of the Bragg-Brentano geometry,

$$V = \int_0^\infty \left(\frac{A_0}{\sin\theta_\mathrm{B}}\right) \exp\left(\frac{-2\mu z}{\sin\theta_\mathrm{B}}\right) \mathrm{d}z, \tag{2.12}$$

$$= \frac{A_0}{2\mu}. \tag{2.13}$$

Note that the effective volume is not dependent on θ_B.

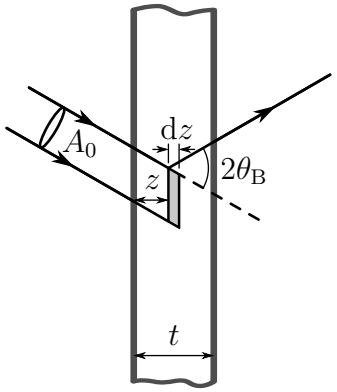
The effective volume for this geometry follows derivations from [1, 3]. The author has used the same method to derive the effective volume for other geometries and is shown below.

Symmetric back reflection from a finite slab

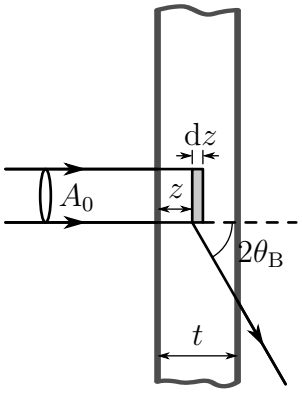
The assumption of an infinitely thick sample can be removed by making the change $\infty \to t$ in (2.12), where t is now the thickness of the sample as depicted in Figure 2.3(b). This yields an effective volume

$$V = \int_0^t \left(\frac{A_0}{\sin\theta_\mathrm{B}}\right) \exp\left(\frac{-2\mu z}{\sin\theta_\mathrm{B}}\right) \mathrm{d}z, \tag{2.14}$$

$$= \left(\frac{A_0}{2\mu}\right) \left[1 - \exp\left(-\frac{2\mu t}{\sin\theta_\mathrm{B}}\right)\right]. \tag{2.15}$$



(a) Symmetric incident and reflected beam in transmission mode.



(b) Asymmetric incident and reflected beam in transmission mode.

Figure 2.4: Geometries used in the calculation of the effective volume for X-ray diffraction in transmission mode.

Asymmetric back reflection from a finite slab

For an X-ray beam at normal incidence to the sample, reflected rays will form an angle $2\theta_B - \pi/2$ with the sample surface and the volume element is simply $dV = A_0\,dz$. The path length in this case is

$$l(z) = z + \frac{z}{\sin\left(2\theta_B - \frac{\pi}{2}\right)} = z\left(1 - \frac{1}{\cos 2\theta_B}\right). \tag{2.16}$$

This leads to an effective volume

$$V = \int_0^t A_0 \exp\left[-\mu z\left(1 - \frac{1}{\cos 2\theta_B}\right)\right] dz, \tag{2.17}$$

$$= \left(\frac{A_0}{\mu\left(1 - \sec 2\theta_B\right)}\right)\left\{1 - \exp\left[-\mu t\left(1 - \frac{1}{\cos 2\theta_B}\right)\right]\right\}. \tag{2.18}$$

2.6.2 X-ray diffraction in transmission mode

Symmetric forward reflection from a finite slab

X-ray diffraction of a beam in the forward direction can be calculated using a similar method as in the back-reflected case. When the incident and reflected angles with respect to the target surface are identical, the total path length is

$$l = \frac{t}{\cos\theta_{\mathrm{B}}}. \tag{2.19}$$

Note that there is no dependence on z in this expression. The volume element for this geometry is $\mathrm{d}V = A_0\,\mathrm{d}z/\cos\theta_{\mathrm{B}}$. The diffracted intensity will thus be modified given by

$$V = \int_0^t \left(\frac{A_0}{\cos\theta_{\mathrm{B}}}\right) \exp\left(-\frac{\mu t}{\cos\theta_{\mathrm{B}}}\right) \mathrm{d}z, \tag{2.20}$$

$$= \left(\frac{A_0\, t}{\cos\theta_{\mathrm{B}}}\right) \exp\left(-\frac{\mu t}{\cos\theta_{\mathrm{B}}}\right). \tag{2.21}$$

Asymmetric forward reflection from a finite slab

The path length in transmission mode for an X-ray beam at normal incidence as represented by Figure 2.4(b) is

$$l(z) = z + \frac{t-z}{\cos 2\theta_{\mathrm{B}}} = z\left(1 - \frac{1}{\cos 2\theta_{\mathrm{B}}}\right) + \frac{t}{\cos 2\theta_{\mathrm{B}}}. \tag{2.22}$$

The effective volume is therefore

$$V = \int_0^t A_0 \exp\left[-\mu z\left(1 - \frac{1}{\cos 2\theta_{\mathrm{B}}}\right) - \frac{\mu t}{\cos 2\theta_{\mathrm{B}}}\right] \mathrm{d}z, \tag{2.23}$$

$$= \left[\frac{A_0 \exp\left(-\mu t \sec 2\theta_{\mathrm{B}}\right)}{\mu\left(1 - \sec 2\theta_{\mathrm{B}}\right)}\right] \left\{1 - \exp\left[-\mu t\left(1 - \frac{1}{\cos 2\theta_{\mathrm{B}}}\right)\right]\right\},$$

$$= \left(\frac{A_0}{\mu\left(1 - \sec 2\theta_{\mathrm{B}}\right)}\right) \left[\exp\left(-\frac{\mu t}{\cos 2\theta_{\mathrm{B}}}\right) - \exp\left(-\mu t\right)\right]. \tag{2.24}$$

This geometry is of particular interest experimentally due to the ease of implementation in situ, requiring the powder target to be placed relatively normal to the beam and the detector situated at some angle $2\theta_{\mathrm{B}}$ to the target. Contrasting with standard X-ray crystallography experiments, the use of a bespoke diffractometer would not be required, which would otherwise be problematic in laser-plasma experiments.

2.6.3 General X-ray diffraction

The author has derived the attenuation factor for a more general configuration by following the derivations above in a vector form. This general form allows the calculation of the effective volume in a scenario where the target normal vector, the incident ray and the reflected ray do not all lie in the same plane (i.e. the plane of the paper). To the author's knowledge, this has not been done elsewhere.

If we let $\mathbf{k}_0$ ($\mathbf{k}$) be the direction vector of the incident (reflected) ray and $\mathbf{n}$ is the normal vector of the rear surface of the material, i.e., $\mathbf{k}_0 \cdot \mathbf{n} > 0$ (and assume the front and rear surfaces are parallel), the total path length travelled by the ray through the material can be calculated as

$$l(z) = \begin{cases} z\left(\dfrac{1}{\mathbf{k}_0 \cdot \mathbf{n}} - \dfrac{1}{\mathbf{k} \cdot \mathbf{n}}\right), & \text{for } \mathbf{k} \cdot \mathbf{n} < 0 \text{ (Reflection)}, \quad (2.25a) \\ z\left(\dfrac{1}{\mathbf{k}_0 \cdot \mathbf{n}} - \dfrac{1}{\mathbf{k} \cdot \mathbf{n}}\right) + \dfrac{t}{\mathbf{k} \cdot \mathbf{n}}, & \text{for } \mathbf{k} \cdot \mathbf{n} > 0 \text{ (Transmission)}. \quad (2.25b) \end{cases}$$

The volume element in the vector case is given by $\mathrm{d}V = A_0/(\mathbf{n} \cdot \mathbf{k}_0)\,\mathrm{d}z$, leading to an effective volume in the case of reflection of

$$\begin{aligned} V &= \iiint_V \exp\left[-\mu l(z)\right] \mathrm{d}V, \\ &= \int_0^t \left(\frac{A_0}{\mathbf{k}_0 \cdot \mathbf{n}}\right) \exp\left[-\mu z \left(\frac{1}{\mathbf{k}_0 \cdot \mathbf{n}} - \frac{1}{\mathbf{k} \cdot \mathbf{n}}\right)\right] \mathrm{d}z, \quad (2.26) \\ &= \left[\frac{A_0}{\mu\left(1 - \frac{\mathbf{k}_0 \cdot \mathbf{n}}{\mathbf{k} \cdot \mathbf{n}}\right)}\right] \left\{1 - \exp\left[-\mu t \left(\frac{1}{\mathbf{k}_0 \cdot \mathbf{n}} - \frac{1}{\mathbf{k} \cdot \mathbf{n}}\right)\right]\right\}. \quad (2.27) \end{aligned}$$

Similarly, in the case of the transmission of a diffracted beam,

$$V = \int_0^t \left(\frac{A_0}{\mathbf{k}_0 \cdot \mathbf{n}}\right) \exp\left[-\mu z \left(\frac{1}{\mathbf{k}_0 \cdot \mathbf{n}} - \frac{1}{\mathbf{k} \cdot \mathbf{n}}\right) - \mu t \left(\frac{1}{\mathbf{k} \cdot \mathbf{n}}\right)\right] \mathrm{d}z, \tag{2.28}$$

$$= \left[\frac{A_0 \exp\left(-\frac{\mu t}{\mathbf{k}\cdot\mathbf{n}}\right)}{\mu\left(1 - \frac{\mathbf{k}_0\cdot\mathbf{n}}{\mathbf{k}\cdot\mathbf{n}}\right)}\right] \left\{1 - \exp\left[-\mu t \left(\frac{1}{\mathbf{k}_0 \cdot \mathbf{n}} - \frac{1}{\mathbf{k} \cdot \mathbf{n}}\right)\right]\right\}. \tag{2.29}$$

These expressions for the effective volume can be shown simplify to the expressions for the scenarios previously described.

2.7 Reflectivity Calculation

The sections above have outlined the factors which affect the intensity of X-ray diffraction from a powdered material. Taking these into consideration, the ratio of reflected to incident intensity, which will be referred to as the *reflectivity*, for diffraction from the *hkl* set of planes is given by

$$R_{hkl} = \left(\frac{r_\mathrm{e}^2 \lambda^3 V}{v^2}\right) |F_{hkl}|^2 \, M_{hkl} L P \, e^{-2W(T)}. \tag{2.30}$$

The derivation for the reflectivity above follows the *kinematic theory of diffraction* whereby X-rays are considered to scatter once, at most, before detection. This differs from the *dynamical theory of diffraction* which accounts for secondary effects such as multiple reflections in a perfect crystal which can lead to changes in the measured intensity of a diffracted beam. The dynamical theory, first described in [52, 53], is reviewed in detail in [54] and can be found in many other texts [2, 55, 56]. For diffraction from a powder, the consequences of dynamical diffraction are not observed since they are applicable only for large single crystals.

2.8 Summary

The theory describing the diffraction of X-rays was presented in this chapter. Starting with basic Thomson scattering from an electron, the theory was extended to account for other effects in the case of scattering from a powdered material. The effective volume were derived for a number of geometries, including the famous Bragg-Brentano geometry as well as other geometries which would be promising in laser-plasma experiments.

An expression was presented to calculate the ratio of the energy diffracted from a specific family of lattice planes to the energy of the incident beam and is given by (2.30). The expression is used in Chapter 3 to calculate the probability of an X-ray diffracting into a specific cone in order to simulate the diffraction pattern produced by a beam of X-rays normally incident on a powder slab.

Chapter 3

X-Ray Characterisation by Energy-Resolved Powder Diffraction

3.1 Introduction

As mentioned in Chapter 1, X-ray beams are widely used in scientific and medical applications. In many of these applications, it is important to know the properties of the X-ray beam. This is particularly true for therapeutic applications, where it is imperative that the energy and number of X-ray photons delivered are known. The properties of well established and stable sources—such as X-ray tubes or synchrotron beam lines—can be determined in separate calibration measurements. However, other X-ray sources, particularly those in an early stage of their development, can suffer from large shot-to-shot fluctuations in their properties. For these sources, it is highly desirable to characterise the X-rays delivered to a target in a given time frame or, for the case of pulsed beams, in a single shot. This requires the development of techniques for single-shot, non-destructive characterisation of X-ray beams.

Many of the measurement methods mentioned in Section 1.2.3 destroy the X-ray beam, preventing the simultaneous characterisation and application of the beam. Often there are other limitations: for example, unless filters with a narrow bandwidth are available, determining the spectrum from the relative transmission through different filters requires that the shape of the spectrum is known. This chapter introduces a new technique which may be able to address a number of these limitations, detailing the theory and supporting results through simulations.

3.2 Concept of XCERP Diffraction

The novel method is based on a combination of X-ray powder diffraction and energy-resolved photon counting, whereby the essential idea is to diffract a small fraction of the X-ray beam from a thin sample of a powdered crystal, and to detect inidividual quanta of diffracted X-rays with a CCD. The energy spectrum of the diffracted X-rays, and hence that of the incident beam, can be determined directly from the distribution of CCD counts. Further, as shown later, the angular dependence of the spectrum can be found from the spatial distribution of the diffracted photons about the Debye-Scherrer rings produced by a zero-divergence beam. Since only a fraction of the incident photons are diffracted (of order 10^{-4}), the measurement is essentially non-destructive, and the remaining beam can be used simultaneously for applications if the material has a low attenuation coefficient.

We note that the proposed method, named *X-ray Characterization by Energy-Resolved Powder* (XCERP) *diffraction* [43], is similar to *Single-Hit Energy-resolved Laue Diffraction* (SHiELD). In the latter method energy-resolved photon counting of Laue diffraction from a single crystal, measured with a CCD array, is used to determine changes in the crystal structure when under dynamic stress [57]. Also closely related, is *Energy Dispersive X-Ray Diffraction* (EDXRD) which uses multi-channel pulse-height analysers to investigate various structural phenomena in materials as listed in [58]. With

XCERP diffraction, this concept is inverted so that diffraction from a *known* crystal structure is used to determine properties of the *unknown* incident X-ray beam.

Figure 3.1 shows schematically an experimental arrangement which could be used for XCERP diffraction. An X-ray beam is incident on a thin sample of a powdered crystal of known crystallographic structure. A small fraction of the entire incident X-ray beam is diffracted by the crystal and detected by an X-ray CCD. This method of sampling the beam brings several advantages: (i) most of the beam propagates through the powdered crystal and can then be used in applications; (ii) the density of photons reaching the detector will be sufficiently low to allow *photon counting* [59]; (iii) the whole beam is sampled, which allows beams with an angularly dependent spectrum to be characterised.

3.3 Theory of XCERP Diffraction

The spectrum of the diffracted X-ray beam $S_{\text{diff}}(E)$ can be found straightforwardly from the distribution of CCD counts using standard photon counting techniques [37, 59]. This involves direct detection of X-rays on a CCD with the requirement that the number of photons incident on a given pixel is either one or zero. In the case that an X-ray is captured, the number of photoelectrons created is directly proportional to the energy of the X-ray (c.f. Section 5.3.1). Hence, each pixel acts as a spectrometer and so the diffracted spectrum can be found from a histogram of the pixel values.

The spectrum of the incident beam $S_{\text{inc}}(E)$, prior to diffraction, is related to the spectrum of the diffracted beam $S_{\text{diff}}(E)$, but is not directly proportional since the probability of diffraction depends on the energy of the X-ray, as shown in Chapter 2. The spectra are related by $S_{\text{diff}}(E) = \mathcal{R}(E)S_{\text{inc}}(E)$, where $\mathcal{R}(E)$ is the probability that an incident photon of energy E will be diffracted from the sample to the detector. The response function $\mathcal{R}(E)$ will depend on the experimental geometry and the crystal used, and can be found by calculating the spectrum of diffracted photons for a spectrally-flat incident spectrum, since $S^{\text{flat}}_{\text{diff}}(E) = \mathcal{R}(E)S^{\text{flat}}_{\text{inc}}$. Hence the spectrum of an unknown

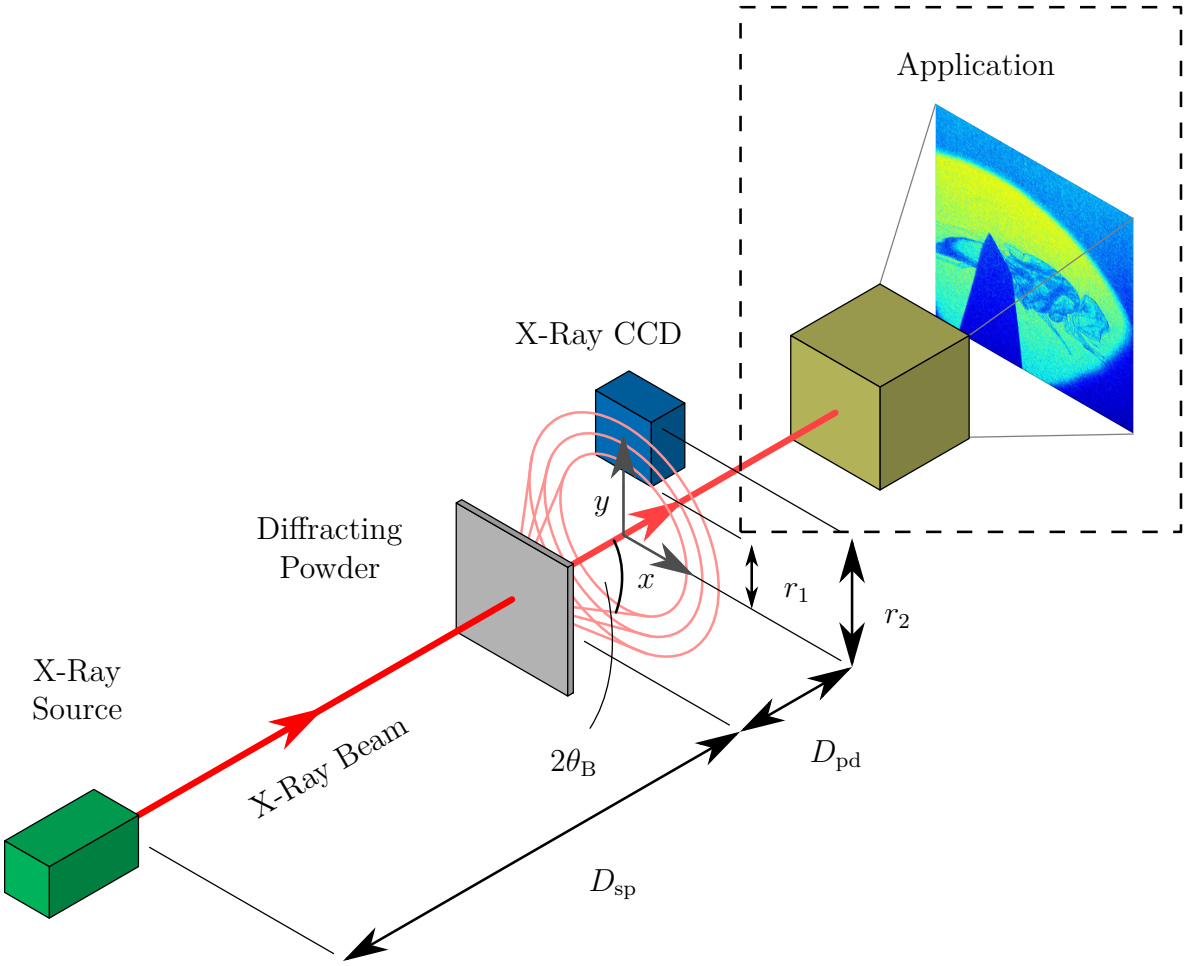


Figure 3.1: Geometry of an XCERP diffraction measurement. A broadband X-ray beam is incident normally on a powdered target. Diffraction from the powder sample produces Debye-Scherrer rings with angular radii which vary with photon energy and lattice plane spacing. The distance along the axis from source to powder is D_{sp} and the distance from powder to detector is D_{pd}. The radial distances of the detector's upper and lower edges from the beam axis are r_1 and r_2, respectively. Most of the X-ray beam is not diffracted and can be used for application such as, in this case, phase-contrast imaging. Image of fly courtesy of James Cowley (University of Oxford).

source is given by $S_{\text{inc}} = (S_{\text{inc}}^{\text{flat}}/S_{\text{diff}}^{\text{flat}})S_{\text{diff}}$. Alternatively, $\mathcal{R}(E)$ could be measured using a known source with a broad X-ray spectrum.

The use of X-ray CCDs provides information not only on the energy of incident radiation, but also the position of captured photons. Since diffraction at a given energy occurs at fixed angles, as determined by the Bragg law (2.3), information about the divergence of the X-ray source can be retrieved from looking at the spread of hits about the predetermined angle. This is true for cases where the beam divergence is much larger than the width of the diffraction line.

3.4 MATLAB Implementation

As a first test of the XCERP diffraction, the author wrote a code using the MATLAB programming language in order to simulate the propagation and diffraction of a beam of X-rays, while allowing the user to generate a beam with predetermined energy and angular spectrum. Since, the properties of the generated beam are known, the XCERP diffraction method can be applied to the simulated diffraction pattern and the resulting retrieved spectrum can be compared with the initial spectrum. The generation of the initial beam and its properties is handled algorithmically as described in Section 3.4.1 while a description of the diffraction process is given in Chapter 2.

3.4.1 Markov chain Monte Carlo sampling

The X-ray beam is generated through a random sampling procedure whereby each photon in the beam is assigned an energy and direction such that the aggregate properties of the whole beam follows the desired spectrum and divergence. The sampling method makes use of a *Markov chain*—a series of random draws where the probability of each draw depends only on the previous draw. There are many algorithms which are based on a Markov chain and the usage of these types of algorithms in order to sample from a

target distribution is known as *Markov Chain Monte Carlo* (MCMC) *sampling*. Details of how a Markov chain can generate samples from a posterior (target) distribution can be found in [60].

MCMC sampling has a number advantages over other sampling methods such as inverse transform sampling or importance sampling. For instance, it may be difficult to find the inverse function of the sampling distribution, but this is not required in the MCMC approach. Furthermore, the distribution does not need to be normalised for MCMC sampling.

The *Metropolis-Hastings algorithm* [61] is a specific implementation of MCMC sampling which has been used in this work to create a random set energies and angles which follow their corresponding density distributions. If we let $P(x)$ be the probability of drawing x in a sampling distribution, then in pseudocode, the Metropolis-Hastings algorithm is as follows:

1. Choose starting value x_0, calculate $P(x_0)$ and go to step 3
2. If the desired number of states have been generated, finish, else go to step 3
3. Propose a new state X_{i+1} from x_i and calculate $P(X_{i+1})$
4. Accept X_{i+1} (i.e. $x_{i+1} = X_{i+1}$) if $P(X_{i+1}) \geq P(x_i)$ and go to step 2, else go to step 5
5. Generate a uniform random number y in the interval $[0, 1]$
6. Accept X_{i+1} if $P(X_{i+1})/P(x_i) > y$ else accept X_i (i.e. $x_{i+1} = x_i$), then go to 2

As shown above, each iteration begins by proposing the next value in the Markov chain (step 3), based on the previous value in the chain. In this work, the next value X_{i+1} is generated by randomly choosing a number in the interval $[x_i - \delta, x_i + \delta]$ with uniform distribution. The value of δ determines how quickly the chain can span the target distribution and it also determines the rate of acceptance, since a large value of δ

can cause the chain to propose values of X_{i+1} which are far from probable regions of the distribution, whereas a small value causes the sequence of x_n to remain localised and highly correlated. The value of δ was dynamically adjusted such that there was approximately 50% acceptance [61] and at this acceptance rate, it was found that the target distribution was well-sampled.

Since each new draw depends on the previous state (specifically, it is within δ of the last state), a strategy to de-correlate sampled states is to keep only every n-th state. There is also a *burn-in* period after the initial value of x_0 to ensure the chain does not begin in a low density region of the distribution. Using 1000 iterations for the burn-in period and 100 iterations between states yielded satisfactory distribution sampling (see Section 4.4).

3.4.2 Ray tracing

A number of functions were created in MATLAB to handle the ray tracing aspects required for generating a diffraction pattern from individual X-rays. Using these functions, the trajectories of each ray could be calculated, including the point of intersection with the powder and the position of the resulting diffracted ray on a virtual CCD. Figure 3.2 shows an example of a diffraction pattern in the plane of the detector. Rays which are not diffracted (i.e. propagate through the powder without interaction) are not shown, but would intersect at the origin.

The propagation of rays was implemented using a few assumptions as described here. Each ray, which is generated with a given energy and direction as in Section 3.4.6, propagates in a straight line. The thickness of the powder is sufficiently thin such that the difference in the trajectory of rays diffracted at the front surface compared to those at the rear surface is negligible. The source size is also assumed to be negligible, implying that rays are emitted from a single point in space. This is reasonable for a betatron source which has a very small source size, on the order of a few µm [31, 62]. Identical

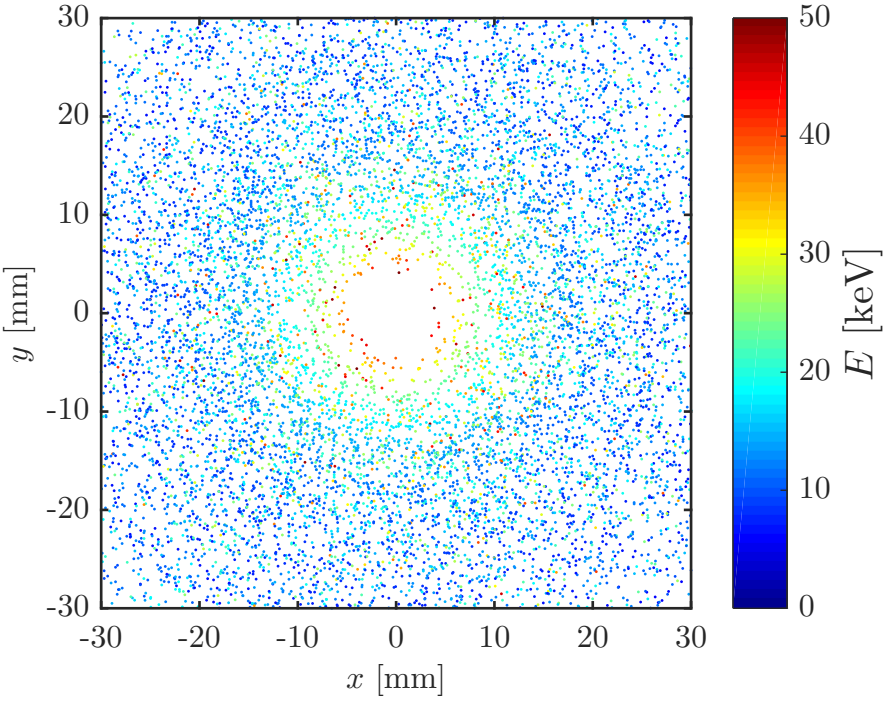


Figure 3.2: Scatter plot of the location (x, y) and energy E of photons arriving in the plane of the detector for the case of diffraction by powdered silicon of an X-ray beam with a synchrotron spectrum of $E_c = 20\,\text{keV}$ and $\sigma_\varphi = 2.5\,\text{mrad}$. The number of photons used in the simulation was $N_{\text{sim}} = 10^5$.

rays are diffracted into cones of zero thickness. In other words, peak broadening effects are not accounted for. This assumption is acceptable if the divergence of the beam would be expected to dictate the peak widths. A more detailed discussion is given in Section 3.4.3.

3.4.3 Material considerations

In general, high-Z elements should be avoided in the powdered crystal to prevent strong attenuation of the transmitted (and diffracted) beam. A suitable candidate for the powder material is silicon as it is commonly used in diffraction measurements as a calibration standard. In order to obtain high quality diffraction lines for the experiment described in Chapter 5, a silicon powder Standard Reference Material (SRM) was used which is primarily used for powder diffraction calibrations. This certified material (under the name of SRM 640e) ensures high purity silicon which is well-characterised [63], such

as lattice parameter $a_0 = 0.543\,117\,9\,\text{nm} \pm 0.000\,008\,\text{nm}$, 4.1 µm median particle size and 0.4 µm mean volume-weighted domain size.

In order to retrieve information on the angular distribution of the X-ray beam, the diffraction peak broadening effects due to the sample itself must be small in comparison to the beam divergence. This can be said to be true for the silicon SRM 640e which is certified to have negligible microstrain, which would otherwise cause broadening proportional to $\tan\theta$. The Scherrer equation, first mentioned in Section 2.5.2, provides an expression for the peak broadening due to the size of crystallites and is given as [1, 3]

$$B = \frac{k\lambda}{L\cos\theta}, \tag{3.1}$$

where B is the angular full width at half maximum (FWHM) of the diffraction peak in radians, k is a constant which is dependent on the shape of the peak profile, and L is the crystallite (domain) size. For an X-ray energy of 5 keV ($\lambda = 2.5$ Å), domain size as above ($L = 0.4$ µm), a relatively large diffraction angle ($\theta = 45\,^\circ$) and making the common assumption of a Gaussian profile ($k = 0.94$), the broadening is calculated to be $B = 0.8$ mrad which is much smaller than the expected beam divergence of a betatron source which is typically on the order of 10 mrad [30, 64].

The Target Fabrication group in the Central Laser Facility at the Rutherford Appleton Laboratory was able to create a powder sample from SRM 640e combined with acrylic to hold the powder in place, with a total thickness of approximately 100 µm. The approximate percentage mass of silicon powder in the mixture, i.e. the packing factor (c.f. Section 2.6), was 50%. Other details of the powder target used in experiment can be found in Section 4.2.

Due to the amorphous nature of the acrylic, it would be expected that scattering from this material would result in an approximately flat background level on top of which diffraction peaks from the silicon powder would sit. The contribution due to the acrylic support has not been modelled in these simulations (see Section 3.6).

3.4.4 Reflectivity calculation

The diffraction process is modelled in the code by calculating the probability of diffraction from a given X-ray (2.30) and using a pseudorandom number generator to dictate whether the ray is successfully diffracted. Here the implementation of the various factors in (2.30) is discussed.

The atomic scattering factor f as described in Section 2.3 was calculated using formulae which provide a close fit to the aforementioned tables as a function of the quantity $\sin\theta/\lambda$ [47]:

$$f\left(\frac{\sin\theta}{\lambda}\right) = \begin{cases} \sum_{i=1}^{4} a_i \exp\left[-b_i\left(\frac{\sin\theta}{\lambda}\right)^2\right] + c, & 0 < \frac{\sin\theta}{\lambda} < 2\,\text{Å}^{-1}, \quad (3.2a) \\ \exp\left[\sum_{j=0}^{3} d_j\left(\frac{\sin\theta}{\lambda}\right)^j\right], & 2 < \frac{\sin\theta}{\lambda} < 6\,\text{Å}^{-1}, \quad (3.2b) \end{cases}$$

where the coefficients a, b, c and d are fitted parameters pertaining to a specific element. This allowed the calculation of the structure factor given by (2.4).

The multiplicity for a cubic crystal system was based on Appendix 6 in [65] and generated for all $\{hkl\}$ combinations up to $h, k, l = 10$. Consequently, diffraction was limited in the code to combinations in this range, which is more than sufficient due to the drop-off in the reflectivity as h, k, l increases.

The Debye-Waller factor was calculated using (2.7) with B taken from tables found in [66] compiled for various elements at 293 K. The parameter recommended for silicon is $B = 0.45\,\text{Å}^2$.

For the geometry shown in Figure 3.1 for XCERP diffraction, the effective volume is calculated using the expression for asymmetric forward reflection from a finite slab given in (2.23).

3.4.5 Scaling of rays

As mentioned previously, ideal powder diffraction produces radiation in multiple cones, centred on the axis of the incident beam. To simulate a CCD which lies off-axis, only a small fraction of the Debye-Scherrer rings would be captured. Hence, the computational efficiency was increased by constraining the rays to diffract into an azimuthal angle ϕ subtended by the modelled detector from the beam axis. The pattern produced by N rays constrained to the angular range would then be equivalent to $N\phi/(2\pi)$ unconstrained rays. In order to apply this enhancement, it must be assumed that there is no *preferred orientation*, meaning that the crystallites in the powder is ideally random such that the intensity is uniform around the full Debye-Scherrer ring.

A further scaling factor was used to artificially increase the reflectivity. This was required since the low reflectivity value, on the order 10^{-4}, would have otherwise required a vast number of initial photons to be generated in order to build up a significant diffraction pattern. The scaling factor used was

$$\alpha' = \max\left(\left\{\sum^{hkl} R_{hkl}\right\}_i\right) \qquad (i = 1, 2, \ldots, N_{\text{sim}})\,, \tag{3.3}$$

where the summation of the reflectivity (2.30) is over all Miller indices and is calculated for each of the N_{sim} photons. For each X-ray, a random number u was drawn from the uniform distribution in the interval $[0, 1]$. The i-th ray in the simulation would then be successfully diffracted if $u_i \leq (\sum R_{hkl})_i/\alpha'$.

The combined scaling factor can be found, $\alpha = \alpha'\phi/(2\pi)$. Hence, the number of photons N_{inc} required in a real experiment can be related to the number of simulated incident photons by $N_{\text{inc}} = N_{\text{sim}}/\alpha$.

3.4.6 Beam generation

Using the Metropolis-Hastings algorithm described above, a series of photons with energy E and angle φ (the angle between the direction of particular photon and the average direction of the beam) were generated from a distribution $P_{\text{inc}}(E, \varphi)$.

The energy of the X-rays were constructed by using an approximated spectrum for betatron radiation from a laser wakefield acceleration. More specifically, the on-axis betatron spectrum in the asymptotic limit of large betatron oscillations [26, 41, 67–69] (see (1.6), setting $\theta = 0$) was used which is given as

$$\left.\frac{\mathrm{d}^2 I}{\mathrm{d}\omega\,\mathrm{d}\Omega}\right|_{\theta=0} \propto \gamma^2 \xi^2 \mathcal{K}_{2/3}^2(\xi), \tag{3.4}$$

where ω is the radiation frequency, θ is the angle made between the point of oservation and the plane of oscilliation, γ is the Lorentz factor of the relativistic electron bunch, $\mathcal{K}_m$ is the modified Bessel function of the second kind and

$$\xi = \frac{\omega}{\omega_{\text{c}}} \left(1 + \gamma^2 \theta^2\right)^{3/2}. \tag{3.5}$$

The *critical frequency* ω_{c} (as used when discussing undulators and wigglers) is defined as $\omega_{\text{c}} = 3 a_\beta \gamma^2 \omega_\beta$, where a_β is a measure of the transverse deflection of the electrons as they perform betatron oscillations (this parameter is often denoted as K, but is avoided here so as not to be confused with the Bessel function), and ω_β is the frequency of the betatron oscillations [70]. Characteristic of this type of radiation is the critical frequency, which corresponds to the point at which half of the total energy is obtained when integrating the power spectrum of the radiation over frequencies. The equivalent *critical energy* is $E_{\text{c}} = \hbar \omega_{\text{c}}$.

The distribution used is then:

$$\begin{aligned} S(E) &= \int \mathrm{d}\varphi \; P(E,\varphi) \\ &= C_E \left(\frac{E}{E_\mathrm{c}^2}\right) \left[\mathcal{K}_{2/3}\left(\frac{E}{E_\mathrm{c}}\right)\right]^2, \end{aligned} \tag{3.6}$$

where C_E is a normalisation constant.

For simplicity, the beam is assumed to have no correlation between photon energy and incident angle, and the angular distribution Φ is of the form of a Gaussian distribution with a standard deviation σ_φ:

$$\begin{aligned} \Phi(\varphi) &= \int \mathrm{d}E \; P(E,\varphi) \\ &= C_\varphi \exp\left(-\frac{\varphi^2}{2\sigma_\varphi^2}\right), \qquad 0 \leq \varphi < \frac{\pi}{2}, \end{aligned} \tag{3.7}$$

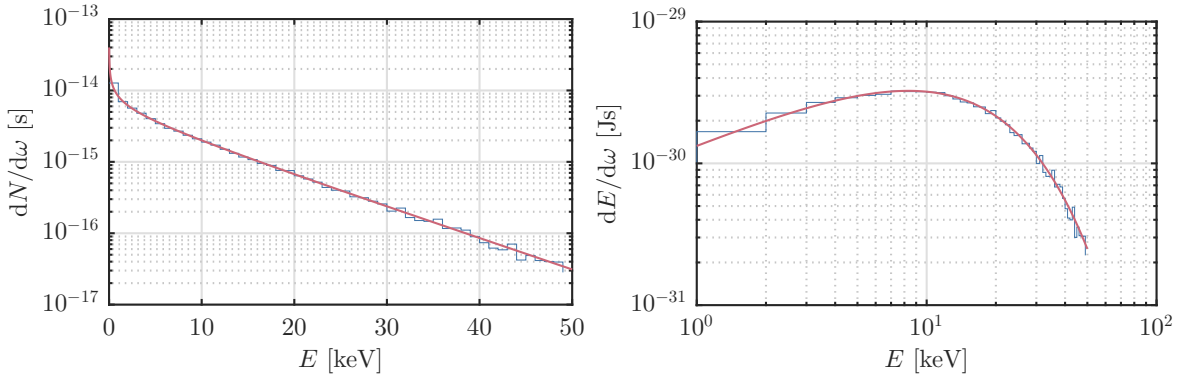
where C_φ is a normalisation constant and φ is the angle between a given photon and the nominal beam axis.

An example of a generated spectrum, simulating $N_\mathrm{sim} = 10^5$ photons and a critical energy $E_\mathrm{c} = 20\,\mathrm{keV}$, is shown in Figure 3.3, represented by the blue lines. It can be seen that this spectrum matches the desired spectrum (3.6), shown as red lines, very well. The left and right graphs represent the number spectral density and the energy spectral density, respectively. The latter is shown for reference as the spectrum is most often represented in this form.

3.5 Simulation examples

3.5.1 Spectrum retrieval

For the work described here the powdered crystal was assumed to be silicon [47, 71]; the sample thickness was assumed to be 50 µm; and the distances from source to powder and



(a) (b)

Figure 3.3: Comparison of energy spectrum generated using MCMC sampling with the desired energy spectrum. The spectrum is based on betatron emission (3.4) for a critical energy of $E_\mathrm{c} = 20\,\mathrm{keV}$. 10^5photons are generated.

from powder to detector were taken to be $D_\mathrm{sp} = 100\,\mathrm{mm}$ and $D_\mathrm{pd} = 50\,\mathrm{mm}$, respectively.

In order to apply the XCERP diffraction method, it was necessary to calculate $\mathcal{R}(E)$. This was achieved by simulating a spectrally flat beam and propagating it through the Monte-Carlo code. Following this, a test simulation was carried out using a beam with a betatron spectrum and with a Gaussian angular divergence. The betatron spectrum could then be reconstructed from the diffracted spectrum of the test simulation through the use of the previously calculated $\mathcal{R}(E)$.

Figure 3.4(a) and Figure 3.4(b) compare the incident and retrieved spectra for a synchrotron spectrum with $E_\mathrm{c} = 20\,\mathrm{keV}$, $\sigma_\varphi = 2.5\,\mathrm{mrad}$ and an estimated 1.2×10^8 and 6.0×10^6 incident photons, respectively. In both cases the retrieved spectrum is in excellent agreement with the incident spectrum, but, as expected, the agreement is better for the larger number of incident photons. These photon numbers may be compared with the approximately 10^8–10^9 X-ray photons generated by betatron oscillations in laser-plasma accelerators of electrons with energies of order $\sim 200\,\mathrm{MeV}$ [6, 32, 72, 73].

For reference, the simulation for Figure 3.4(a) uses $N_\mathrm{sim} = 10^5$ simulated incident photons, $\alpha = 8.5 \times 10^{-4}$, leading to an equivalent of $N_\mathrm{inc} = 1.2 \times 10^8$ photons in a real experiment. The resulting number of diffracted photons which then fall on the CCD, which we assume for the sake of the simulation consists of 1000×1000 pixels of length

20 µm, is 8.2×10^3.

In order to demonstrate the flexibility of XCERP diffraction we also simulated the retrieval of the complex spectrum shown in Figure 3.4(c). Even in this extreme case the retrieved spectrum is seen to be in close agreement with that of the incident beam, demonstrating the utility of XCERP diffraction in cases for which the *shape* of the incident spectrum is unknown or the form of the spectrum cannot be characterised by a small number of parameters.

As can be seen from Figure 3.4, the spectrum can only be retrieved for photon energies above some lower bound, determined by the photon energy $E_{\min}$ for which $2\theta_{\max} = \Theta_{\mathrm{d}}$ where $\Theta_{\mathrm{d}} = \tan^{-1}(r_2/D_{\mathrm{pd}})$ is the maximum angle subtended by the detector at the sample and $\theta_{\max}$ is the Bragg angle associated with the crystal's largest plane separation $d_{\max}$. In the arrangement shown in Figure 3.1, the lower bound is found to be $E_{\min} = hc/[2\, d_{\max} \sin(\Theta_{\mathrm{d}}/2)]$. For the geometry assumed in the simulations shown in Figure 3.4(a), we find that $E_{\min} = 7.4\,\mathrm{keV}$ for diffraction from the $\{111\}$ set of planes in silicon (the $\{100\}$, $\{110\}$ and $\{200\}$ reflections do not exist since their respective structure factors are $|F_{hkl}|^2 = 0$ for the diamond cubic crystal structure of silicon); this agrees with the lower cutoff observed in the retrieved spectra.

The spectral range can be extended to lower photon energies by adjusting the experimental geometry, for example, by increasing the ratio r_2/D_{pd}. However, there is an intrinsic lower bound to the detectable photon energy which occurs in transmission (reflection) geometry when the diffracted photon is perpendicular (anti-parallel) to the incident beam. The minimum detectable photon energy $\mathcal{E}_{\min} = \beta hc/d_{\max}$ where $\beta = 1/(2\sqrt{2})$ for transmission and $\beta = 1/2$ for reflection. For silicon, this leads to intrinsic minima of 2.8 keV for transmission and 2.0 keV for reflection.

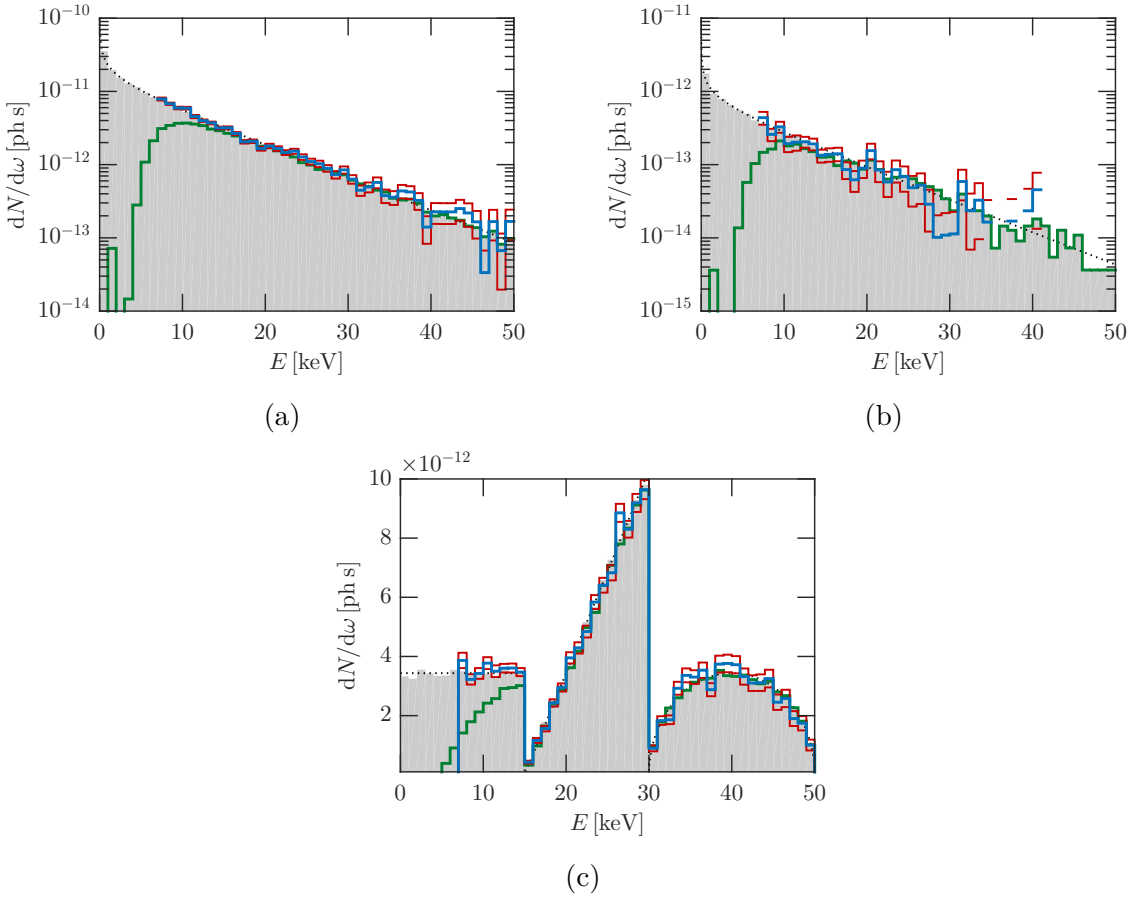


Figure 3.4: Comparison of the incident and retrieved (blue) spectra for the case of diffraction by powdered silicon; for the incident beam, the underlying spectrum is shown by the dashed black line and that of the sample generated by the Monte-Carlo code is shown by the gray bins. (a) and (b) show the spectra for an incident beam with a synchrotron spectrum with $E_\mathrm{c} = 20\,\mathrm{keV}$ and $\sigma_\varphi = 2.5\,\mathrm{mrad}$ and: (a) 1.2×10^8 photons; (b) 6.0×10^6 photons. Shown in (c) are the incident and deduced spectra for a beam of 1.2×10^8 photons with a complex spectrum. For all plots the spectrum of the beam transmitted through the powder sample is shown in green, and the error bars (red) are calculated assuming the number of photons *detected* within each energy bin follows a Poisson distribution.

3.5.2 Divergence retrieval

Further information about the incident beam may be obtained by plotting the radial position r of each detected photon against its energy, as shown in Figure 3.5. The solid curves show the radii $r_{hkl}(E)$ of the Debye-Scherrer rings produced by diffraction from the hkl planes of photons incident along the beam axis with energy E in the plane of the detector and can be calculated by

$$r_{hkl}(\theta_\mathrm{B}) = D_\mathrm{pd} \tan(2\theta_\mathrm{B}). \tag{3.8}$$

From (2.3), $\theta_\mathrm{B} = \sin^{-1}(\lambda/(2\,d_{hkl})) = \sin^{-1}(hc/(2\,d_{hkl}E))$ and making use of the trigonometric identities,

$$\tan 2x = \frac{2\tan x}{1-\tan^2 x}$$

and

$$\tan\left(\sin^{-1}(x)\right) = \frac{x}{\sqrt{1-x^2}},$$

the expected radial position r_{hkl} as a function of the photon energy E can be expressed as

$$r_{hkl}(E) = 2D_\mathrm{pd}\frac{\sqrt{(E/\chi)^2-1}}{(E/\chi)^2-2} \tag{3.9}$$

where $\chi = hc/(2\,d_{hkl})$.

Photons detected away from these calculated curves, i.e. with $r \neq r_{hkl}$, must have been incident with $\varphi \neq 0$. Hence the distribution of detected photons about these curves $\Psi(E, r)$ gives information on the angular distribution of the incident radiation $P(E, \varphi)$. For comparison, three cases have been shown with $\sigma_\varphi = 2.5\,\mathrm{mrad}, 1.0\,\mathrm{mrad}$ and $5.0\,\mathrm{mrad}$.

It is not straightforward to deduce $P(E, \varphi)$ from the measured distribution about the r_{hkl} curves, $\Psi_\mathrm{exp}(E, r)$. However, assuming a given form for the angular distribution of the incident beam $\Phi_\mathrm{model}(\varphi, \mathbf{p})$ – where $\mathbf{p}$ represents the model parameters – allows

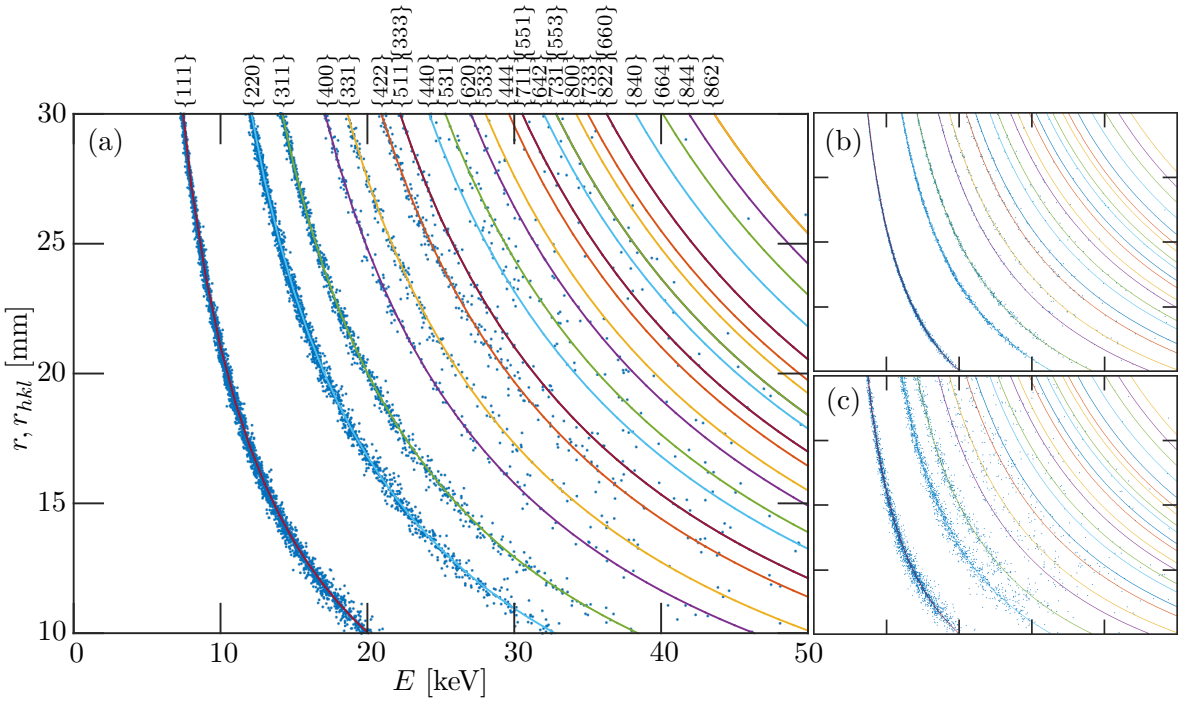


Figure 3.5: Scatter plots of radial distance r from the beam axis as a function of photon energy. The solid lines show the radii of the Debye-Scherrer rings r_{hkl} for photons incident along the beam axis. The assumed properties of the incident beam used for Figure 3.5(a) are as in the data shown in Figure 3.4(a), with $\sigma_\varphi = 2.5\,\text{mrad}$. Fig. 4(b) and (c) show the plots for simulations with $\sigma_\varphi = 1.0\,\text{mrad}$ and $\sigma_\varphi = 5.0\,\text{mrad}$, respectively.

the expected distribution of photons about each curve $\Psi_{\mathrm{model}}(E, r)$ to be compared with the measured distribution $\Psi_{\mathrm{exp}}(E, r)$. Minimising the difference between the measured and calculated distributions then allows the best fit parameters of the model angular distribution to be found.

For the cases considered in this work, we have found that for a given photon energy, the radial offset $r - r_{hkl}$, and hence $\Psi(E, r)$, does not depend strongly on the diffraction plane $\{hkl\}$. In general for this to hold true we require: (i) the angle subtended by the detector at the powder sample to be sufficiently small that $r_2 \lesssim D_{\mathrm{pd}}$; and (ii) the divergence of the incident beam to be much less than 1 rad (this second constraint is easily satisfied for the X-ray sources of interest). Alternatively, conditions (i) and (ii) need not be satisfied if instead $D_{\mathrm{sp}} \gg D_{\mathrm{pd}}$. These conditions come from considering the maximum deviation of a ray r_{max} whose incident angle is φ_{max}:

$$r_{\mathrm{max}} = D_{\mathrm{sp}} \tan(\varphi_{\mathrm{max}}) + D_{\mathrm{pd}} \tan(\varphi_{\mathrm{max}} + 2\theta_{\mathrm{B}}). \tag{3.10}$$

Using the identity

$$\tan(x + y) = \frac{\tan x + \tan y}{1 - \tan x \tan y},$$

and the small-angle approximation when $\varphi_{\mathrm{max}} \ll 1$, (3.10)

$$r_{\mathrm{max}} \simeq D_{\mathrm{sp}}\, \varphi_{\mathrm{max}} + D_{\mathrm{pd}} \left(\varphi_{\mathrm{max}} + \tan 2\theta_{\mathrm{B}} + \varphi_{\mathrm{max}} \tan^2 2\theta_{\mathrm{B}} \right). \tag{3.11}$$

Hence, r_{max} is weakly dependent on θ_{B} (i.e. the dependence on the energy and diffraction plane) when the conditions above are satisfied.

Retrieval of energy-independent divergence

To demonstrate retrieval of the angular distribution by XCERP diffraction, we first use the same simulation data as shown in Figure 3.4(a), which assumed an incident beam with an on-axis synchrotron spectrum and an energy-independent angular distribution.

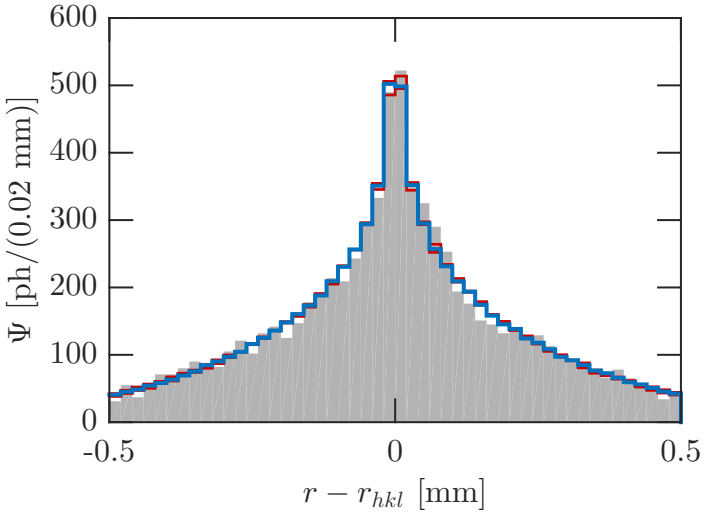


Figure 3.6: Distributions of photons $\Psi(r)$ for diffraction by powdered silicon and an incident X-ray beam with the same parameters as in Figure 3.4(a) calculated: by the Monte-Carlo diffraction code (grey bars); and for a Gaussian angular distribution $\Phi_{\text{model}}(\varphi, \sigma_{\text{test}})$ after least squares minimisation (blue). The best fit corresponds to a divergence of $\sigma_{\text{test}} = (2.51 \pm 0.08)\,\text{mrad}$. The red lines show error bars calculated assuming that the number of photons in each radial bin follows a Poisson distribution.

To analyse this case, we assumed a Gaussian model $\Phi_{\text{model}}(\varphi, \sigma_{\text{test}})$ with a standard deviation σ_{test}. Figure 3.6 shows the 'measured' distribution Ψ_{exp} (gray histogram) calculated by the Monte-Carlo diffraction code and the best-fit model distribution Ψ_{model} (blue line) after least squares minimization to determine the optimum σ_{test}. This procedure yields $\sigma_{\text{test}} = (2.51 \pm 0.08)\,\text{mrad}$, which is in remarkable agreement with the value $\sigma_\varphi = 2.50\,\text{mrad}$ for the input beam. We note that typical values of the *full-angle* divergence of a plasma accelerator betatron source, for example, are of order 10 mrad [29, 32, 74] and so would be measurable with XCERP diffraction.

Retrieval of energy-dependent divergence

In general the X-ray spectrum depends on the angle of emission. In this case we can divide plots like Figure 3.5 into energy bins and perform the least squares fit procedure described above to the set of points within each bin.

To demonstrate this we simulated the diffraction of a synchrotron source with an

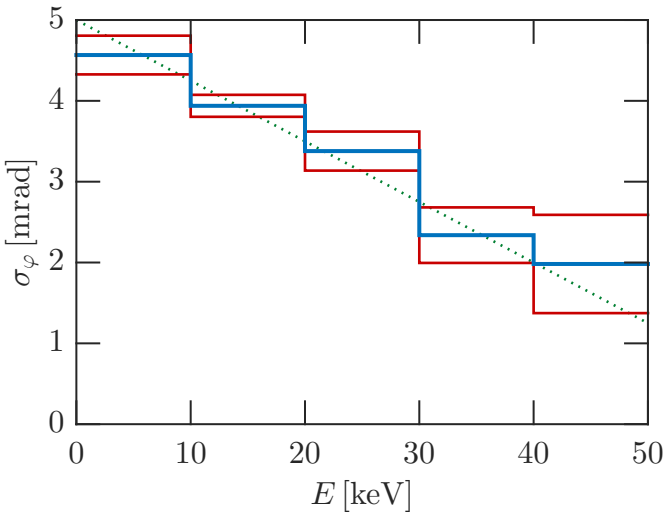


Figure 3.7: Demonstration of the retrieval of an energy-dependent divergence with XCERP diffraction for an incident beam with the same parameters as Figure 3.4(a) except for an energy-dependent divergence for photons in the range $0\,\text{keV} < E < 50\,\text{keV}$ given by $\sigma_\varphi[\text{mrad}] = 5 - 0.075\,E[\text{keV}]$. The retrieved divergence for each 10 keV energy bin is shown in blue; error bars, calculated assuming the number of photons detected within each energy bin are Poisson distributed, are shown by the solid red lines; the standard deviation used to generate the simulation's incident beam is shown by the dotted green line.

energy-dependent angular divergence for photons in the range $0\,\text{keV} < E < 50\,\text{keV}$ given by a Gaussian whose standard deviation varies as $\sigma_\varphi[\text{mrad}] = 5 - 0.075\,E[\text{keV}]$; the other parameters of the beam were as for Figure 3.4(a). As shown in Figure 3.7, the retrieved divergence for each energy bin (blue) is in very good agreement with that of the incident beam (dotted green), demonstrating the potential for XCERP diffraction to measure angularly-resolved spectra.

These retrieval methods may be combined to produce an angularly-resolved spectrum in which the only assumption made is the form of the divergence as a function of photon energy. Figure 3.8 shows that the angularly-resolved spectrum retrieved by XCERP diffraction is in very good agreement with that of the input beam for parameters corresponding to Figure 3.7, represented by the coloured and gray mesh, respectively.

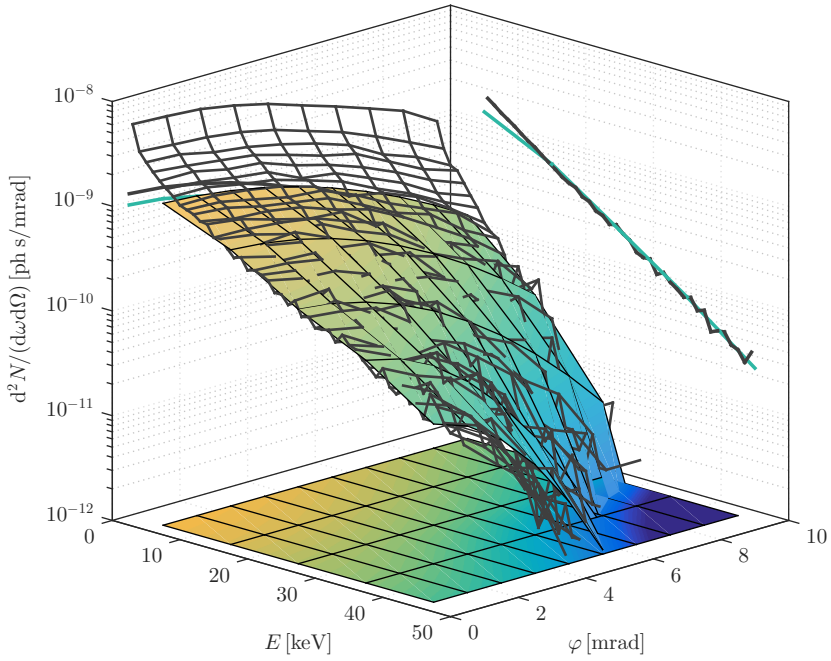


Figure 3.8: Comparison of the angularly-resolved spectrum retrieved by XCERP diffraction (coloured surface) with that of an input beam with the parameters as in Figure 3.7 (gray mesh). The side panels show the angularly-resolved spectra integrated over energy (left) and angle (right) for the retrieved (blue line) and input (gray line) spectrum. The integrated spectra have been scaled so that they can be displayed on the same z-axis.

3.5.3 Polarisation effects

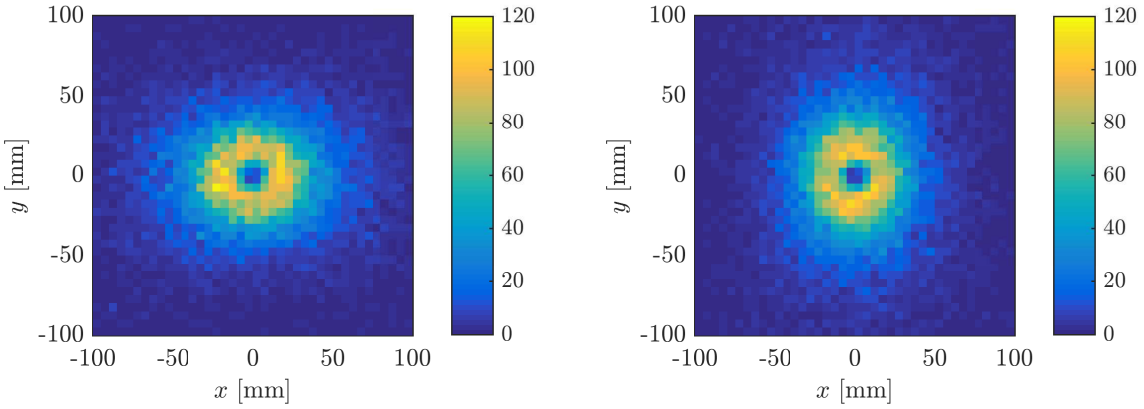
The work above was performed assuming the beam was unpolarised. For betatron radiation, this can be assumed if the electrons all oscillate in different planes. This scenario is reasonable if the electrons are injected symmetrically about the beam axis. However, it would be possible to create polarised betatron radiation if the electrons are preferentially injected on one side of the axis (or if the electrons all recieve a transverse kick in a single plane).

The polarisation dependence was implemented in the MATLAB code following the factors set out in Section 2.2. Depending on the polarisation state of the beam, different diffraction patterns were produced by the code, as shown by the preliminary results in Figure 3.9. It can be seen that for polarisation along the y-axis, there is stronger diffraction along the opposite direction and conversely for the x-axis, whereas there is no preferred diffraction direction for an unpolarised beam. This is what might be expected since the polarisation factor in the plane of polarisation ($P = \cos^2 2\theta$) is smaller than the polarisation factor in the transverse direction ($P = 1$).

Additional work in this area may allow the polarisation state of the incident beam to be inferred non-destructively from a measured diffraction pattern. This might prove to be a useful tool in further developing techniques to induce polarised X-ray beams as discussed in [75–77].

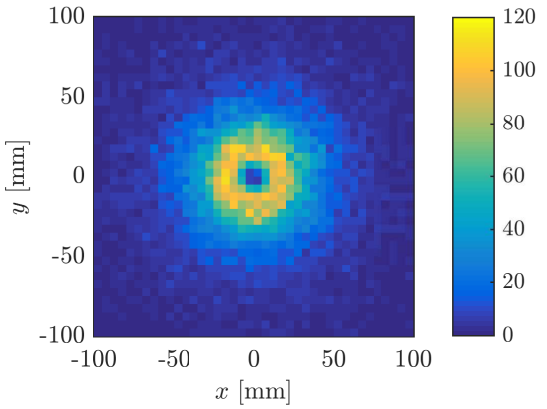
3.6 Discussion

A number of factors have to be considered when designing an XCERP diffraction measurement. The properties of the crystalline material affect both the diffracted and transmitted beams. Additionally, the geometry of the experiment, and the crystal used, should be chosen so that the minimum detectable photon energy $E_{\min}$ is below the photon energies of interest. Many of the factors which affect the diffraction measurement



(a) Polarised in y

(b) Polarised in x



(c) Unpolarised

Figure 3.9: Comparison of the diffraction patterns for different beam polarisations.

have been outlined above. Here, other factors not covered previously are discussed.

The experimental geometry has a significant effect on the retrieval. For example, the ratio $D_{\mathrm{sp}}/D_{\mathrm{pd}}$ affects the maximum divergence which can be retrieved: for larger $D_{\mathrm{sp}}/D_{\mathrm{pd}}$ undesirable merging of the Debye-Scherrer rings will occur for higher beam divergence. To quantify this, we see from Figure 3.5 that for the case considered, the majority of detected photons diffract from the {111}, {220} and {311} planes. The smallest radial separation of these rings is between those arising from the {220} and {311} planes, and hence this separation limits the maximum divergence which can be retrieved. In this case, to measure the beam divergence we require

$$\frac{D_{\mathrm{sp}}}{D_{\mathrm{pd}}} \lesssim \frac{\tan\left(2\theta_{\mathrm{B}}^{311} - 2\sigma_{\varphi}\right) - \tan\left(2\theta_{\mathrm{B}}^{220} + 2\sigma_{\varphi}\right)}{2\tan\left(2\sigma_{\varphi}\right)}, \tag{3.12}$$

where $\theta_{\mathrm{B}}^{hkl}$ is the first order Bragg angle for the $\{hkl\}$ set of planes at a given energy. We emphasize that even when (3.12) is not satisfied, retrieval of the *energy spectrum* will still be possible as long as the width of the Debye-Scherrer rings due to the beam divergence is smaller than the dimensions of the detector.

On the other hand, in principle, it is possible to determine sub-milliradian divergences. However, effects which broaden the diffraction peaks – such as the effect of finite sizes of the source and crystallites – become important when retrieving low source divergences on the order of $\sim 1\,\mathrm{mrad}$ (c.f. Section 3.4.3). Hence, the distribution Ψ_{exp} would be convoluted with the profiles of each broadening mechanism and an accurate divergence retrieval would not be possible. These effects are not important for the case shown in Figure 3.7 since Ψ_{exp} is dominated by the divergence of the source.

It is clear that no information can be retrieved about the spectrum in the range of energies for which there is not an associated diffraction peak. As an example with reference to Figure 3.5, if the detector only spanned the range between 20 mm to 30 mm, then no information could be retrieved on the energy range between 10 keV to 12 keV which is not covered by the {111} nor the {220} set of planes.

As is well known, determining the spectrum by photon counting requires that a sufficiently high number of photons are detected to ensure good statistics, whilst ensuring that the average number of photons reaching each pixel is much less than one [37, 59].

Throughout this work we have assumed a perfect detector. In practice, the detector quantum efficiency (DQE) typically has a peak of over 90% near photon energies of 5 keV, but the response can extend to a few tens of keV with DQE $\approx$ 10%. We note that detectors are being developed with enhanced DQE in the tens of keV range; for example, a combination of a back-illuminated CCD with a scintillator has been shown [78] to allow single photon detection up to 80 keV. If the DQE is below unity then the number of photons incident on the detector would need to be increased by a factor of 1/DQE in order to prevent loss of resolution. In a later simulation, using a version of the code which implements the quantum efficiency of a real X-ray camera and input parameters identical to that of Figure 3.4(a) (i.e. an equivalent of 1.2×10^8 photons incident on the powder), it was found that the spectrum could still be effectively retrieved in the high quantum efficiency energy region as shown in Figure 3.10. However, the addition of the quantum efficiency in the simulation resulted in as few as 320 photons being detected as opposed to 8.2×10^3 from before.

A number of steps could be taken to improve the signal level. For example, a transverse array of detectors with a central aperture through which the un-diffracted beam can pass could be employed [79]. The dynamic range sets an upper limit for the number of energy bins which can be used in the spectrum retrieval, but since the dynamic range is typically above 10^3 this should not impose significant limitations.

As was noted for the SHiELD technique [57], noise—for example, arising from fluorescence—could be eliminated to a large extent since it will occur at pixel positions which are uncorrelated with the photon energy and the expected position of the Debye-Scherrer rings. This also applies to the scattering due to any amorphous support material since the rays would not be scattered into any particular direction for a given photon energy.

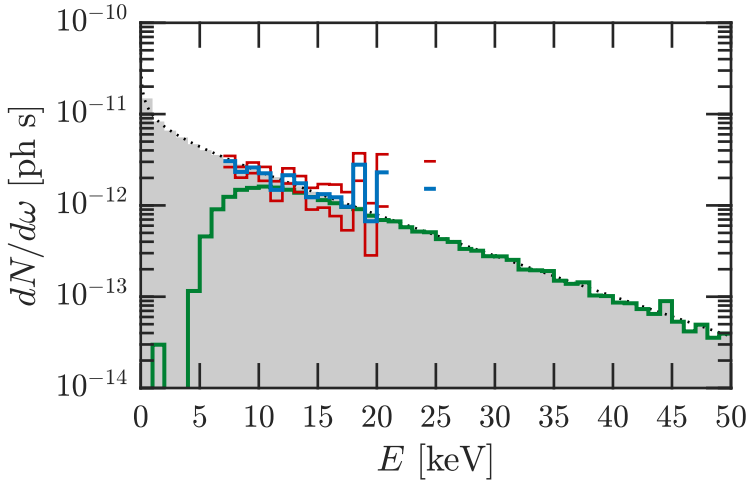


Figure 3.10: Comparison of the incident and retrieved (blue) spectra for the case of diffraction by powdered silicon when quantum efficiency is accounted for; for the incident beam, the underlying spectrum is shown by the dashed black line and that of the sample generated by the Monte-Carlo code is shown by the gray bins. The spectrum of the beam transmitted through the powder sample is shown in green, and the error bars (red) are calculated assuming the number of photons *detected* within each energy bin follows a Poisson distribution.

Errors arising from imperfect knowledge of the experiment geometry would only marginally affect the results. The greatest impact would be on the divergence retrieval since errors of this type would result in incorrect calculation of the positions of the Debye-Scherrer rings (3.8) and hence an incorrect fit of Ψ_{model}. In many cases, errors of this type would be detected; for example, for a cylindrically symmetric X-ray beam the distribution Ψ_{exp} should be symmetric, for a given photon energy, about the r_{hkl} curves, and hence deviations from this would indicate incorrect calculation of the r_{hkl} curves. In such cases it would be possible to use the experimental geometry as parameters in a fit procedure to match the set of r_{hkl} curves calculated by (3.8) with the experimental data.

3.7 Summary

In this chapter, the author has presented a novel technique, XCERP diffraction, for single-shot, non-destructive measurement of the spectrum and divergence of X-ray beams

based on energy-resolved X-ray powder diffraction. To demonstrate this, a Monte-Carlo code was developed and used to simulate data for X-ray beams with parameters similar to those generated by betatron oscillations in a laser-driven plasma accelerator. The retrieved X-ray spectra were found to be in excellent agreement with those of the input beams for realistic numbers of incident photons. Further, it was demonstrated that the angular divergence of the X-ray beam could be deduced from the displacement of the detected photons from the expected Debye-Scherrer rings of X-rays propagating along the beam axis. This allowed the angular divergence to be retrieved as a function of photon energy, and hence the angularly-resolved spectrum of the beam to be determined. The author expects that the XCERP diffraction technique will be particularly useful for simultaneous characterisation and application of X-ray beams with fluctuating properties.

Chapter 4

Astra Gemini Experiment

4.1 Introduction

This chapter focuses on an experiment the author was heavily involved in during the summer of 2016, and took place at the Astra Gemini facility at the Rutherford Appleton Laboratory in the UK. The main objective of this experiment was to demonstrate electron acceleration via the Two-Pulse Ionisation Injection (2PII) scheme [80] with some time at the end to attempt XCERP diffraction. The XCERP diffraction method has been described in Chapter 3 and [43].

The 2PII scheme provides a method of injecting electrons into quasilinear wakefields to generate high quality electron beams. This is achieved by trailing a tightly focused laser pulse behind a primary drive pulse which has an intensity too low to generate an electron beam via self-injection or ionisation-induced injection. By introducing an appropriate dopant into the background medium, the higher intensity focus of the injection pulse can ionise the dopant particles in a small volume of the wakefield produced by the leading drive pulse. Although the injection pulse superimposes a wakefield of its own, this wakefield is short-lived due to the strong diffraction of the pulse, allowing the compact bunch of injected electrons to be trapped and accelerated by the wakefield driven by the drive pulse. This confined injection, both spatially and

temporally, combined with the control afforded by using two separate laser pulses, should allow the emittance of electron beam after acceleration to be minimal. Simulations using a particle-in-cell code by Bourgeois et al. show that a relative energy spread of 2% and normalised transverse emittance of 2 µm are achievable [80].

Unfortunately, the demonstration of the above methods proved unsuccessful for a number of reasons. It was found that the pointing stability of the drive beam in particular was poor, jumping up to a full spot size and resulted in difficulties maintaining spatial overlap between the drive and injection beam. The poor stability stems from the fact that the 6 m focusing optic of the drive beam required a long propagation distance to reach focus and was achieved using a folding mirror mounted on a separate pedestal approximately 2.5 m away from the main target chamber. Additionally, it was found that it was very challenging to maintain the delay between the drive an injection beam to the required precision (a fraction of the plasma period, i.e. to within approximately 10 fs). Measurements using a spectrometer found that the relative temporal jitter was on the order of 10 fs, but importantly, there was also a systematic relative drift which was eventually tracked down to be (at least partially) due to fluctuations in the temperature of the laser room and was approximately 80 fs/°C. With the temperature fluctuating by approximately 1 °C every 20 minutes combined with the pointing stability, it was not possible to collect the data required to show proof-of-principle of the 2PII scheme. With regards to the latter experiment, analyses for XCERP diffraction could not be performed as the data acquired by the relevant CCD was unreliable due to a camera fault which was not discovered until the conclusion of the experiment.

Despite these complications, self-injection at higher gas densities and drive beam energies did allow the generation of electron beams and betatron radiation. Hence, the focus of this chapter is the measurement of the electron beams and betatron radiation produced during the LWFA interactions in the Gemini Astra experiment. The author designed the systems required for these measurements and they will be described below followed by some experimental results.

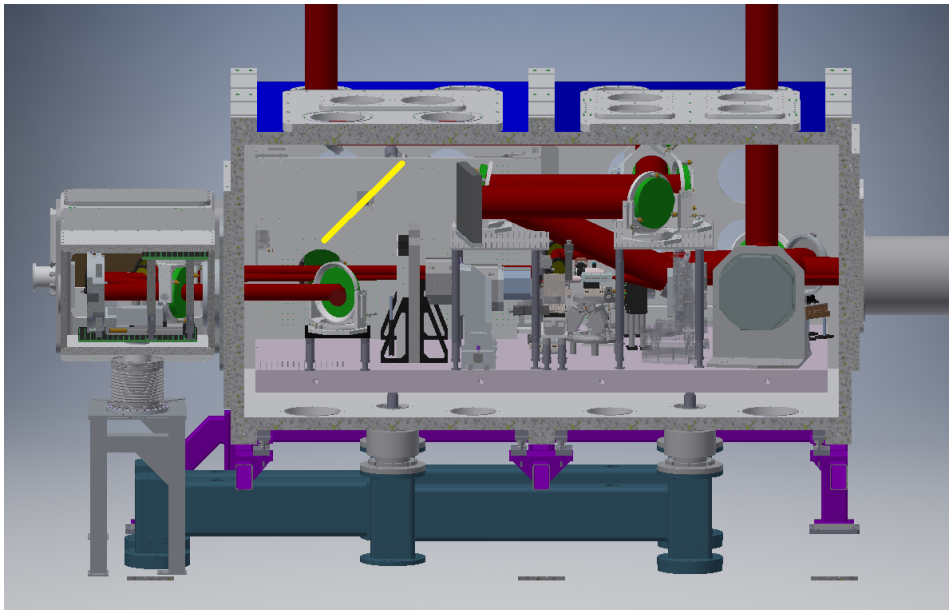


Figure 4.1: CAD drawing of target chamber at the Astra Gemini facility. The yellow line indicates where the low energy Lanex screen was situated.

4.2 Experimental Setup

The Astra Gemini facility [81] is a petawatt class laser system which provides two synchronised laser beams on target. The energy in each beam can be varied independently using waveplates with a maximum energy of approximately 15 J in each beam. These beams are named North and South beam for convenience. The South beam was used as the main driving pulse which was focused by an F/40 paraboloid, yielding a spot size on target of approximately 40 µm. The North beam propagated around the upper level of the chamber and was focused using a F/2 paraboloid with a hole in the centre, allowing co-propagation of the North and South beams. The North beam focused to approximately 10 µm. Both beams entered the chamber with a diameter of 150 mm and had a full-width at half-maximum duration of 55 fs. Figure 4.1 shows a CAD drawing of the chamber setup.

Hydrogen-filled gas capillaries were used throughout the campaign with various lengths available: 15 mm, 33 mm, 50 mm, 70 mm and 100 mm. Only lengths up to 50 mm were used due to difficulties aligning the capillaries to the laser axis. The

capillary diameters varied between 200 µm and 400 µm. An automated alignment tool was designed by the author using LabVIEW to control a Physik Instrumente 6-axis hexapod to aid in the alignment procedure, reducing the alignment time from a couple hours to approximately half an hour. The details of operation are not described in this work for brevity.

The laser beams could be guided in the capillary using a discharge waveguide by applying a high voltage across the capillary length using a novel discharge circuit [82]. Alternatively, the capillaries could be used in a 'gas cell' mode [83] whereby the hydrogen gas was ionised by the laser pulse instead of a current discharge.

Electrons generated during the laser-plasma interaction were deflected away from the laser axis using an electron spectrometer, the details of which are discussed in Section 4.3.

The camera used to measure the on-axis betatron signal was the Andor DX420-BN which has 1024×255 pixels of length 26 µm. For most of the experiment, the betatron radiation was sampled through a wedge with a 10 mm hole in the centre, located 2.2 m downstream from the interaction point. The drive laser beam was steered by this wedge to a diagnostic table. The Andor chip was shielded from visible light using a total of 36 µm of Mylar. The betatron measurement is detailed in Section 4.4.

It was intended that XCERP diffraction would be tested experimentally during the Astra Gemini campaign as an additional two week experiment. As such, the CLF target fabrication laboratory created some powder diffraction targets. The samples consisted of a mixture of powdered silicon and acrylic. In order to obtain high quality diffraction lines, the silicon powder used was a Standard Reference Material (SRM) which is primarily used for powder diffraction calibrations. This certified material consists of high purity silicon which is well-characterised [63], such as lattice parameter $a_0 = (0.543\,118 \pm 0.000\,008)$ nm, 4.1 µm median particle size and 0.4 µm mean volume-weighted domain size. The approximate percentage mass of silicon powder in the mixture was 50%, with an average thickness of 100 µm with variations of up to 30 µm. The

acrylic used was LOCTITE® 358, which is an adhesive cured under UV exposure. The chemical name is urethane methacrylate ester which is primarily composed of hydrogen, carbon and oxygen. The chemical formula is believed to be $C_7H_{11}O_4N$. The density was not specified but is expected to be proximate to that of similar materials. For instance, the density of another ester, methyl methacrylate is $0.94\,\mathrm{g/cm^3}$. The powder samples were later used in another experiment, detailed in Chapter 5.

For the runs attempting to measure XCERP diffraction, a tape drive was installed approximately 0.875 m downstream of the IP to protect the powder material from laser damage. The tape used was a 25.4 µm thick Kapton tape. At this distance, the drive pulse would have had an intensity of $4.8 \times 10^{13}\,\mathrm{W/cm^2}$ for a laser pulse of 10 J. This is comparable to the ionisation intensity for typical plasma mirror materials [84], but may lead to suboptimal plasma mirror formation unless higher intensities are achieved. The surface intensity could be increased by moving the tape drive closer to the interaction point. However, its main purpose was to protect the silicon powder and not to maximise the reflection of the laser pulse and it was found that the reduction in transmitted laser intensity was sufficient to prevent powder damage. Furthermore, it was preferable to have the tape drive located after the electron spectrometer magnets to minimise interference with the electron beam.

The X-ray CCD used to measure the XCERP diffraction was the Andor DX436-BV-9HS which has 2048×2048 pixels of length 13.5 µm. Unfortunately, as mentioned previously, a fault with the connector was found after the experiment had concluded. It was confirmed that the damaged pins were specific to data transmission and images recorded by the controller card were spurious. Curiously, the software still allowed images to be captured.

4.3 Electron Energy Measurement

To characterise the electrons produced during the experiment, an electron spectrometer was designed. This consisted of a set of three permanent dipole magnets which allowed generated electrons to be deflected onto a set of three Kodak Lanex Regular screens; the electron energy spectrum could then be inferred from a measurement of the beam deflection.

The primary component of Lanex screens, $Gd_2O_2S : Tb$ (gadolinium oxysulphide phosphor), emits light at 545 nm when subjected to ionising radiation. This allowed for the indirect detection of energetic electrons in the experiment. Bandpass filters were used to minimise other sources of visible radiation. In the experiment, 546 nm central wavelength filters were used with a 10 nm full width-half maximum and a transmission of approximately 98%.

The angular distribution of the visible light emitted by Lanex screens is commonly assumed to be Lambertian, i.e., the screen radiance is isotropic, although there is a systematic deviation from this distribution depending on a number of factors such as the grain size and material thickness [85]. Emission following . Deviations from the ideal distribution is reduced when the energy deposited in the screen is independent of the depth, as is the case for highly energetic electrons [86]. Hence, deviations from Lambertian emission were assumed to be negligible for the screens used in this experiment. Previous experiments have produced calibrations for various Lanex screen models [86, 87], which provide the relation between the number of incident electrons and the number of photons emitted.

The cameras used to detect the radiation emitted by the Lanex screens were triggered no more than 25 µs after the laser was fired. Upon initial reaction with the electron beam, emission at 545 nm decays approximately exponentially on the timescale of 1 ms [87, 88]. Hence, the camera exposure time was set to be 100 ms, allowing the detector to capture the full signal decay. The Andor Neo sCMOS DC-152Q-C00-FI camera was

used to image the Lanex screens, and has a quantum efficiency of 57% at 546 nm.

Imaging plates are an alternative method of measuring the charge produced by an electron beam [89, 90], whereby electrons in the phosphor material are excited to a metastable state. The imaging plate can then be processed later using a scanning device which induces photostimulated luminescence. The proper calibration of an imaging plate is complex due to its variable emission characteristics which depend on the temperature, scanner model and time taken between exposure and readout [91]. In this campaign, imaging plates were used during a single run to allow cross-calibration between the imaging plates and Lanex screens, however, due to time constraints, the calibration was not performed for the imaging plates.

In order to calibrate the Lanex screens, code was written to model the experimental setup and obtain a relation between the spatial distribution of electrons on a screen with known position for a given electron energy. This process is shown below.

4.3.1 Theory

The trajectory of an electron traversing the magnetic field of the spectrometer can be calculated if the initial position and energy of the electron is known. The motion is governed by the relativistic Lorentz force law,

$$\mathbf{F} = \frac{\mathrm{d}(\gamma m_\mathrm{e}\mathbf{v})}{\mathrm{d}t} = -e\left(\mathbf{E} + \mathbf{v}\times\mathbf{B}\right), \tag{4.1}$$

where $\gamma = \left(1 - |\mathbf{v}|^2/c^2\right)^{-1/2}$ is the Lorentz factor.

Code was written in MATLAB by the author to trace the path of an electron by solving a scaled form of the equations of motion where $\boldsymbol{\zeta} = \mathbf{p}/(m_\mathrm{e}c)$. With this scaling,

we can rewrite the Lorentz factor as $\gamma = \sqrt{1 + |\boldsymbol{\zeta}|^2}$. Thus,

$$\frac{\mathrm{d}\mathbf{x}}{\mathrm{d}t} = \frac{c\,\boldsymbol{\zeta}}{\sqrt{1 + |\boldsymbol{\zeta}|^2}}, \tag{4.2}$$

$$\frac{\mathrm{d}\boldsymbol{\zeta}}{\mathrm{d}t} = -\frac{e}{m_\mathrm{e}}\left(\frac{\mathbf{E} + \boldsymbol{\zeta} \times \mathbf{B}}{\sqrt{1 + |\boldsymbol{\zeta}|^2}}\right). \tag{4.3}$$

Using MATLAB's `ode45` differential equation solver function, (4.2) and (4.3) can be solved given a set of initial conditions. Momentum scaling was employed in order to improve the MATLAB solver accuracy. Note that it was not necessary to explicitly calculate the electron acceleration since the calibration of the electron spectrometer relies solely on the intersection position of the electrons and the Lanex screen. The acceleration could in theory be calculated using:

$$\mathbf{a} = -\frac{e}{\gamma m_\mathrm{e}}\left(\mathbf{E} + \mathbf{v} \times \mathbf{B}\right) + \frac{e}{\gamma m_\mathrm{e} c^2}\mathbf{v}\left(\mathbf{v} \cdot \mathbf{E}\right). \tag{4.4}$$

4.3.2 Comparison of code with theory

In order to test the particle tracking code, a simple test case was constructed which consisted of an electron with fixed energy propagating in a static homogeneous magnetic field, $\mathbf{B}$. The position traced by the electron in the simulation was compared with theory, in the relativistic and non-relativistic case, by calculating the gyroradius,

$$r = \frac{\gamma m_\mathrm{e} |\mathbf{v}|}{e\,|\mathbf{B}|}. \tag{4.5}$$

Three electron energies were chosen for this purpose: 50 keV, 5 MeV and 5 GeV. Using a magnetic flux density of 1 T, the corresponding radii for these electron energies were 7.72×10^{-4} m, 1.83×10^{-2} m and 16.7 m, or more conveniently, diameters of 1.54×10^{-3} m, 3.66×10^{-2} m and 33.4 m, respectively.

The trajectory for the 5 GeV electron is shown as an example in Figure 4.2, revealing

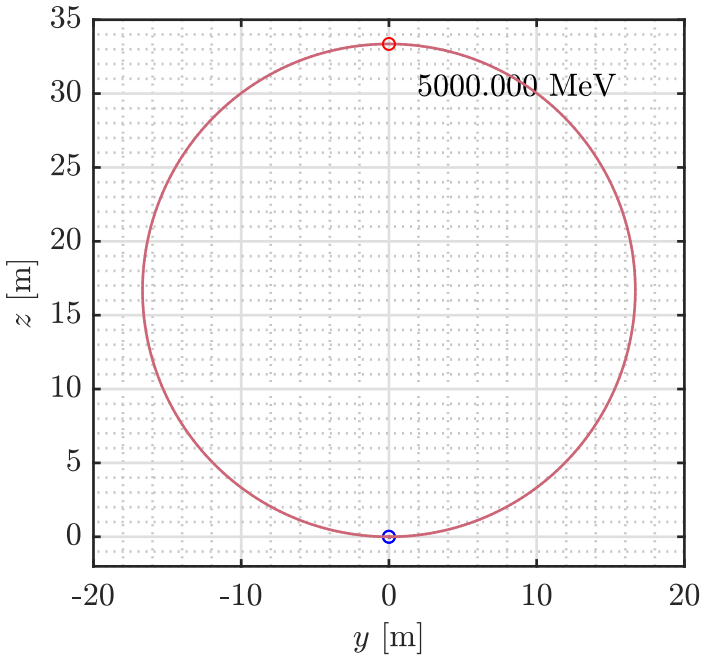


Figure 4.2: Plot of electron trajectory in the yz-plane for an energy of 5 GeV.

the expected circular motion for a charged particle in a constant magnetic field. The blue marker corresponds to the initial position, whereas the red marker highlights the point of largest displacement s. Figure 4.3 plots the displacement s as a function of time t for the three electron energies. The maxima are shown and match very well with the expected values to within 1 part in 10^4. The simulated trajectories of interest in the Gemini experiment are expected to have less error (assuming perfect knowledge of the magnetic fields) since the electrons would exit the magnetic field structure in a shorter time frame.

4.3.3 Simulations using Gemini parameters

The field map for the permanent magnets used in the Gemini experiment is shown in Figure 4.4 (courtesy of Jonathon Wood, Imperial College London). Using the vertical axis in the figure, the laser axis and hence, the generated electron beams were nominally at a height of 23 mm. The field was positive in the x-direction (out of the page) and the laser beam propagated along the y-axis. The trajectories for a few electron energies are

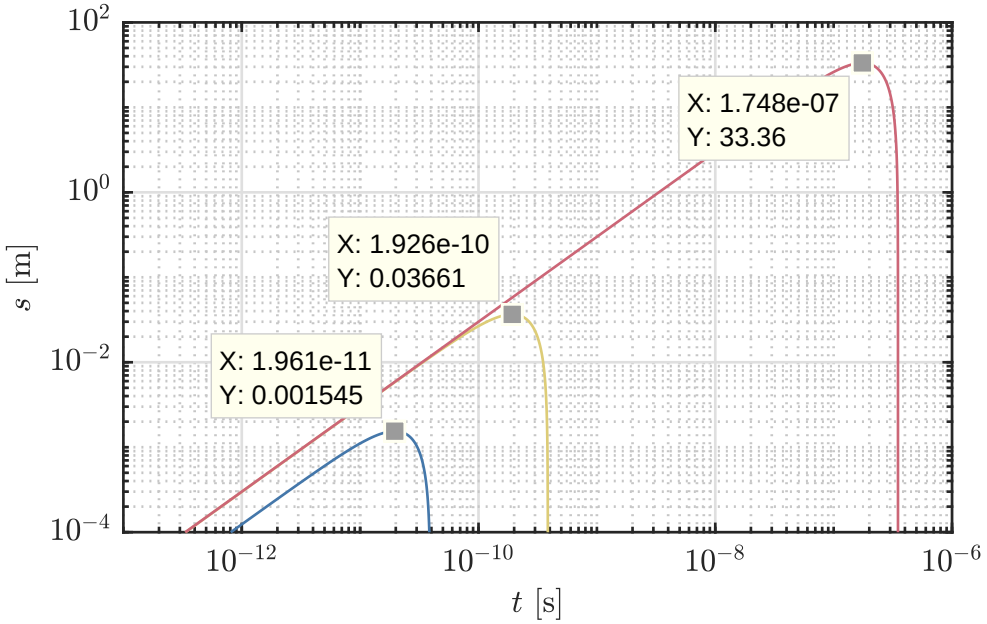


Figure 4.3: Plot of electron displacement s as a function of time t for energies of 50 keV (blue), 5 MeV (yellow) and 5 GeV (red).

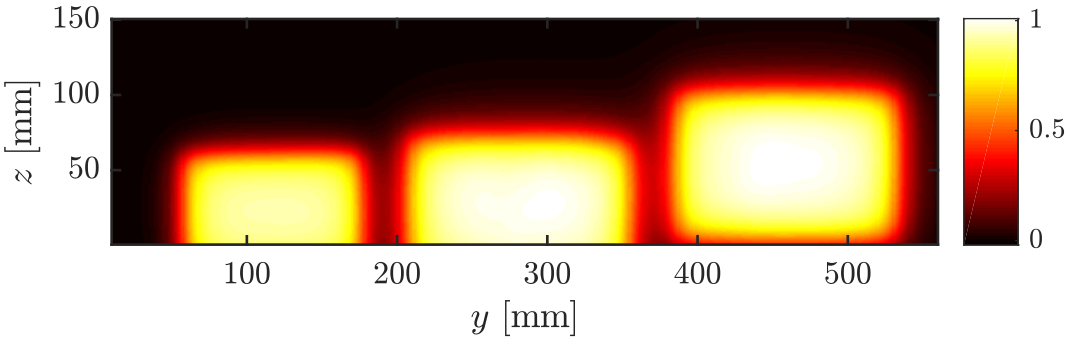


Figure 4.4: Magnetic flux density of permanent magnets in units of teslas.

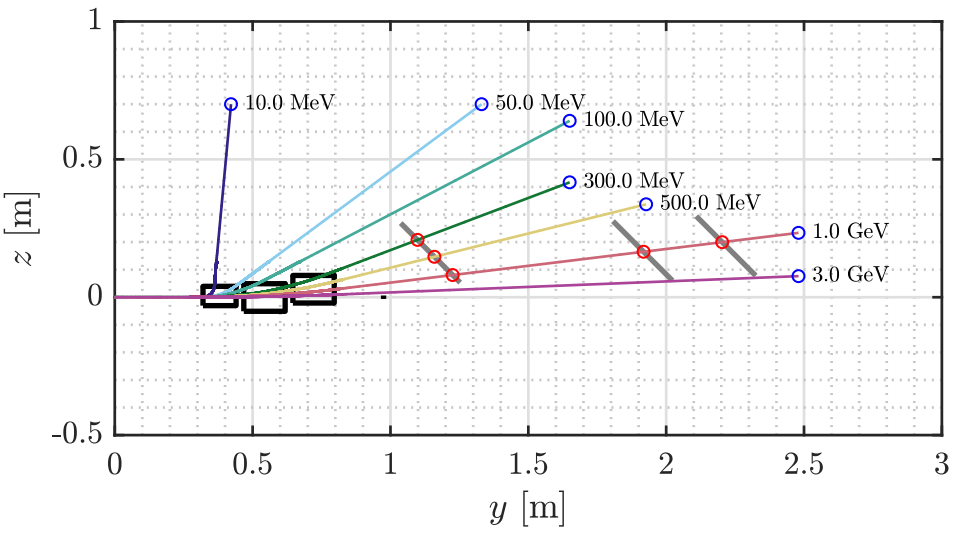


Figure 4.5: Simulation of electron trajectories of energies between 10 MeV to 3 GeV through a series of permanent dipole magnets (black). Intersections with the Lanex screens (gray) are indicated by red markers.

shown in Figure 4.5. The magnets are represented by black rectangles and the Lanex screens marked as gray lines.

A set of calibration curves were generated from the list of intersection positions of the electron trajectories with the Lanex screens for predetermined kinetic energies. The curves, one for each screen, are shown in Figure 4.6 and Figure 4.7. The blue, yellow and red curves corresponds to the Lanex screens from left to right as shown in Figure 4.5 and will be referred to as the 'low', 'medium' and 'high' energy screens, respectively. The energy ranges covered by each screen are: 141 MeV to 1.56 GeV for the low energy screen, 556 MeV to 2.91 GeV for the medium energy screen, and 647 MeV to 2.70 GeV for the high energy screen.

The calibration is sensitive to a number of factors. For instance, the measurements of the Lanex screen positions are only accurate to a few millimetres. Bowing of various elements in the chamber could also occur during cycling of the pressure in the target chamber, further exacerbating the effect. A liberal 5 mm vertical shift (z-direction) in the screens was simulated and is represented by the coloured regions surrounding each line in Figure 4.6. The width of the band tends to increase for increasing energies, as

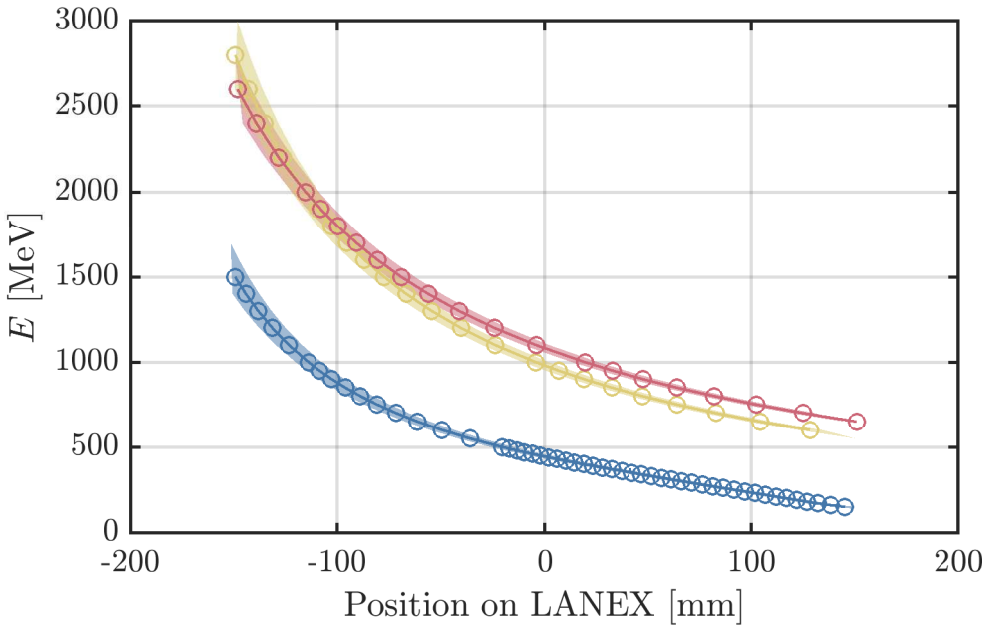


Figure 4.6: Energy calibrations for the three Lanex screens (blue, yellow and red) shown in Figure 4.5 (from left to right, respectively). Bounds indicate the effect on the curves for a vertical shift in the screen positions of 5 mm.

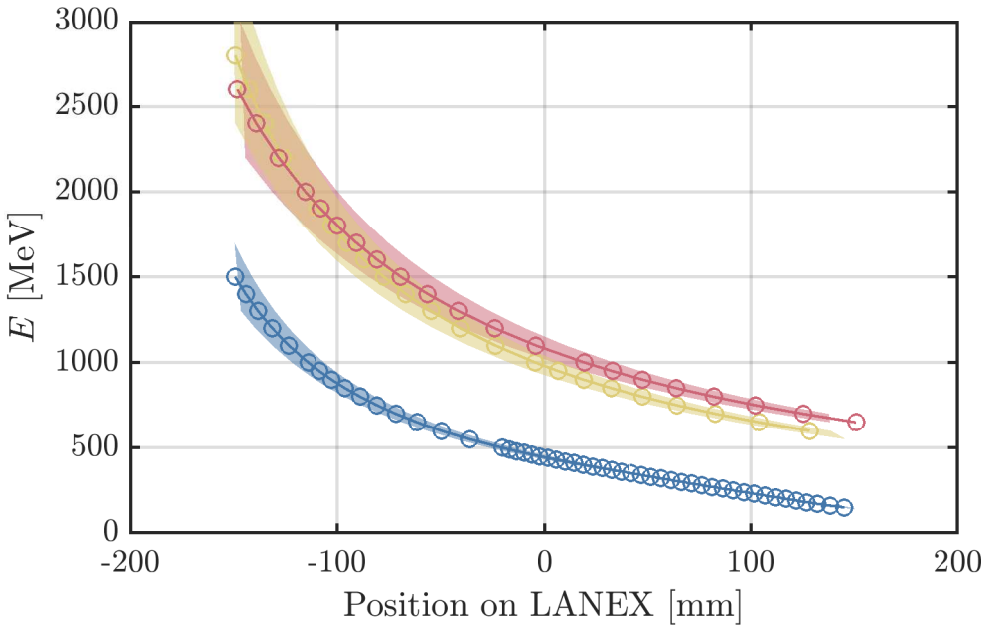


Figure 4.7: Energy calibrations for the three Lanex screens (blue, yellow and red) shown in Figure 4.5 (from left to right, respectively). Bounds indicate the effect on the curves for a pointing discrepancy of 5 mrad from the electron source.

expected, since energy measurements are more sensitive at higher energies. Specifically, a change in the position on the Lanex screen has a greater effect on the change in measured energy at high energies where increasingly more energetic electrons are deflected less and less due to their increasing relativistic mass.

Shot-to-shot variations in the laser pointing and exit position of the electron bunch in the wakefield could be expected to affect the incident electron trajectory into the magnetic fields and cause large deviations from their nominal paths. As a result, there would be no single solution to map an electron of given energy to a specific point on a Lanex screen. Typical values of the electron pointing jitter lies in the few milliradian range [92]. To visualise the effect in this experiment, simulations were run with a 5 mrad vertical deflection. The result is shown in Figure 4.7. It is clear that even with a pessimistic estimate of the shift in Lanex position, the calibration is most sensitive to the pointing stability.

Multiple screens to track the propagation of discernable features in the spectrum have been used by other groups to provide a unique solution to the equations of motion [93] or comparing experimental spectra to Monte-Carlo simulations with an assumed electron spectrum and angular distribution [94]. Unfortunately, it was found that the camera observing the high energy screen had been misaligned, or in other runs, was triggered incorrectly, and so no results have been shown for this energy range. This also meant that the method of using multiple screens could not be used between the medium and high energy Lanex screens.

4.3.4 Application to the Gemini experiment

Since the detectors did not view the Lanex screens at normal incidence, a slight distortion of the screen was present due to perspective foreshortening. A projective transformation was used to correct this effect. Namely, the conversion of a given pixel coordinate to position on the Lanex screens was carried out by identifying the pixel positions of the

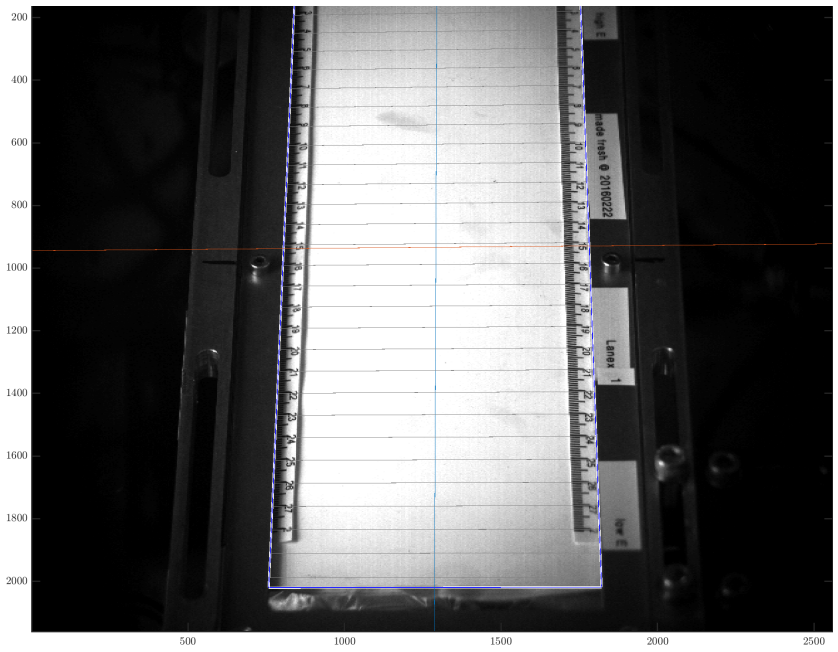


Figure 4.8: Image of low energy Lanex screen with projection of horizontal lines with respect to the screen, corresponding to contours of equal electron energy.

Lanex corners, which correspond to local coordinates in the screen frame of reference when the length and width are known. The origin was chosen to be the centre of the Lanex screen. A map was obtained using MATLAB's `fitgeotrans` function, which could be used with the energy calibrations shown previously (Figure 4.6) to give a pixel position to electron energy calibration.

Figure 4.8 shows an image of a Lanex screen outlined in blue. The cyan and orange lines show the central axes and cross at the local origin of the Lanex screen. Grey lines were superimposed at 1 cm intervals on the image of the screen to allow comparison with the paper rules fixed to the edge of the screen. Excellent agreement can be seen. This provided sound evidence that the transformation map was correctly determined. Finer adjustment of the map could be made if a significant discrepancy was found in the rulings, as would be the case if the Lanex dimensions were incorrectly measured.

Since the Lanex screens are sensitive to all forms of ionising radiation, it was found that there was a somewhat uniform background level on the Lanex screens due

to bremsstrahlung radiation. To account for this, a 3×3 median filter was applied to smooth the image and then the median pixel value across the whole screen was subtracted (in addition to the dark frame), before applying analyses. This isolated luminescence due to bremsstrahlung from that due to the electron beam. It was found that a further threshold was required as any remaining bremsstrahlung background, significantly impacted the analyses. The threshold used was taken to be twice the standard deviation of the pixel values in the full Lanex area (after the median filter). These corrections were most effective when the area of the electron beam on the Lanex screen was small.

It is desirable to measure the electron beam charge which scales as the number of photons collected. Furthermore, the electron spectrum can be obtained by finding the charge as a function of electron energy. This could not be done so simply with the raw data image as the electron energy contours were not completely parallel to the pixel rows as was seen in Figure 4.8. Therefore, instead of summing the pixel values along individual rows, the image was binned into areas of equal electron energy (according to the calculated calibration Figure 4.6), similar to the regions between the grey lines shown in Figure 4.8. The areas were chosen to be 1 mm wide in the Lanex coordinate frame. For reference, this was equivalent to splitting the image into strips of approximately 8 pixels wide and yields an energy resolution of 1.2 MeV at the low energies, and 22 MeV at the higher energies for the low energy screen shown. As an example, Figure 4.9 shows one of the captured low energy electron spectrometer images. The retrieved spectrum for this is shown in Figure 4.10.

The scaling between camera counts and charge incident on the Lanex screen has been approximated for the low energy screen. The calculation is based on [86, 95].

$$\frac{\mathrm{d}Q}{\mathrm{d}E}(E_0) = \left(\frac{\mathcal{C}(E_0)}{\delta s_\mathrm{L}}\right)\left(\frac{\mathrm{d}s_\mathrm{L}}{\mathrm{d}E}\right) \times \left(\frac{\mathcal{Q}\,T\,\Omega\cos\theta_\mathrm{out}}{\mathcal{S}}\right)^{-1} \times \left(\frac{\kappa_\mathrm{L}}{\cos\theta_\mathrm{in}}\exp\left[-\frac{t_\mathrm{d}}{\tau_\mathrm{L}}\right]\right)^{-1}, \quad (4.6)$$

where $\mathcal{C}$ is the total number of counts between the Lanex position s_L and $s_\mathrm{L} + \delta s_\mathrm{L}$, which

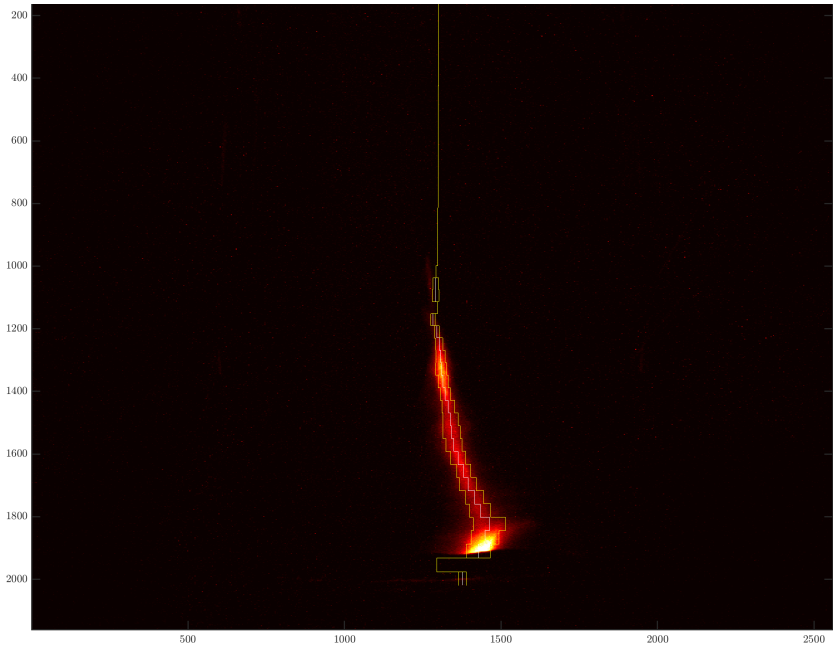


Figure 4.9: Example of photoluminescence of low energy Lanex screen due to a LWFA-produced electron beam.

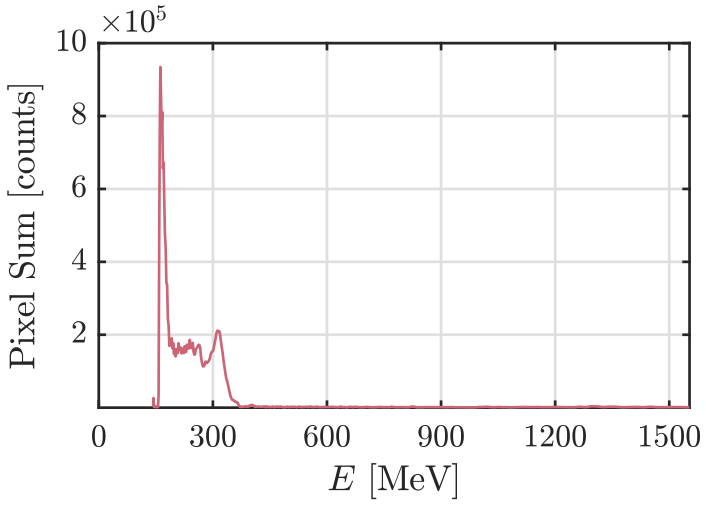


Figure 4.10: Example of electron energy spectrum as measured by the low energy Lanex screen, corresponding to Figure 4.9. The spectrum is truncated at low energies (<150 MeV) due to the limits of the Lanex screen.

corresponds to the electron energy range with a central energy value E_0. Recall, the width of the Lanex strip was chosen to be $\delta s_\mathrm{L} = 1\,\mathrm{mm}$. The energy dispersion $\mathrm{d}s_\mathrm{L}/\mathrm{d}E$ can be computed from the calibration in Figure 4.7. The central term accounts for the detector quantum efficiency $\mathcal{Q} = 0.57$ (fraction of incident visible photons detected) and detector sensitivity $\mathcal{S} = 1.81\,\mathrm{electrons/count}$ (number of detected photons per count). The solid collection angle Ω and transmission of the optical system T determine the fraction of emitted photons which reach the detector. Since the distance from Lanex screen to detector lens $D \approx 2\,\mathrm{m}$ is much greater than the maximum lens diameter $d \approx 62\,\mathrm{mm}$, the collection angle can be approximated as $\Omega = \pi d^2/(4D^2) = 7.5 \times 10^{-4}\,\mathrm{sr}$. However, the actual collection angle may be smaller due to internal apertures in the zoom lens. The transmission of the zoom lens used could not be found, hence the total transmission could only be approximated as 90%. The cosine term accounts for the Lambertian emission distribution when the detector views the Lanex at an angle $\theta_\mathrm{out} = 45\,^\circ$. The total number of photons emitted by the screen per incident unit charge per unit solid angle κ_L is taken from the absolute calibration in [87] for the Kodak Lanex Regular screen which is $6.95 \times 10^9\,\mathrm{photons/sr/pC}$. The exponential term gives the fraction of photons emitted after a period t_d, which for this case is $25\,\mu\mathrm{s}$. The decay time of the Lanex screen τ_L is 0.66 ms [88]. The cosine term accounts for the extra emission resulting from a beam incident on the Lanex screen at an angle θ_in to the screen normal. The angle of incidence was estimated assuming all electrons travel from the centre of the magnets (longitudinally) to the centre of the Lanex screen, giving $\theta_\mathrm{in} = 29\,^\circ$. Making the approximation that Ω, θ_out and θ_in are all constant w.r.t. E_0, the charge density is then

$$\frac{\mathrm{d}Q}{\mathrm{d}E}(E_0) \approx \left(\frac{\mathcal{C}(E_0)}{\delta s_\mathrm{L}}\right)\left(\frac{\mathrm{d}s_\mathrm{L}}{\mathrm{d}E}\right) \times 8.65 \times 10^{-7}\,\mathrm{pC/count}. \tag{4.7}$$

The uncertainty in the calibration can be estimated from the uncertainty associated with the collection angle which is expected to be the main source of error. Using a

conservative estimate of the uncertainty in D of 20 cm and a 20% error in the lens diameter (no information could be found which relates the effective aperture diameter with the zoom setting), the relative uncertainty in the collection angle and thus the uncertainty in a measurement of the total charge is 45%. Clearly the calibration is highly sensitive to the collection angle due to the square dependence of the lens diameter d and camera-Lanex separation D. It should be noted that although the absolute charge value may only be accurate to within an order of magnitude, the error is systematic, so measurements can be compared with one another.

Whereas a spectral measurement could be found from splitting the image into horizontal sections in the Lanex frame of reference (sections perpendicular to the plane dispersion), the image could be split into vertical slices (sections parallel to the plane dispersion) and summed to give the beam profile in the direction parallel to the magnetic field. An estimate of the beam divergence can then be found using a Gaussian fit. A disadvantage of this method is it can overestimate the divergence if the beam has a centre which is not constant with energy, i.e., the dispersed beam is not perpendicular to the B-field, as in Figure 4.9 which shows an electron spectrum which trails to the right at low energies.

To compensate the divergence measurement for this effect, the image was first split into horizontal slices (at a lower resolution than when measuring the electron spectrum) and then each slice fit to a Gaussian distribution as above. The centres are plotted in Figure 4.9 as white lines and the standard deviations as yellow lines on each side. An improved value of the divergence could then be calculated by taking the weighted average of the slice standard deviations, where the weights were calculated as the proportion of the pixel sum in a given slice to the total pixel slice in the Lanex region. For the example shot shown, the rough standard deviation was $\sigma' = (6.7 \pm 0.8)$ mm and the weighted standard deviation was $\sigma'_{\mathrm{w}} = (2.99 \pm 0.06)$ mm. The divergence was approximated by assuming the total distance travelled by electrons was simply the direct line of sight distance between the centre of the screen to the interaction point (1.16 m). This led to

a measured half-angle divergence of $\sigma = 5.8\,\mathrm{mrad}$ and $\sigma_\mathrm{w} = 2.6\,\mathrm{mrad}$, respectively. It should be noted that this method of fitting a Gaussian distribution over multiple slices is sometimes inaccurate, as it is possible for the beam width to be comparable to the width of the vertical slices. This can lead to the shape of the beam not being resolved and poor Gaussian fitting. It was found that using thinner slices led to aliasing due to too few pixels in each slice. In other cases, it was found that the beam profile was not Gaussian-like and comparison using the rough divergence measurement is more suitable.

In order to provide a simple means to compare the single-shot energy spectrum of each shot, multiple cut-off energies were defined. Specifically, they were the energies below which 25%, 50% and 75% of the total charge was contained.

4.3.5 Limitations of the model

A potential problem with the simulation of the electron spectrometer is the edge of the field map which terminates at 50 mT on the y-scale, resulting in a loss of the field structure which may otherwise perturb electron trajectories by a small amount. This could be partially compensated for in future work by extrapolating the field, but has been assumed to have a negligible effect in this work. Another factor which may cause differences between the actual magnetic field and the simulated field is that the magnets could have physically changed since the time of measurement, e.g. chips in the magnet which would alter the field.

Although electrons are spawned at the origin in the simulation, this may not necessarily be a singular point in the experiment since it would be expected that electrons are generated in a volume during the laser wakefield interaction. Combined with day-to-day variations in the longitudinal laser focus position, the distance between the magnets and the electron generation point may vary by a few millimetres.

In principal, electron energy contours would not simply correspond to horizontal lines in the Lanex frame of reference, since it would be expected that particles travelling

towards the edges of the screen would experience the magnetic field for longer given their increased path length, resulting in energy contours which arc away from the nominal beam axis. However, this effect was assumed to be insignificant since the majority of the electrons landed near the central axis of the screen.

The cut-off energy only accounts for the electrons which were detected by the low energy Lanex. However, in many shots, it was clear that the spectrum extended to lower energies which could not be measured by this experimental setup.

4.4 Betatron Radiation Measurement

The betatron radiation produced in the Gemini Astra experiment was measured using an X-ray CCD. The CCD, when placed on-axis, resulted in a large number of X-rays incident on each pixel. Hence, the energy deposited in each pixel will come from photons across the whole energy spectrum and it is not possible to distinguish the contribution from a given energy range. More sophisticated methods may be used to measure the betatron radiation spectrum produced by a laser plasma accelerator.

The method chosen in this experiment was to observe the transmission of the beam through various filters. There are a few variations on this method, however, a common method is to use *Ross filters* [34, 72, 77, 96], also known as differential filters, because they can *in theory* allow the spectral properties within a thin energy band to be inferred simply by comparing the transmission between a pair of filters without any complicated analysis.

4.4.1 Theory

The mass attenuation coefficient μ/ρ (c.f. (2.9)) which determines the intensity of a beam transmitted through a material is wholly dependent on the elemental composition of the material. Figure 4.11 shows the mass attenuation coefficient for aluminium

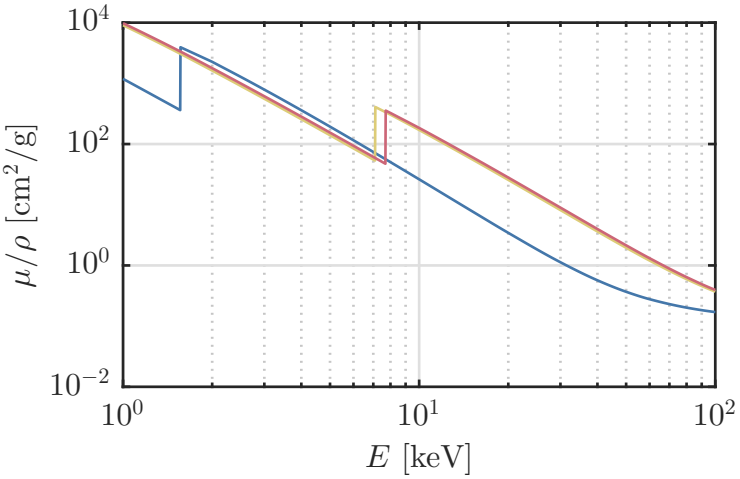


Figure 4.11: Mass attenuation coefficient of aluminium (blue), iron (yellow) and cobalt (red) as a function of photon energy.

(blue), iron (yellow) and cobalt (red). The atomic numbers of these elements are 13, 26 and 27, respectively. It can be seen that there is a discontinuity in each of the lines, corresponding to an increase in the absorption when the photon energy matches the K-edge of the material. Additionally, the mass attenuation coefficients are very similar for consecutive elements in the periodic table as can be seen for iron and cobalt, with the main difference due to the different K-edges. Hence, the spectral properties of a beam transmitted through one of these compared to the other will differ mainly in the region between their K-edges. By careful consideration of the thickness of each material, it is possible to better match, or balance, the transmission through each material [97], referred to hereafter as the *transmittance* which is the ratio of transmitted to incident intensity (c.f. (2.9)). Figure 4.12 shows the comparison of a balanced versus unbalanced pair of Fe-Co filters. The transmittance is calculated for a 10 µm thick iron filter (yellow), 10 µm thick cobalt filter (red solid) and a correctly balanced 8.1 µm thick cobalt filter (red dashed).

By using many balanced filter pairs, the transmittance in each energy range can be used to directly determine the spectrum of the incident beam. In the (typical) case that only a few filter pairs are used, the spectrum can still be inferred if the spectral *shape* is assumed [34]. When dealing with betatron radiation in the scenario of few filters, the

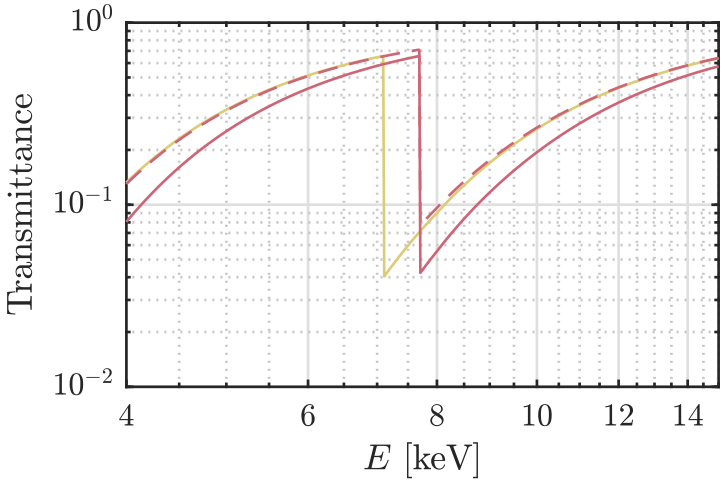


Figure 4.12: Transmittance for a balanced pair of iron and cobalt filters as a function of photon energy, corresponding to 10 µm iron (yellow) and 8.1 µm cobalt (red, dashed). An unbalanced cobalt sheet of 10 µm thickness is shown for comparison (red, solid).

spectrum is fit to the measured data by varying the critical energy E_c as a parameter.

4.4.2 Filter wheel design

In the Astra Gemini experiment, the author designed a filter wheel which would be able to measure the spectrum in the range of 1 keV to 30 keV. Careful selection of the materials allowed a single filter to be used in multiple Ross filter pairs, i.e. the K-edge can be used as both an upper and lower energy limit.

A bespoke MATLAB script was written by the author to calculate optimal thicknesses, given a list of materials. The script made use of functions written by Jaroslaw Tuszynski [98] to retrieve the mass attenuation coefficients μ/ρ from the NIST database [99]. The list of materials were sorted according to their binding energies in order to determine which materials should be matched to form Ross pairs. Starting at a given thickness t_1 and corresponding density ρ_1 for the first material, i.e. the material with the lowest energy K-edge, the thickness of the next material t_2 with density ρ_2 was determined by minimising the difference in the transmittance curves of the materials (as seen in

Figure 4.12) such that:

$$\begin{aligned} T_1 &= T_2, \\ \exp\left[-\left(\frac{\mu_1}{\rho_1}\right)\rho_1 t_1\right] &= \exp\left[-\left(\frac{\mu_2}{\rho_2}\right)\rho_2 t_2\right], \\ \Rightarrow \frac{\mu_1}{\rho_1} &= \left(\frac{\rho_2 t_2}{\rho_1 t_1}\right)\left(\frac{\mu_2}{\rho_2}\right). \end{aligned} \tag{4.8}$$

The fit procedure takes the form of $y = ax$, where $y = \mu_1/\rho_1$, $x = \mu_2/\rho_2$ and $a = \rho_2 t_2/(\rho_1 t_1)$. Recalling that x and y are the known mass attenuation coefficients, which are a function of energy, the best fit value of a was evaluated, allowing the optimal thickness to be calculated $t_2 = a\rho_1 t_1/\rho_2$.

The minimisation was performed, excluding the energy region between the pair of K-edges—referred to hereafter as the *K-band*—resulting in transmittance curves which overlap except in a narrow range. Note, in some materials, other edges were present in the full energy range of interest, particularly for heavier elements. These edges could also be used instead of the K-edges, but for convenience, this text will continue to refer to the edge of interest as the K-edge. For the materials with multiple edges, it was chosen to optimise their thickness by additionally excluding the region beyond immediately adjacent edges from the minimisation. A consequence of this is there would be an increased mismatch in the transmittance curves in the excluded region.

A slightly better approach to the minimisation could have been used, whereby an exponential fit is used instead of the linear fit above:

$$\begin{aligned} T_1 &= T_2, \\ \exp\left[-\left(\frac{\mu_1}{\rho_1}\right)\rho_1 t_1\right] &= \exp\left[-\left(\frac{\mu_2}{\rho_2}\right)\rho_2 t_2\right], \\ \Rightarrow \exp\left(-\frac{\mu_1}{\rho_1}\right) &= \exp\left[-\left(\frac{\rho_2 t_2}{\rho_1 t_1}\right)\left(\frac{\mu_2}{\rho_2}\right)\right]. \end{aligned} \tag{4.9}$$

The fit procedure in this form could be solved via $y = \exp(ax)$, where $y = \exp\left(-\mu_1/\rho_1\right)$,

$x = \mu_2/\rho_2$ and $a = -\rho_2 t_2/(\rho_1 t_1)$, such that $t_2 = -a\rho_1 t_1/\rho_2$. This approach was not implemented for the Astra Gemini experiment, but it was found that both approaches gave very similar values of t_2 for materials with a single edge in the range of interest. A further improvement could also be made if the fit was weighted towards higher energies, since mismatches in the transmittance at a higher photon energy would have a greater effect on the signal recorded by a CCD than that of a lower energy (disregarding the drop-off in quantum efficiency at higher energies).

In general, for a given initial thickness t_1, the difference in transmittance of subsequent material pairs continually reduces due to the reduction in the mass attenuation coefficient with increasing energy. In other words, at higher energies, the transmittance tends to unity and the difference in transmittance tends to zero. In order to compensate for this, the thickness was 'reset' after every few K-edges, with subsequent materials matched to the the new thickness.

In theory, there is an optimum thickness for each material—in the sense that the height of the K-edge is maximal—given by [100, 101]

$$t_{\text{opt}} = \frac{\ln(\mu_{\text{L}}/\mu_{\text{U}})}{\mu_{\text{L}} - \mu_{\text{U}}}, \tag{4.10}$$

where μ_{L} is the lower value of the attenuation coefficient at the K-edge and μ_{U} is the upper value of the attenuation coefficient at the K-edge. However, this was used mainly as a guideline since the material thicknesses were dependent on each other.

A proposed list of materials and their thicknesses is shown in the legend of Figure 4.13. The figure displays the difference in transmittance for the material pairs. The materials used were mostly compiled from those used in previous experiments by other groups [102–104]. The spectral resolution using this set of filters decreases above 10 keV due to the scarcity of non-hazardous or available materials suitable for measurements in the higher energy range. The reset in thickness can be identified by large discontinuities in the overall shape of Figure 4.13, such as the curves corresponding to lead with 52.2 µm

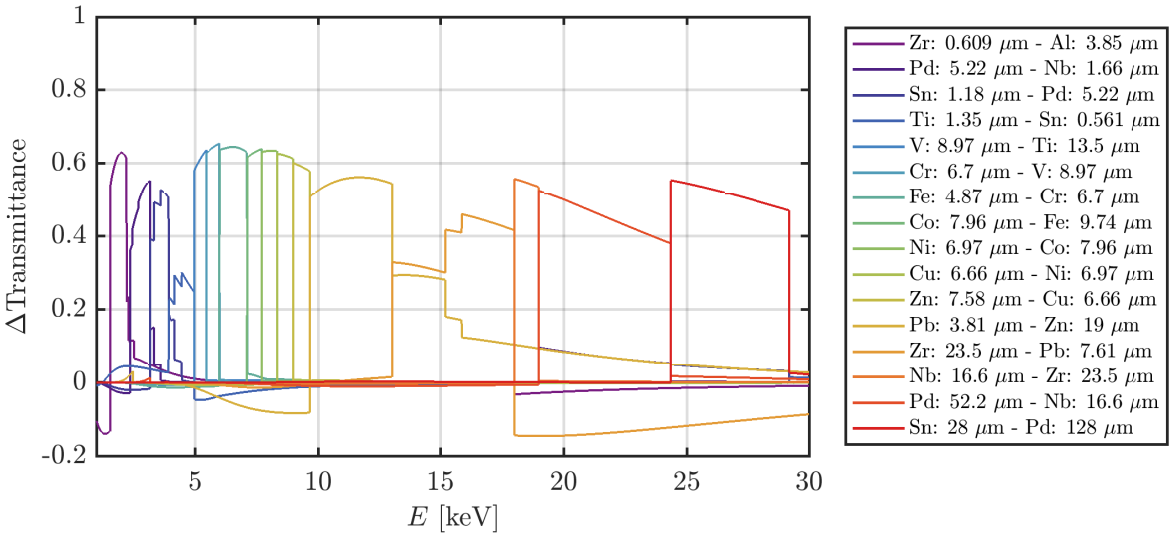


Figure 4.13: Transmittance difference for balanced Ross pairs as indicated in the legend for the energy range between 1 keV to 30 keV.

and 128 µm.

Due to a limitation on availablity and resources, not all materials shown in Figure 4.13 could be sourced and of those that could, the thickness was restricted to certain values. Through multiple iterations, a new list was generated as shown in Figure 4.14. With the thicknesses predetermined by the supplier, it can be seen that this results in a more significant deviation from zero for the transmittance difference in regions outside the K-bands. Hence, the accuracy of a given pair will depend on the ratio of the area under the curve in the K-band to the total area over the whole energy range. This ratio will be referred to as the *K-band ratio* later in the text.

An image of one (out of two) of the filter wheels fabricated is shown in Figure 4.15. The set of filters were placed on a 23 µm sheet of Mylar (a branded polyester with high tensile strength) to support the thin slices of metal.

4.4.3 Methods

Here, the retrieval of the spectrum through the use of the filter wheel, described above, is presented. First, the energy deposited E in the CCD by a beam with energy spectral

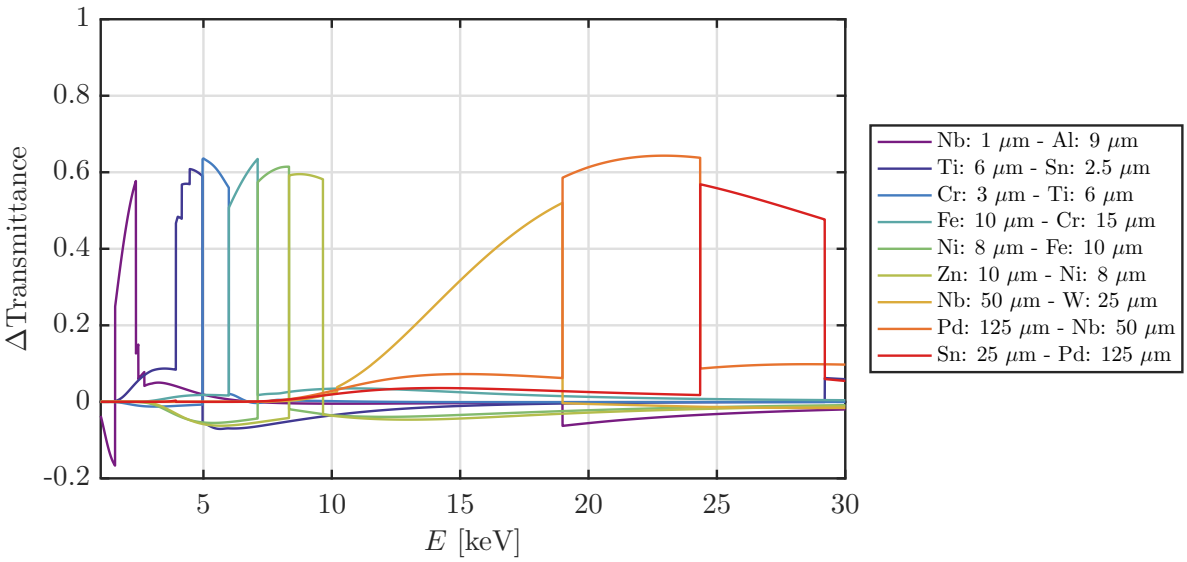


Figure 4.14: Transmittance difference for quasi-balanced Ross pairs as indicated in the legend for the energy range between 1 keV to 30 keV.

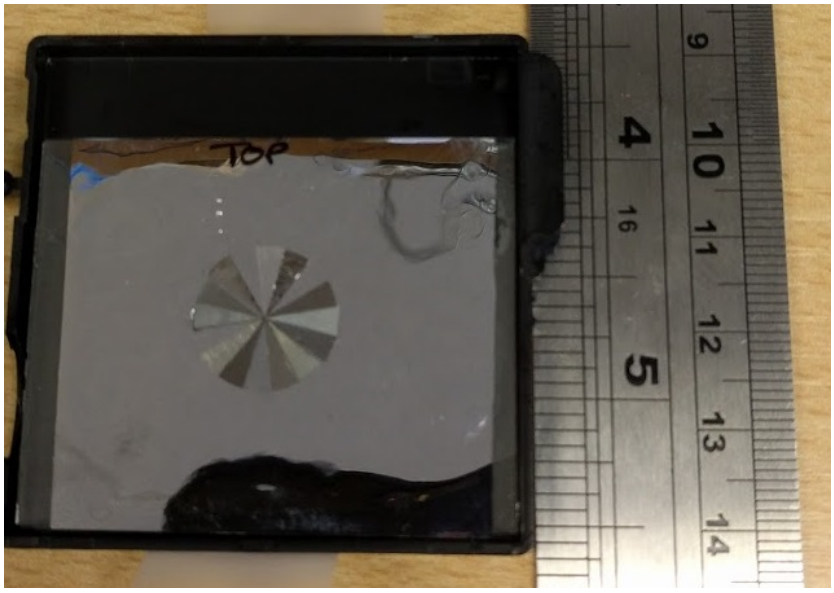


Figure 4.15: Image of a filter wheel fabricated by the Target Fabrication group in the Central Laser Facility.

density $\mathrm{d}E/\,\mathrm{d}\omega$ through a given filter is given by

$$E = \int \frac{\mathrm{d}E}{\mathrm{d}\omega} \mathcal{Q}\, T_0\, T\, \mathrm{d}\omega, \tag{4.11}$$

where $\mathcal{Q}$ is the quantum efficiency of the camera, T is the transmittance of the filter and T_0 is the combined transmittance of the other sources of attenuation (such as the Mylar light shield and tape drive). For convenience, $\mathcal{Q}\, T_0\, T$ will be referred to as the *effective transmittance*, which is a function of photon frequency.

By subtracting the transmission of one material from another, the energy spectral density can be inferred in the the range $\omega_{K_1} \leq \omega \leq \omega_{K_2}$, i.e. the K-band, where $\omega_{K_{1,2}}$ is the frequency corresponding to the relevant edge of the first and second material. Hence,

$$\begin{aligned} \Delta E_{12} &= E_2 - E_1, \\ &= \int \frac{\mathrm{d}E}{\mathrm{d}\omega} \mathcal{Q}\, T_0\, T_2\, \mathrm{d}\omega - \int \frac{\mathrm{d}E}{\mathrm{d}\omega} \mathcal{Q}\, T_0\, T_1\, \mathrm{d}\omega, \\ &= \int \frac{\mathrm{d}E}{\mathrm{d}\omega} \mathcal{Q}\, T_0\, (T_2 - T_1)\, \mathrm{d}\omega, \end{aligned} \tag{4.12}$$

where ΔE_{12} is the difference in the energy captured by the camera through filter 1 and 2. When the filters are very well matched, $(T_2 - T_1)$ is close to zero for values of ω outside the K-band and thus the integral in (4.12) need only be evaluated between the K-band. If it is assumed that $\mathrm{d}E/\,\mathrm{d}\omega$ is approximately constant in this range, then it can be taken outside the integral and (4.12) can be rearranged to give

$$\left.\frac{\mathrm{d}E}{\mathrm{d}\omega}\right|_{\omega=\bar{\omega}_K} = \Delta E_{12} \left[\int_{\omega_{K_1}}^{\omega_{K_2}} \mathcal{Q}\, T_0\, (T_2 - T_1)\, \mathrm{d}\omega\right]^{-1}, \tag{4.13}$$

where $\bar{\omega}_K$ is defined as $\bar{\omega}_K = (\omega_{K_1} + \omega_{K_2})/2$. By evaluating this expression for each pair of filters, $\mathrm{d}E/\,\mathrm{d}\omega$ can be calculated at different energies, thereby retrieving the energy spectral density.

Using f as a shorthand for the integral in (4.13), the error in $\mathrm{d}E/\,\mathrm{d}\omega$ was estimated

by calculating the error in ΔE and f,

$$\frac{\delta\left(\mathrm{d}E/\,\mathrm{d}\omega\right)}{\mathrm{d}E/\,\mathrm{d}\omega} = \sqrt{\left(\frac{\delta\Delta E}{\Delta E}\right)^2 + \left(\frac{\delta f}{f}\right)^2}. \tag{4.14}$$

The error in δE is addressed here by examining the measurement for each slice. An accurate mean pixel value for each slice could be obtained through adequate subtraction of the background level. The background is not flat for X-ray CCDs due to thermal charge accumulation as the image is read out. Assuming a constant readout rate, this results in a relatively linear gradient across the image. Additionally, it was expected that secondary radiation, generated in various parts of the chamber, would be incident on the camera. For instance, the use of a capillary can result in bremsstrahlung production due to interaction of electrons with the sides of the capillary walls [40]. Gamma radiation would also be produced when the electron bunch is steered into the chamber walls by the magnets. The effect of this on the measured CCD measurement would be to increase the overall background level. These combined effects can be (at least partially) removed from the image by estimating the linear gradient in a portion of the image which is blocked from betatron radiation (but may be transparent to gamma radiation) and subtracting this from the whole image. Figure 4.16 shows an example of an image after background removal with the filter slices outlined in blue. The dark area on the right hand side was used in this instance for the background subtraction. It should be noted that normally, it should be sufficient to simply subtract a dark frame (which may be composed of multiple images), in order to account for the linear gradient. In this case, the poor level of temperature stabilisation in the CCD, meant that the dark current changed from shot and so the linear gradient was estimated on a per shot basis. It was found that the region on the right of the image was not completely void of lower energy radiation, resulting in the background level subtracted from the rest of the image being too high, which in turn caused the mean pixel value in optically thick slices of the filter to become negative, in some cases. Although not ideal, the filter means were corrected

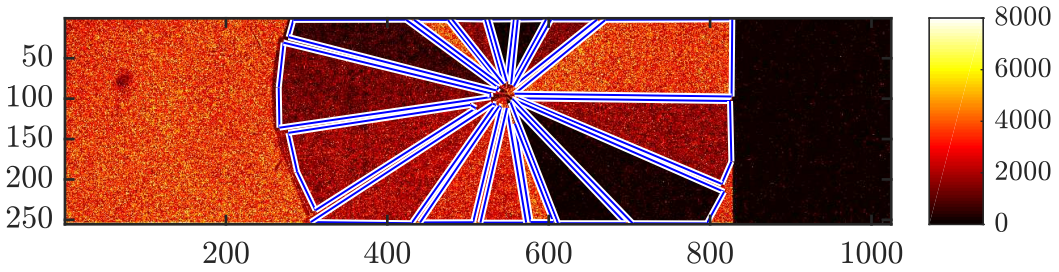


Figure 4.16: Image of filter wheel illuminated by betatron radiation. Areas outlined by blue correspond to different slices in the filter wheel.

by subtracting the minimum filter mean value when any slice was less than zero.

The variation in the number of counts in each pixel (a.k.a. the pixel value) associated with a given slice (on the order of 1000s of counts) far outweighs the measurement error due to other sources of noise such as readout noise (1.8 counts as stated by the camera specifications). Hence, the uncertainty in the mean pixel value was simply taken as the standard deviation of the mean σ of the relevant set of pixels. The energy deposited *per pixel* E through the material is then calculated from the mean number of counts $\mathcal{C}$, using the camera sensitivity $\mathcal{S}$ of 10 electrons/count (for a 1 MHz readout speed). The energy required to create an electron-hole pair in silicon $E_{\text{eh}} = 3.65\,\text{eV}$.

$$E = \mathcal{C}\mathcal{S}E_{\text{eh}}. \tag{4.15}$$

Therefore, $\delta\Delta E$ was calculated as $\delta\Delta E_{12} = \Delta E_{12}\sqrt{(\sigma_1/\mathcal{C}_1)^2 + (\sigma_2/\mathcal{C}_2)^2}$.

The error associated with the integral f from (4.13) primarily stems from uncertainties in the calculated transmittances of the filters which are dependent on the accuracy of the requested thickness of the materials. The stated tolerances for the filters varied from material to material, with a $\pm 25\,\%$ tolerance for thicknesses below 10 µm, $\pm 15\,\%$ tolerance for thicknesses between 10 µm and 50 µm, and $\pm 10\,\%$ tolerance for thicknesses above 50 µm.

Figure 4.17 displays the plot of $\mathcal{Q}\,T_0\,(T_{\text{Cr}} - T_{\text{Ti}})$ for 5 different thickness combinations:

- Dark blue represents the desired thicknesses of 3 µm chromium (Cr) and 6 µm

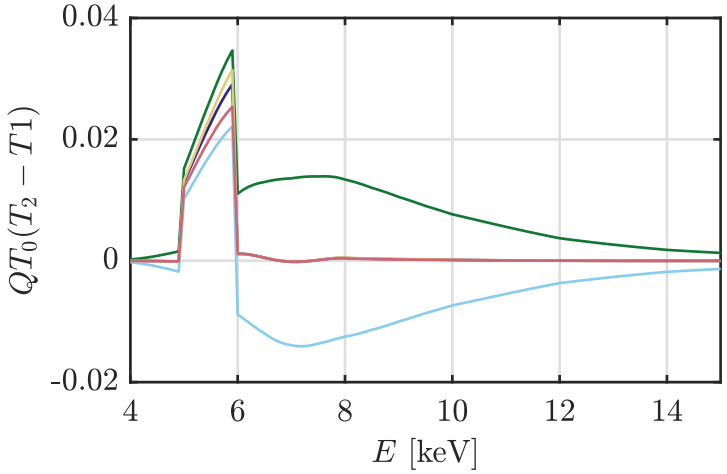


Figure 4.17: Comparison of the effective transmittance difference of chromium and titanium for various thicknesses, centred on the nominal balanced thicknesses of 3 um and 4.5 µm, respectively.

titanium (Ti);

- Light blue represents thicker Cr (3.75 µm) with thinner Ti (4.5 µm);
- Red represents thinner Cr (2.25 µm) with thinner Ti (4.5 µm);
- Yellow represents thicker Cr (3.75 µm) with thicker Ti (7.5 µm);
- Green represents thinner Cr (2.25 µm) with thicker Ti (7.5 µm).

The yellow, dark blue and red lines mostly overlap over the majority of the energy scale. In contrast, the worst case scenario is when the material pair have thicknesses differing from their desired values in opposing directions (green and light blue), the result of which is to cause large deviations in the transmittance difference in regions outside the K-band, meaning the materials are no longer matched.

An estimate of the relative error in the integral $\delta f/f$ was found by evaluating the integral *over all energies* in the worst case scenario of each pair differing in thickness from their desired values in opposite directions, and comparing to the integral using the

nominal thickness.

$$\frac{\delta f}{f} \approx \frac{\int_{-\infty}^{\infty} \mathcal{Q}\, T_0\, (T_2' - T_1')\, \mathrm{d}\omega - \int_{-\infty}^{\infty} \mathcal{Q}\, T_0\, (T_2 - T_1)\, \mathrm{d}\omega}{\int_{-\infty}^{\infty} \mathcal{Q}\, T_0\, (T_2 - T_1)\, \mathrm{d}\omega}, \tag{4.16}$$

This approach likely overestimated the calculated uncertainty, but accurate measurements of the materials were not available at the time of writing.

Due to the limited availability of material thicknesses, an alternate approach to retrieving the spectrum was pursued by calculating the expected average number of counts associated with each filter slice, *assuming* a betatron spectrum. The number of counts $\mathcal{C}$ expected can be calculated by combining (4.11) and (4.15) such that

$$\mathcal{C} = \frac{1}{\mathcal{S} E_{\mathrm{eh}}} \int \frac{\mathrm{d}E}{\mathrm{d}\omega} \mathcal{Q}\, T_0\, T\, \mathrm{d}\omega. \tag{4.17}$$

Assuming $\mathrm{d}E/\,\mathrm{d}\omega$ is of the form given by (3.6), a numerically calculated number of counts $\mathcal{C}_{\mathrm{cal}}$ was obtained for each filter and compared to the experimentally measured number of counts $\mathcal{C}_{\mathrm{exp}}$. The parameters C_E (scaling factor) and E_{c} (critical energy) (c.f. (3.6)) were varied to give the best match between $\mathcal{C}_{\mathrm{cal}}$ and $\mathcal{C}_{\mathrm{exp}}$. It is worth noting that the equation given in (3.6) represents a spectral number density, and so was multiplied by the photon energy E to convert to a spectral energy density. A weighting factor W was initially placed on each filter which was based on the sensitivity of the term $\mathcal{Q}\, T_0\, T$ to a variation in thickness. The factor was calculated such that a weight of $W \approx 1$ was obtained when a change in the material thickness made little difference to the integral of $\mathcal{Q}\, T_0\, T$. The smallest weight of $W = 0.5$ was placed on the material which was most sensitive to changes in thickness. The expected number of counts was recalculated using equal weights and it was found that the best fit parameters did not change significantly and so, the fit using equal weights was adopted for simplicity.

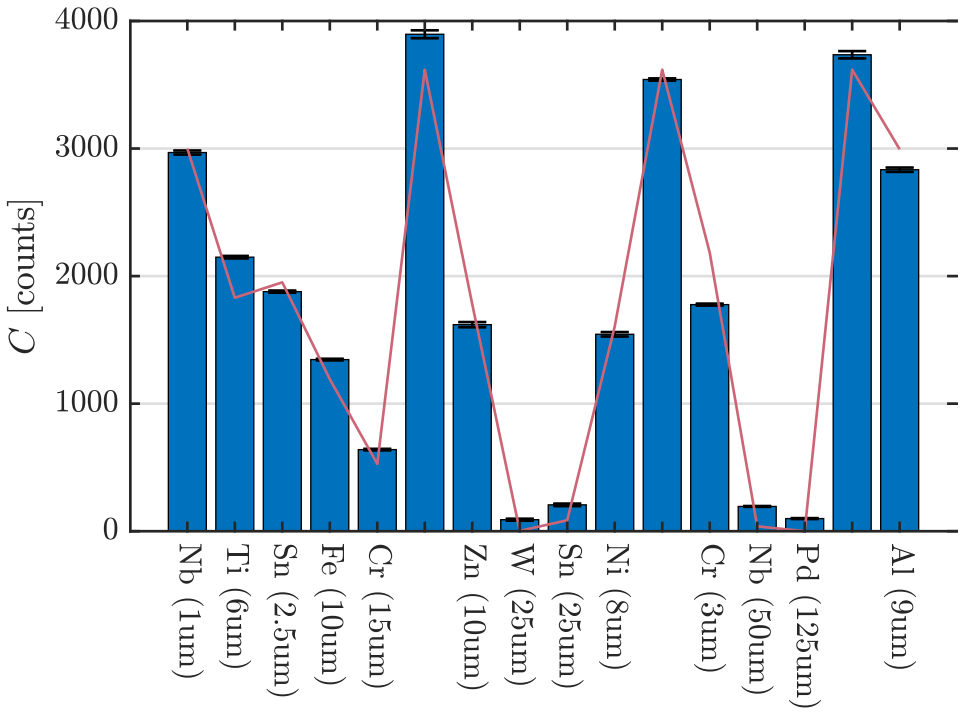


Figure 4.18: Comparison of experimentally measured CCD counts (blue histogram) through various filters with a modelled number of CCD counts (red line) fit to the experimental data assuming a betatron spectrum. Purple error bars indicate the standard error of the mean in a given filter slice.

4.4.4 Example betatron spectrum retrieval

Figure 4.18 provides an example of $\mathcal{C}_{\text{exp}}$, shown as blue bars with the standard error of the pixels associated in purple. The best fit number of counts is represented as a red line and corresponds to a critical energy of $(5.8 \pm 1.6)\,\text{keV}$.

A comparison of the energy spectral density retrieved via the two analyses above can be found in Figure 4.19. The betatron spectrum based on the best fit critical energy of $E_{\text{c}} = 5.8\,\text{keV}$ is shown in red. The energy spectral density as calculated from the Ross filter pairs is shown in blue along with the approximate uncertainties as determined by (4.14). The size of the marker for each point has been scaled in proportion to the K-band ratio mentioned previously, meaning that points with a large marker is likely to be more accurate than those with small markers.

Figure 4.19 shows that there is a reasonable level of agreement between the two methods in the range of 6 keV to 15 keV, which is where the K-band ratio is seen to be

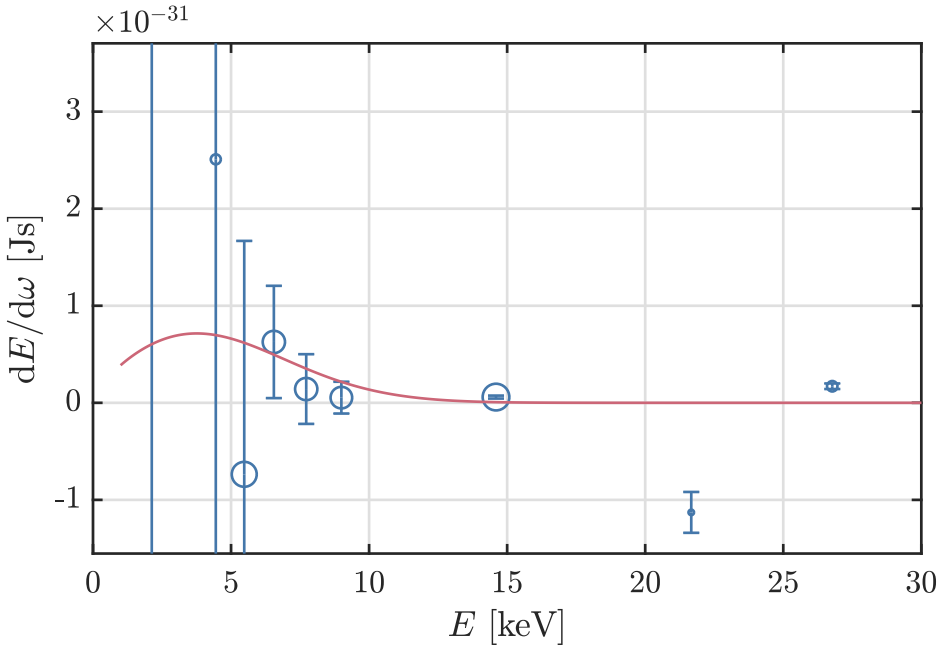


Figure 4.19: Energy spectral density for betatron radiation as estimated using Ross filter pairs (blue). Assuming an on-axis betatron spectrum, the best fit spectrum of 5.8 keV was calculated and plotted (red).

largest. However, the point slightly above 5 keV deviates significantly from the expected energy spectral density and should clearly not be negative. Combined with the fact that there is a complimentary large overestimation in the preceding data point, this suggests that the thickness of the common material, i.e. titanium, could be significantly different from the desired thickness of 6 µm.

The first data point lies multiple orders of magnitude above all others, with even larger error bars, but it also has the smallest K-band ratio by a large margin. The reason for this is that the T_0 term in (4.11) is very small in this K-band energy range. Equivalently, at higher energies, the K-band ratio increases and then decreases significantly above 20 keV where the quantum efficiency term drops substantially. To remedy both of these effects, prior knowledge of $\mathcal{Q}\,T_0$ is essential during the initial design of the filter wheel, allowing the minimisation process described in Section 4.4.2 to account for the weighting effect of the quantum efficiency and the transmittance of light shielding at different energies.

The latter method of fitting to a betatron spectrum shows decent agreement between the computed mean counts through each filter to the experimentally measured mean counts. Additionally, it is more robust since it does not rely on the materials being matched to each other in thickness. However, the choice of the spectrum to fit to can be subject question. If the X-ray beam could be fully captured on the CCD, the angularly-integrated form of the betatron spectrum (recall (1.9)) may be a better choice. In this case, only a portion of the X-ray beam fit on the CCD meaning that the on-axis form of the spectrum was likely an acceptable choice. However, it was found that there was some spatial variation in the intensity of radiation, even within the same filter slice. This can also be seen in Figure 4.18 when comparing the count level for the 3 blank entries which correspond to the 3 empty slices in the filter wheel containing no filter. In the ideal scenario, they should have the same mean value. If the beam were cylindrically symmetrical, one could imagine using this to obtain an angularly-dependent spectrum, given a suitable assumption for the spectral form and creating a new fit at different radii.

4.5 Experimental Results

There were a small number of runs which yielded excellent electron beams and betatron radiation. Run 69, shown in Figure 4.20 is an example. In this run, a 33 mm long discharge capillary was filled with 130 mbar of hydrogen (and 5% nitrogen mix) and shot with approximately 5 J on target. It can be seen that although many beams were created during the run, the generation was inconsistent and there were significant variations in the beam charge. For following figures, shots which produced no charge, negligible betatron radiation or were poorly fit during the analysis have been removed from the data set to improve clarity.

Figure 4.21 shows the 25%, 50% and 75% cut-off energies, as defined in Section 4.3.4, for this run. The position of the 50% cut-off gives an indication of the degree to which

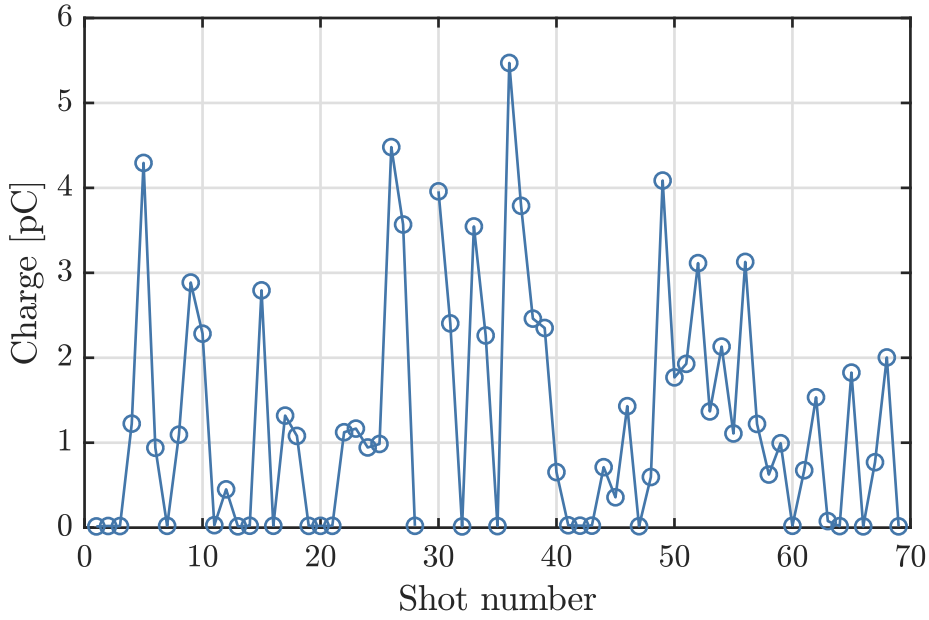


Figure 4.20: Charge measurement on the low energy Lanex screen after processing for Run 69.

the spectrum was asymmetric, meaning that if it is, say, near the upper limit, then the beam was comprised of a high energy bunch with a long low energy tail. For the most part, the electron energy spectra spanned between 200 MeV and 500 MeV, meaning few to no electrons reached the high energy screens.

Using the method described previously, Figure 4.22 shows the weighted electron beam divergence as a function of shot number. For reference, the Gaussian fits were performed using a polynomial fit to the logarithm of the section lineouts (see [105, 106]). Most shots had a divergence close to 1.2 mm, or 1.03 mrad (conversion to angle can be made using distance from Lanex to IP). In general, large error bars stemmed from low charge shots which resulted in unreliable fits after processing the image to remove bremsstrahlung radiation. In other cases, the beam profile was highly non-Gaussian, leading to a poor fit.

It was found that for many shots the signal recorded on the lanex screen of the electron spectrometer was not distributed symmetrically about a single line normal to the B-field, but instead exhibited curves or 'wiggles'. An example is shown in Figure 4.23 (shot 8 and also Figure 4.9 taken from a different run). Using the Gaussian centre from

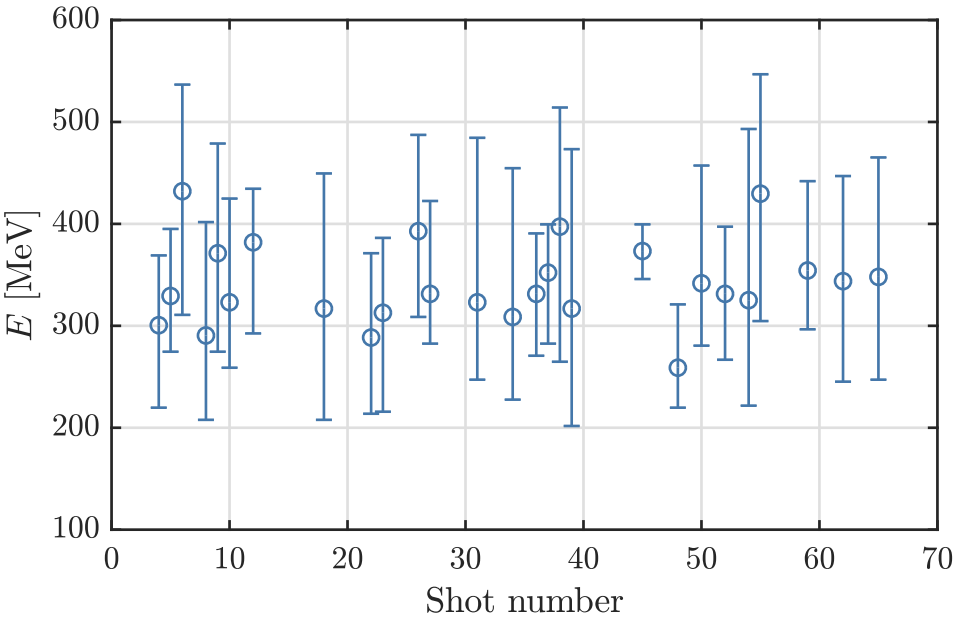


Figure 4.21: Plot of the 25%, 50% and 75% cut-off energy on the low energy Lanex screen for Run 69. The central point (circle) indicates the energy below which 50% of the charge was contained, whereas the upper and lower limits indicate the energies below which 25% and 75% of the charge was contained, respectively. Therefore, half of the total charge was contained between the limits and provide a reasonable measure of the energy spread.

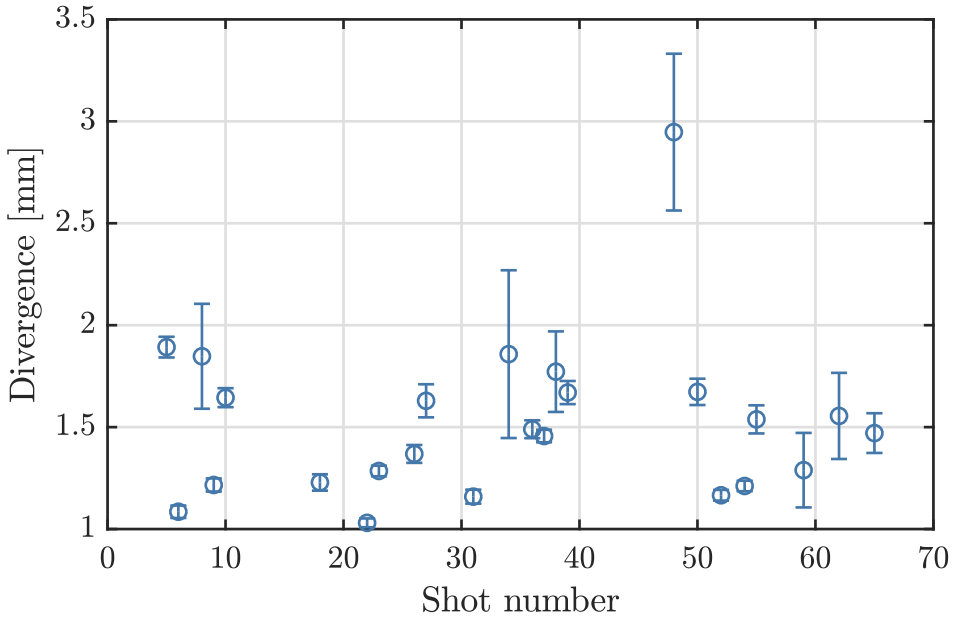


Figure 4.22: Electron divergence measurement on the low energy Lanex screen for run 69.

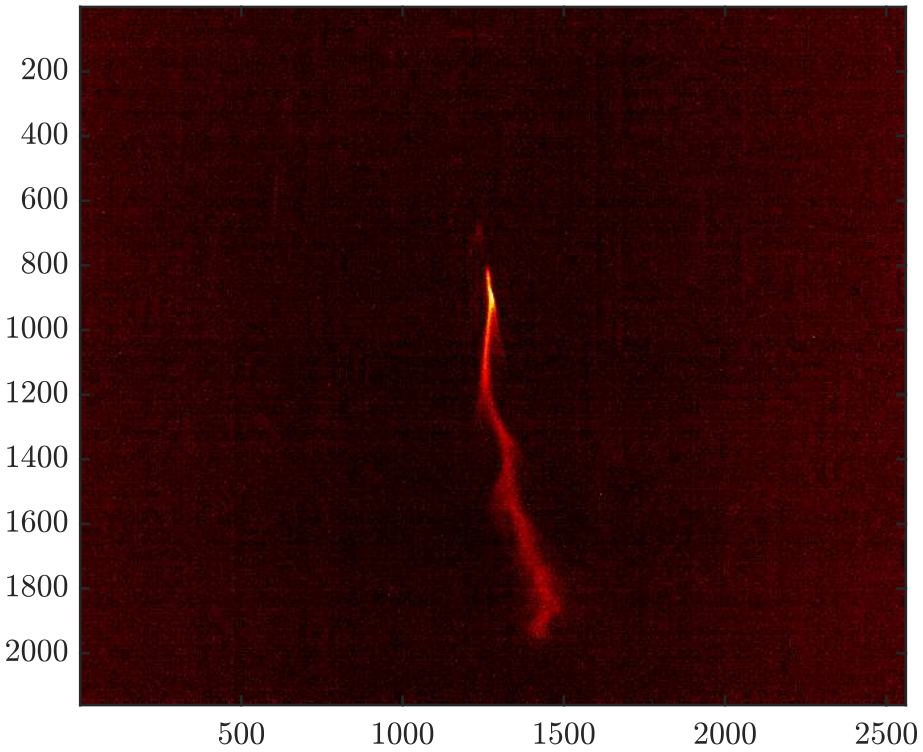


Figure 4.23: Example of beam whose transverse position varies with energy.

the Gaussian fit of energy slices (used for calculating a weighted beam divergence), a measure of the spread of centre values was made by calculating the standard deviation of the centre differences. The difference between consecutive slices was used to ensure that a straight, but tilted spectrum would not yield a large standard deviation. The results of this analysis for Run 69 are shown in Figure 4.24. It can be seen that a large portion of shots had a standard deviation of centres close to 0.5 mm, corresponding to line-like streaks as is usually seen in electron spectrometer measurements, like in Figure 4.25 (shot 26).

To compare with the measurements for the electron spectra are the fit parameters obtained from the betatron radiation measurement, namely the critical energy E_c and the scaling factor for the on-axis betatron spectrum C_E. These are shown in Figure 4.26 and Figure 4.27. The error bars shown for E_c and C_E were the 95% confidence intervals obtained directly from MATLAB's fitting routine.

For the majority of shots, the critical energy was found to be approximately 8 keV.

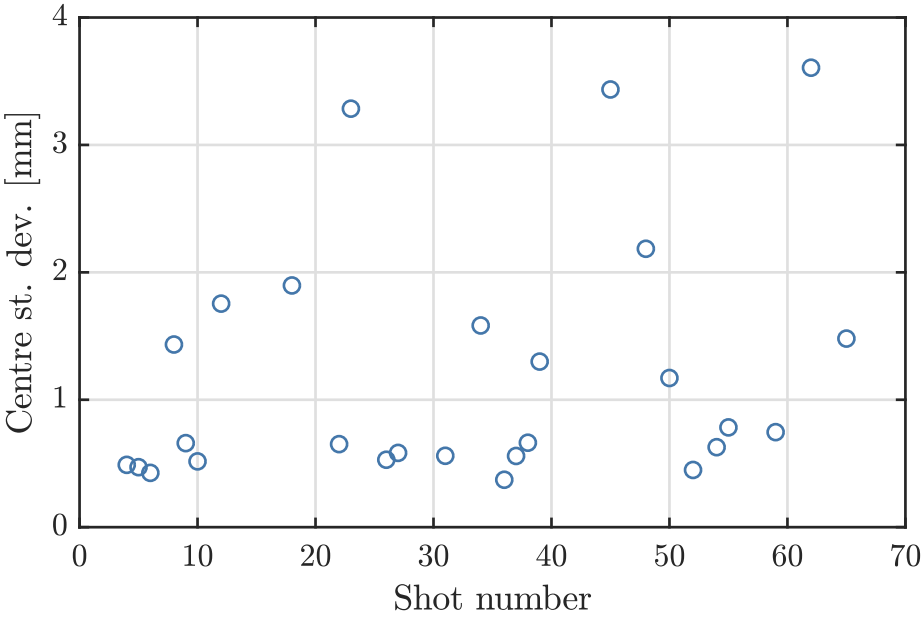


Figure 4.24: Standard deviation of the centres of a Gaussian fit to energy cross sections of the electron spectrum on the low energy Lanex screen for run 69.

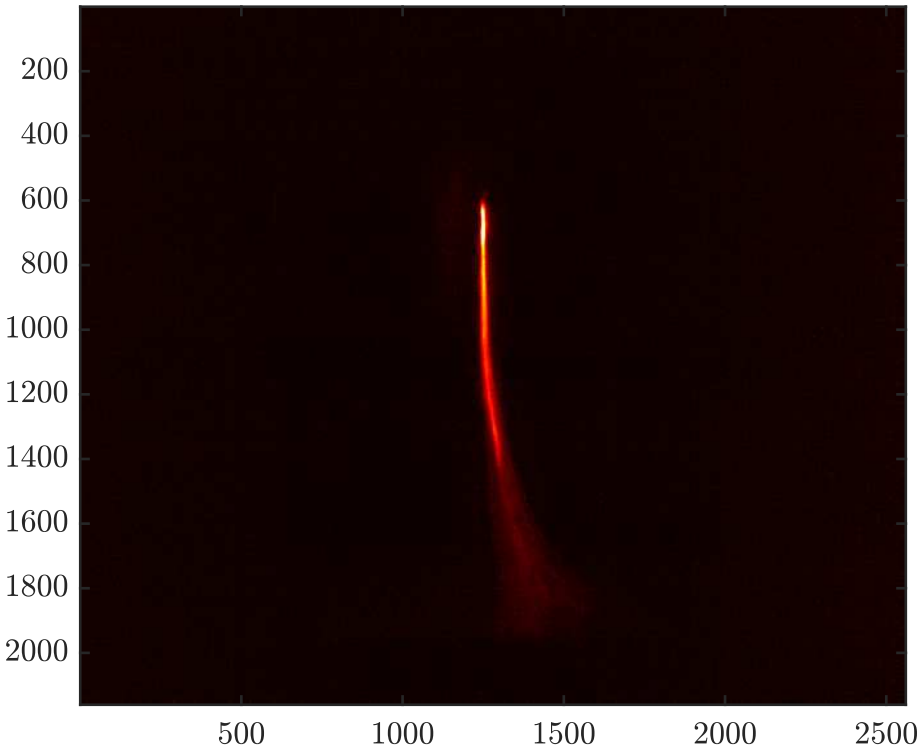


Figure 4.25: Example of streak-like electron beam.

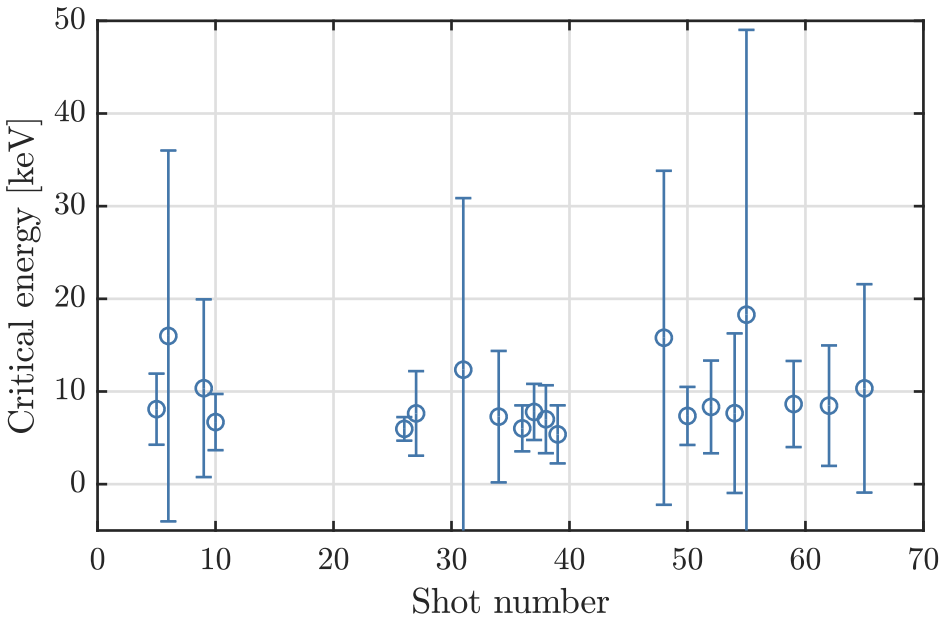


Figure 4.26: Best fit betatron radiation critical energy for run 69.

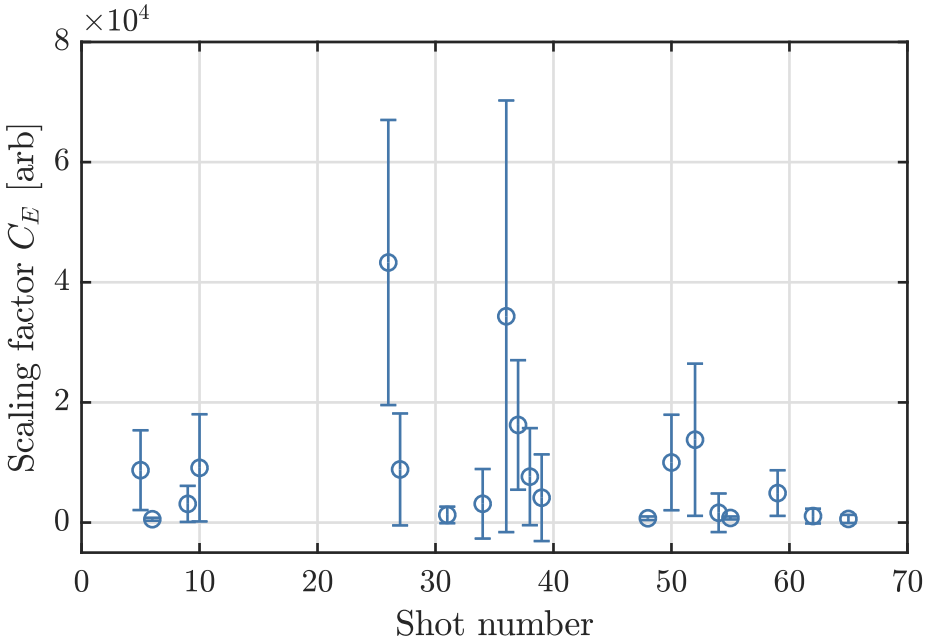


Figure 4.27: Best fit betatron radiation scaling factor for run 69.

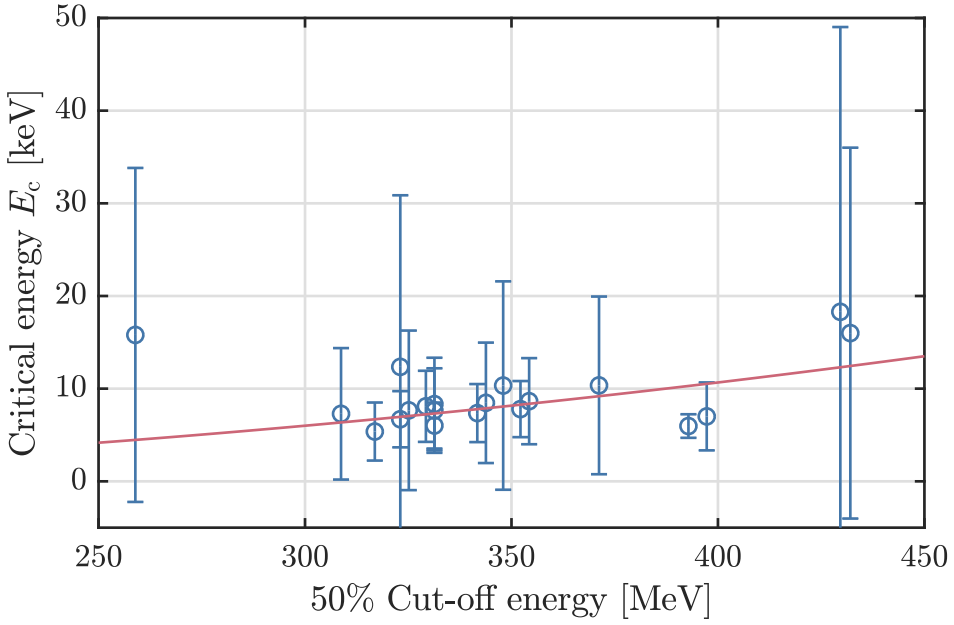


Figure 4.28: Plot of best fit betatron radiation critical energy as a function of the 50% cut-off electron energy. The red line indicates a square dependence fit by hand to the data set.

There were a number of shots with failed fits, with the fit returning 50 keV, which is the upper constraint for the critical energy. These points always correspond to images with very low signal-to-noise ratios.

4.6 Discussion

From theory, the critical energy for betatron radiation, varies with electron energy and the betatron strength parameter (1.8). The plot of the 50% cut-off against critical energy is shown in Figure 4.28. A general trend of increasing critical energy with cut-off energy is visible between 250 MeV and 370 MeV, but caution is placed in this assertion due to size of the confidence intervals. A curve of the square of the energy was added in red (scaled by eye) as a preliminary check.

It may be expected that the radiation properties should be determined by the highest energy electrons as the total energy radiated is a strong function of the electron energy (1.5). However, the trend could is not as convincing when using the 90% cut-off energy

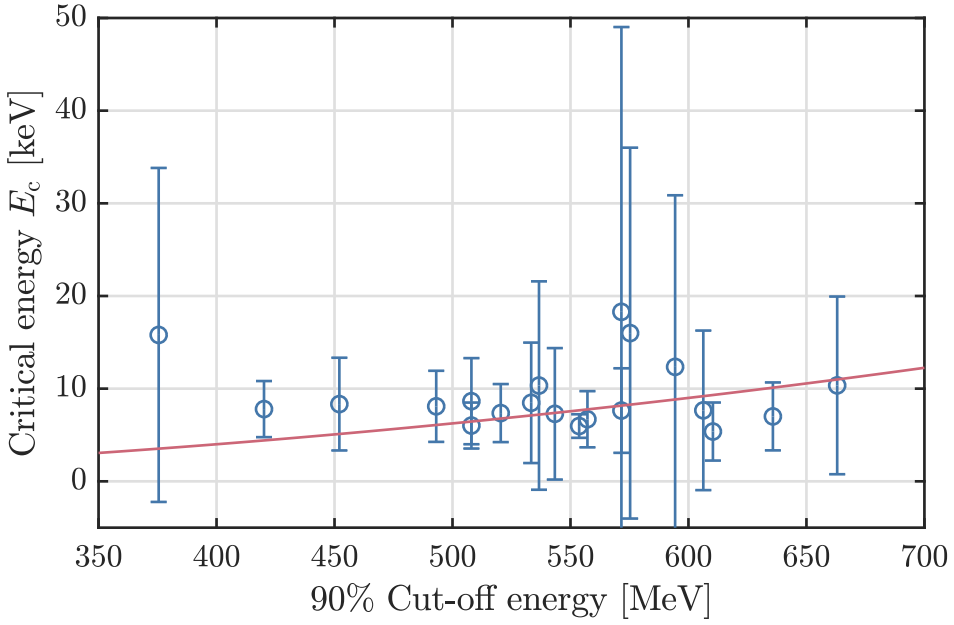


Figure 4.29: Plot of best fit betatron radiation critical energy as a function of the 90% cut-off electron energy.

Figure 4.29.

Since betatron radiation is emitted into a cone whose opening angle scales with the oscillation amplitude [107], it is expected that there should be positive correlation between the electron beam divergence and the critical energy. This plot is shown in Figure 4.30. Unfortunately, this trend was not present and there even seems to be an opposite trend, with the critical energy decreasing as the divergence increases from 1 mm to 1.5 mm (albeit with large confidence intervals).

The scaling factor C_E used in the betatron spectrum fit encapsulates a γ^2 term (3.4), so the 50% cut-off energy is plotted against the scaling factor in Figure 4.31. It is not convincing that such a squared dependence applies to the majority of data points. The two quadratic curves show that although there does appear to be a correlation of increasing C_E with cut-off energy, the relationship is not a square dependency. Again, the 90% cut-off energy is plotted and no square dependence could be found Figure 4.32.

Additionally, the electron beam charge is plotted against the scaling factor as this should be linear if the electrons radiate independently. It can be seen in Figure 4.33

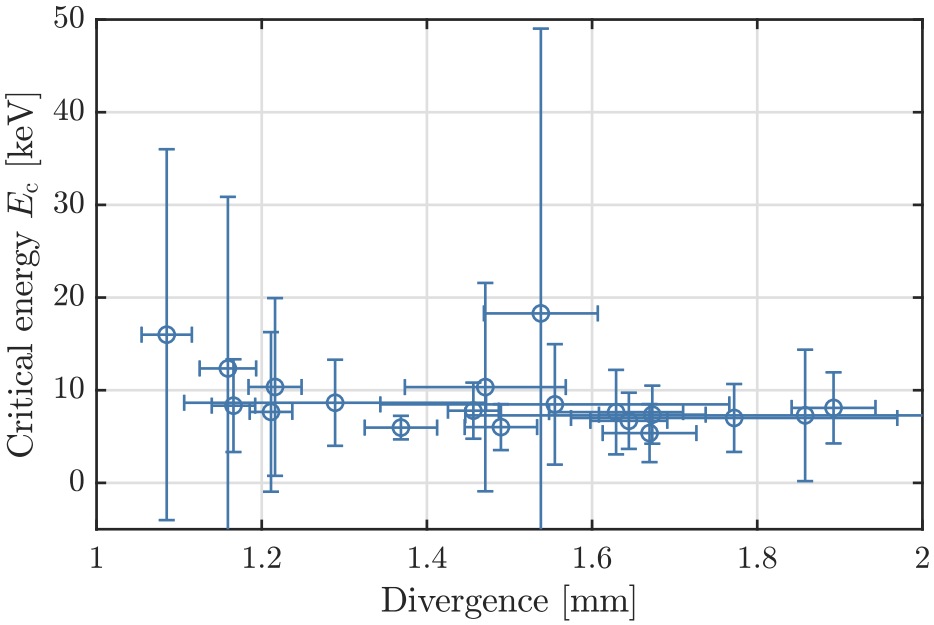


Figure 4.30: Plot of best fit betatron radiation critical energy as a function of electron beam divergence.

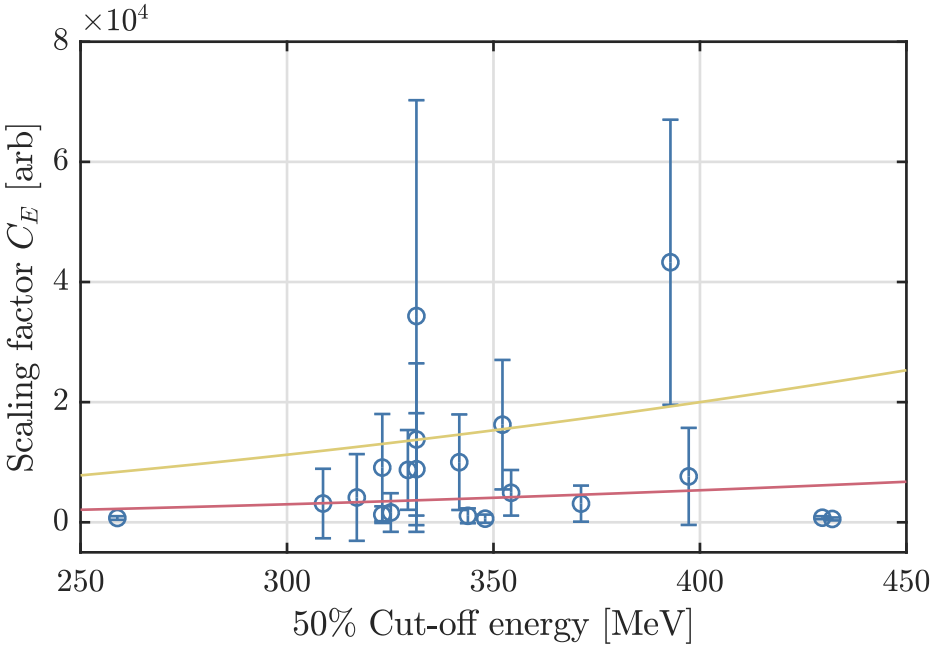


Figure 4.31: Plot of best fit betatron radiation scaling factor as a function of the 50% cut-off electron energy.

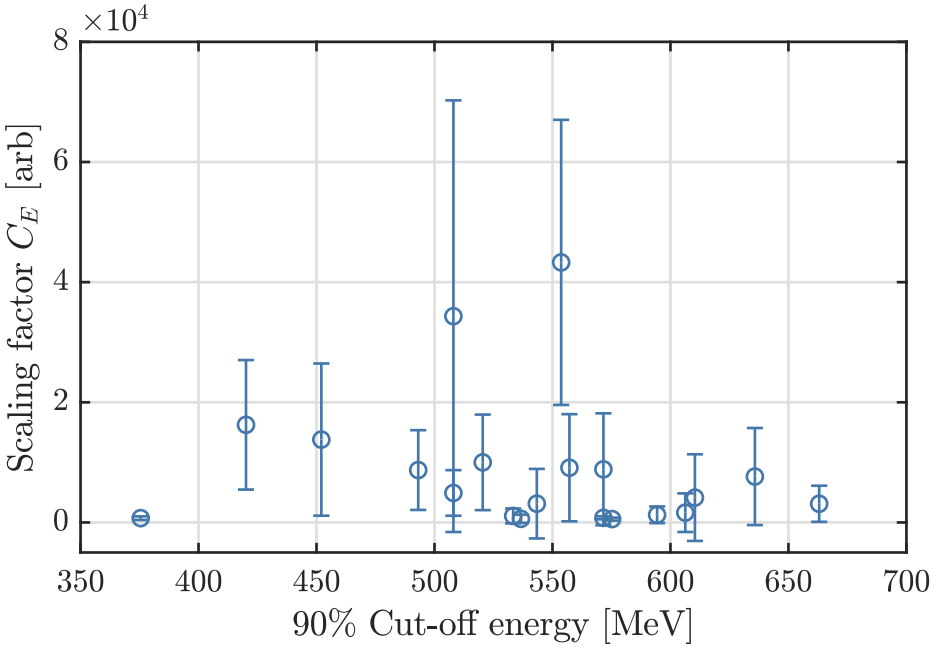


Figure 4.32: Plot of best fit betatron radiation scaling factor as a function of the 90% cut-off electron energy.

that the scaling factor C_E does increase approximately linearly for bunch charges above 2 pC. The apparent threshold in the charge likely arises from the poor signal-to-noise ratio for weak betatron signals and possibly incorrect background subtraction.

For several graphs above, the expected relationships were not easily identifiable. There are a number of potential reasons for this. The most obvious is the plots are collated from shots with a wide range of different energy spectra, such as differently skewed tails and likely different capillary alignments over the course of the run due to a drift in pointing. Hence, it is difficult to observe the ideal trends without maintaining almost identical experimental conditions from shot to shot, such that stable and reproducible electron beams with narrow energy spread can be generated.

It is also important to recall that the electron spectrum was cut off at low energies (as it was outside the spectrometer range), hence the charge and cut-off energies would be inaccurate when the electron beam tail extends off-screen. Furthermore, it was found that a number of shots contained a weak pedestal of low energy electrons which was much more divergent than the higher energy beam. This pedestal was usually

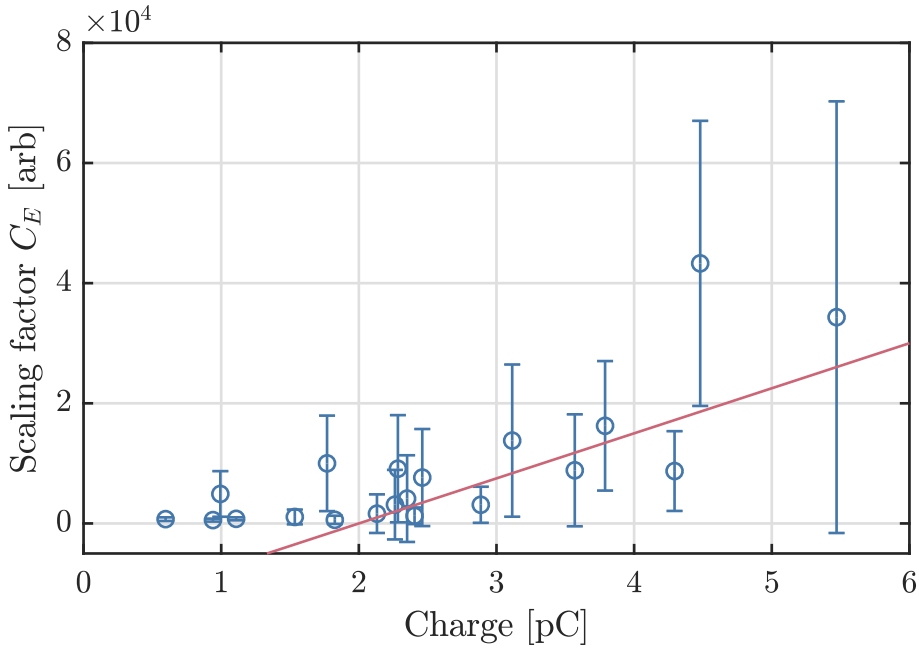


Figure 4.33: Plot of best fit betatron radiation scaling factor as a function of the electron beam charge.

filtered out during the bremsstrahlung filtering step, but most likely contained charge comparable to that measured in the thin streak. However, it could be argued that the highest energy electrons dominate the betatron emission as the power radiated by an accelerated electron strongly scales with its energy.

There were a number of other quantities which are of interest, including the betatron beam divergence. However, this could not be measured as the beam was larger than the area of the CCD chip; all that can be said is that the betatron divergence was at least 10 mrad (calculated from the chip size and distance to the interaction point).

Although a single run has been presented here, there were a number of other runs which have not yet been analysed, including runs which vary laser energy and gas pressure (albeit with fewer shots at a given configuration). This could be included in future work to potentially provide interesting insights on the X-ray generation from laser-plasma acceleration.

In this run, the medium and high energy Lanex screens were not in operation. There were seldom shots which were visible on the medium Lanex screen amongst all runs,

but a preliminary analysis found that the spectrum obtained from the medium energy Lanex screen matched well with the overlapping portion of the low energy Lanex screen.

The method employed here to determine the betatron spectrum, i.e. calculating the expected number of counts in each filter bin, could also be improved as this method assumes perfect knowledge of the filter transmissions, which are dependent on the precise thicknesses. If possible, accurate measurements of the filter thicknesses should be made and then incorporated into the analyses, although there may be scope to deduce this (or at least improve the assumed thicknesses) by looking at systematic mismatches between the calculated counts and measured counts.

The Ross filter method may be improved too through an iterative process of calculating the energy spectral density for one energy range and using this knowledge to improve estimates of the other densities.

4.7 Summary

In this chapter, two important pieces of diagnostic equipment used during the Astra Gemini experiment have been presented. The first of these is the electron spectrometer, which has been shown to successfully retrieve details of the electron beam such as the beam charge, transverse divergence and energy spread. Details of the methods to retrieve these have been shown. The energy calibration is based on a particle tracking code written by the author. The spectrum retrieval method uses knowledge of the Lanex dimensions to produce a map between pixel coordinate and electron energy. This has an advantage over typical electron spectrum measurements which use simple row/column lineouts in that the screen can be viewed at oblique angles.

The other measurement pertains to the betatron radiation produced during the laser-plasma interaction. Through the use of multiple elemental filters, the method of retrieving the spectrum has been outlined alongside the relevant theory. The analyses were performed on a single run taken during the experiment and the results discussed.

Chapter 5

CALA Experiment

5.1 Introduction

A short experimental campaign was performed at the Centre for Advanced Laser Applications (CALA) in Munich as a first dedicated attempt of the XCERP diffraction technique to characterise radiation produced by a laser wakefield accelerator. The experiment was carried out with the help of Prof. Dr. Stefan Karsch of Ludwig-Maximilians-Universität (LMU) and his group, who prepared the laser each day and assisted in the running of the XCERP diffraction experiment.

This chapter presents the methods used to analyse the data taken during the campaign, including the bespoke background removal procedure and an algorithm, also written by the author, to identify X-ray events on a CCD. The experimental outcomes for a set of runs is then provided.

5.2 Experimental Setup

A Ti:sapphire laser system was used to produce short laser pulses which were then stretched, amplified and recompressed using the common chirped pulse amplification (CPA) technique [18]. The output pulses were of approximately 30 fs duration and had

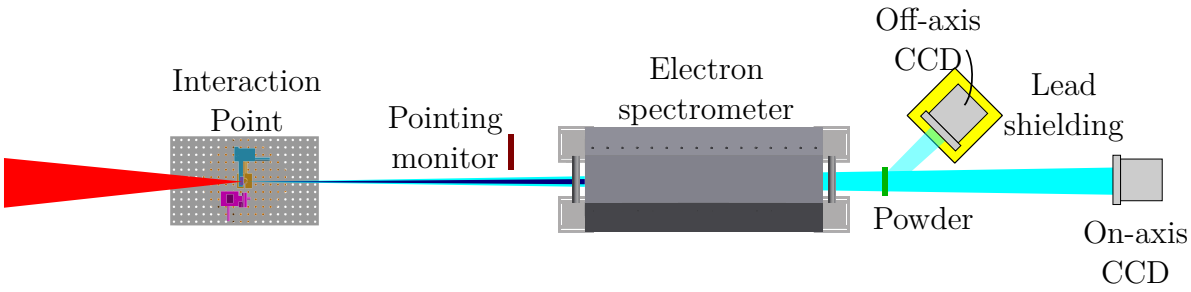


Figure 5.1: Schematic of XCERP diffraction setup at the Centre for Advanced Laser Applications. The tightly focused laser is represented by red, while the betatron radiation is represented by cyan. The electron beam is shown by dark blue and is steered into the the plane of the paper by the electron spectrometer where it is imaged.

an on-target energy of about 2 J. The 100 mm diameter output beam of the laser was focused by a $f = 2.5$ m off-axis paraboloid (F/25) to yield a focus with a spot size of 25 µm near the exit of a supersonic gas jet.

By partially obstructing the nozzle of the jet with a knife edge, a shock front was produced with a sharp downwards ramp in density in order to provide controlled electron injection [108, 109]. The effect of this density downramp was to increase the plasma wavelength and reduce the plasma phase velocity such that the plasma electrons outran the plasma wave, i.e., wave breaking [110, 111], leading to localised injection of electrons into the wakefield. This allowed fine control of the injection process since the positions of the edge, nozzle and laser focus were all adjustable through use of a 6-axis hexapod and multiple linear stages. By controlling the relative positions of these components, it was possible to create relatively stable and reproducible electron beams.

A scintillating screen was mounted on a flip mount after the interaction point to monitor the electron beam shape and divergence. Beyond this was an electron spectrometer, consisting of an array of permanent magnets which steered the wakefield-generated electron beams toward a long strip of scintillating material near the floor of the chamber. The details of operation for the electron spectrometer are similar to that used in Chapter 4. Using a camera to image the strip allowed the measurement of the electron energy spectrum in the range of energies between 30 MeV to 600 MeV.

Two silicon chip X-ray CCD detectors were used during the experiment: one was

placed on-axis at the end of the vacuum chamber to measure the betatron signal, while the other was used to detect X-ray diffraction scattered off-axis from a powder target. The on-axis camera (Princeton Instruments PIXIS-XO: 2048B) was a back-illuminated, deep-depletion CCD with 2048×2048 pixels and a pixel separation, or pitch, of 13.5 µm in each direction. It was attached via a flange directly to the chamber wall. The off-axis camera (Andor DO432-BN-DD) was also back-illuminated and used deep-depletion, but had a lower resolution, with 1252×1152 pixels and a pitch of 22.5 µm. This was placed in an aluminium cube inside the chamber. Air was circulated inside the cube using a flexible aluminium hose and gas pump. The silicon chip was exposed to the chamber vacuum via a bespoke flange on one side of the cube.

Both cameras were thermoelectrically cooled via the Peltier effect, which can produce temperature differences of approximately 80 °C. The cameras were typically cooled to a temperature around −40 °C. Lower temperatures could have been reached using a liquid heat sink as opposed to the ambient air, but this was not available at the time.

5.3 CCD Operation

Unlike the experiment described in previous chapters, the usage of charge-coupled devices (CCDs) in this experiment differs in that single photon detection is considered, for the purposes of detecting XCERP diffraction. In measuring radiation at very low flux levels and using a CCD for direct spectral measurements, it is useful to develop a deeper understanding of CCD operation, hence a brief description is presented here.

5.3.1 Basic overview

CCDs are commonly used detectors of electromagnetic radiation for a large portion of the electromagnetic spectrum. At low energies, such as in the visible regime, a single electron is photoionised; in contrast, at high photon energies many photoelectrons can

be generated by a single X-ray in proportion to the energy of the photon.

The CCD is comprised of an array of many elements—or pixels—which can either be arranged in a single line or a 2D grid. Detection in a pixel occurs when electrons are created in the silicon chip. For *front-illuminated* devices, the electrode structure, which the photoelectrons drift toward, is at the surface of the chip and can result in strong attenuation of photons. *Back-illuminated* devices circumvent this by having the electrode structure on the rear surface. In this scenario, particles would need to traverse the bulk silicon layer, i.e. a field-free region, before reaching the depletion region, resulting in loss of resolution. This is prevented by removing, or thinning, the bulk material. These types of CCDs are often referred to as being *back-thinned*. In order to increase detection to higher energies, the depletion layer can be made thicker, allowing photoelectrons created by more penetrating particles to be captured.

In order to read out photoelectrons, an electric field is applied to electrodes on the chip, creating potential wells which can be varied in such a way to sweep trapped electrons towards the readout register where they are converted to a voltage (on the order of a few µeV) and amplified.

Thus, it is imperative that the transfer of photoelectrons between lines of pixels is as efficient as possible. Major efforts are undertaken to improve this so called charge transfer efficiency (CTE) with progress now reaching the point such that losses are less than one part in a million [112].

5.3.2 Sources of noise

The image created at the end of the process described above is subject to various sources of noise: *Readout noise* arises during the process of converting charge to *analogue-to-digital units* (ADUs), which have previously been referred to as *counts*. This type of noise is due to the amplifiers and other electronics on the chip and can vary with camera setting. For the Andor DO432-BN-DD, there were 4 possible settings of the readout

speed: 1 µs/pixel, 2 µs/pixel, 16 µs/pixel and 32 µs/pixel. These correspond to a readout rate of 1 MHz, 500 kHz, 62 kHz and 31 kHz, respectively. For each speed setting, the stated read noise in units of electrons is 14.4, 15.2, 4.2 and 4.3 when the chip is cooled to −64 °C. The readout noise level is independent of the exposure time, meaning that if the readout process is the dominant source of noise, then a slower readout speed should be adopted.

Dark current refers to the build-up of electrons in the CCD that is not due to incident radiation. Typically, this is due to thermally generated electrons and can be vastly reduced exponentially by cooling the chip. At approximately −65 °C, the dark current is 3 electrons/s/pixel, rising to 30 electrons/s/pixel at −40 °C and 300 electrons/s/pixel at −25 °C. Since the dark current is time-dependent, it will depend on both the exposure time and readout rate, and leads to images in which the background increases along the direction of charge transfer.

The readout noise and dark current comprise the majority of noise in the detection system. A lesser source of noise arises from variations in the manufacture of individual pixels which can affect their sensitivity to radiation. According to the specification sheet of the camera used, the response uniformity is less than 1% when cooled to −64 °C. This value is the root-mean-square (RMS) deviation of the pixels from the average response under uniform illumination. Blemishes at specific positions of the CCD image, such as hot spots, can also be found, but these were excluded from the data set during analysis.

5.3.3 Energy conversion

An electron-hole pair is created in silicon for every 3.65 eV of energy in the X-ray [112, 113]. The number of counts recorded scales linearly with the number of photoelectrons created. The relationship between the two is given by the *sensitivity* and has units of electrons/count. For the Andor camera, the sensitivity was 7 electrons/count, 7 electrons/count, 5 electrons/count and 2.5 electrons/count for a readout rate of 1 MHz,

500 kHz, 62 kHz and 31 kHz, respectively.

If the CCD is operated such that each pixel is irradiated, at most, by a single X-ray, then each pixel will provide a spectral measurement for the incident X-rays . As an example, detection of a 10 keV X-ray would result in 391 counts when using a 1 MHz readout rate. This corresponds to a conversion of 25.55 eV/count.

5.4 Noise Analysis Methods

As mentioned above, there are a number of sources of noise present in a given image acquisition and their contributions can be dependent on the camera settings. Here, the effects of varying a few of the key Andor X-ray CCD settings are presented.

A typical dark frame, taken from a collection of 100 dark frames captured at a single temperature (−30 °C), readout speed (1 µs/pixel) and exposure time (100 ms), is shown in Figure 5.2 and has been scaled to show the variation counts across the full image. Here, the term *dark frame* is used to refer to an image which was taken with the same camera settings used for actual data acquisition, but without any incident radiation source. The maximum value (2.8×10^4 counts) was found in the defective regions seen as vertical white lines. There was also a clear gradient in the counts along the vertical direction. This can be attributed to the dark current which continuously accumulates during the reading out of the image.

An average (mean) image was computed over the 100 images. The mean pixel value for the average image was then found in the vertical direction as shown in Figure 5.3. The lines which required removal before further analyses can be identified by the large peaks in the curve, corresponding to the white lines in Figure 5.2. The smaller peaks (approximately 1 count or less in height) were due to cosmic rays and as such, were not constant in position over time. The curve in general was not entirely flat, likely due to variations in the temperature over the CCD surface. Notably, the number of counts increase significantly at the horizontal edges of the image, so these regions were also

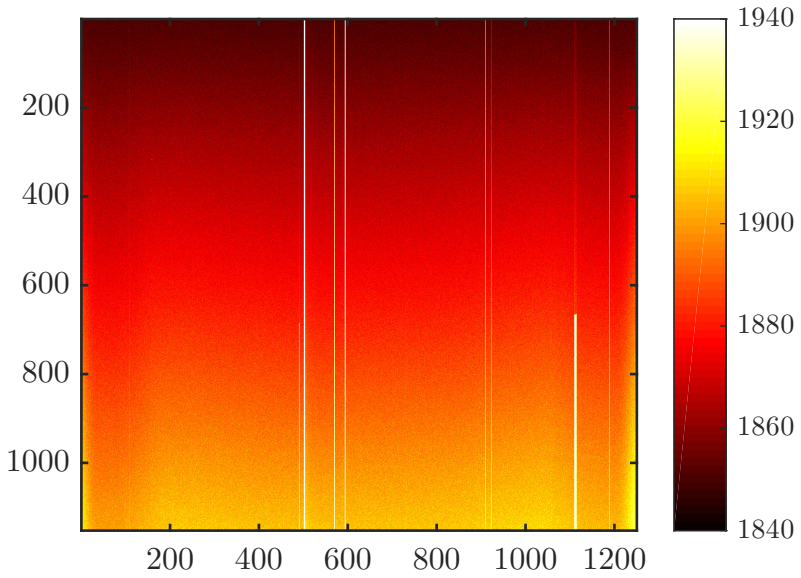


Figure 5.2: Example dark image of the Andor DO432-BN-DD at −30 °C, 100 ms exposure time and 1 µs/pixel readout speed.

removed.

Using the same scale, a set of images were also taken at temperatures of −40 °C and −50 °C as shown in Figures 5.4-5.7. There is a strong reduction in the dark current with decreasing CCD temperature as expected.

For each temperature, the average image at that temperature setting was subtracted from each image and the resulting mean pixel value was calculated and plotted as a function of frame number, shown in Figure 5.8. Across all temperatures, there was a sharp drop in the mean pixel value followed by a slow linear decrease, spanning approximately 2 counts. This variation was probably due to changes in the temperature over time. In this instance, it seems likely the chip had not physically reached thermal equilibrium before the images were taken. However, it should be noted the software indicated the temperature had reached the specified temperature before the start of each set. This demonstrates the difficulty of finding a background image to subtract from a data image, since the background image should not only be averaged over many shots in *identical conditions*, but also the data images should be acquired under the same conditions.

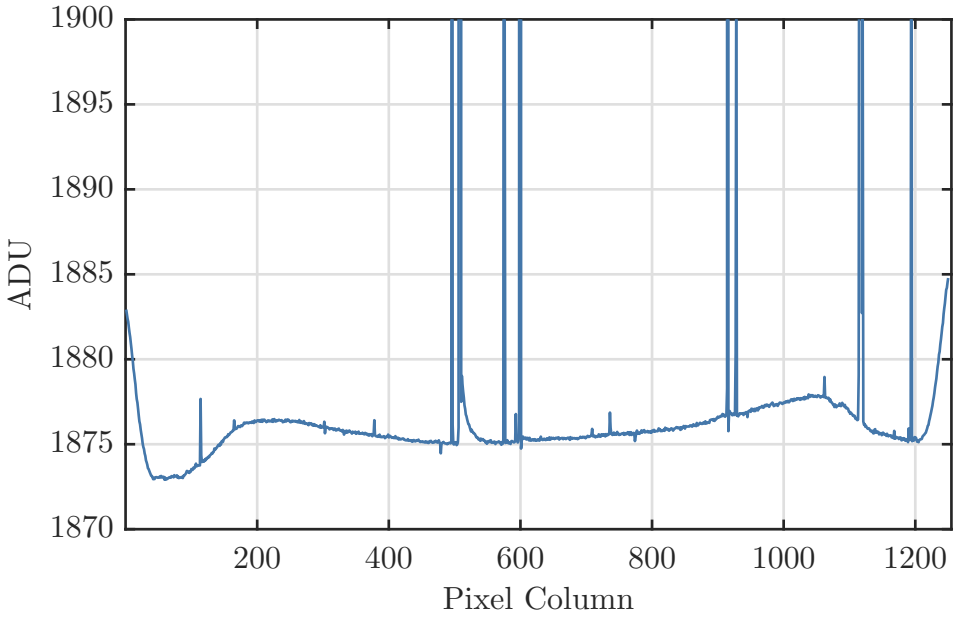


Figure 5.3: Mean CCD counts along pixel columns for a set of dark images at −30 °C. Large spikes reveal pixel columns which do not function normally.

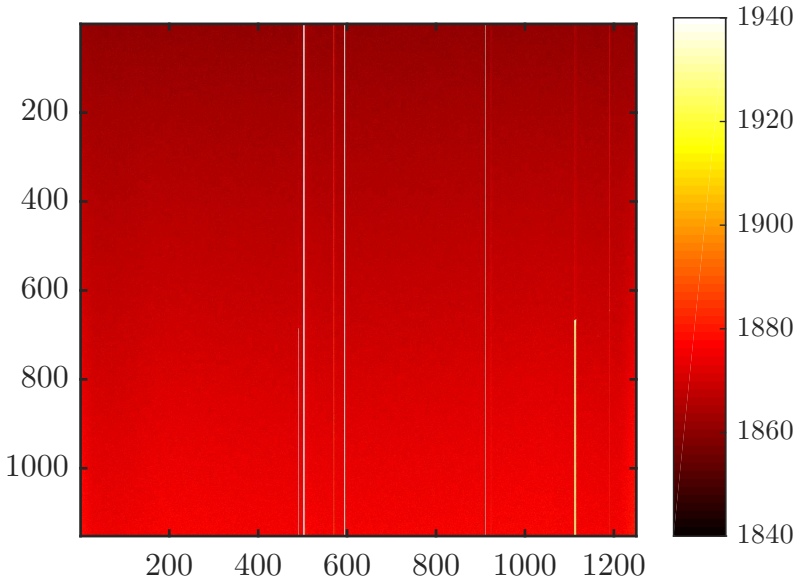


Figure 5.4: Example dark image at −40 °C, 100 ms exposure time and 1 µs/pixel readout speed.

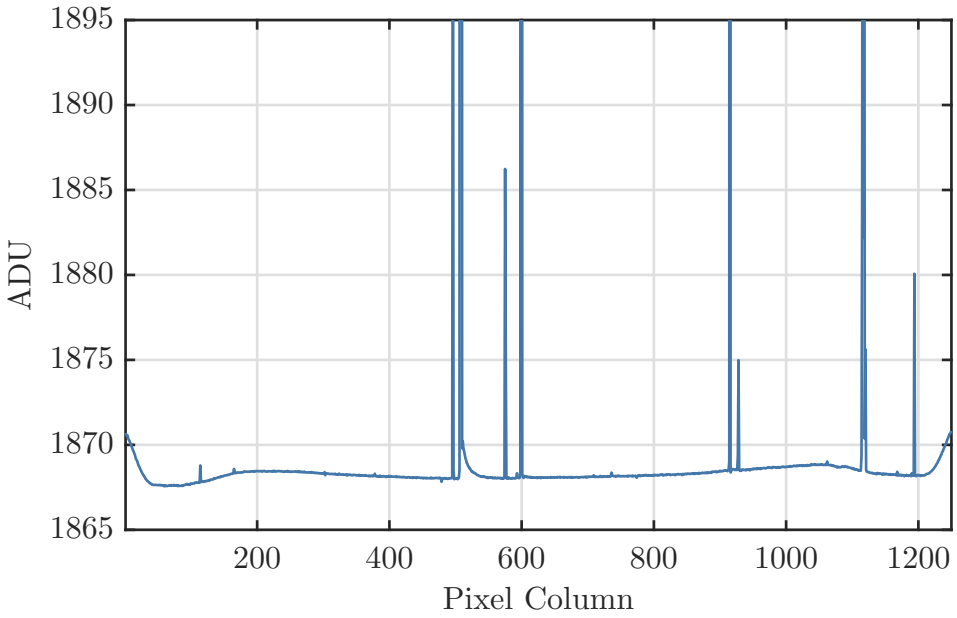


Figure 5.5: Mean CCD counts along pixel columns for a set of dark images at −40 °C.

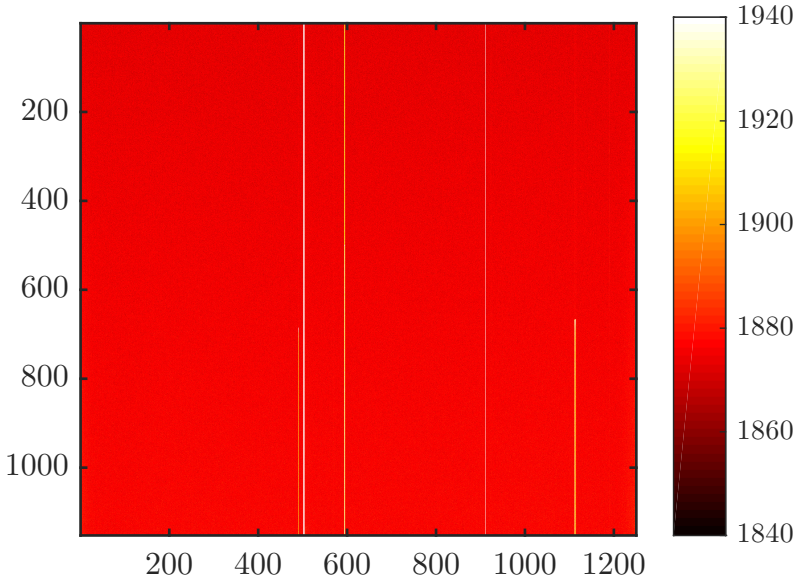


Figure 5.6: Example dark image at −50 °C, 100 ms exposure time and 1 µs/pixel readout speed.

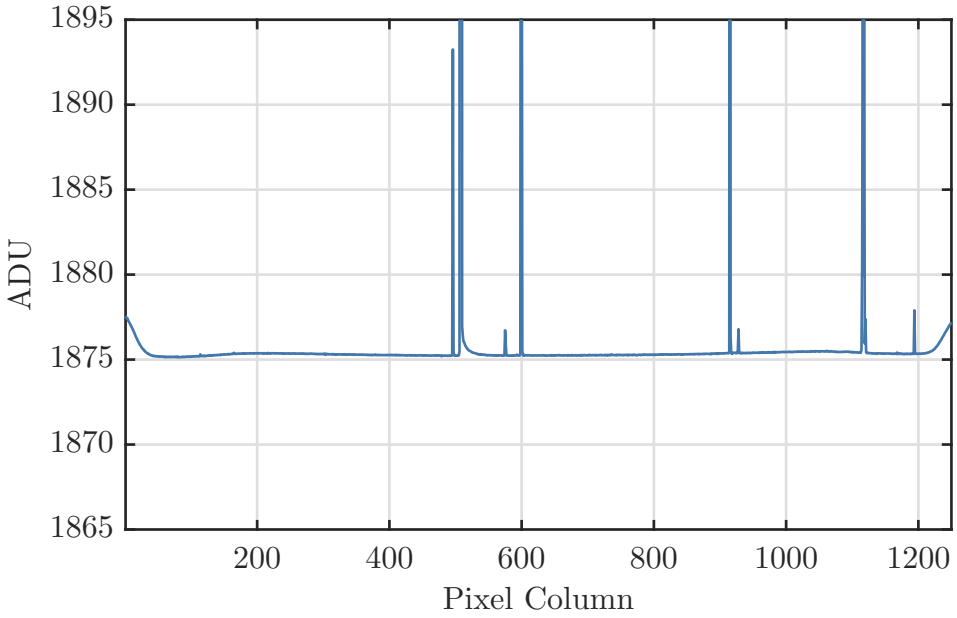


Figure 5.7: Mean CCD counts along pixel columns for a set of dark images at −50 °C.

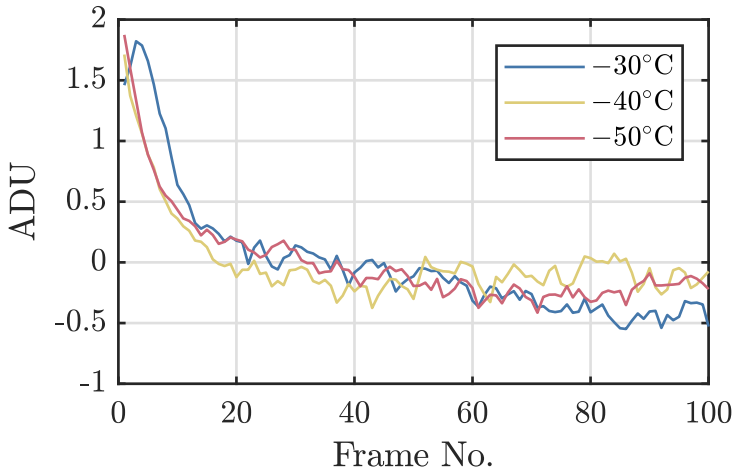


Figure 5.8: Mean pixel value of 100 consecutive images after subtraction of the average image.

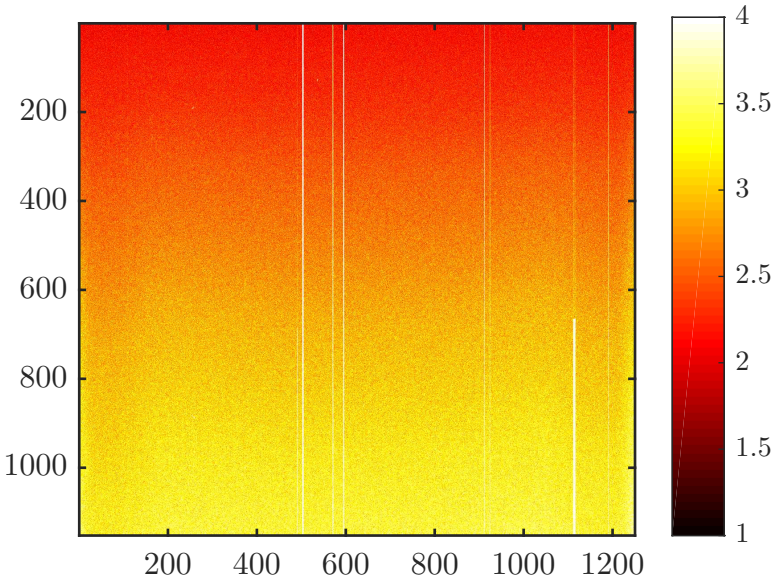


Figure 5.9: Standard deviation of each pixel across 100 consecutive dark images.

Variations in the output of a single pixel could be found by looking at the standard deviation of the pixel site over a number of images. This was calculated for each pixel in the dark image at $-30\,^{\circ}\mathrm{C}$, corresponding to Figure 5.2, and is shown in Figure 5.9. There is a clear gradient in the standard deviations along the direction of charge transfer, implying that the noise is dependent on the time taken to read out each row.

5.4.1 Background removal

A new method of removing the background level was developed by the author for cameras operating at low light levels. The method circumvents the need for background images, avoiding the issues associated with shot-to-shot variations in the noise level between consecutive images and also any potential differences in condition between the background acquisition and data acquisition.

When operating the CCD at lower temperatures, it was shown that the vertical sum becomes more linear (c.f. Figure 5.7). Fluctuations in the pixel values along any given row were found to be Gaussian distributed. Hence, the average pixel count was estimated using the median value μ_{mid}. The interquartile range (IQR) was used to estimate the

standard deviation of the noise in each row. Direct calculation of the standard deviation resulted in an overestimation due to X-ray events having large weight. The standard deviation was then approximated by $\sigma_{\mathrm{IQR}} \approx \mathrm{IQR}/1.349$. The scaling factor used here comes from the IQR of the standard normal distribution.

It was assumed that any pixel with a count less than $\mu_{\mathrm{mid}} + 3\sigma_{\mathrm{IQR}}$ was due to inherent image noise. Excluding pixels above this threshold allowed calculation of the 'true' mean and standard deviation of the noise in each row through the usual formulae

$$\mu_i = \frac{1}{N'_{\mathrm{col}}} \sum_{j=1}^{N'_{\mathrm{col}}} X_{i,j}, \tag{5.1}$$

$$\sigma_i = \sqrt{\frac{1}{N'_{\mathrm{col}}} \sum_{j=1}^{N'_{\mathrm{col}}} (X_{i,j} - \mu_{\mathrm{i}})^2}, \tag{5.2}$$

where $X_{i,j}$ is the number of counts in pixel (i, j), μ_i is the mean pixel value in row i *after pixel exclusion* and N'_{col} is the number of pixels in row i whose value is *below* $\mu_{\mathrm{mid}} + 3\sigma_{\mathrm{IQR}}$.

The background was then be removed from the data image by subtracting μ_i from each row. An example of this process applied to a dark image taken at $-50\,^{\circ}\mathrm{C}$ can be seen in Figure 5.10. To distinguish X-ray hits from noise, a threshold can be set using σ_i (instead of the standard deviation estimate, σ_{IQR}).

For background removal at higher temperatures, the nonlinearity seen in Figure 5.3 can be approximately accounted for by replacing $\mu_i \to \mu_{i,j} = \mu_i f(j)$, where f_j is proportional to the *mean pixel value of row* j. A comparison of background removal with and without accounting for the nonlinearity at $-30\,^{\circ}\mathrm{C}$ is shown in Figure 5.11. There is an obvious improvement in the background removal when using this extra step for higher temperatures, but there is clearly room for improvement.

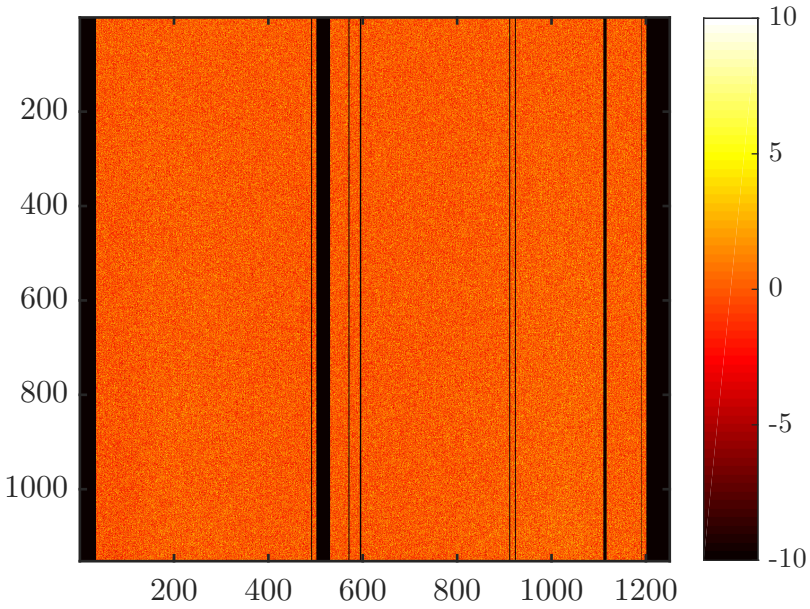
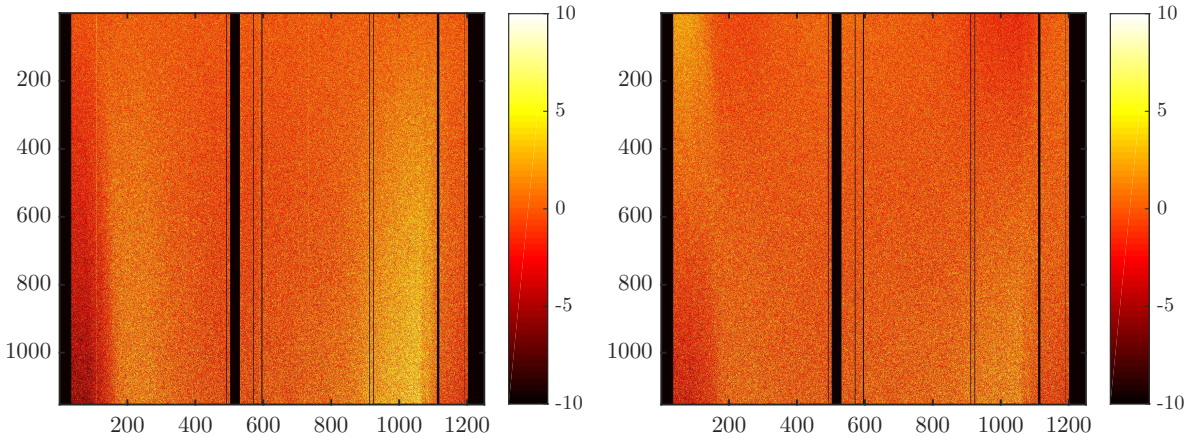


Figure 5.10: Example image after novel background subtraction at −50 °C.



(a) (b)

Figure 5.11: Example image after novel background subtraction at −30 °C. The image in (b) attempts to account for the horizontal variations across pixel columns using Figure 5.3, whereas (a) does not.

5.5 Event Recognition Algorithm

5.5.1 Particle signatures

CCDs are also sensitive to other sources of ionising radiation such as protons and electrons, which also produce electron-hole pairs in the CCD chip. Hence, to measure XCERP diffraction, CCD hits due to X-rays must be distinguished from these other sources. Ionising particles incident on a CCD produce events with different spatial signatures. For example, muons can continuously interact with the chip as they propagate through it, resulting in linear streaks across the image [114, 115], whereas electrons, whose mass is much lower, can be multiply scattered into significantly different directions, producing "worm-like" signatures [114, 116].

X-rays typically deposit their energy in a much smaller volume in comparison, creating a single photoelectron, which then goes on to generate a cloud of electrons of radius $r \simeq 0.012(E[\text{keV}])^{1.75}\mu\text{m}$ [117, 118]. A photon with an energy of 10 keV would thus create a charge cloud with a radius of approximately 0.7 µm, which is much smaller than the pixel size of a typical CCD. However, the structure of the CCD and depth in the silicon at which an interaction occurs can play a large role in the final size of the charge cloud.

As the cloud drifts towards the electrodes, diffusion causes the cloud to expand. Hence, the size of the charge cloud is kept at a minimum when it is created near the electrode structure. If the charge is created in the field-free region of the silicon wafer, the centre of the cloud remains stationary and the cloud diffuses over time. If a fraction of the cloud diffuses into the depletion layer, this fraction can be collected, but will have a radius much larger than if the photoionisation occurred in the depletion layer to begin with. Further details of the diffusion process in a CCD can be found in [113, 117–121].

The assumption is normally made that the cloud generated by a photon is Gaussian in shape and symmetric in the plane of the detector. Hence, it is expected that X-ray

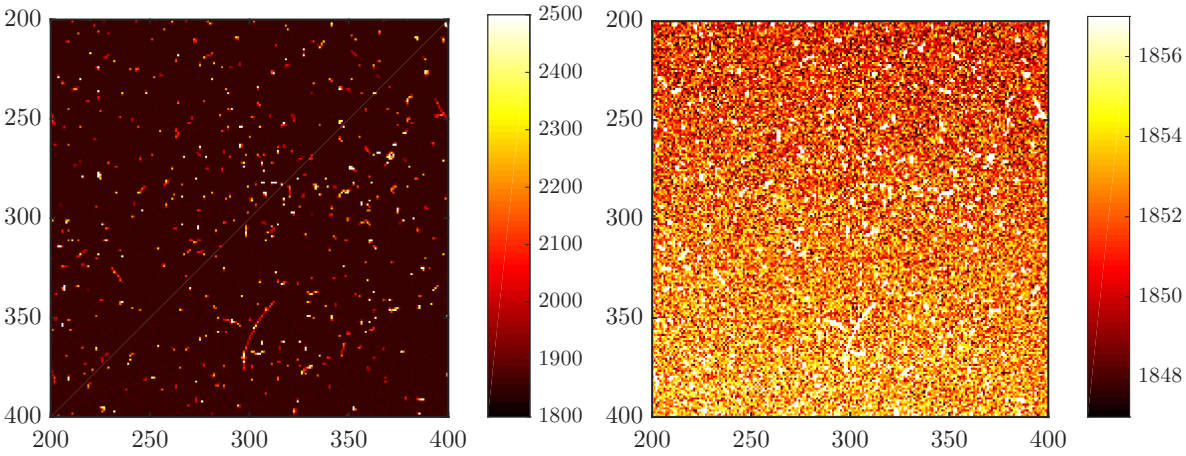


Figure 5.12: Example of a subimage of a single data image at two different colour scales. (a) emphasises contrast in events, whereas (b) emphasises contrast in background level.

events can be identified as approximately circular spots when the charge cloud extends across multiple pixels.

An algorithm was written in MATLAB to identify X-rays in the form of *single pixel events* (SPE) and *multiple pixel events* (MPE). Here, a multiple pixel event is defined as a group of pixels whose counts are above the background level and are connected by pixel edges. Events due to X-rays were identified by selecting only 'round'-shaped events.

5.5.2 Algorithm description

The algorithm for identifying X-ray events was applied to a portion of one of the data images (Figure 5.12) for illustration and is described below:

1. Subtract the background from the data image using the method described in Section 5.4.1. Figure 5.13(b) reveals proper compensation of the gradient and is correctly centred about zero.

2. Create a binary mask of pixels above event threshold (Figure 5.14). The threshold is based on the standard deviation of the background noise, specifically $3\sigma_i$ (note

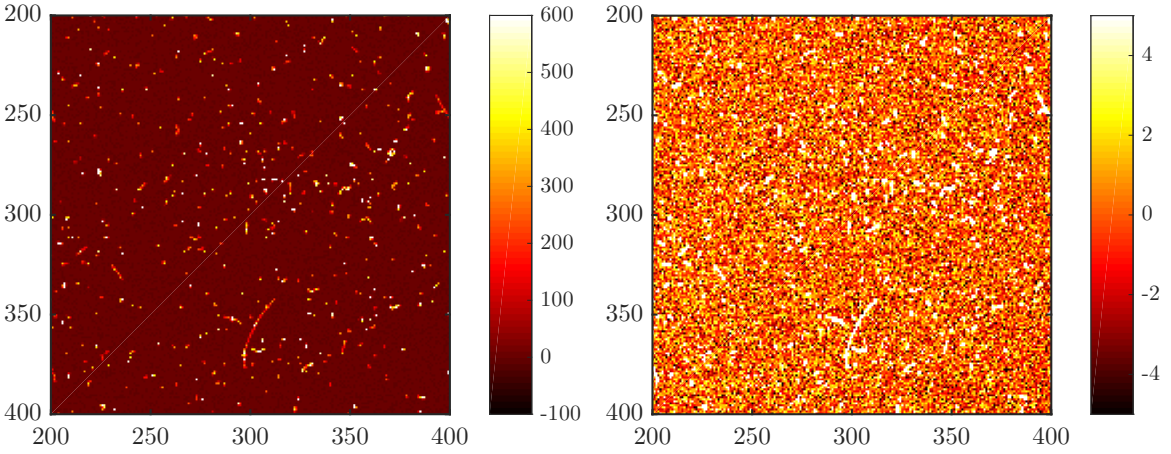


Figure 5.13: Example of a subimage of a single data image at two different colour scales after background subtraction. (a) emphasises contrast in events, whereas (b) emphasises contrast in background level

the threshold varies with row number).

3. Use the MATLAB function `bwconncomp` to find all connected regions in the mask. Pixels diagonal to each other are not considered to be connected here.

4. Discard connected regions larger than 4 pixels. Here, an assumption is made that the charge cloud created by an X-ray does not diffuse sufficiently to span more than 4 pixels.

5. Keep connected regions which are round. For regions containing 3 pixels, this corresponds to an L-shape. The corner pixel must contain the largest number of counts. For regions containing 4 pixels, the region must be square. The corner containing the largest number of counts must be opposite the corner containing the least number of counts. Regions which do not satisfy these conditions are not considered X-ray events. An example of classified regions is shown in Figure 5.15.

6. Regions which are adjacent to white/dead lines are discarded since it is not possible to identify whether charge has spread to these unused areas, and may overestimate the number low energy events.

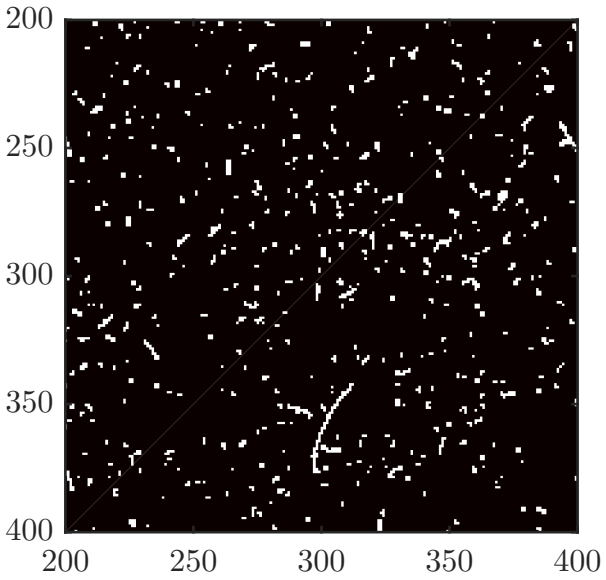


Figure 5.14: Example of binary mask, identifying regions of the image above background level.

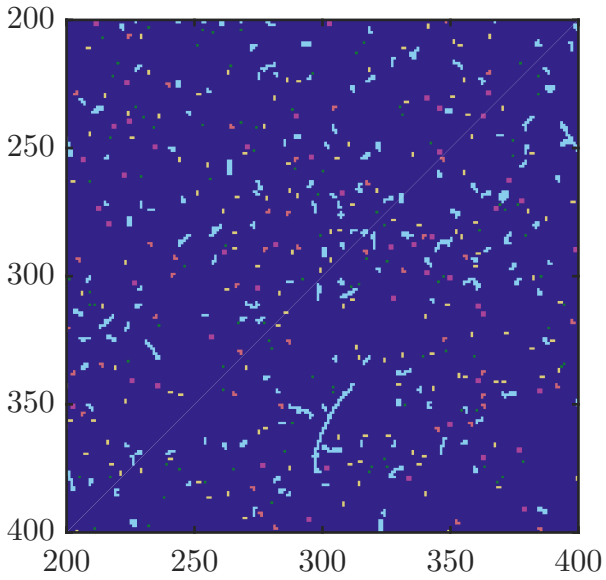


Figure 5.15: Events classified by shape and size: Green are single pixel events; yellow are double pixel events; orange are L-shaped triple pixel events; purple are square-shaped quad pixel events; and light blue evens are irregular events to be discarded.

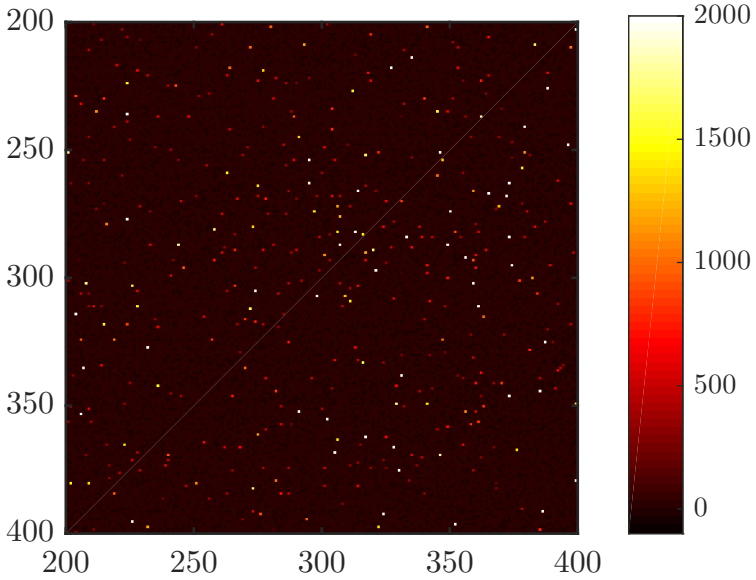


Figure 5.16: Example of processed data image, containing only X-ray events.

7. Replace each kept region with a single pixel containing the sum of the counts in the region. The new pixel is located at the maximum in the region and is referred to as the 'event centre'. This is shown in Figure 5.16.

In principle, a better estimate of the event centre can be obtained from a centroid calculation, or better yet, a fit to a 2D gaussian function (improving on the estimate which is constrained to integer values). Strictly speaking, the latter should involve a double integration of the 2D normal distribution along the directions of the pixel axes, giving the fraction of the signal which lies in a given pixel. For the analyses hereafter, knowledge of the event centre to an accuracy of one pixel is sufficient.

The output of the algorithm allows the energy spectrum to easily be found by plotting the histogram of the processed image. Details of the events types are also kept, allowing spectra to be plotted for each type of event.

5.6 Experimental Results

A histogram generated by the analysis underestimates the number of photons incident on the CCD surface because not all X-rays traversing the chip are absorbed. The quantum

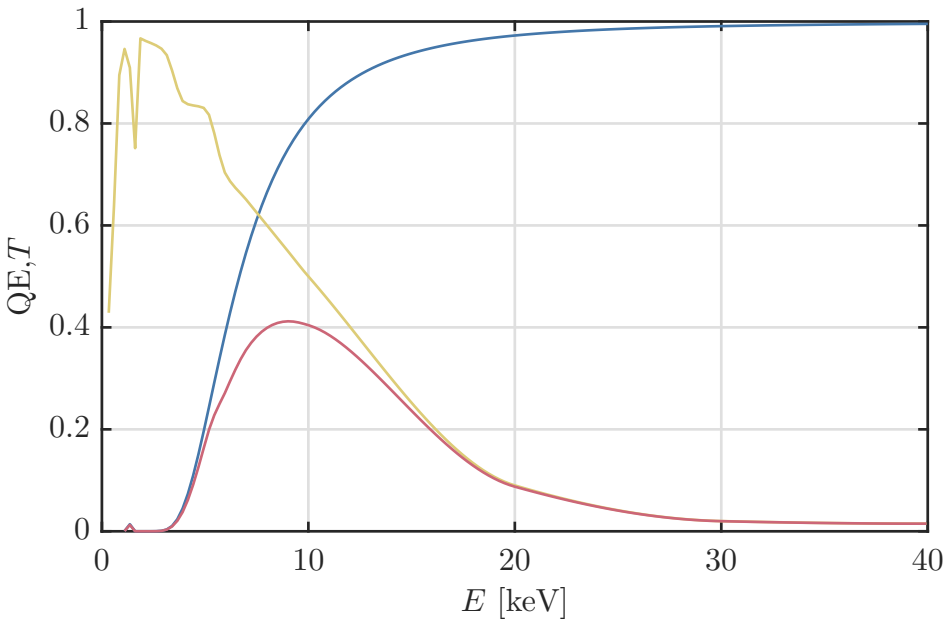


Figure 5.17: Quantum efficiency QE of the Andor DO432-BN-DD (yellow) and probability of transmission T through a 30 µm aluminium foil (blue), plotted against the photon energy E. The resulting probability of detection is shown in red.

efficiency (QE) $\mathcal{Q}$ of a detector determines the probability of photoabsorption and depends on the CCD material, thickness and the photon energy. The QE was obtained from the camera manufacturer. Another factor which modifies the incident spectrum is the attenuation of the beam en route to the CCD. A 30 µm sheet of anodised aluminium was used to shield the CCD from visible light. Using the MATLAB code by Jaroslaw Tuszynski [98], the transmittance T was calculated, which is based on the absorption coefficients from NIST [99]. Figure 5.17 shows the energy dependence of each factor and their combined effect. The CCD is most sensitive at 9 keV, below which, the attenuation due to the aluminium is significant, and above which, the quantum efficiency in silicon drops. The spectrum of the initial X-ray beam can be reconstructed by dividing the measured spectrum by the factor $\mathcal{Q}T$.

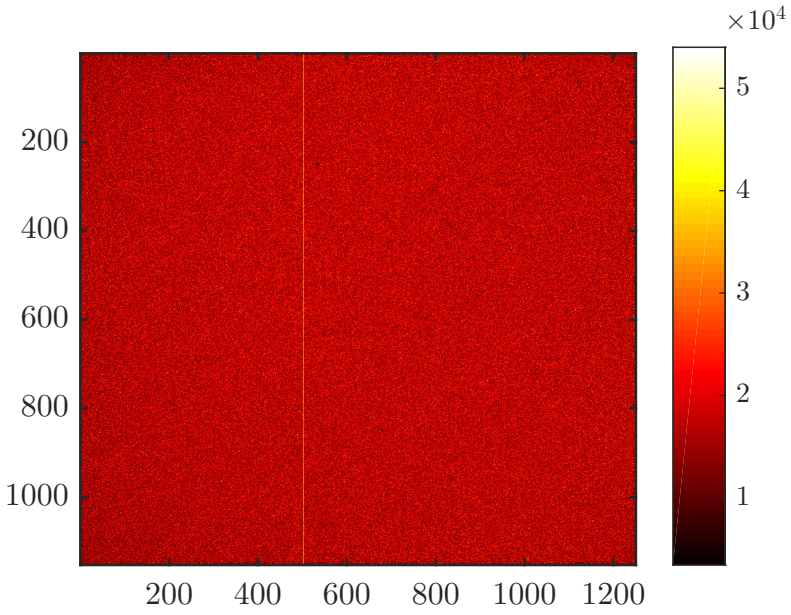


Figure 5.18: Example raw data image with minimal shielding.

5.6.1 Reducing background radiation

The off-axis Andor camera, measuring XCERP diffraction from a powder target, was initially located approximately 60 cm downstream of the interaction point in order to minimise the divergence of the X-ray betatron beam. A 20 µm steel tape drive was used to reflect the laser beam, as the laser intensity was high enough to destroy the powder target at just 40 cm from focus. Even with the additional X-ray attenuation provided by the tape drive, the CCD was flooded with radiation whenever an electron beam was generated, resulting in a uniformly illuminated image from 1×10^4 counts up to 4×10^4 counts at each pixel. It was found that additional radiation shielding was required as the signal with and without the powder target was qualitatively identical. The high level signal could not be reproduced when the gas jet was disabled or the laser pulse duration was increased and it could be seen that count level scaled with the charge of the electron beam. An example image is shown in Figure 5.18.

The shielding was improved over multiple iterations, reducing the CCD counts to the point where not every pixel was registering above the dark image level of ~ 1900 counts. Figure 5.19 reveals that there was still a significant number of bright pixels. A lead

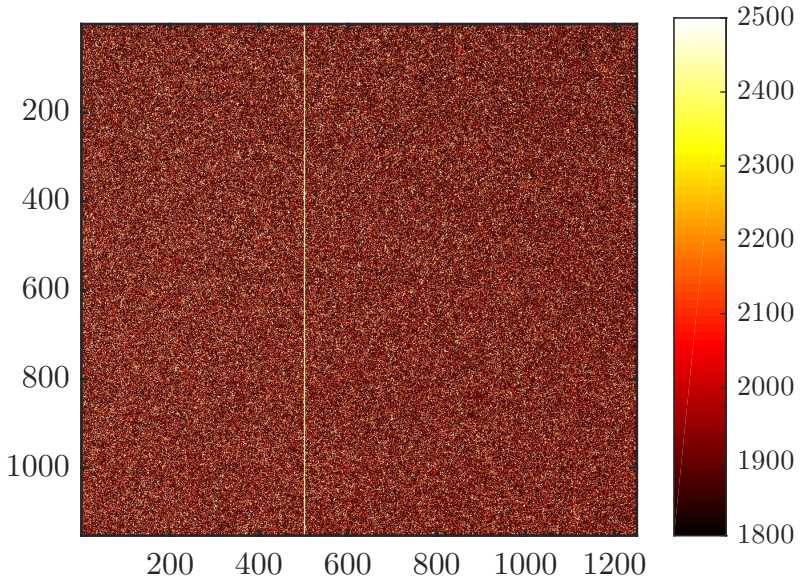


Figure 5.19: Example raw data image with additional lead shielding

sheet was also placed over the CCD aperture to verify whether this signal disappeared. However, it was found that although the number of bright pixels was reduced, bright pixels were not completely removed. Since lead is a strong attenuator of X-rays, it implies there were other sources of ionising radiation incident on the camera. These possible sources are explored in more detail Chapter 6.

In order to measure the signal generated by XCERP diffraction, a further reduction in this unwanted signal was required. This was achieved (Figure 5.20) by moving the camera further downstream, at the expense of a reduced betatron fluence due to beam divergence. It should be noted that at 3.25 m downstream of the interaction point, the tape drive was no longer required to shield the powder target from the laser beam. It was found that only $\sim 3\,\%$ of pixels had a count 3 standard deviations above the mean count level, making this setup suitable for photon counting applications.

A comparison of the raw histograms of the above images is shown in Figure 5.21. It compares the images captured at the initial camera position with (yellow) and without (blue) the lead sheet blocking the camera chip, and the case when the camera is moved further downstream (red). An order of magnitude reduction in the number of bright pixels can be seen with the latter configuration. Additionally, a number of small peaks

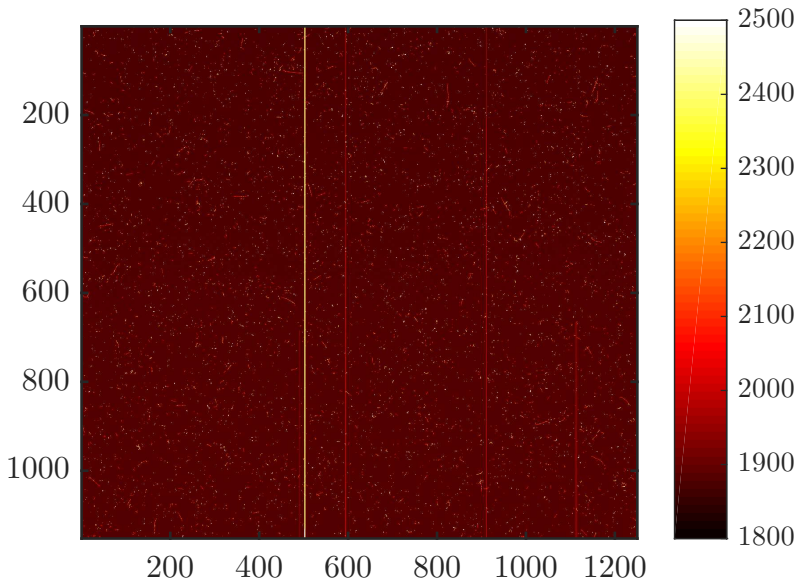


Figure 5.20: Example raw data image with additional lead shielding and increased distance from interaction point.

can be found, which might be assumed to be from fluorescence of materials in the vicinity. The energies retrieved from applying the conversion of 25.6 eV/count to the peak positions were in the range 0.53 keV to 10.3 keV. A number of these did not straightforwardly match a tabulated fluorescence line, but some seemed to match well with some materials found in the chamber, most notably, aluminium at 1.48 keV (K_α), chromium at 0.57 keV (L_α) and lead at 10.5 keV (L_α). However, other lines which would have been expected were absent such as iron at 6.4 keV (K_α) and chromium at 5.4 keV (K_α). As a result, it may be desirable to perform a cross-calibration using a known radioactive source in order to check that the number of counts is proportional to the reference energy in accordance to the previously calculated conversion.

After inserting the powder target in the path of the betatron radiation, it was expected that CCD events due to diffraction could be differentiated from those due to 'background radiation' as the diffraction events would have a spatial dependence at a given photon energy (c.f. Figure 3.5). The signal which was not due to X-ray diffraction would be expected to have no such dependence.

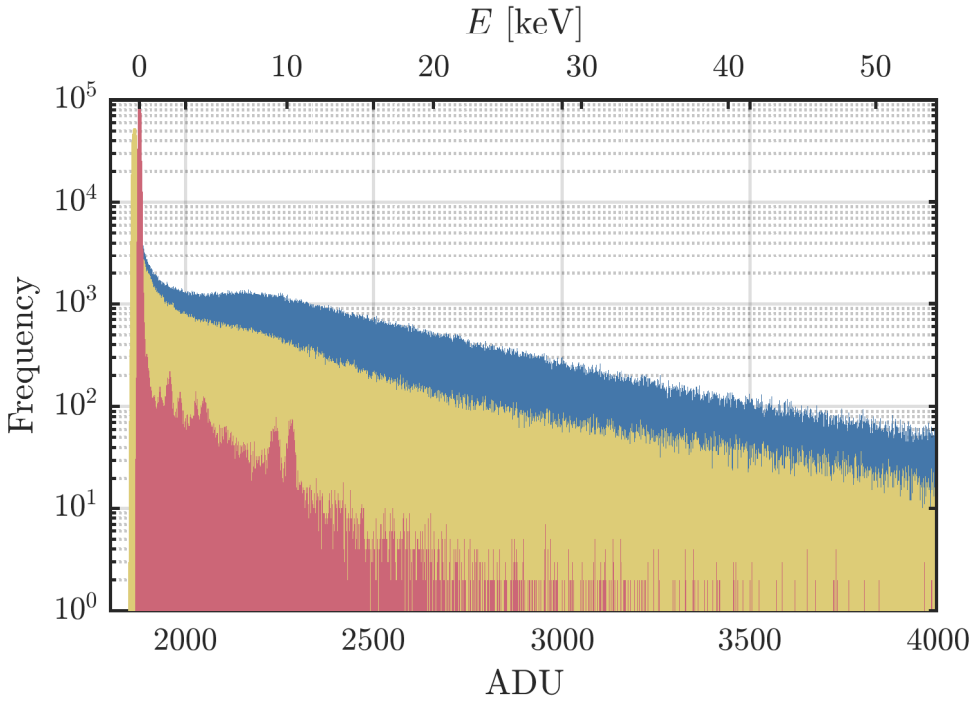


Figure 5.21: Histograms of Figure 5.18 (blue), 5.19 (yellow) and 5.20 (red), corresponding to data images with little radiation shielding, with additional lead shielding, and at an increased distance to the IP, respectively.

5.6.2 Data selection

A number of runs were performed to demonstrate XCERP diffraction using the betatron radiation produced in a laser wakefield accelerator. For each run using the powder target, there was a corresponding run which did not use the powder in order to help distinguish the CCD hits due to X-ray diffraction and those inherently detected when an electron beam was generated. The runs without the use of the powder target are referred to in this work as *reference runs* for convenience whilst those using the powder are referred to as *powder runs*.

In order to compare a shot from a powder run with that of a reference run, the betatron emission must be similar. Using the on-axis betatron camera to compare runs is not immediately useful since there is extra attenuation due to the silicon powder. It is shown in [122, 123] and Section 4.6 that the betatron emission can be correlated to the electron characteristics. Hence, the electron spectrometer was used as a measure of

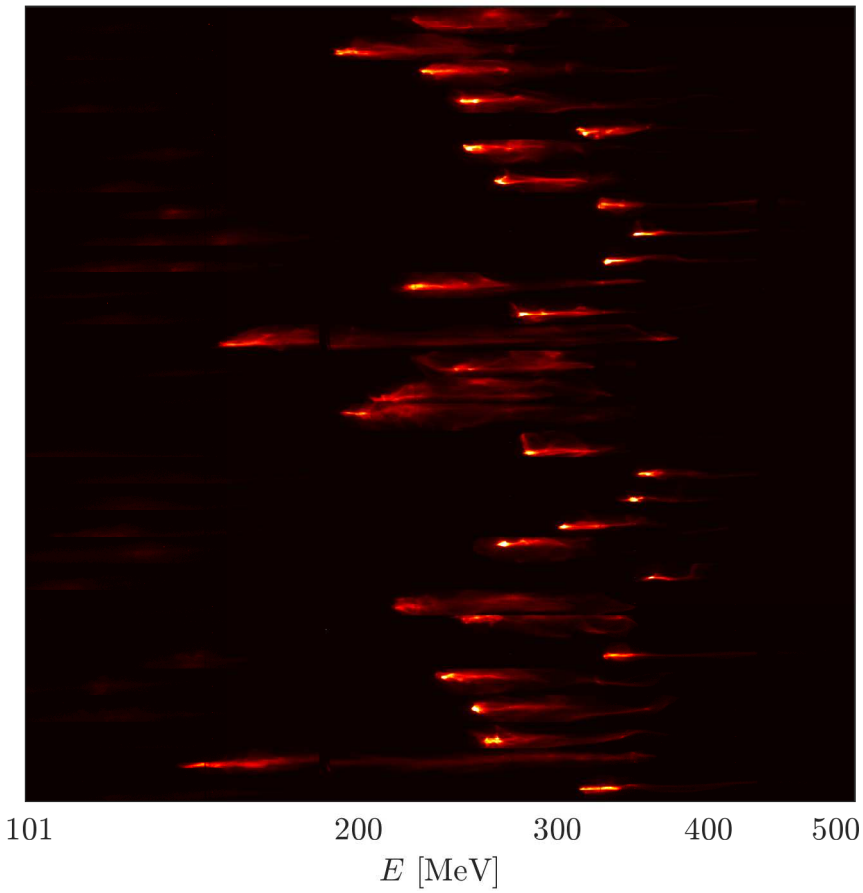


Figure 5.22: Electron spectrometer images for consecutive shots showing unstable electron beam production.

similarity between shots.

It was found that there could be significant shot-to-shot variation in a single run, depending on a number of factors such as the gas pressure, laser focus position and the placement of the knife-edge producing the shock front. An example of a run in which there were no parameter changes between shots, but resulted in high variation in beam generation is shown in Figure 5.22.

In order to identify shots in which the generated electron beam, and hence betatron radiation, were similar, the measured electron energy spectra were compared. The electron spectrometer image from each shot was summed along the transverse direction (i.e. the vertical direction in Figure 5.22), producing a quantity proportional to the charge in a given energy slice. A single image was chosen from one of the more stable

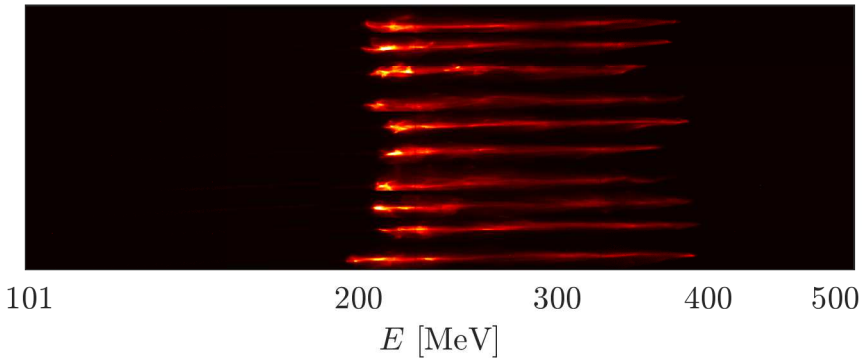


Figure 5.23: Electron spectrometer images for similar shots. The top spectrum is the spectrum chosen to compare against and represents the qualitatively most typical spectrum. The top 5 spectra are taken from a reference run, while the bottom 5 are from a powder run. The average charge (calibration courtesy of Hao Ding of LMU) is 325 pC.

pairs of powder and reference runs and the summation was performed. By calculating the squared residuals of the pseudo-charge with respect to this image, similar electron spectrometer images were found. These shots were then assumed to have produced comparable betatron radiation. The resulting subset is shown in Figure 5.23.

The respective Andor camera images for the subset of shots were found to be very similar to the image shown in Figure 5.20, for both the powder and reference runs. Identical camera settings were used over the full subset, which were a readout time of 1 µs/pixel, exposure time of 100 ms and temperature of −30 °C. A higher temperature was used during these runs due to difficulties with temperature stabilisation at lower temperatures. Therefore, the high temperature approach to background removal was used as described in Section 5.4.1.

By following the algorithm described in Section 5.5.2 for the full image corresponding to the sub-image in Figure 5.24, a set of histograms were retrieved (Figure 5.25) which represent the number of X-ray events recorded of a given type. The spectra show slight variation between event types, with a larger number of double pixel events with energy

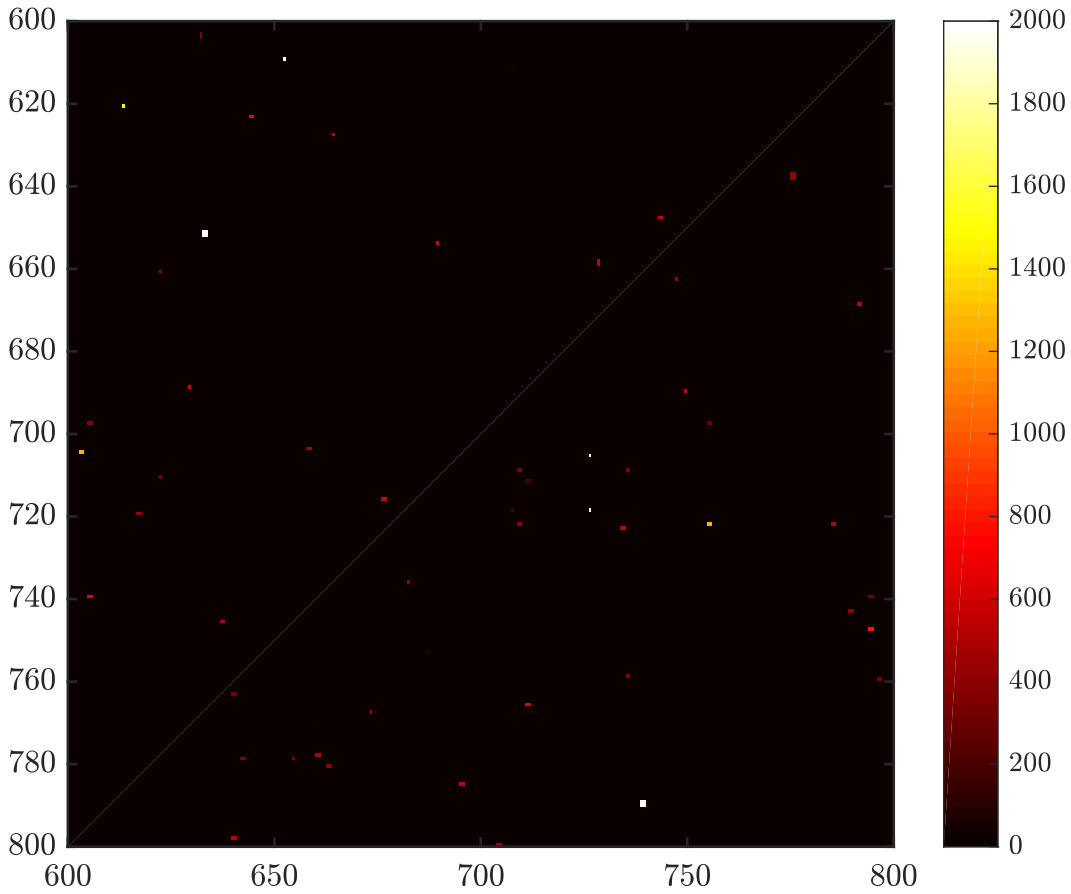


Figure 5.24: Sample section of an image of X-ray events after processing. Each event shown may originally have been a multiple pixel event.

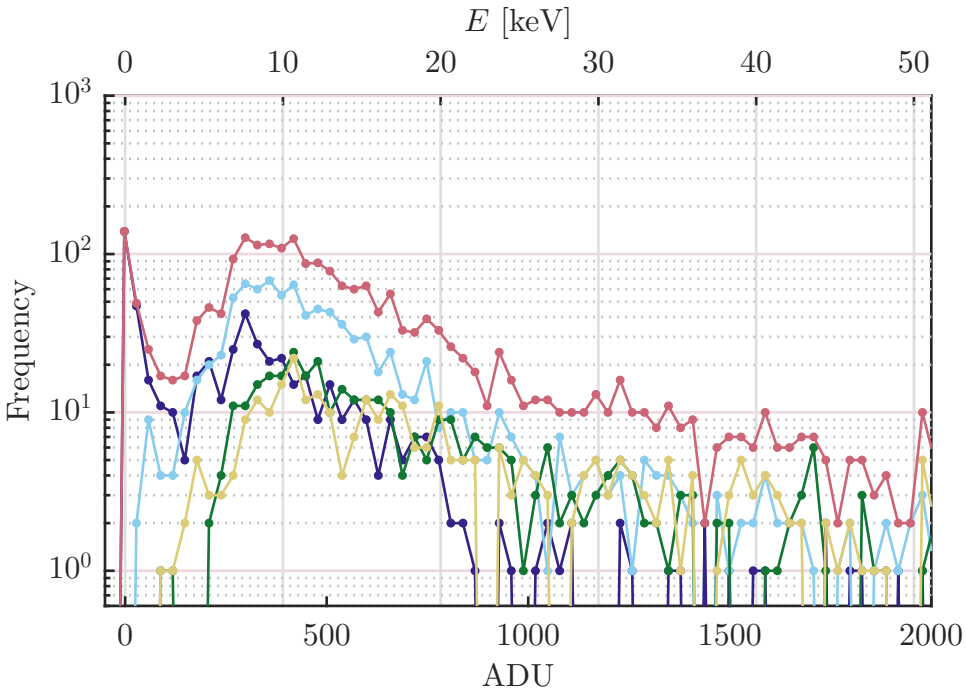


Figure 5.25: Histogram of X-ray energies for single pixel events (dark blue), double pixel events (light blue), triple pixel events (green), quad pixel events (yellow), and all events types (red). Bin widths of 20 ADUs are used. The data is based on Figure 5.24.

less than 20 keV compared to other types. The number of single pixel events above 20 keV were much lower than other event types. This may be expected as the charge cloud created is larger at high energies and would be more likely to manifest as MPEs. A large number of single pixel events were found with an energy less than 1 keV. This feature was not reproduced by the histograms for larger event shapes and likely indicates imperfect background subtraction at the higher camera temperature. The total number of events identified in this image was 2248 events, which is 0.2% of the total number of pixels (although the number of pixels above background was on the order of 2%, but most of these did not satisfy the criteria for single pixel or multiple pixel events).

Each pixel on the CCD corresponds to an angle taken between the laser beam axis and the line formed by the powder centre to the pixel location. With the centre of the CCD 21.0 cm from the laser axis and 20.3 cm downstream of the powder, the angular range was between 43° and 49°. Figure 5.26 shows the mapping between pixel location and angle.

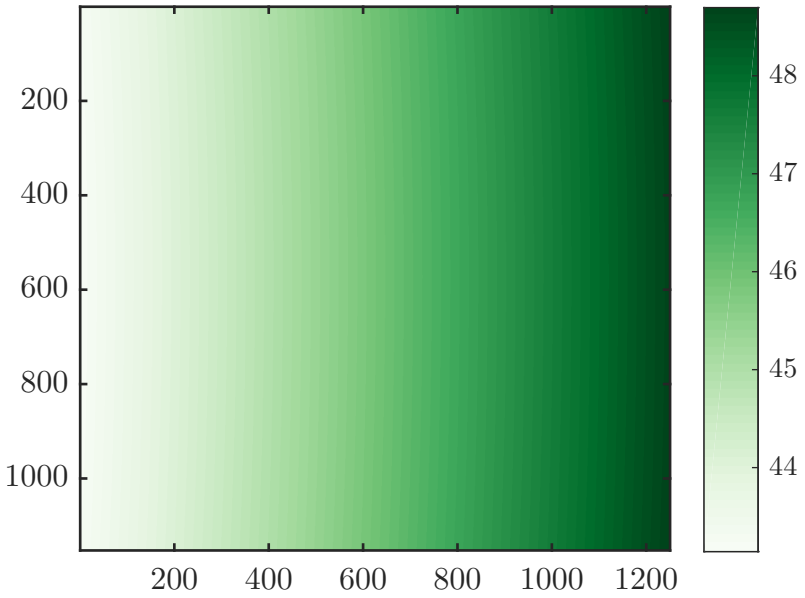


Figure 5.26: Map of pixel location to angle in degrees.

Applying the map to Figure 5.24, it was possible to construct a 2D histogram of the X-ray hits as a function of energy and angle as shown in Figure 5.27. The highest density can be seen in the bottom left corner corresponding to multiple low energy events along the left side of the CCD image. This can be attributed to the imperfect background subtraction for $-30\,^{\circ}\mathrm{C}$ and corresponds to the top left corner of Figure 5.11(b).

5.7 Discussion

It is reasonable to assume that the number of X-ray events in the low energy region is also slightly overestimated. This is because energy which is deposited over multiple pixels will be recorded as a lower energy event if the charge created does not cause every associated pixel value to rise above the threshold used in step 2 of the event recognition algorithm. Therefore, the remaining pixels which do exceed the threshold value will be summed together and be counted as due to an X-ray with a lower energy. This effect is more important when the initial energy is comparable to the threshold value (which is typically on the order of a few 100 eV).

The 5 reference shots in the data subset (corresponding to the top half of Figure 5.23)

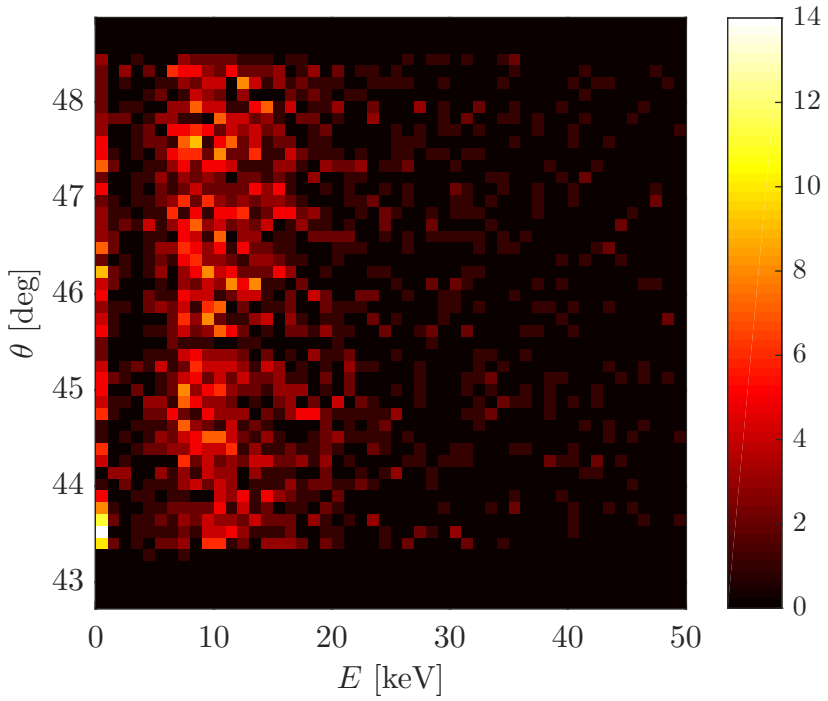


Figure 5.27: Histogram of X-ray events binned against energy and angle. The histogram is split into 50 bins in each direction for the ranges shown.

were processed similarly and the retrieved spectra were averaged to give Figure 5.28 (dark blue). It is plotted alongside the spectrum incident on the CCD (dark red), inferred by accounting for the quantum efficiency and transmission through the light shield (c.f. Figure 5.17). Errors for this line, shown as the dark red shaded area, were calculated assuming Poisson noise in the measured spectrum and allowing for a 5 % deviation in the thickness of the aluminium shield. Ignoring energies below 5 keV, the spectrum is relatively flat.

The 2D histograms for the 5 images were summed and is shown in Figure 5.29. The horizontal dark lines near 45.5°, 47.2° and 48° correspond to regions of the CCD which were excluded from the images due to bright pixel lines and/or dead pixels. This effect could be mitigated by rotating the CCD by 90° so that unused pixel lines are distributed over the full angular range.

The same plots were produced for shots with similar electron spectra, but included diffraction from the powder target (bottom 5 shots of Figure 5.23). These are shown

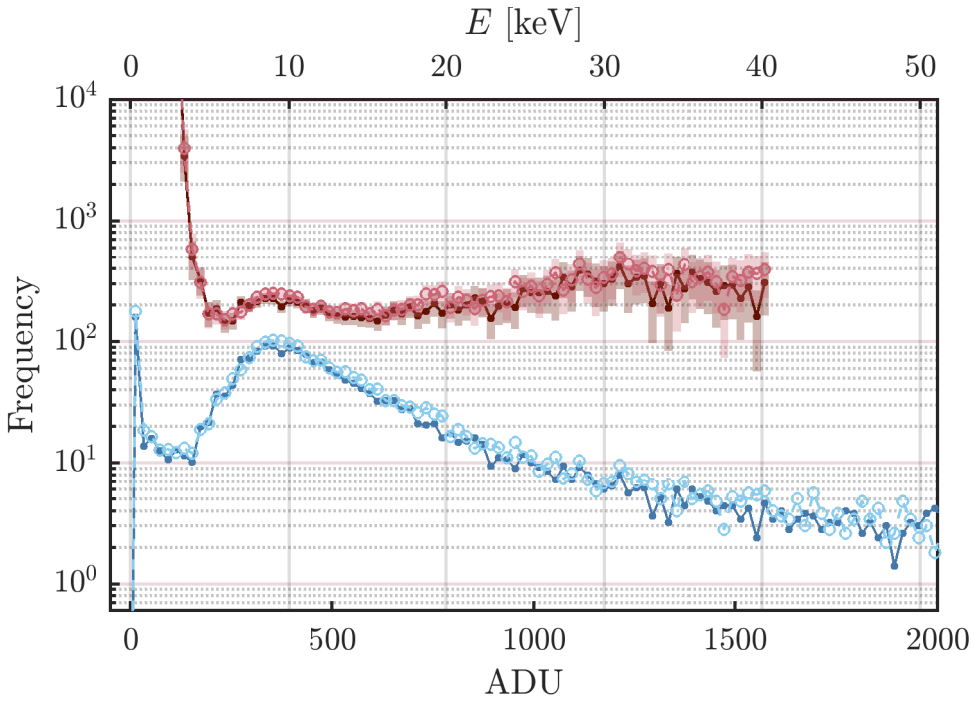


Figure 5.28: Retrieved X-ray spectra for all event types, using data from a reference run (dark blue) and a powder run (light blue). Division by the quantum efficiency and transmittance of the CCD aluminium light shield gives the spectra incident on the CCD for the reference (dark red) and powder (light red) run. Bin widths of 20 counts were used.

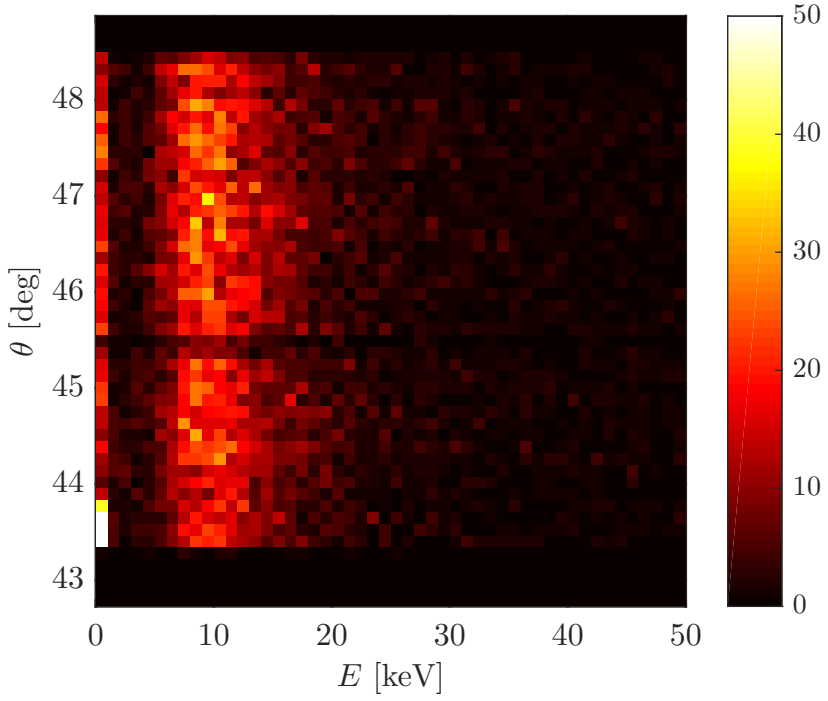


Figure 5.29: Histogram of X-ray events binned against energy and angle for 5 reference shots. The histogram is split into 50 bins in each direction for the ranges shown.

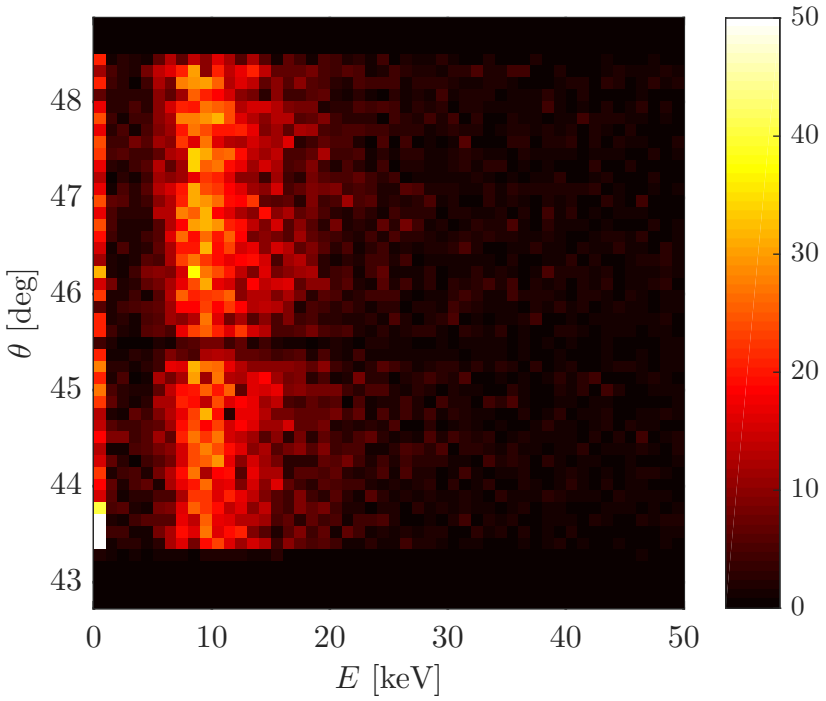


Figure 5.30: Histogram of X-ray events binned against energy and angle for 5 powder shots. The histogram is split into 50 bins in each direction for the ranges shown.

in Figure 5.28 (light blue, light red) and 5.30. Unfortunately, there is no discernible difference between the powder run and reference run spectra as would be expected if there was a significant diffraction signal. The fact that the spectrum also does not reduce in energy when the powder is placed on-axis implies that the source of the measured radiation is not caused by the betatron beam.

To reinforce this result, the energy-angle histogram for the reference run was subtracted from that of the powder run. For a diffraction signal, there should be an energy-dependent feature similar to those in Figure 3.5. Figure 5.31 shows the resulting subtraction. No clear trend could be found, with the bins varying about zero. The largest differences in the histograms can be seen around the $E = 10\,\text{keV}$ line, which is due to the higher signal in this region (and hence higher variance).

Preliminary analyses of other runs during the experiment showed very similar results. Interestingly, it was previously thought that the retrieved X-ray spectra for the powder and reference shots differed appreciably from each other for a few pairs of runs. However,

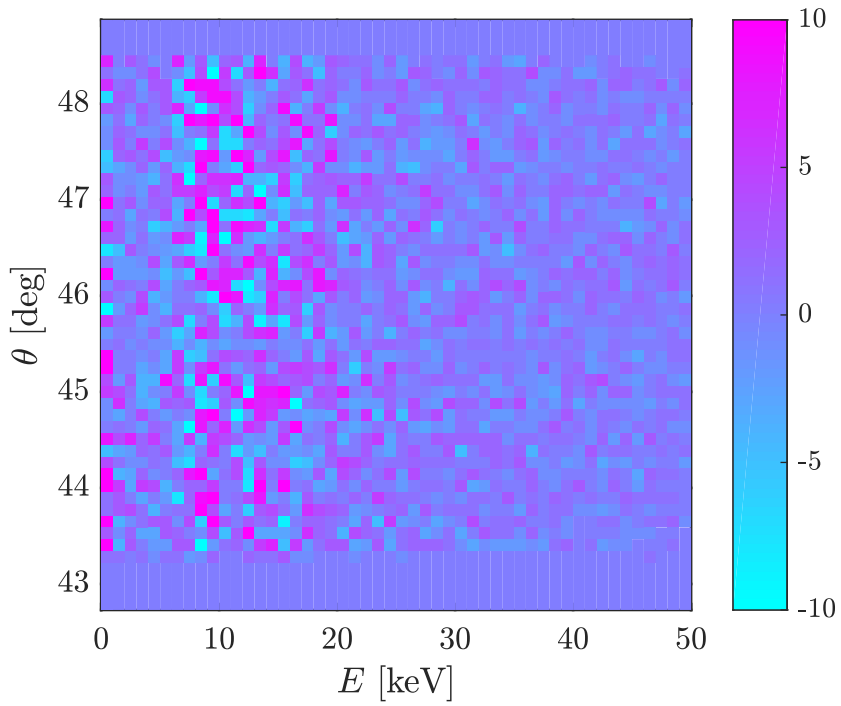


Figure 5.31: Difference in histogram of X-ray events for 5 powder shots and 5 reference shots binned against energy and angle. The histogram is split into 50 bins in each direction for the ranges shown.

it was later found that this was caused by differences in the electron spectra. This motivated the data selection described in Section 5.6.2.

The XCERP diffraction simulation code from Chapter 3 was used to check what might be expected if a strong diffraction signal was present. Using measurements of the experimental setup, Figure 5.32 shows the desired relation between angle and energy for powder diffraction. Unlike Figure 3.5, we see that the curves corresponding to Debye-Scherrer rings (solid lines) are almost vertical, meaning that there is, in fact, very little correlation between the position of a diffracted X-ray striking the CCD and its energy, as previously thought. The main reason for this is that the position-energy relation is most pronounced at shallow angles, but in the experiment there was a minimum distance required between the CCD and the laser axis in order for the undiffracted portion of the betatron radiation to propagate past the camera. The CCD would need to be moved further downstream w.r.t. the powder to achieve this, but simultaneously this would reduce the total angle subtended by the CCD (and therefore the total fraction of

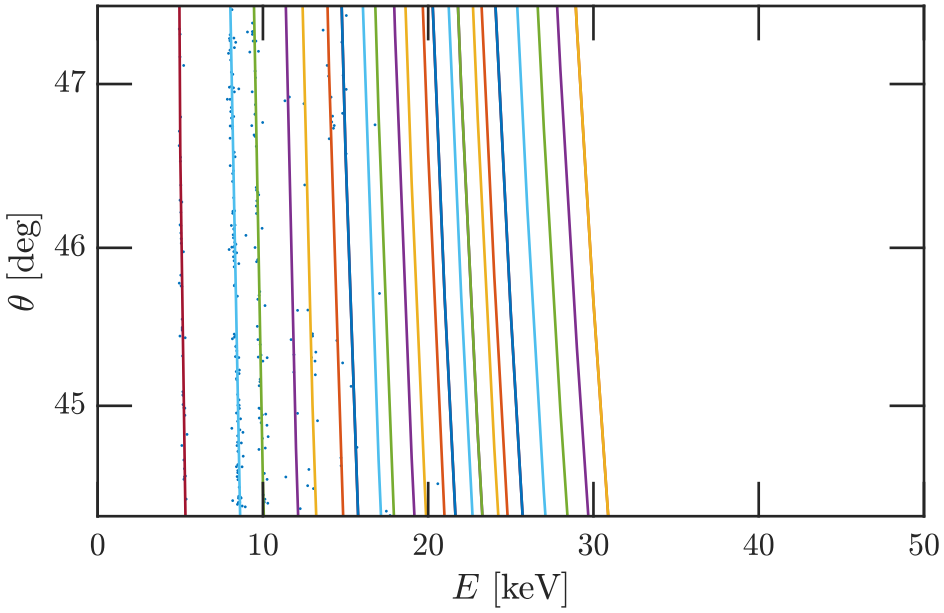


Figure 5.32: Simulated scatter plot of angle from powder centre to detector w.r.t. the beam axis as a function of photon energy for the geometry used at CALA. 10^5 photons were simulated.

diffracted radiation) to a minuscule level.

Figure 5.32 also reveals that the majority of diffracted radiation would be near 10 keV, which coincides with the signal peak of the inherent background radiation. Consequently, the diffracted signal would have needed to be especially strong in order to be distinguished from the radiation seen in the reference runs. Conversely, it is possible that an XCERP diffraction signal is present in the data taken, but is simply dominated by the background radiation.

If a follow-up campaign were to be executed, improvements to the setup could be implemented to further increase the chance of a successful XCERP diffraction retrieval. A number of these have been described in Section 6.8 and relate to improved shielding. It would also be ideal to incorporate liquid cooling as well, as it has been shown that the image background can be vastly improved (in terms of homogeneity) if the CCD is cooled to below −50 °C. In the data shown here and for the vast majority of runs during the campaign, the fastest readout rate was used in order to acquire data at an acceptable rate. However, it may be advantageous to capture images at a slower

rate, which has the advantage of using a more desirable sensitivity setting which would increase the signal-to-noise ratio by up to 3-fold. This would provide a better insight into the characteristics of the retrieved spectra.

5.8 Summary

An experiment performed at the CALA facility in Munich, and the analysis of the data obtained, has been described. The image data, in the single photon regime, was processed using a number of novel algorithms, the first of which is a background removal procedure, which does not require a background image to be acquired for each session. X-ray data was identified using a separate algorithm and has been detailed above. Using a subset of the data, the X-ray energy spectrum was retrieved for an off-axis camera pointed at a powder target subjected to bright betatron radiation. This was compared with the same scenario but with the powder removed. It was shown that the radiation recorded by the CCD was dominated by radiation which had not been diffracted from the XCERP powder. The potential sources of this non-diffracted radiation are explored in Chapter 6.

Chapter 6

Geant4 Simulations

6.1 Introduction

For the experiment that took place in the Centre for Advanced Laser Applications (c.f. Chapter 5), it was useful to check whether the X-ray camera was adequately shielded from sources of radiation other than X-ray powder diffraction.

In order to identify and quantify other potential sources of radiation present in this experiment, the propagation of high energy particles and their interaction with matter was simulated. GEANT4 (GEometry ANd Tracking) was used for this purpose as it is a well-established Monte-Carlo code which has been used extensively since its development in 1999. The inherent object-oriented style of the C++ language employed by GEANT4 allows the software to be used as a toolkit, allowing users to pick and choose individual modules to cater to their needs. As a result, the scope of GEANT4 spans many areas of physics such as particle physics, nuclear physics and medical physics [124].

The interaction between GEANT4 and a typical user is often a passive one, with GEANT4 being embedded in some software package such that 'end users' are able to drive the software with minimal coding experience. However for the purposes of this work, the role of 'application programmer' [124] was adopted by the author, involving simulations being generated from the ground up from a standalone version of the code.

The version used in this work is `geant4-10-00-patch-02`. Details of the implementation of GEANT4 are described below.

6.2 Modelling the Geometry

To capture the main details of the experiment, a virtual portion of the target area was constructed. The main components were:

- the target area
- the vacuum chamber
- the electron spectrometer
- the X-ray camera housing
- the lead shielding

Each component had a number of properties which needed to be specified in GEANT4, such as the shape, size, position and material. Many of the measurements and details used to recreate these components were provided courtesy of Johannes Götzfried of LMU in addition to a CAD file provided by Gregor Schilling of LMU.

A number of the materials simulated were taken from pre-built definitions using the NIST database, which included details such as the chemical composition and density (at standard temperature and pressure (STP), as used by NIST, of 293.15 K and one atmosphere, or 101.325 kPa [125]). These materials can be identified by the prefix `G4_`. For example, `G4_H` represents the NIST definition of hydrogen.

A full construction of the geometry modelled is shown in Figure 6.1. A number of particles have been propagated as a demonstration. A wireframe view has been assumed to aid visibility of both the aluminium cube inside the lead shielding, and the particle tracks, especially inside dense materials. A brief description of each component is outlined below.

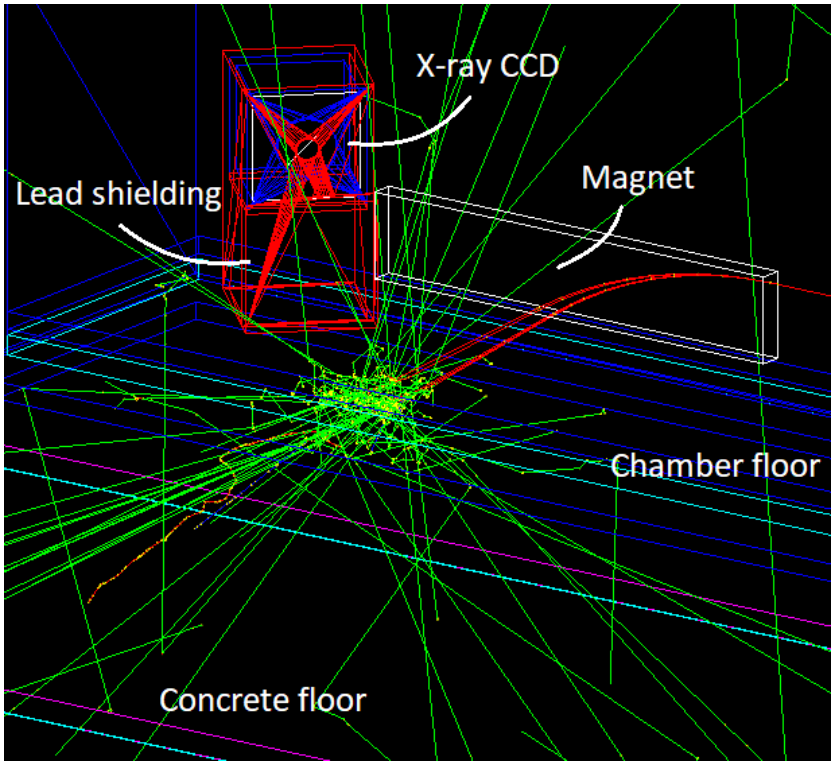


Figure 6.1: Example of GEANT4 geometry with 5 incident electrons as indicated by red paths. Green paths represent photons. Components are outlined depending on their material: lead (red); aluminium (dark blue); steel (light blue); gypsum (pink). The white box shows the volume containing magnetic field, but is of the same material as the surrounding medium, i.e. vacuum (low-density air).

6.2.1 Target area

The target area was essentially determined by the simulation box, which has been defined as a $(6 \times 6 \times 2)$ m box filled with air, approximated using the in-built NIST material `G4_AIR` which has a density of $1.204 \times 10^{-3}\,\mathrm{g/cm^3}$.

The floor of the target area was raised 600 mm from the 1 m concrete foundation (`G4_CONCRETE`) and was separated by an air gap for miscellaneous cables and the vacuum pumps to sit in. The raised floor was comprised of 1 mm stainless steel (`G4_STAINLESS-STEEL`) and 39 mm plaster which has been approximated by `G4_GYPSUM`.

6.2.2 Vacuum chamber

The contents of the vacuum chamber was derived from `G4_AIR` but has been defined with a density of $1.188 \times 10^{-11}\,\mathrm{g/cm^3}$, which corresponds to a vacuum pressure of 10^{-5} mbar ($\rho = P/(R^{\mathrm{air}}_{\mathrm{spec}} T)$). The walls and roof of the chamber was made from 25 mm aluminium (`G4_Al`) whereas the base was made of 35 mm stainless steel (`G4_STAINLESS-STEEL`). In the actual experiment, the frame of the chamber was in fact made entirely of steel. However, the attached aluminium covers/doors meant that the majority of the inner surface area was aluminium and so, with the exception of a steel floor, the chamber was modelled to be entirely aluminium in order to simplify the construction of the chamber in GEANT4.

The breadboard was a 30 mm aluminium (`G4_Al`) plate. The chamber itself, sits on a 30 mm aluminium (`G4_Al`) rack approximately 500 mm above the raised floor.

To reduce complexity and minimise the number of computations required, only a portion of the vacuum chamber was modelled. This consisted of the bulk elements in the chamber which were downstream of the interaction point where electrons would be generated. Other components in the chamber which were not modelled include optics, cables and flanges.

6.2.3 Electron spectrometer

For simplicity, the electron spectrometer was modelled as a uniform magnetic field constrained to a volume of similar dimensions to the space between the permanent magnets used in the CALA experiment. Hence, a cuboid of dimensions $(800 \times 150 \times 40)$ mm was constructed with same vacuum material as used in Section 6.2.2. The field value used was the approximate value at the centre of the magnets of 0.85 T. Previous measurements of the electron beam showed the divergence ranged between 1 mrad to 2 mrad, which for a distance of approximately 3 m between the end of the magnets and the interaction point (the position at which the initial electron beam is created), gave a beam diameter much less than the acceptance width of the spectrometer (40 mm). Hence, direct bombardment of the magnets would not be expected from a beam with stable pointing. This allowed the omission of the magnet geometry in the simulation.

6.2.4 X-ray camera and shielding

The housing for the X-ray camera consisted of a 10 mm thick aluminium (`G4_Al`) shell in the shape of a cube with a 100 mm diameter circular aperture, whose centre was suspended 300 mm above the breadboard. The aluminium layer was surrounded by a 5 mm thick layer of lead (`G4_Pb`) with a 38 mm circular aperture concentric to the aluminium aperture for the camera to image through. The lead layer extended down to the breadboard and represents the lead sheeting which was used to wrap around the aluminium cube in the CALA experiment. At the base of the GEANT4 aluminium cube, on the side facing upstream, was a 50 mm thick lead layer to mimic lead bricks also used for shielding. This whole assembly was then shifted 220 mm transversely and rotated 45 ° to allow for an on-axis beam to propagate past the detector unhindered.

The camera itself was not included in the simulation due to the lack of details available such as the material of the camera housing and component geometry in the camera. For information concerning the detection of particles, see Section 6.5.

6.3 Modelling Physical Processes

6.3.1 Tracking of particles

After creating a simulation geometry for particles to propagate and interact in, some framework is required to track the evolution of particles in the simulation. This is done in GEANT4 by using the a class which stores information for a given instance of a particle at some point in space (or time for stationary particles) and is called a *track*. Changes in a track are executed by objects called *processes*, with each process representing a different interaction, such as the energy loss of electrons due to ionisation as they travel through a material. As such, the user can make specific types of particles be affected only by certain processes. The list of processes and the particles they are associated with can be assembled by hand or using precompiled lists (c.f. Section 6.3.2).

The changes themselves take place over a *step*. Depending on the interaction, the change can occur during the step or at the end of a step. Multiple steps can be seen in Figure 6.1 as represented by yellow dots along the trajectories of the particles, most notably in the electron track (red path) between the chamber and the floor.

At the beginning of a step, each physical process proposes a length for the particle to travel. This *step size* is calculated by randomly sampling from a distribution based on the mean free path of the interaction and the process returning the smallest step size determines the limiting process for that step.

Once the limiting process (or processes) for a given step is determined, the properties of the primary particle is updated and any particles created during the step are added to a list for future tracking. The variables used to calculate the next step size are then recalculated since they may depend on the particle energy or the material, in the case that the particle has propagated to a new volume. Through consecutive iterations of this procedure, the particle is tracked to zero kinetic energy (or annihilation). This process is then applied to each particle created. A more detailed summary of the stepping

algorithm can be found in [126].

6.3.2 Physics list

To model the physical processes involved in the simulation, a pre-packaged *physics list* named `G4EmStandardPhysics_option4` was used, which contains details of all the models and cross sections describing potential interactions between particles. More specifically, the electromagnetic processes from this list were employed as it combines the most accurate models from the available standard physics lists across the full energy range (from 100 eV to > 100 GeV) [127].

The remaining processes were taken from a *reference physics list*—physics lists which have been rigorously tested and validated against experimental data—called `QGSP_BIC`, which is often used in medical applications [127].

6.3.3 Step size

As mentioned above, a step consists of a particle being propagated through space and time, during which a physical process can occur, modifying the state of the particle. Any secondary particles which may be created as a result of the process are introduced at the end of the step.

The size of each step can play an important role in dictating the accuracy of simulations and for the most part, does not require user intervention since GEANT4, by default, calculates recommended step sizes for each process. The method of using a distribution dependent on the mean free path as described previously is used for many processes, but is not applicable for all processes. For instance, in the case of the continuous energy loss of charged particles traversing a material, the cross sections are dependent on energy, implying that a very small step size is required in order for the cross sections to remain approximately constant over the step. One of the solutions used in GEANT4 is to choose a step size such that the stopping range does not change by

more than 20% over the step, which provides a reasonable compromise between accuracy and computation time [128].

The user is also able to implement a custom step size limit for cases where the calculated step size may be too large, for instance, if the detector geometry is small in comparison to the proposed step sizes. This can potentially lead to poor angular distributions of transmitted beams and it is recommended that a maximum step size is chosen such that multiple steps occur in each volume.

For the simulations below, a `G4UserLimits` has been assigned to each volume in the simulations which constrains the step size to be less than 300 mm in air and vacuum, and 0.5 mm in all other materials. The latter was chosen to account for the smallest material thickness in the simulation, which is 1 mm for the steel floor plate. This ensures multiple steps take place in each volume and should improve simulation accuracy. The constraint in air and vacuum was relaxed since the number of processes which would be expected in these low density materials is significantly lower than the other solid components, thus reducing the computational load.

6.3.4 Cut in range

In Section 6.3.1, the creation of particles invoked by processes was mentioned. In relation to this is the idea of a *cut in range*, or *range cut*, and refers to a limit imposed by GEANT4 to inhibit the generation of low energy secondary particle. This is important in processes for which the (differential) cross section increases as the energy of the secondary particle decreases, leading to the creation of many low energy particles—known as the problem of infrared divergence [126].

The cut in range can be related to the *stopping range* R of particles such as electrons and positrons, which is the mean distance the particle will travel before losing its kinetic energy. For photons (which have no defined range), the cut in range relates to the *absorption length* defined as $L_{\text{abs}} = 5/\sigma_{\text{abs}}$, where σ_{abs} is the sum of the cross

sections of the photoelectric effect, Compton scattering and pair production. The analogous concept of range for photons is the distance over which there is a high probability P_{abs} that a photon will undergo an interaction which reduces its energy—$P_{\text{abs}} = 1 - \exp(-L_{\text{abs}}\sigma_{\text{abs}}) = 1 - \exp(-5)$. It should be noted that the concept of a length is used instead of an energy as the limiting quantity for the creation of particles in GEANT4, because it emphasises accuracy of spatial deposition in some geometry as opposed to accuracy of energy deposition in each material [128]. Additionally, the idea of a range is more intuitive for many processes such as particle decay.

GEANT4 automatically converts the range cut to a *production threshold*—not to be confused with the energy threshold for processes such as the photoelectric effect—for each combination of particle and material used in the simulation. The production threshold is the energy limit below which there is no discrete production of secondary particles. However, to maintain the accuracy of simulations, energy loss due to the creation of low energy secondaries is treated as a continuous process, without adding any secondary particles to the simulation. This contrasts with energy loss due to the creation of secondaries whose kinetic energy is above the production threshold, whereby energy is removed from the primary particle in discrete steps.

The cut in range is highly recommended to be equal for all parts of the simulation geometry and has a default value of 0.7 mm, but it can be redefined by the user to suit their applications. To choose a sensible value for the cut in range, the table of production thresholds was generated at different cut values. Table 6.1 shows these thresholds for electrons and photons when interacting in aluminium and lead.

Since the X-ray CCD used in the experiment was sensitive between approximately 0.1 keV to 20 keV (quantum efficiency above 10%), it was intuitive to choose a range cut such that the production threshold was at the lower limit of the camera detection range of 0.1 keV. The table clearly shows that the default cut value of 700 µm would be insufficient to accurately model the physical processes in the energy range of interest. However, it was found that there is a significant trade-off in the number of core hours

Table 6.1: Production thresholds of photons and electrons for aluminium and lead for various values of the range in cut. The default minimum production threshold was reduced from 990 eV to 100 eV.

Range in Cut [µm]	Production Threshold [keV]			
	Photons (`gamma`)		Electrons (`e-`)	
	Al	Pb	Al	Pb
0.5	0.10	0.10	0.32	2.24
1.0	0.10	1.22	1.09	6.60
5.0	0.10	3.69	15.9	38.3
10.0	0.10	5.98	34.4	58.0
50.0	1.69	18.2	87.1	153.7
700.0 (Default)	5.84	94.8	464.2	1007

required when reducing the range in cut. For instance, earlier simulations showed that a run of 10^5 initial electrons and a cut in range of 0.5 µm required 10 hours to simulate compared to a run with a cut in range of 50 µm which took just 40 minutes. A value of 1 µm was chosen as an acceptable compromise for the range in cut for the simulations shown below. This implies that the secondary photons created through processes such as bremsstrahlung would have an energy no less than 0.1 keV in aluminium and 1.2 keV in lead. For secondary electrons, the initial kinetic energy would be no less than 1.1 keV in aluminium and 6.6 keV in lead.

In addition to specifying the cut in range, there was a default minimum for the production threshold which required overwriting. This was changed from 0.99 keV to 0.1 keV and was applied during the generation of production thresholds shown in Table 6.1.

6.4 Particle Generation

As mentioned in Section 6.2.2, only components of the geometry which lie downstream of the interaction point were simulated. The beam of high energy electrons were created at the edge of the simulation box at the start of each run to be tracked.

A number of options were available when creating the beam, allowing customisation of the direction, position, energy and particle type. For further flexibility, the class `G4GeneralParticleSource` was used, which allowed some of these properties to follow a pre-defined distribution or a custom user-defined distribution. As an example, the energy could be set as a Gaussian distribution with a specified mean and standard deviation.

Using the calibrations of the electron spectrometer in Munich, as calculated by Hao Ding of LMU, a simple model of the electron beam produced by the laser wakefield interaction was constructed in GEANT4. This consists of a triangular energy distribution with a maximum at 200 MeV which linearly decreases to 0 at 300 MeV. This distribution was chosen since the shape approximately matches with a large proportion of the measured spectra from Munich. The energy range was chosen to be within the variation of energies in the experiment which had peaks between 150 MeV and 250 MeV. There was also some variation to the energy spread, but for the purposes of this study, the parameters described here should be acceptable to simulate a *typical* beam produced during the experiment. An example of the energy distribution of a beam generated in GEANT4 is shown in Figure 6.2 alongside some sample spectra taken during the experiment. The figure has been scaled for ease of comparison.

A comparison of the suggested step size and cut in range described in this section has been compared with smaller values is shown in Section 6.9.

6.5 Particle Detection

One could in principle model the camera geometry exactly and then track the energy deposited in the detector in order to simulate the detection of particles [129]. The procedure can be further refined to account for effects after the creation of electrons in the detection region such as diffusion and recombination as they are collected, providing a better model to compare with experimental results [130]. These strategies involve the

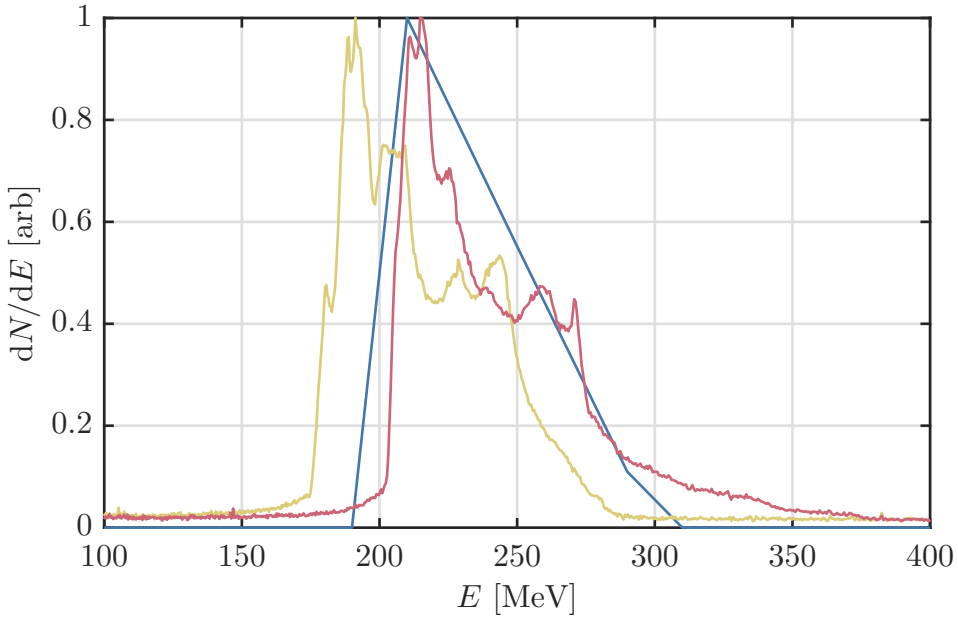


Figure 6.2: Comparison of electron energy spectrum used in GEANT4 (blue) and as measured in experiment (red and yellow). The spectra have been scaled for comparison.

creation of GEANT4 *sensitive detectors*, allowing more information to be extracted from each particle reaching the designated sensitive detector volume such as the change in particle properties at each step while the particle traverses the sensitive detector region.

This study used a simpler approach, whereby the number of particles entering the CCD was tracked, along with their respective energies. This was achieved through the use of a *scorer*, which tracks particles passing through a specified volume. This volume can be split into multiple cells to measure the same quantities in each cell. A number of details can be obtained from using scorers such as the number of steps taken and number of secondaries generated in the volume. There are a number of in-built *primitive* scorers which can be used to measure basic quantities. A more detailed description of scorers can be found in [127]. Through the rest of this work, the term *scorer* refers to the object which performs the measurement, while a *score* refers to the measurement itself.

The primitive scorer `G4PSFlatSurfaceCurrent` was used which counts the number of particles entering and/or leaving the $-z$ face of the volume (the side closest to the incident beam) per unit area [126]. Only the particles entering the volume were counted

since particles leaving the volume would necessarily have travelled through the bulk camera material which was not modelled. It was also possible to specify the type of particle to track and as such, a different scorer was created to track electrons and photons separately.

Another capability of these scorers is to add an energy filter. Therefore, a spectrum can be measured by creating multiple filters for the same particle type. The filters used in this work were chosen to measure spectra between 0 MeV and 100 MeV with bin widths increasing from 2 keV at low energies to 10 MeV at high energies.

The size of the scorer used in simulation was chosen to span the full width and height available inside the aluminium cube which houses the X-ray CCD leading to a scorer with a (180×180) mm area. Longitudinally, the scorer lies in the approximate position of the CCD chip. The scorer was split into a $100 \times 100 \times 1$ cell array to reveal spatial information of incident particle tracks.

A significant advantage of using the in-built scorers is the reduced complexity in setting up a simulation since the user is not required to create additional class definitions and scorers can be created at run time. It should be noted that a primitive scorer exists which can track energy deposition in a volume. However this has not been used since other details of the detector geometry would be required in order to get an accurate measure of the energy deposited in the photosensitive layer. Instead, a simple measure of the number of particles reaching the CCD was tracked in order to assess the shielding efficiency.

6.6 Comparison to Experiment

Several simulations were run using the setting described above as the default setup. In order to compare the quantities measured in a simulation with experimental measurements, a scaling factor was used which varies with the number of simulated electrons. For instance, a simulation with 10^5 electrons could be used to replicate the results from

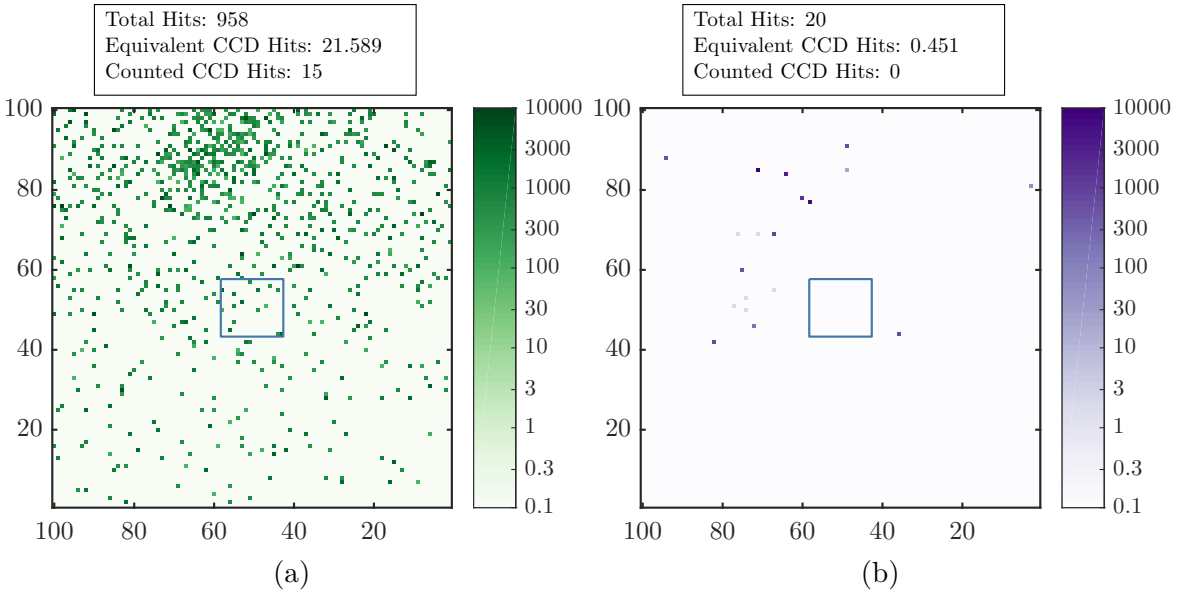


Figure 6.3: GEANT4 simulation of 10^5 electrons. (a) shows the score for photons with energy between 0 MeV and 100 MeV; (b) shows the score for electrons with energy between 0 MeV and 100 MeV. The maximum step size is 0.5 mm and 30 mm in solids and gases, respectively. The cut in range is set to 1 µm.

a typical experimental electron beam of 200 pC (200 pC/e = 1.25×10^9 electrons) by applying a scaling factor of 1.25×10^4 to the simulation measurements.

For a simulation where 10^5 electrons were generated and propagated through the geometry as described in Section 6.3.1, the scorer detected a large number of photons with energies in the few 100 keV range and a few low energy electrons on the order of 1 keV. Figures 6.3(a) and 6.3(b) show the captured hits of photons and secondary electrons, respectively. The colour scale represents the energy of each hit in units of keV. Multiple hits in a single cell have been summed.

The rectangle in the centre of the score represents the actual size and approximate position of a CCD chip ((28.1 × 25.9) mm for Andor DO432-BN-DD) relative to the scorer. If the distribution of hits across the score is homogeneous, then the number of particles incident on the CCD rectangular area can be better approximated by scaling the total number of hits across the score according to the relative areas of CCD chip size and scorer size. This is particularly useful in scenarios when the total number of hits is low, leading to a large variance in the number hits in the CCD area from simulation

to simulation. Such a strategy is useful, for example, in Figure 6.3(b) where averaging over the whole score gives approximately 0.5 electrons for an input beam of 10^5 incident particles in contrast with the 'Counted CCD Hits' of 0. For the Figure 6.3(a), the hits are clearly more heavily distributed to the top of the score, so the absolute number of hits in the CCD area should be used.

Using the scaling factor for 10^5 simulated electrons mentioned above, the scaled number of photons traversing the CCD area after shielding for a 200 pC beam is 1.9×10^5, whereas the scaled number of electrons is 5.6×10^3. Upon closer inspection of the data, it was found that no photons were in the 0 keV to 20 keV sensitive range of an X-ray CCD. There were 7 electrons in this same range, however, 6 of these were below 2 keV.

The total spectrum of combined photon and electron energies is shown in Figure 6.4. The spectrum has been scaled by a factor of 10 in order to be compared with another simulation using 10^6 electrons instead. This simulation was performed in an attempt to obtain better estimates of the particle fluxes caused by a 200 pC electron beam. There are a number of peaks visible in the figure—the largest peak above 2 keV can be found in the 70 keV to 80 keV energy range, followed by another peak at approximately 500 keV, both of which are due to gamma rays reaching the scorer. Although it is not possible to track the history of particles reaching the primitive scorer, it would make sense that the peaks are due to the lead K_{α_1} line emission at 75 keV and gamma radiation from electron-positron annihilation (511 keV). The peak at low energy between 0 keV to 20 keV is comprised mainly of low energy electrons in both simulations.

Shown in Figure 6.5 are the scores for photons and electrons for the simulation of 10^6 initial electrons. The number of photons incident on a CCD, scaled for a 200 pC beam, is 1.5×10^5, compared to the value of 1.9×10^5 from 10^5 initial electrons while the number of electrons incident is 5.1×10^3 for 10^6 initial electrons. The spatial distribution of particles reaching the scorer is more evident from using a larger number of initial electrons. Notably in Figure 6.5(b), there is a relatively large number of low energy electrons to the northwest of the CCD rectangle. Above this is a number of higher

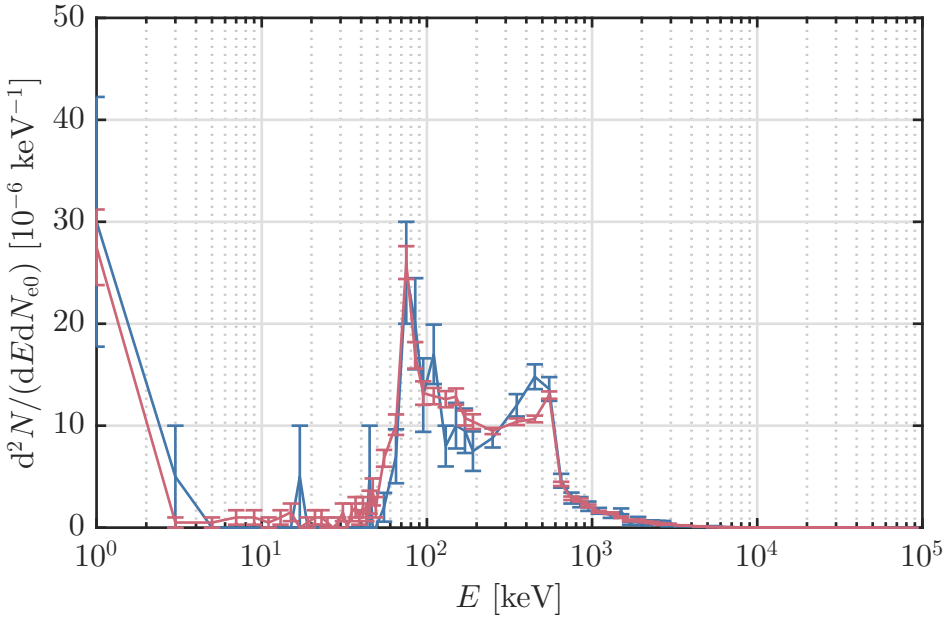


Figure 6.4: Comparison of energy spectra of scored particles from GEANT4 simulations of 10^5 (blue) and 10^6 (red) initial electrons. Units are in number of particles per keV per 10^6 initial electrons.

energy electrons which seem to coincide spatially with a large number of gamma rays as can be seen in Figure 6.5(a). In this simulation, there was 1 photon with an energy less than 20 keV, more specifically, in the 12 keV to 14 keV range, and 59 electrons less than 20 keV, with most of these being less than 4 keV and in the local area mentioned previously.

As well as a higher density of hits towards the top half of the score for photons, an interesting feature is the concentration of photon and electron hits slightly left of centre near the top of the score. This is due to a direct line of sight from the scorer, through the aperture in the shielding to the area of contact between the initial beam and the breadboard. The hits that can be seen outside of the spot region is due to either the transmission of particles which have survived propagation through the aluminium and lead, or some interaction occurring in the shielding which produces photons and electrons in the direction of the scorer. The reduced number of hits below row 60 can be attributed to the lead brick layer at the base of the camera array as described in Section 6.2.4, causing additional attenuation.

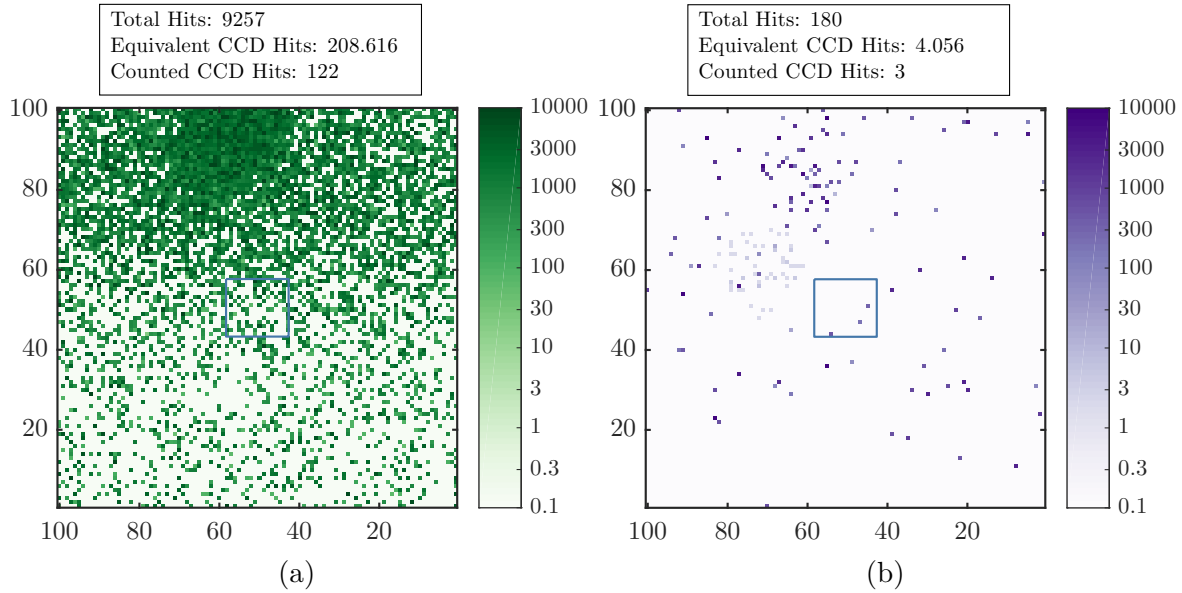


Figure 6.5: GEANT4 simulation of 10^6 initial electrons. (a) shows the score for photons with energy between 0 MeV and 100 MeV; (b) shows the score for electrons with energy between 0 MeV and 100 MeV. The maximum step size is 0.5 mm and 30 mm in solids and gases, respectively. The cut in range is set to 1 µm.

As a reference, Figure 6.6 shows the scores as produced by a simulation of 10^5 initial electrons but without the aluminium cube and lead shielding surrounding the scorer. A much more uniform distribution of hits can be seen here, but there is a slight gradient in the vertical direction again, with more hits towards the lower end of the score. Scaling the simulation results, again to estimate an equivalent 200 pC beam, results in 3.7×10^6 photons and 8.4×10^4 electrons arriving in the CCD area. A qualitative comparison with the bright spot in the 10^5 shielded case (Figure 6.3) suggests that the density in the spot is roughly equal to density over the full score in the unshielded case. Hence, any inaccuracies in the simulated geometry positions may cause a slight change in the position of the spot and introduce a discrepancy between the computed score and an experimentally captured signal. For the calculations presented below, it is assumed the geometry was sufficiently well-modelled such that the spot region does not affect the distribution of hits over the CCD region.

It was possible to identify the dominant source of the scored photons and electrons by comparing the spectrum of Figure 6.4 with spectra obtained from simulations with a

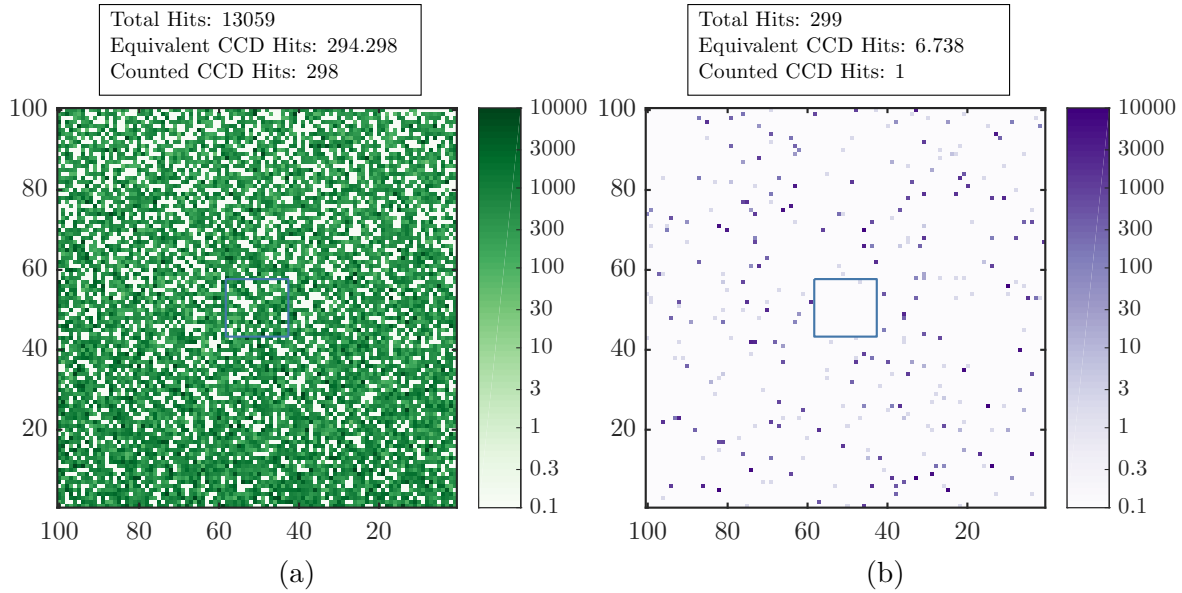


Figure 6.6: GEANT4 simulation of 10^5 initial electrons and no aluminium or lead shielding. (a) shows the score for photons with energy between 0 MeV and 100 MeV; (b) shows the score for electrons with energy between 0 MeV and 100 MeV. The maximum step size is 0.5 mm and 30 mm in solids and gases, respectively. The cut in range is set to 1 µm.

fewer chamber elements. Figure 6.7 reveals that the breadboard—the first component interacting with the initial electron beam after being steered by the magnets—contributes slightly towards the the total energy spectrum as indicated by the yellow line. In this simulation, the only elements included in the geometry were the electron spectrometer, the aluminium camera housing, the lead shielding and the aluminium breadboard. By also including the steel chamber floor, the resulting energy spectrum as shown by the red line, can be seen to be very similar to the original simulation which models the full chamber geometry. Hence it can be said that the majority of scored hits are due to bremsstrahlung photons created in the steel layer and, to a lesser extent, the aluminium breadboard. There is essentially no contribution from other chamber components.

It is evident from these simulations that the shielding, as modelled, does not fully prevent ionising radiation from reaching the detector. The source of the ionising radiation, in this case, results primarily from high energy electrons bombarding the steel chamber floor. It is instructive to compare the simulation with experimental data and is addressed

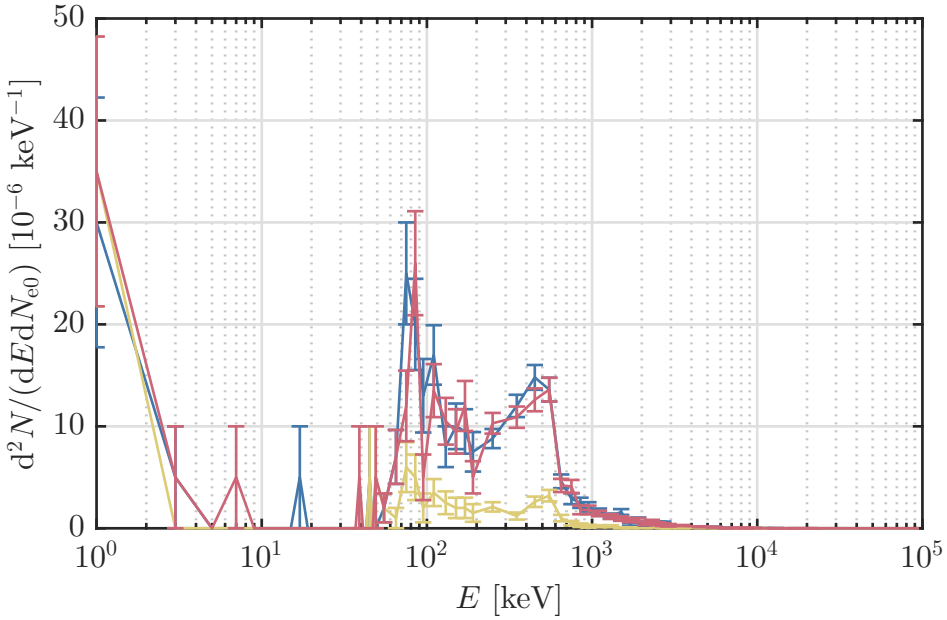


Figure 6.7: Comparison of energy spectra of scored particles from GEANT4 simulations of 10^5 initial electrons with: the full geometry (blue) (c.f. Section 6.2); the breadboard only (yellow); and the breadboard and chamber floor only (red). The aluminium cube and lead shielding is included in each simulation. Units are in number of particles per keV per 10^6 initial electrons.

in the next section.

6.7 Estimation of Detected Particles

It is currently not trivial to accurately model the response of a detector using GEANT4 to incident radiation. Bespoke software exists [131] to simulate the detection process accounting for effects that are not readily incorporated in GEANT4 such as the electronic noise contribution due to amplification of collected charge during the readout phase of a CCD. Instead, the emphasis is placed on retrieving the quantity of particles incident on the detector and an estimate of 'detected particles' is obtained as described below.

As shown in the previous section, the majority of particles reaching the CCD region in the GEANT4 simulations are gamma rays in the few hundred keV range. At these energies, photoionisation in silicon is improbable and instead, the total photon cross section is dominated by Compton scattering. The differential cross section of a photon

scattering from a single free electron is given by the Klein-Nishina formula [132]

$$\frac{\mathrm{d}\sigma}{\mathrm{d}\Omega} = \frac{r_\mathrm{e}^2 f(E_{\gamma 0},\theta)^2}{2}\left[f(E_{\gamma 0},\theta) + f(E_{\gamma 0},\theta)^{-1} - \sin^2\theta\right], \tag{6.1}$$

where r_e is the classical electron radius, $E_{\gamma 0}$ is the initial photon energy, θ is the angle of between initial direction and scattered photon direction. The function f is the ratio of final photon energy E_γ to initial photon energy $E_{\gamma 0}$

$$f(E_{\gamma 0},\theta) \equiv \frac{E_\gamma}{E_{\gamma 0}} = \left[1 + \frac{E_{\gamma 0}}{m_\mathrm{e}c^2}(1-\cos\theta)\right]^{-1}. \tag{6.2}$$

In the backscattering case, where $\theta = \pi$, the gamma ray recoils with energy $E_{\gamma,\min} = E_{\gamma 0}/(1 + 2E_{\gamma 0}/m_\mathrm{e}c^2)$. For the case of $E_{\gamma 0} = 100\,\mathrm{keV}$, the minimum scattered photon energy is $\sim 72\,\mathrm{keV}$ which still has a very low quantum efficiency in a silicon detector. On the other hand, it would be possible for the Compton-scattered *electrons*, which have energy $E_\mathrm{e} = E_{\gamma 0} - E_\gamma$, to be absorbed and detected in the chip. To find an estimate of the expected number of detected electrons, tables for the electron stopping power and range in silicon as provided by NIST [133] were used. For silicon with a density of $2.33\,\mathrm{g/cm^3}$, the average path length, or range R, will equal the typical thickness for a back-illuminated deep-depletion chip of $50\,\mu\mathrm{m}$ when the electron energy is $77\,\mathrm{keV}$. We denote this value by $E_{\mathrm{e},R}$ which is an approximation for the maximum energy an electron can have while being fully absorbed—through ionisation or otherwise—in an X-ray CCD.

It is clear from (6.2) that the polar angle θ can be expressed in terms of the scattered photon energy E_γ, allowing the differential cross section to be rewritten in terms of E_γ

$$\frac{\mathrm{d}\sigma}{\mathrm{d}\Omega} = \frac{r_\mathrm{e}^2}{2}\left(\frac{E_\gamma}{E_{\gamma 0}}\right)^2\left(\frac{E_\gamma}{E_{\gamma 0}} + \frac{E_{\gamma 0}}{E_\gamma} - \left\{1 - \left[1 - \left(\frac{1}{E_\gamma} - \frac{1}{E_{\gamma 0}}\right)m_\mathrm{e}c^2\right]^2\right\}\right). \tag{6.3}$$

The differential cross section as a function of polar angle and scattered photon energy is plotted in Figure 6.8(a) and Figure 6.8(b), respectively, for multiple initial photon

energies. The transition from the low-energy limit, corresponding to classical Thomson scattering as shown in black, to Compton scattering for 100 keV (green), 300 keV (yellow) and 1 MeV (red) can be seen in Figure 6.8(a).

The total cross section for the *atom* can be calculated by integrating (6.1) over the polar angle θ and azimuthal angle ϕ and multiplying by the atomic number Z

$$\sigma = Z \int_0^{2\pi} \int_0^{\pi} \frac{\mathrm{d}\sigma}{\mathrm{d}\Omega} \sin\theta \, \mathrm{d}\theta \, \mathrm{d}\phi. \tag{6.4}$$

The change of variable for integrating over energy is performed as follows:

$$E_\gamma = E_{\gamma 0} \left[1 + \frac{E_{\gamma 0}}{m_\mathrm{e} c^2} (1 - \cos\theta) \right]^{-1}, \tag{6.5}$$

$$\frac{\mathrm{d}E_\gamma}{\mathrm{d}\theta} = -\frac{E_{\gamma 0}^2 \sin\theta}{m_\mathrm{e} c^2} \left[1 + \frac{E_{\gamma 0}}{m_\mathrm{e} c^2} (1 - \cos\theta) \right]^{-2}, \tag{6.6}$$

$$\Rightarrow \sin\theta \, \mathrm{d}\theta = -\frac{m_\mathrm{e} c^2}{E_\gamma^2} \, \mathrm{d}E_\gamma. \tag{6.7}$$

Hence, the total cross section is calculated from

$$\sigma = 2\pi Z \int_{E_{\gamma,\min}}^{E_\gamma 0} \frac{\mathrm{d}\sigma}{\mathrm{d}\Omega} \frac{m_\mathrm{e} c^2}{E_\gamma^2} \, \mathrm{d}E_\gamma. \tag{6.8}$$

If we replace the lower limit $E_{\gamma,\min}$ with $\max(\{E_{\gamma,\min}, E_{\gamma 0} - E_{\mathrm{e},R}\})$, then evaluating the integral of the differential cross section—which we call σ_R—gives a quantity which relates to the probability that there will be a Compton event in which the scattered electron has an energy E_e between 0 and $E_{\mathrm{e,max}} = E_{\gamma 0} - \max(\{E_{\gamma,\min}, E_{\gamma 0} - E_{\mathrm{e},R}\}$. Assuming all electrons up to this energy are fully absorbed, the probability $P_{\mathrm{e},R}$ that a Compton-scattered electron would be detected by an X-ray CCD can be calculated. This is done by considering the probability of survival of the corresponding incident photon after travelling through the chip. The probability of a Compton event occurring

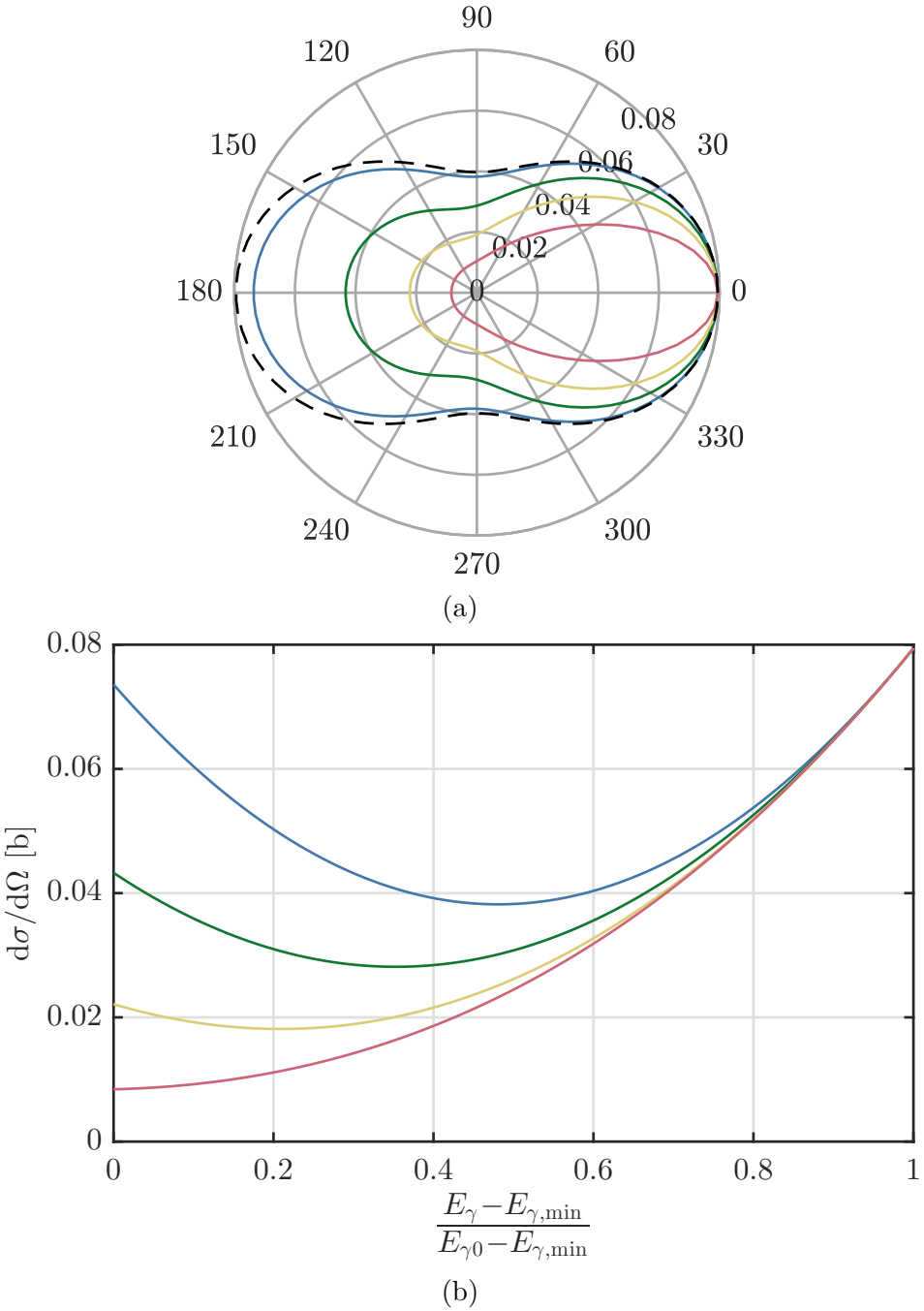


Figure 6.8: Differential cross section as a function of (a) polar angle and (b) scattered photon energy for different incident photon energies. Blue: 10 keV, green: 100 keV, yellow: 300 keV, red: 1 MeV. The black dashed line corresponds to the differential cross section for Thomson scattering.

is simply the complement of this survival probability

$$P_{\mathrm{e},R} = 1 - \exp\left[-\left(\frac{\rho N_{\mathrm{A}}}{M}\right)\sigma_R L\right], \tag{6.9}$$

where N_{A} is the Avogadro constant, M is the molar mass of the detector material, ρ is the material density and L is the material thickness. The exponential term is essentially the Beer-Lambert attenuation law with the mass attenuation coefficient calculated via $\mu/\rho = \sigma N_{\mathrm{A}}/M$. In reality, although an electron with energy above $E_{\mathrm{e},R}$ would not be fully absorbed in the chip, it would still deposit a finite and detectable amount of energy. This contribution is partially offset by the fact that many electrons will be born midway into the material, resulting in a reduced length L' for them to be fully absorbed.

A more detailed calculation can be used to better estimate the probability $P_{\mathrm{e},R}$ as follows: replace the expression in (6.9) with the integral

$$P_{\mathrm{e},R} = \int_0^L \left(\frac{N_{\mathrm{A}}}{M}\sigma(x)\right)\exp\left[-\left(\frac{\rho N_{\mathrm{A}}}{M}\right)\sigma(x)x\right]\mathrm{d}x. \tag{6.10}$$

This calculates the probability of a Compton scattering event occurring over the distance x to $x + \mathrm{d}x$ for each x, the sum of which gives the probability of a Compton event over the total length L. Note the cross section σ is now dependent on x since the lower limit of integration should be given by $\max\left(\{E_{\gamma,\min}, E_{\gamma 0} - E_{\mathrm{e},R}(x)\}\right)$ (recall the adjusted lower limit for (6.8)), where $E_{\mathrm{e},R}(x)$ is the energy of an electron with a range R equal to the *remaining path length* L_{rem} given that it originates at x.

The remaining path length varies as a function of the scattered electron angle ϕ, calculated as

$$\phi(E_\gamma) = \tan^{-1}\left[\frac{\cot\left(\theta(E_\gamma)/2\right)}{(1 + E_{\gamma 0}/m_{\mathrm{e}}c^2)}\right], \tag{6.11}$$

assuming the initial direction of the photon is normal to the face of the CCD. The remaining path length would then be given by $L_{\mathrm{rem}} = (L - x)/\cos(\phi(E_\gamma))$. A plot of $L_{\mathrm{rem}} - R$ is shown in Figure 6.9 for various values of x, assuming $E_{\gamma 0} = 100\,\mathrm{keV}$. The

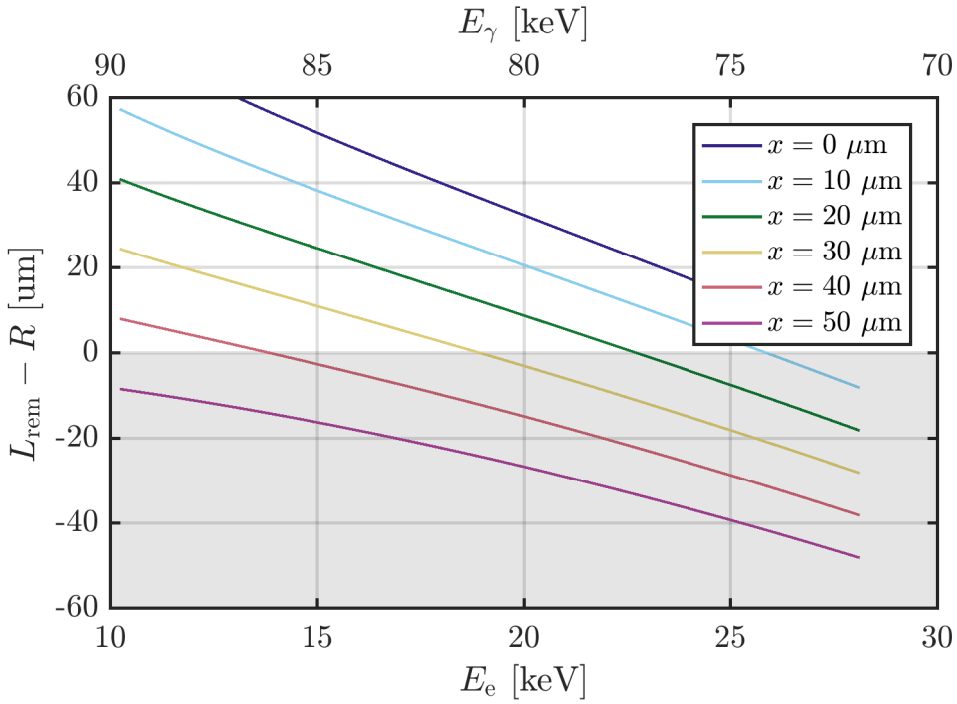


Figure 6.9: Difference of path length remaining L_{rem} and range R of an electron plotted against electron energy for different distances x into a material of total length L.

value of $E_{\mathrm{e},R}$ for a given x would then be taken as the value of E_e when the corresponding line crosses 0 µm on the y-axis.

Evaluating (6.10), however, would still not account for detection events due to electrons which are not stopped in the length $L - x$. One possible solution is to reintroduce the lower energy limit used in (6.8) ($E_{\gamma,\mathrm{min}} = E_{\gamma 0}/(1 + 2E_{\gamma 0}/m_\mathrm{e}c^2)$) and assume that every electron scattered in the material will be detected to some extent regardless of its range. For the goal set out in Section 6.1, (6.9) is used as a rough estimate of the probability of particle detection.

Using MATLAB, (6.8) and (6.9) have been evaluated through numerical integration for various values of $E_{\gamma 0}$. These results are tabulated in Table 6.2. For scattering of photons of energy 100 keV and lower, $\sigma = \sigma_R$ since the path length of the most energetic Compton-scattered electron has an average stopping range shorter than the thickness of a typical deep-depletion CCD, i.e. $R < L$.

Table 6.2: Table of cross sections σ, mass attenuation coefficients μ and probability of Compton scattering, for various photon energies. The corresponding quantities are recalculated for electrons with a range less than 50 µm in silicon and are denoted by the subscript R.

$E_{\gamma 0}$ [keV]	σ [b]	μ [cm^2/g]	P_e	σ_R [b]	μ_R [cm^2/g]	$P_{\mathrm{e},R}$
10	8.97	0.192	2.24×10^{-3}	8.97	0.192	2.24×10^{-3}
50	7.86	0.169	1.96×10^{-3}	7.86	0.169	1.96×10^{-3}
100	6.90	0.148	1.72×10^{-3}	6.90	0.148	1.72×10^{-3}
200	5.69	0.122	1.42×10^{-3}	4.73	0.101	1.18×10^{-3}
300	4.95	0.106	1.24×10^{-3}	2.43	0.052	6.06×10^{-4}
500	4.05	0.087	1.01×10^{-3}	1.01	0.022	2.52×10^{-4}
1000	2.96	0.063	7.38×10^{-4}	0.27	0.006	6.70×10^{-5}

6.7.1 Simulation calculations

Referring back to the GEANT4 simulation from Figure 6.5, an estimate for the average photon energy measured by the scorer can be used to calculate $P_{\mathrm{e},R}$. Using the number of particles in each energy bin as a weighting factor, the arithmetic mean is 920 keV, the geometric mean is 454 keV and the harmonic mean is 112 keV. The arithmetic mean must be avoided due to the large weighting assigned to high energy values. Since $P_{\mathrm{e},R}$ decreases with increasing energy, the worst case scenario can be taken by using the harmonic mean. Recalling the simulation of 10^6 initial electrons from Section 6.6, the equivalent 200 pC beam would yield approximately 1.5×10^5 photons and 5.1×10^3 electrons arriving at the CCD. Approximating the average photon energy as 100 keV, Table 6.2 shows a value of $P_{\mathrm{e},R} = 1.72 \times 10^{-3}$ meaning that of the 1.5×10^5 gamma rays incident on a 50 µm thick silicon CCD, ~ 260 Compton-scattered electrons would be generated. Thus, the number of resulting Compton electrons pales in comparison to the estimated number of electrons impinging on the CCD (5×10^3 electrons), implying that to reduce the number of events captured by a CCD under these experimental conditions, an emphasis on shielding from external electrons should be enforced. The author points out that even with 10^6 electrons in the initial beam (taking ~ 50 hours to track), very

few electrons reach the score and so the estimate for the electron flux from a 200 pC beam is prone to relatively large variations from simulation to simulation.

A number of assumptions have been made for the estimates above: The direction of the incident gamma ray is normal to the plane of the CCD. The range uses the continuous slowing down approximation (CSDA), which assumes electron energy loss at each point along its path is equal to the stopping power. Also, this range does not account for large deviations in the electron pointing as they lose energy due to, for example, Coulomb collisions. The *projected range* is thus defined as the average distance travelled by an electron before coming to a stop in the initial direction of incidence and is typically, at least in silicon, a factor of approximately 3 smaller than the CSDA range [134].

If the assumption that electrons with range larger than the remaining path length are still detected, then the value of σ can be used with the usual limits between $E_{\gamma,\min}$ and $E_{\gamma 0}$, and P_{e} can be used in place of $P_{\mathrm{e},R}$ (c.f. Table 6.2). In this instance, the estimates above remain unchanged.

Multiple scattering in a silicon CCD can also affect the estimate, potentially leading to the generation of many tertiary particles which can be detected. Additionally, other scattering processes have not been included since the energy range of the scored spectrum with the highest flux was in the Compton range. At 50 keV and below, photoelectric absorption dominates, but as mentioned above, the simulations produced little to no X-rays in this energy range. In scaling the simulations to estimate the spectrum from a 200 pC beam, small fluctuations in this low-signal range would yield an error of the order of the scaling factor, which for the 10^6 electron simulation is 1.25×10^3.

6.8 Improvements to the Shielding

The previous simulations have shown that a significant number of particles reach the CCD when using the aluminium and lead shielding described in Section 6.2. This

section shows the results of further simulations after introducing changes to the GEANT4 geometry in order to investigate their effects on the number of particles reaching the scorer.

For the following simulations, a 30 µm aluminium foil layer has been inserted in front of the scorer, which represents the shielding from optical light used during the LMU experiment. The results shown previously did not include this thin material as it was expected that the effect on highly energetic particles should be insignificant.

6.8.1 Additional aluminium shield

The effect of this shielding is demonstrated in Figure 6.11, which shows the combined spectrum of electrons and photons with and without a 30 µm aluminium light shield. The spectra can be seen to match very closely for energies above $\sim 20\,\text{keV}$. The large peak between 0 keV and 2 keV disappears when the light shield is included. This effect can easily be seen in the difference between Figure 6.3(b) and Figure 6.10(b), implying that the low energy electrons are absorbed by the aluminium sheet. This result modifies the estimate for the number of electrons impinging on the score for a 200 pC beam since the scaling now uses the average number of electrons in the CCD area of 2.3 instead of 4.1, resulting in 2.8×10^3 electrons as opposed to the previous estimate of 5.1×10^3 electrons.

6.8.2 Adding plastic layer

In order to reduce the ionising radiation which can reach the CCD, increased shielding can be incorporated. For Bremsstrahlung radiation, the emission scales with atomic mass and it is intuitive to use a material composed of light elements to slow energetic electrons slowly. Plastics are often used for this purpose [135]. One candidate material is polypropylene (C_3H_6) which would be suitable for use in vacuo since it is not hygroscopic—that is, it does not retain water from the atmosphere. It is shown in [136] that

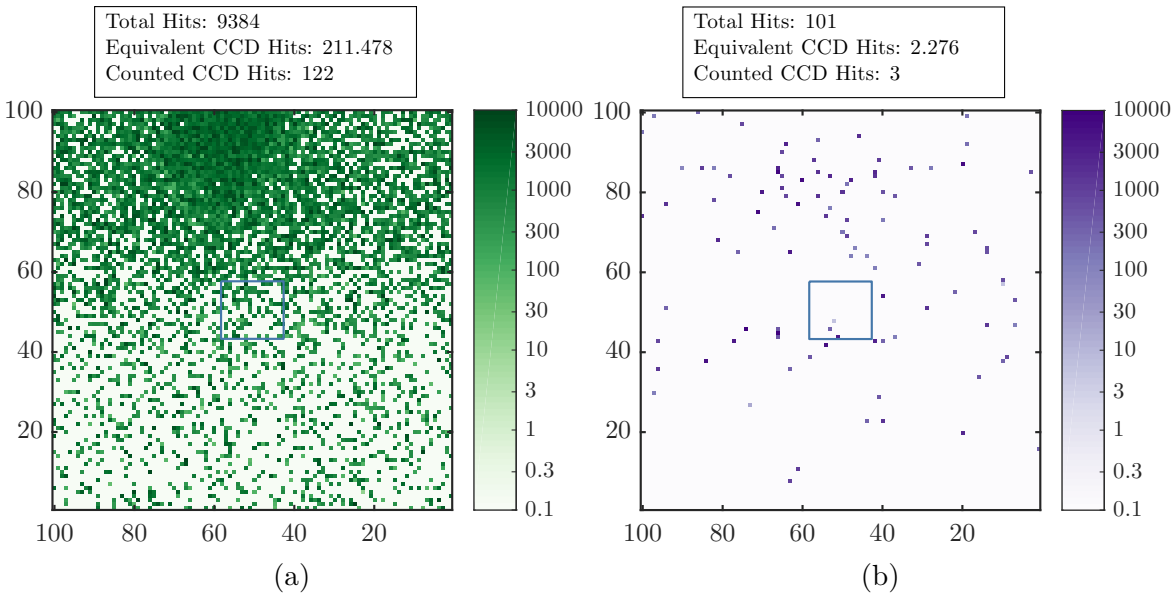


Figure 6.10: GEANT4 simulation of 10^6 initial electrons with an additional 30 µm aluminium shield. (a) shows the score for photons with energy between 0 MeV and 100 MeV; (b) shows the score for electrons with energy between 0 MeV and 100 MeV. The maximum step size is 0.5 mm and 30 mm in solids and gases, respectively. The cut in range is set to 1 µm.

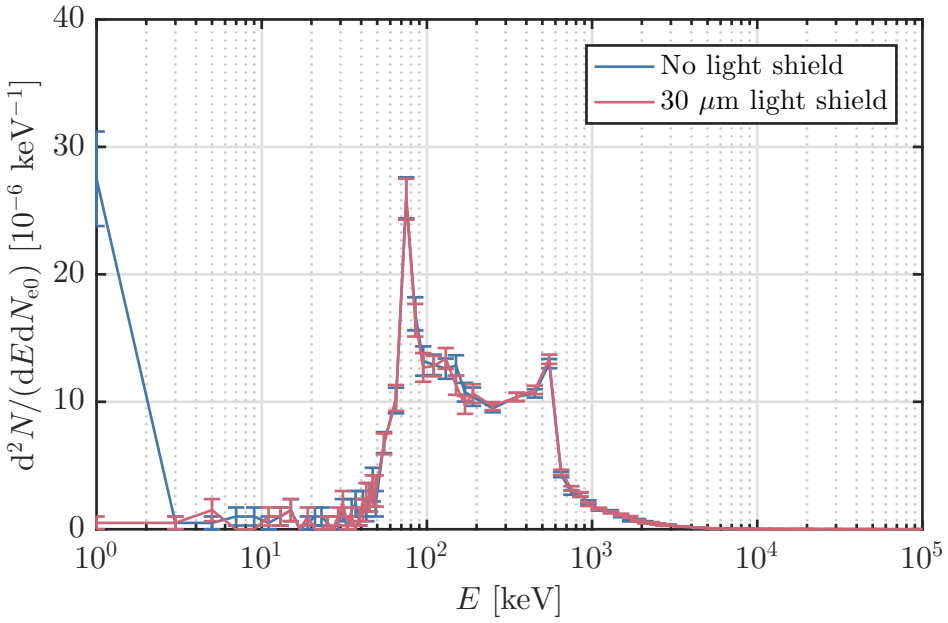


Figure 6.11: Comparison of energy spectra of scored particles from GEANT4 simulations of 10^6 initial electrons with (red) and without (blue) a 30 µm layer of aluminium in front of the scorer. Units are in number of particles per keV per 10^6 initial electrons.

polypropylene has very favourable Bremsstrahlung emission in comparison to other common plastics, but has the drawback of the maximum range of incident electrons being larger, meaning that a thicker layer of plastic is required to fully stop high energy electrons compared to a denser material such as aluminium.

Figures 6.12 and 6.13 show the effect of adding a 25 mm slab of polypropylene on top of the aluminium breadboard for a 10^6 initial electron beam. The number of photons have been reduced to approximately one third of its original number over the whole score and a half when looking at counts in only the CCD area. The number of electrons reaching the score was found to reduce to slightly more than a half over the whole score. A comparison in only the CCD area is not possible in this scenario due to the limited number of hits.

It can be seen in Figure 6.13, there appears to be a significant number of particles scored in the low energy tail of the spectrum for the case of using the plastic layer for 10^6 initial electrons as shown in yellow. However, it should be noted that this contribution was neither due to photons or electrons (and additionally was not positrons, muons, antimuons or protons). Furthermore, this spike was absent from the same simulation but with fewer initial electrons as shown in red. This could potentially be a bug in the simulation and may require further investigation to resolve.

Nevertheless, the effect of an additional layer of plastic appears to successfully reduce the flux of both electrons and photons reaching the CCD area by a factor of two when slowing the initial electron beam with a 25 mm slab of plastic. To further reduce the flux, the plastic layer could be made thicker.

6.8.3 Increasing lead shielding

Simulations were run for the case of thicker lead shielding surrounding the aluminium cube. Shown in Figure 6.14 is the photon flux when using a 10 mm sheet of lead instead of 5 mm (the lead bricks at the base are unchanged). The resulting score reveals that

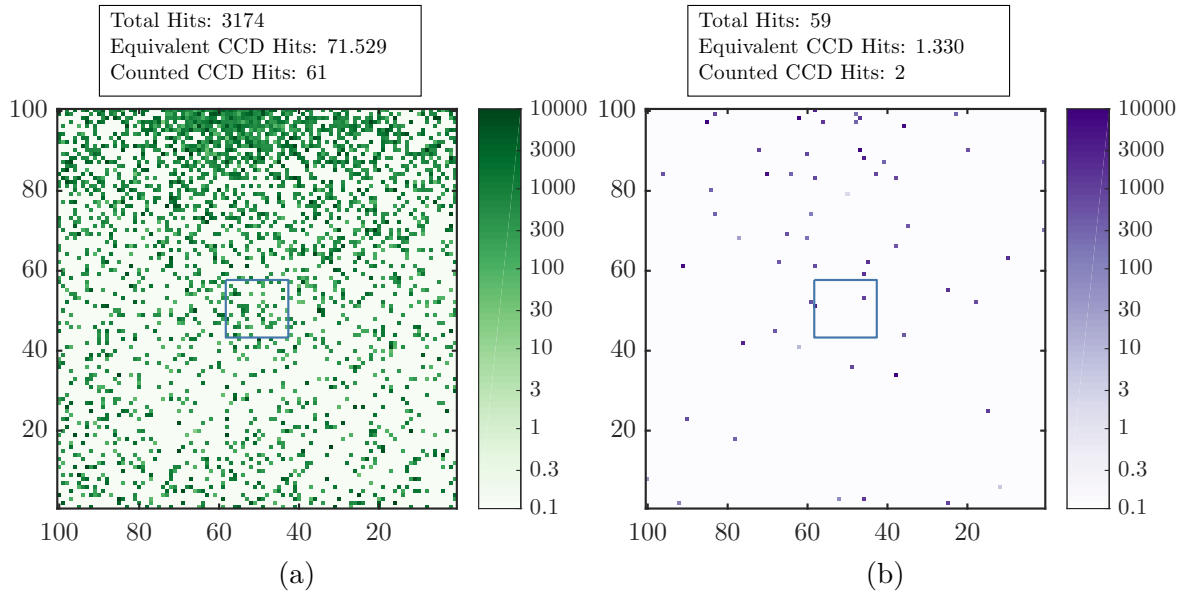


Figure 6.12: GEANT4 simulation of 10^6 initial electrons with a 25 mm plastic layer covering the aluminium breadboard and an additional 30 µm aluminium shield. (a) shows the score for photons with energy between 0 MeV and 100 MeV; (b) shows the score for electrons with energy between 0 MeV and 100 MeV. The maximum step size is 0.5 mm and 30 mm in solids and gases, respectively. The cut in range is set to 1 µm.

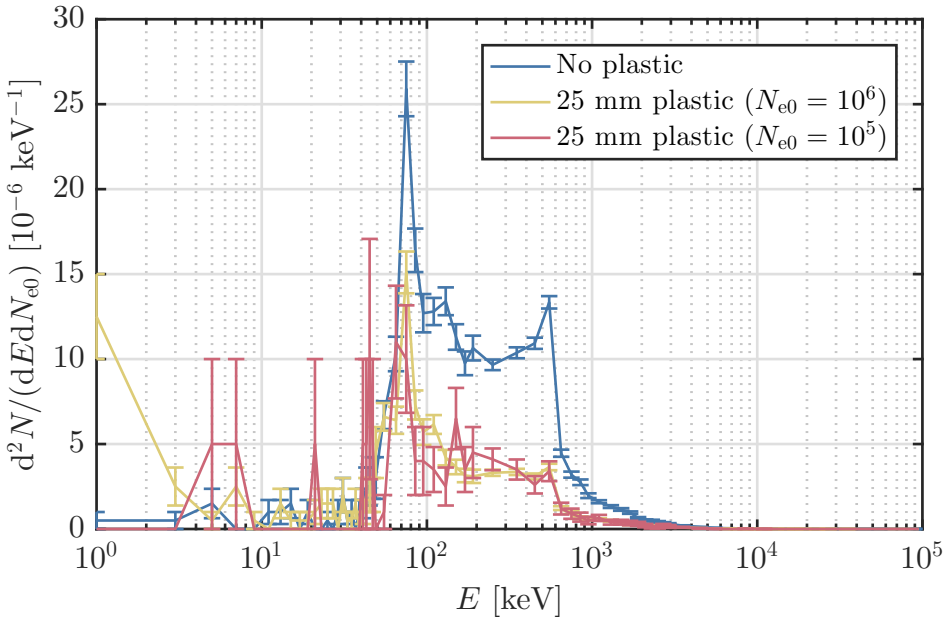


Figure 6.13: Comparison of energy spectra of scored particles from GEANT4 simulations of 10^6 initial electrons with (yellow) and without (blue) a 25 mm plastic layer covering the aluminium breadboard and an additional 30 µm aluminium shield, and 10^5 initial electrons (red) with a 25 mm plastic layer covering the aluminium breadboard and an additional 30 µm aluminium shield. Units are in number of particles per keV per 10^6 initial electrons.

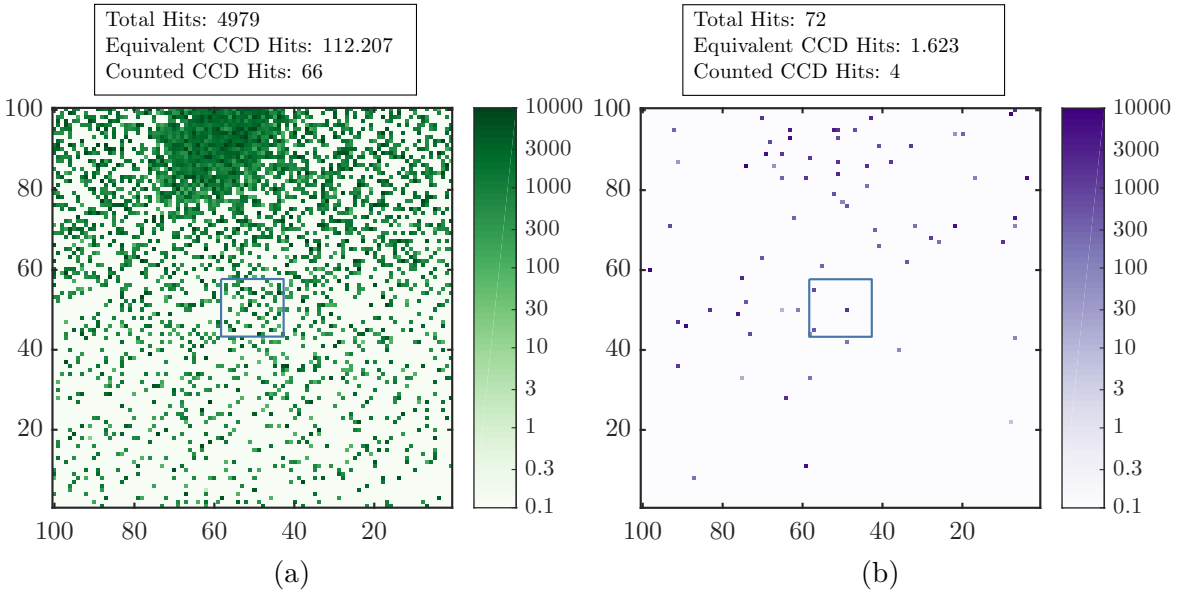


Figure 6.14: GEANT4 simulation of 10^6 initial electrons with increased lead shielding from 5 mm to 10 mm and an additional 30 µm aluminium shield. (a) shows the score for photons with energy between 0 MeV and 100 MeV; (b) shows the score for electrons with energy between 0 MeV and 100 MeV. The maximum step size is 0.5 mm and 30 mm in solids and gases, respectively. The cut in range is set to 1 µm.

the photon flux is approximately halved and the number of electrons reduced by a third. When the lead shielding is replaced with 50 mm bricks, forming a cube surrounding the aluminium cube, the flux is further reduced as shown in Figure 6.15. The total photon count drops to less than a tenth of its original number and the electron count drops to a fifth. It can be seen that the concentration of gamma rays near the top of the score disappears with this configuration. This is likely due to the acceptance angle of the aperture due to the increased width being reduced to zero as the direct line of sight from the scorer to the breadboard is blocked. Accounting for this, a comparison using only hits in the CCD area indicates the photon reduces to a quarter instead of a tenth of the 5 mm default scenario when using a 50 mm cube. The spectra of all three lead cases are shown in Figure 6.16.

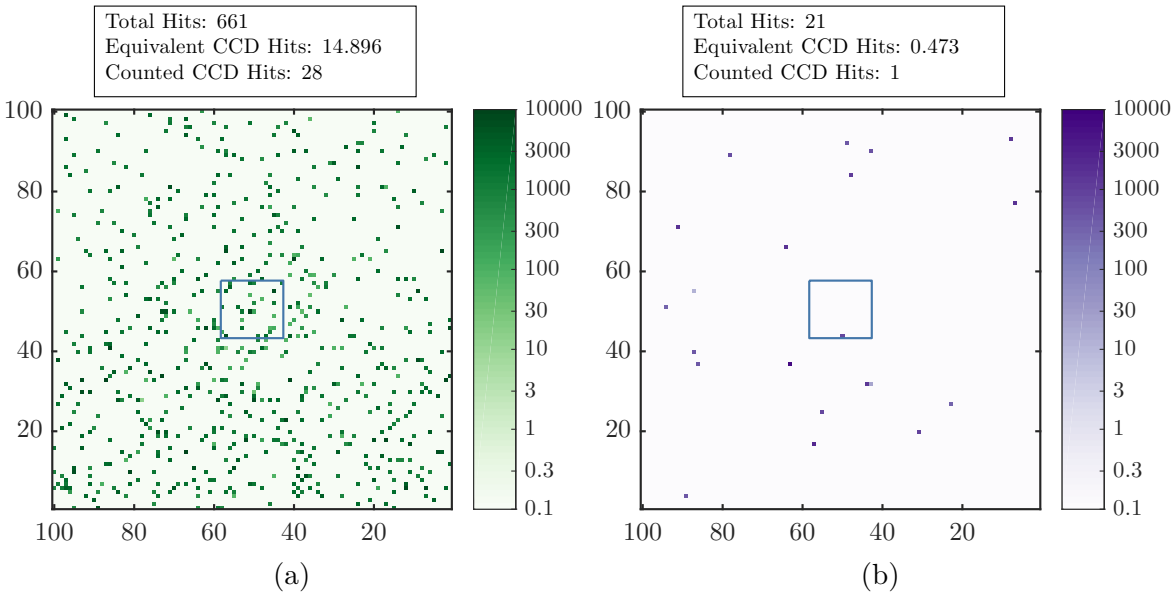


Figure 6.15: GEANT4 simulation of 10^6 initial electrons with increased lead shielding from a 5 mm layer extending to the chamber floor to a 50 mm cube surrounding the aluminium cube, and an additional 30 µm aluminium shield. (a) shows the score for photons with energy between 0 MeV and 100 MeV; (b) shows the score for electrons with energy between 0 MeV and 100 MeV. The maximum step size is 0.5 mm and 30 mm in solids and gases, respectively. The cut in range is set to 1 µm.

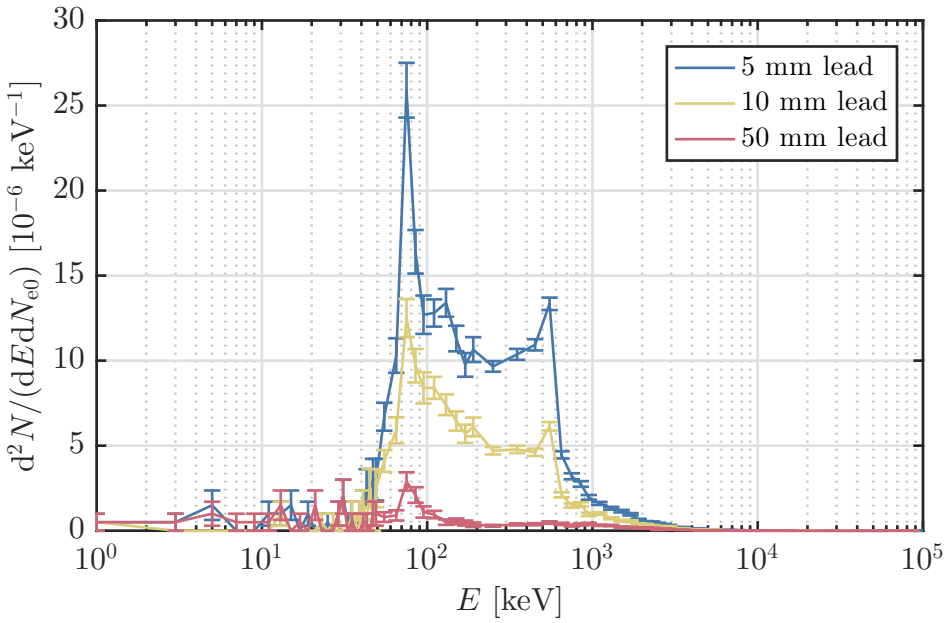


Figure 6.16: Comparison of energy spectra of scored particles from GEANT4 simulations of 10^6 initial electrons with 5 mm thick (blue), 10 mm (yellow) and 50 mm (red) lead shielding and an additional 30 µm aluminium shield. Units are in number of particles per keV per 10^6 initial electrons.

6.8.4 Discussion

From these simulations, it is evident that using a combination of plastic to slow electrons hitting the breadboard, and lead to reduce bremsstrahlung and absorb any remaining electrons, will reduce the flux of ionising radiation reaching an X-ray CCD. However, a future study would be required to optimise this geometry.

There are a number of considerations in implementing these solutions for minimising the radiation incident on a CCD in the chamber. For instance, the size of the chamber may be insufficient to house a thick layer of plastic, or there may be other diagnostics which require space on the breadboard. Increasing the amount of lead could also be problematic due to the additional weight. As such, a simpler solution may be to move the source of the ionising radiation away from the detector: If the chamber is wide, the magnets could be rotated to bend the beam horizontally, and likewise if the chamber is tall, the beam height could be increased or beam bent towards the ceiling. Another way to achieve more distance is by moving the detector further downstream or moving the magnets further upstream. The former option may not be preferable, however, due to the continuous diverging of the desired betatron radiation. An example of the electron spectrometer being moved 2 m upstream is shown in figures 6.17 and 6.18. The effect on the count rate is very similar to that of the 50 mm lead shielding case.

6.9 Validation Checks

A number of simulations were run to compare with the settings specified in Section 6.3. Specifically, higher resolution settings were used at the expense of computational time while running the first scenario shown in Figure 6.3 in order to ensure the results shown above are valid.

Figure 6.19 reveals that in simulations of 10^5 electrons, decreasing the step size from 0.5 mm to 0.1 mm resulted in a very similar spectrum (yellow) to the spectrum using the

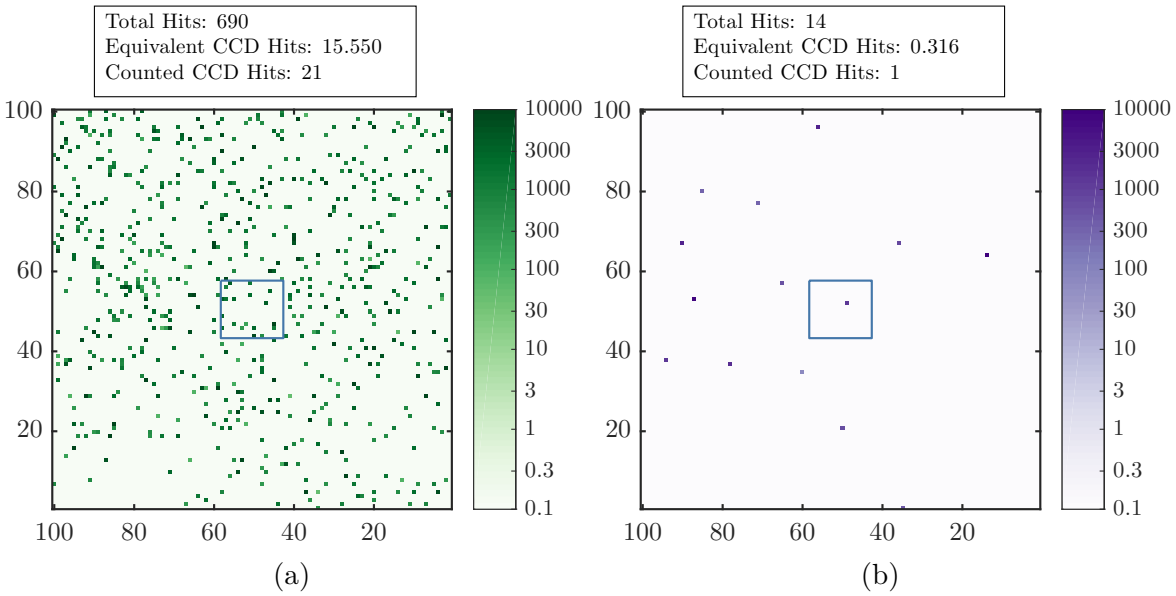


Figure 6.17: GEANT4 simulation of 10^6 initial electrons with an additional 30 µm aluminium shield. The electron spectrometer is positioned ~ 2 m upstream from the scorer compared to ~ 30 cm from previous simulations. (a) shows the score for photons with energy between 0 MeV and 100 MeV; (b) shows the score for electrons with energy between 0 MeV and 100 MeV. The maximum step size is 0.5 mm and 30 mm in solids and gases, respectively. The cut in range is set to 1 µm.

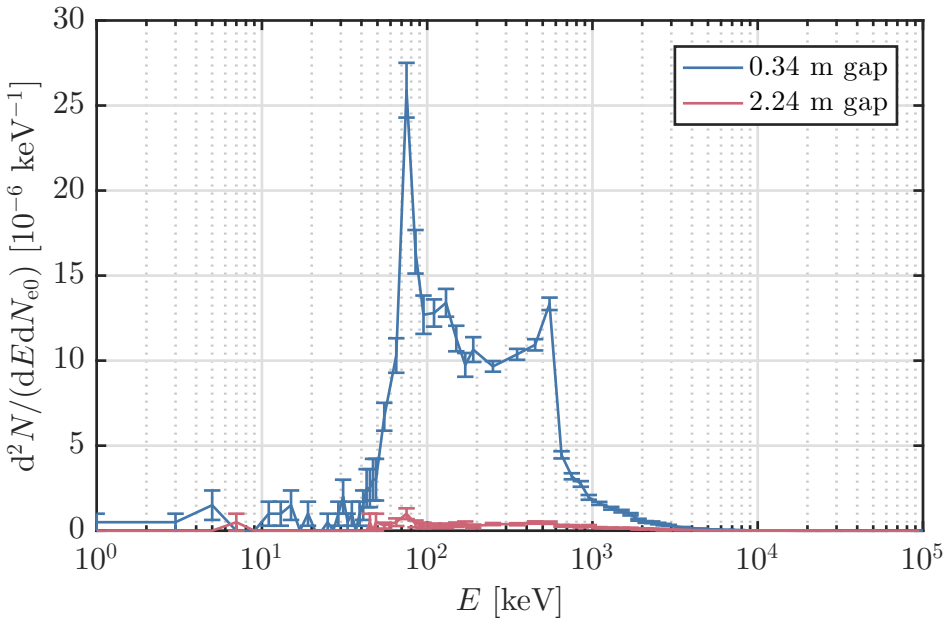


Figure 6.18: Comparison of energy spectra of scored particles from GEANT4 simulations of 10^6 initial electrons with an additional 30 µm aluminium shield. The electron spectrometer is positioned in the default position (blue) and approximately 2 m further upstream (red). Units are in number of particles per keV per 10^6 initial electrons.

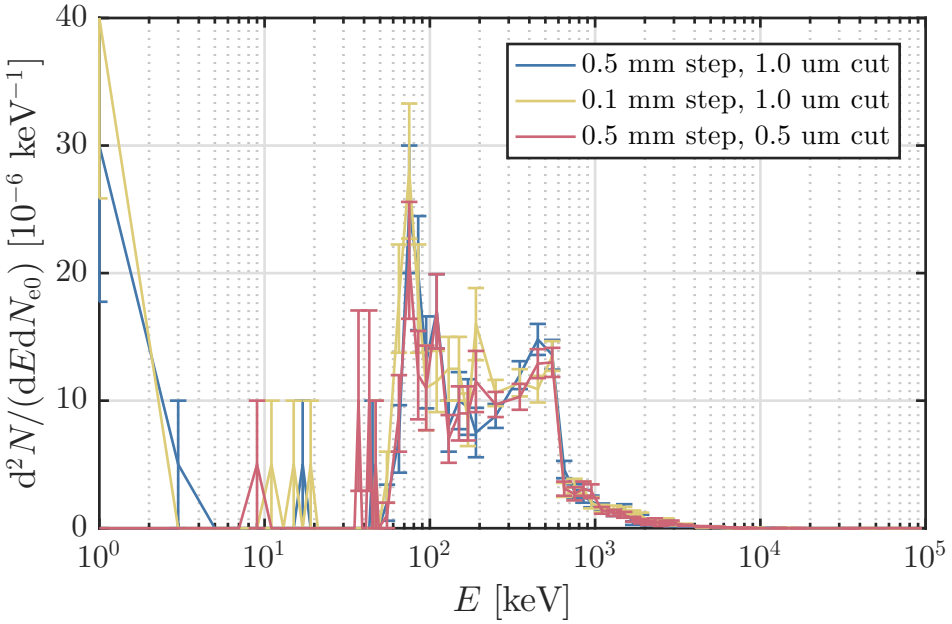


Figure 6.19: Comparison of energy spectra of scored particles from GEANT4 simulations of 10^5 initial electrons with various combinations of step size and cut in range (c.f. Section 6.3). Units are in number of particles per keV per 10^6 initial electrons.

default cut value (blue). Reducing the cut in range from 1 µm to 0.5 µm also resulted in a similar spectrum (red) across the majority of the energy range. However, a smaller cut in range appears to eliminate the low energy tail due to slower electrons. It is possible that the creation of these low energy electrons are due to a bug in GEANT4 as there have been a number of cases where non-physical electrons were generated at transverse angles while propagating through the magnetic field of the electron spectrometer. Regardless, this deviation in the energy spectrum is not expected to change the prior results since electrons of this energy have clearly been shown to be stopped by the 30 µm aluminium shield as demonstrated by Figure 6.11.

6.10 Summary

A series of GEANT4 simulations were used to show that a significant number of energetic particles, generated during the stopping of a high energy electron beam, would have reached the CCD in the experiments described in Chapter 5. In particular, for the

conditions used in the Munich experiment, the GEANT4 simulations show that the shielding used was insufficient to fully eliminate a signal contribution to the X-ray CCD. A number of assumptions have been outlined previously meaning that the actual level contributed to the CCD in the physical experiment is likely to differ from the calculations above. However, it is clear that this source of noise could potentially dominate the desired signal.

The majority of unwanted particles reaching the CCD was shown to be high energy gamma rays created primarily in the floor of the steel chamber. The main interaction with the CCD, at this energy, would be Compton scattering with the silicon chip, creating lower energy electrons which would more readily be detected. It was shown that there was a significant number of electrons which bypass (or originate from) the shielding which would affect X-ray measurements, more so than Compton electrons generated from gamma radiation.

However, initial simulations show that the experimental layout can be improved, such as careful steering of the electron beam or reinforcing the shielding. The number of particles penetrating the shielding was shown to be reduced significantly by incorporating a thick plastic layer to the electron beam dump and moving the dump far from the detector. Additional lead shielding surrounding the detector was shown to be effective. This result suggests that it would be be possible to perform an XCERP measurement after optimisation of the layout. By including more details in the simulation geometry, any spatial distribution of hits and energy spectrum could potentially be predicted such that even in the scenario where not all ionising radiation—due to the stopping of the electron beam—can be eliminated, the flux could be reduced to a level where it is distinguishable from a diffraction signal.

As a basic example, the results shown here can be applied to the experiment at CALA (Chapter 5), which produced electron beams with approximately 300 pC charge, filling approximately 2% of the CCD. Recalling that a tenth of these were then categorised as potential X-ray hits (2250 events), a combination of the 25 mm plastic base layer,

5 mm additional lead shielding and increased distance from the magnets could reduce this unwanted background level by 95% down to approximately 120 events. From recent simulations using the XCERP diffraction code (c.f. Chapter 3) to model the detector geometry used in CALA, 265 diffracted rays reached the camera from 1.6×10^9 initial photons. If this flux can be achieved from a beam charge of no more than 300 pC, then the diffracted rays may be distinguishable from the unblocked electrons reaching the X-ray CCD, therefore allowing a potentially successful XCERP diffraction measurement to be performed.

Chapter 7

Conclusion

Bright X-ray sources continue to find more applications as the properties of the X-ray beams are improved. Hence, it stands to reason that innovations in the measurement techniques would be beneficial. This is particularly true for the generation of betatron radiation from LWFAs, which are often prone to shot-to-shot variations, and can arise from, say, jitter in the laser system. Throughout this thesis, a novel technique for measuring betatron radiation has been presented, named X-ray Characterisation by Energy-Resolved Powder (XCERP) diffraction. Chapters 2 and 3 provides the theoretical framework, conjecturing that analysis of the diffraction pattern from a powder could allow the incident spectrum to be inferred on a single shot basis. Until LWFA technology improves to the point that the betatron emission is stable and reproducible on demand, XCERP diffraction provides means of simultaneously measuring the radiation and employing the transmitted portion elsewhere, e.g. X-ray imaging, as the measurement is *non-destructive*.

A ray-tracing code to simulate powder diffraction was developed which demonstrated that the properties of an X-ray beam of arbitrary shape could successfully be retrieved using only its diffracted signal, as measured by a CCD detector, and knowledge of the powder material. Depending on the exact geometry of the source, detector and powder, the spectrum and potentially, the divergence of X-ray beam can be calculated.

This work included an experiment based at the Astra Gemini facility at the Rutherford Appleton Laboratory. Although the main objectives were not achieved during this campaign, (i.e. to demonstrate two-pulse ionisation injection; to attempt XCERP diffraction), new techniques were developed to accurately characterise the electron beam using an electron spectrometer. The energy calibration was performed through a bespoke particle tracking code. A method of extracting the spectrum from a Lanex screen was described. To the author's knowledge, this is the first time electron spectra have been extracted from Lanex screens at an oblique angle to the detector. This was achieved by accounting for perspective foreshortening. The drawback of this method is the increased complexity and reduced spectral resolution.

Betatron radiation from the Astra Gemini experiment was also measured. To this end, a filter wheel was designed, with the intent of using of Ross filter pairs in order to obtain a spectral measurement without the need for any assumptions about the spectral shape. It was found that practical limitations on the thicknesses of the various filter materials significantly affected the retrieval accuracy. Therefore, an alternative method was employed to measure the betatron radiation. This involved *assuming* a spectral function and calculating the expected counts associated with each material in the filter array. Comparing to the experimentally measured counts, the best fit parameters—which in this case were the betatron critical energy and a scaling factor—could be attained through an in-built fitting algorithm.

The results of a single run were presented which combined the analyses of the filter wheel and electron spectrometer. It could be seen that a correlation might exist between the betatron critical energy and the electron energy as predicted by theory. Likewise, there was a clear trend between the scaling factor (indicative of the total energy in the betatron beam) and the charge of the electron bunch. However, not all results agreed with theory. It was expected that a divergent electron beam would result in a large critical energy, but this was not observed. Also, the total energy radiated should scale strongly with electron energy, but a trend could not be identified.

The first attempt at XCERP diffraction took place at the Centre for Advanced Laser Applications in Munich. A bespoke algorithm was created by the author to identify X-ray hits in the images taken during the CALA experiment. It was found that great lengths must be taken to shield CCDs from unwanted sources of radiation. Even with copious sheets of lead, a signal persisted on the CCD which was found to not vary significantly when a powder target was put in and pulled out of the path of the betatron beam. In order to conclude whether any diffraction was measured, the background radiation would need to be eliminated or further reduced.

Simulations using GEANT4 showed that when an electron beam was driven into the chamber floor, via the electron spectrometer, many gamma rays and electrons were scattered onto the CCD chip. A number of adjustments to the geometry were tested in order to check whether a reduction in the background radiation level could be achieved. It was shown that an implementation of the suggestions to shield the detector better may allow a successful XCERP diffraction measurement to be performed at CALA.

7.1 Outlook

Several suggestions were made in this thesis to move the XCERP diffraction technique forward, in both concept and demonstration. A preliminary study was performed, looking at the effect of polarisation of the betatron radiation on the diffraction signal. Simulations showed that the diffraction profile changes with polarisation and it would be interesting to test whether this is sufficient to measure the polarisation state of the betatron radiation.

There is scope to improve the analyses used in the Astra Gemini experiment. In particular, accurate measurements of the filter thicknesses could improve the betatron fit drastically. With regards to the electron spectrum measurement, spectra which extend outside the Lanex region would clearly not give accurate charge measurements. Hence, it would be interesting to develop a system to exclude these shots in the analysis.

A future experiment would allow the geometry changes found in Chapter 6 to be implemented with the hopes that the background radiation level would be low enough to allow powder diffraction to be identified. If successful, this would prove to be a promising method of allowing single-shot non-destructive measurements of bright radiation sources.

References

[1] Warren, B. E. *X-Ray Diffraction*. Dover Books on Physics. New York: Dover Publications, Inc., 2012.

[2] James, R. W. *The Optical Principles of the Diffraction of X-Rays*. Ed. by L. Bragg. London: G. Bell and Sons Ltd., 1962.

[3] Cullity, B. D. *Elements of X-ray Diffraction*. 2nd. Reading: Addison-Wesley Publishing Company, Inc, 1978.

[4] Higginbotham, A., Patel, S., Hawreliak, J. a., et al. "Single photon energy dispersive x-ray diffraction." In: *The Review of scientific instruments* 85.3 (2014), p. 033906. DOI: 10.1063/1.4867456.

[5] Roentgen, W. C. "On a New Kind of Rays". In: *Nature* 53.1369 (1896), pp. 274–276. DOI: 10.1038/053274b0.

[6] Corde, S., Ta Phuoc, K., Lambert, G., et al. "Femtosecond x rays from laser-plasma accelerators". In: *Reviews of Modern Physics* 85.1 (2013), pp. 1–48. DOI: 10.1103/RevModPhys.85.1.

[7] Liu, H. and Spence, J. C. H. "XFEL data analysis for structural biology". In: *Quantitative Biology* 4.3 (2016), pp. 159–176. DOI: 10.1007/s40484-016-0076-z.

[8] Winick, H. "Fourth generation light sources". In: *Proceedings of the 1997 Particle Accelerator Conference (Cat. No.97CH36167)*. Vol. 1. IEEE, 1997, pp. 37–41. DOI: 10.1109/PAC.1997.749539.

[9] Mallinson, J. C. "One-sided fluxes – A magnetic curiosity?" In: *IEEE Transactions on Magnetics* 9.4 (1973), pp. 678–682. DOI: 10.1109/TMAG.1973.1067714.

[10] Halbach, K. "Design of permanent multipole magnets with oriented rare earth cobalt material". In: *Nuclear Instruments and Methods* 169.1 (1980), pp. 1–10. DOI: http://dx.doi.org/10.1016/0029-554X(80)90094-4.

[11] McNeil, B. W. J. and Thompson, N. R. "X-ray free-electron lasers". In: *Nature Photonics* 4.12 (2010), pp. 814–821. DOI: 10.1038/nphoton.2010.239.

[12] Hooker, S. M. "Developments in laser-driven plasma accelerators". In: *Nature Photonics* 7.10 (2013), pp. 775–782. DOI: 10.1038/nphoton.2013.234.

[13] Leemans, W. P., Gonsalves, A. J., Mao, H.-S., et al. "Multi-GeV Electron Beams from Capillary-Discharge-Guided Subpetawatt Laser Pulses in the Self-Trapping Regime". In: *Physical Review Letters* 113.24 (2014), p. 245002. DOI: 10.1103/PhysRevLett.113.245002.

[14] Tajima, T. and Dawson, J. M. "Laser electron accelerator". In: *Physical Review Letters* 43.4 (1979), pp. 267–270.

[15] Andreev, N. E., Gorbunov, L. M., Kirsanov, V. I., Pogosova, A. A., and Ramazashvili, R. R. *Resonant excitation of wakefields by a laser pulse in a plasma.* 1992.

[16] Krall, J., Ting, A., Esarey, E., and Sprangle, P. "Enhanced acceleration in a self-modulated-laser wake-field accelerator". In: *Physical Review E* 48.3 (1993), pp. 2157–2161. DOI: 10.1103/PhysRevE.48.2157.

[17] Joshi, C., Tajima, T., Dawson, J. M., Baldis, H. A., and Ebrahim, N. A. "Forward Raman Instability and Electron Acceleration". In: *Physical Review Letters* 47.18 (1981), pp. 1285–1288. DOI: 10.1103/PhysRevLett.47.1285.

[18] Strickland, D. and Mourou, G. "Compression of amplified chirped optical pulses". In: *Optics Communications* 55.6 (1985), pp. 447–449.

[19] Faure, J., Glinec, Y., Pukhov, A., et al. "A laserâĂŞplasma accelerator producing monoenergetic electron beams". In: *Nature* 431.7008 (2004), pp. 541–544. DOI: 10.1038/nature02963.

[20] Geddes, C. G. R., Toth, C., Tilborg, J. van, et al. "High-quality electron beams from a laser wakefield accelerator using plasma-channel guiding". In: *Nature* 431.7008 (2004), pp. 538–541. DOI: 10.1038/nature02900.

[21] Mangles, S. P. D., Murphy, C. D., and Najmudin, Z. "Monoenergetic beams of relativistic electrons from intense laserâĂŞplasma interactions". In: *Nature* (2004), pp. 535–538. DOI: 10.1038/nature02930.1..

[22] Ta Phuoc, K., Corde, S., Thaury, C., et al. "All-optical Compton gamma-ray source". In: *Nature Photonics* 6.5 (2012), pp. 308–311. DOI: 10.1038/nphoton.2012.82. arXiv: 1301.3973.

[23] Khrennikov, K., Wenz, J, Buck, A., et al. "Tunable All-Optical Quasimonochromatic Thomson X-Ray Source in the Nonlinear Regime". In: *Physical Review Letters* 114.19 (2015), pp. 1–5. DOI: 10.1103/PhysRevLett.114.195003. arXiv: 1406.6654.

[24] Schlenvoigt, H.-P., Haupt, K., Debus, A., et al. "A compact synchrotron radiation source driven by a laser-plasma wakefield accelerator". In: *Nature Physics* 4.2 (2008), pp. 130–133. DOI: 10.1038/nphys811.

[25] Fuchs, M., Weingartner, R., Popp, A., et al. "Laser-driven soft-X-ray undulator source". In: *Nature Physics* 5.11 (2009), pp. 826–829. DOI: 10.1038/nphys1404.

[26] Chen, M., Esarey, E., Geddes, C. G. R., et al. "Modeling classical and quantum radiation from laser-plasma accelerators". In: *Physical Review Special Topics - Accelerators and Beams* 16.3 (2013), p. 030701. DOI: 10.1103/PhysRevSTAB.16.030701.

[27] Huang, Z., Ding, Y., and Schroeder, C. B. "Compact X-ray Free-Electron Laser from a Laser-Plasma Accelerator Using a Transverse-Gradient Undulator". In: *Physical Review Letters* 109.20 (2012), p. 204801. DOI: 10.1103/PhysRevLett.109.204801.

[28] Fourmaux, S., Corde, S., Ta Phuoc, K., et al. "Single shot phase contrast imaging using laser-produced Betatron x-ray beams." In: *Optics letters* 36.13 (2011), pp. 2426–8.

[29] Kneip, S., McGuffey, C., Dollar, F., et al. "X-ray phase contrast imaging of biological specimens with femtosecond pulses of betatron radiation from a compact laser plasma wakefield accelerator". In: *Applied Physics Letters* 99.9 (2011), p. 093701. DOI: 10.1063/1.3627216.

[30] Cole, J. M., Wood, J. C., Lopes, N. C., et al. "Laser-wakefield accelerators as hard x-ray sources for 3D medical imaging of human bone". In: *Scientific Reports* 5.1 (2015), p. 13244. DOI: 10.1038/srep13244.

[31] Shah, R., Albert, F., Ta Phuoc, K., et al. "Coherence-based transverse measurement of synchrotron x-ray radiation from relativistic laser-plasma interaction and laser-accelerated electrons". In: *Physical Review E* 74.4 (2006), p. 045401. DOI: 10.1103/PhysRevE.74.045401.

[32] Kneip, S., McGuffey, C., Martins, J. L., et al. "Bright spatially coherent synchrotron X-rays from a table-top source". In: *Nature Physics* 6.12 (2010), pp. 980–983. DOI: 10.1038/nphys1789.

[33] Wenz, J., Schleede, S., Khrennikov, K., et al. "Quantitative X-ray phase-contrast microtomography from a compact laser-driven betatron source". In: *Nature Communications* 6.May (2015), p. 7568. DOI: 10.1038/ncomms8568.

[34] Kneip, S., Nagel, S. R., Bellei, C., et al. "Observation of Synchrotron Radiation from Electrons Accelerated in a Petawatt-Laser-Generated Plasma Cavity". In:

Physical Review Letters 100.10 (2008), p. 105006. DOI: 10.1103/PhysRevLett.100.105006.

[35] Rousse, A., Ta Phuoc, K., Shah, R., et al. "Production of a keV X-Ray Beam from Synchrotron Radiation in Relativistic Laser-Plasma Interaction". In: *Physical Review Letters* 93.13 (2004), p. 135005. DOI: 10.1103/PhysRevLett.93.135005.

[36] Albert, F., Shah, R., Ta Phuoc, K., et al. "Betatron oscillations of electrons accelerated in laser wakefields characterized by spectral x-ray analysis". In: *Physical Review E* 77.5 (2008), p. 056402. DOI: 10.1103/PhysRevE.77.056402.

[37] Fourmaux, S., Corde, S., Ta Phuoc, K., et al. "Demonstration of the synchrotron-type spectrum of laser-produced Betatron radiation". In: *New Journal of Physics* 13.3 (2011), p. 33017. DOI: 10.1088/1367-2630/13/3/033017. arXiv: 1104.2243.

[38] Schnell, M., Sävert, A., Landgraf, B., et al. "Deducing the electron-beam diameter in a laser-plasma accelerator using x-ray betatron radiation". In: *Physical Review Letters* 108.7 (2012), pp. 1–5. DOI: 10.1103/PhysRevLett.108.075001.

[39] Ta Phuoc, K., Corde, S., Shah, R., et al. "Imaging Electron Trajectories in a Laser-Wakefield Cavity Using Betatron X-Ray Radiation". In: *Physical Review Letters* 97.22 (2006), p. 225002. DOI: 10.1103/PhysRevLett.97.225002.

[40] Ju, J., Genoud, G., Ferrari, H. E., et al. "Analysis of x-ray emission and electron dynamics in a capillary-guided laser wakefield accelerator". In: *Physical Review Special Topics - Accelerators and Beams* 17.5 (2014), pp. 1–8. DOI: 10.1103/PhysRevSTAB.17.051302.

[41] Esarey, E., Shadwick, B., Catravas, P., and Leemans, W. P. "Synchrotron radiation from electron beams in plasma-focusing channels". In: *Physical Review E* 65.5 (2002), p. 056505. DOI: 10.1103/PhysRevE.65.056505.

[42] Jackson, J. D. *Classical Electrodynamics (2nd ed.)* 2nd ed. New York: John Wiley & Sons, 1975.

[43] Cheung, G. and Hooker, S. M. "X-ray characterization by energy-resolved powder diffraction". In: *Phys. Rev. Accel. Beams* 19.8 (2016), p. 82801. DOI: 10.1103/PhysRevAccelBeams.19.082801.

[44] Compton, A. H. "The Determination of Electron Distributions From Measurements of Scattered X-Rays". In: *Phys. Rev.* 35.8 (1930), pp. 925–938. DOI: 10.1103/PhysRev.35.925.

[45] Raman, C. V. "A classical derivation of the Compton effect". In: *Indian Journal of Physics* 3 (1928), pp. 357–369.

[46] Wentzel, G. "Zur Theorie des Comptoneffekts". In: *Zeitschrift für Physik* 43.1 (1927), pp. 1–8. DOI: 10.1007/BF01397225.

[47] Brown, P. J., Fox, A. G., Maslen, E. N., O'Keefe, M. A., and Willis, B. T. M. "6.1. Intensity of diffracted intensities". In: *International Tables for Crystallography, Vol. C.* Vol. C. Kluwer Academic Publishers, 2006. Chap. 6.1, pp. 554–595. DOI: 10.1107/97809553602060000600.

[48] Coulthard, M. A. "A relativistic Hartree-Fock atomic field calculation". In: *Proceedings of the Physical Society* 91.1 (1967), pp. 44–49. DOI: 10.1088/0370-1328/91/1/309.

[49] Sears, V. F. and Shelley, S. a. "Debye-Waller factor for elemental crystals". In: *Acta Crystallographica Section A Foundations of Crystallography* 47.4 (1991), pp. 441–446. DOI: 10.1107/S0108767391002970.

[50] Lipson, H., Langford, J. I., and Hu, H.-C. "6.2 Trigonometric intensity factors". In: *International Tables for Crystallography, Vol. C.* Vol. C. 2006. Chap. 6.2, pp. 596–598. DOI: 10.1107/97809553602060000601.

[51] Parrish, W. and Langford, J. I. "2.3. Powder and related techniques: X-ray techniques". In: *International Tables for Crystallography, Vol. C.* Vol. C. Kluwer Academic Publishers, 2006. Chap. 2.3, pp. 42–79. DOI: 10.1107/97809553602060000578.

[52] Darwin, C. G. "LXXVIII. The theory of X-ray reflexion. Part II". In: *Philosophical Magazine* 27.160 (1914), pp. 675–690. DOI: 10.1080/14786440408635139.

[53] Darwin, C. G. "XXXIV. The theory of X-ray reflexion". In: *Philosophical Magazine* 27.158 (1914), pp. 315–333. DOI: 10.1080/14786440208635093.

[54] Batterman, B. W. and Cole, H. "Dynamical Diffraction of X Rays by Perfect Crystals". In: *Reviews of Modern Physics* 36.3 (1964), pp. 681–717. DOI: 10.1103/RevModPhys.36.681.

[55] Pinsker, Z. G. *Dynamical scattering of x-rays in crystals.* Berlin: Springer-Verlag, 1978, p. 511.

[56] Authier, A. *Dynamical Theory of X-Ray Diffraction.* Oxford University Press, 2003. DOI: 10.1093/acprof:oso/9780198528920.001.0001.

[57] Patel, S., Suggit, M. J., Stubley, P. G., et al. "Single Hit Energy-resolved Laue Diffraction." In: *The Review of scientific instruments* 86.5 (2015), p. 053908. DOI: 10.1063/1.4921774.

[58] Clark, S. *Thirty Years of Energy-Dispersive Powder Diffraction.* Vol. 8. March 2015. 2002, pp. 57–92. DOI: 10.1080/0889311021000008018.

[59] Maddox, B. R., Park, H. S., Remington, B. A., and McKernan, M. "Calibration and characterization of single photon counting cameras for short-pulse laser experiments". In: *Review of Scientific Instruments* 79.10 (2008), 10E924. DOI: 10.1063/1.2966374.

[60] Tierney, L. "Markov Chains for Exploring Posterior Distributions". In: *The Annals of Statistics* 22.4 (1994), pp. 1701–1728. DOI: 10.1214/aos/1176325750.

[61] Chib, S. and Greenberg, E. "Understanding the Metropolis-Hastings Algorithm". In: *The American Statistician* 49.4 (1995), pp. 327–335.

[62] Köhler, A., Couperus, J., Zarini, O., et al. "Single-shot betatron source size measurement from a laser-wakefield accelerator". In: *Nuclear Instruments and Methods in Physics Research Section A: Accelerators, Spectrometers, Detectors and Associated Equipment* (2016), pp. 1–5. DOI: 10.1016/j.nima.2016.02.031.

[63] NIST. *Standard Reference Material 640e: Line Position and Line Shape Standard for Powder Diffraction (Silicon Powder)*. Tech. rep. Gaithersburg, MD: NIST, 2015, pp. 1–5.

[64] Chen, L. M., Yan, W. C., Li, D. Z., et al. "Bright betatron X-ray radiation from a laser-driven-clustering gas target." In: *Scientific reports* 3 (2013), p. 1912. DOI: 10.1038/srep01912.

[65] Suryanarayana, C. and Grant Norton, M. *X-Ray Diffraction: A Practical Approach*. New York: Plenum Press, 1998.

[66] Butt, N. M., Bashir, J., Willis, B. T. M., and Heger, G. "Compilation of temperature factors of cubic elements". In: *Acta Crystallographica Section A Foundations of Crystallography* 44.3 (1988), pp. 396–399. DOI: 10.1107/S0108767387011929.

[67] Albert, F., Pollock, B. B., Shaw, J. L., et al. "Measuring the angular dependence of betatron x-ray spectra in a laser-wakefield accelerator". In: *Plasma Physics and Controlled Fusion* 56.8 (2014), p. 084016. DOI: 10.1088/0741-3335/56/8/084016.

[68] Albert, F., Pollock, B. B., Shaw, J. L., et al. "Angular Dependence of Betatron X-Ray Spectra from a Laser-Wakefield Accelerator". In: *Physical Review Letters* 111.23 (2013), p. 235004. DOI: 10.1103/PhysRevLett.111.235004.

[69] Kostyukov, I., Kiselev, S., and Pukhov, A. M. "X-ray generation in an ion channel". In: *Physics of Plasmas* 10.12 (2003), p. 4818. DOI: 10.1063/1.1624605.

[70] Horný, V., Nejdl, J., Kozlová, M., et al. "Temporal profile of betatron radiation from laser-driven electron accelerators". In: *Physics of Plasmas* 24.6 (2017), p. 063107. DOI: 10.1063/1.4985687.

[71] Peng, L. M., Ren, G, Dudarev, S. L., and Whelan, M. J. "DebyeâĂŞWaller Factors and Absorptive Scattering Factors of Elemental Crystals". In: *Acta Crystallographica Section A Foundations of Crystallography* 52.3 (1996), pp. 456–470. DOI: 10.1107/S010876739600089X.

[72] Ju, J., Svensson, K., Döpp, A., et al. "Enhancement of x-rays generated by a guided laser wakefield accelerator inside capillary tubes". In: *Applied Physics Letters* 100.19 (2012), p. 191106. DOI: 10.1063/1.4712594.

[73] Cipiccia, S., Islam, M. R., Ersfeld, B., et al. "Gamma-rays from harmonically resonant betatron oscillations in a plasma wake". In: *Nature Physics* 7.11 (2011), pp. 867–871. DOI: 10.1038/nphys2090.

[74] Matsuoka, T., Kneip, S., McGuffey, C., et al. "Synchrotron x-ray radiation from laser wakefield accelerated electron beams in a plasma channel". In: *Journal of Physics: Conference Series* 244.4 (2010), p. 042026. DOI: 10.1088/1742-6596/244/4/042026.

[75] Schnell, M., Sävert, A., Uschmann, I., et al. "Optical control of hard X-ray polarization by electron injection in a laser wakefield accelerator." In: *Nature communications* 4.May (2013), p. 2421. DOI: 10.1038/ncomms3421.

[76] Döpp, A., Mahieu, B., Lifschitz, A., et al. "Stable femtosecond X-rays with tunable polarization from a laser-driven accelerator". In: *Light: Science & Applications* 6.11 (2017), e17086. DOI: 10.1038/lsa.2017.86.

[77] Mangles, S. P. D., Genoud, G., Kneip, S., et al. "Controlling the spectrum of x-rays generated in a laser-plasma accelerator by tailoring the laser wavefront". In: *Applied Physics Letters* 95.18 (2009), p. 181106. DOI: 10.1063/1.3258022.

[78] Miyata, E. "Broadband X-ray Detector Using CCDs and Scintillators". In: *Broadband X-ray Detector Using CCDs and Scintillators*. Proceedings of SNIC Symposium. Stanford, California, 2006, pp. 1–8.

[79] Seibert, M. M., Ekeberg, T., Maia, F. R. N. C., et al. "Single mimivirus particles intercepted and imaged with an X-ray laser." In: *Nature* 470.7332 (2011), pp. 78–81. DOI: 10.1038/nature09748.

[80] Bourgeois, N., Cowley, J., and Hooker, S. M. "Two-Pulse Ionization Injection into Quasilinear Laser Wakefields". In: *Physical Review Letters* 111.15 (2013), p. 155004. DOI: 10.1103/PhysRevLett.111.155004.

[81] Hooker, C. J., Collier, J. L., Chekhlov, O., et al. "The Astra Gemini project âĂŞ A dual-beam petawatt Ti:Sapphire laser system". In: *Journal de Physique IV (Proceedings)* 133 (2006), pp. 673–677. DOI: 10.1051/jp4:2006133135.

[82] Dyson, A. E., Thornton, C., and Hooker, S. M. "A compact, low cost Marx bank for generating capillary discharge plasmas". In: *Review of Scientific Instruments* 87.9 (2016), p. 93302. DOI: 10.1063/1.4961913.

[83] Osterhoff, J., Popp, A., Major, Z., et al. "Generation of Stable, Low-Divergence Electron Beams by Laser-Wakefield Acceleration in a Steady-State-Flow Gas Cell". In: *Physical Review Letters* 101.8 (2008), p. 085002. DOI: 10.1103/PhysRevLett.101.085002.

[84] Shaw, B. H. "Laser-plasma interactions from thin tapes for high-energy electron accelerators and seeding compact FELs". PhD thesis. University of California, Berkeley, 2015.

[85] Giakoumakis, G. E. and Nomicos, C. D. "Light angular distribution of non-granular fluorescent screen excited by X-rays". In: *Physics in Medicine and Biology* 30.9 (1985), pp. 993–1003. DOI: 10.1088/0031-9155/30/9/011.

[86] Glinec, Y, Faure, J., Guemnie-Tafo, A, et al. "Absolute calibration for a broad range single shot electron spectrometer". In: *Review of Scientific Instruments* 77.10 (2006), p. 103301. DOI: 10.1063/1.2360988.

[87] Buck, A., Zeil, K., Popp, A., et al. "Absolute charge calibration of scintillating screens for relativistic electron detection". In: *Review of Scientific Instruments* 81.3 (2010), p. 33301. DOI: 10.1063/1.3310275.

[88] Nowotny, R. and Taubeck, A. "A method for the production of composite scintillators for dosimetry in diagnostic radiology". In: *Physics in Medicine & Biology* 54.6 (2009), p. 1457. DOI: 10.1088/0031-9155/54/6/005.

[89] Tanaka, K. A., Yabuuchi, T., Sato, T., et al. "Calibration of imaging plate for high energy electron spectrometer". In: *Review of Scientific Instruments* 76.1 (2005), p. 13507. DOI: 10.1063/1.1824371.

[90] Zeil, K., Kraft, S. D., Jochmann, A., et al. "Absolute response of Fuji imaging plate detectors to picosecond-electron bunches". In: *Review of Scientific Instruments* 81.1 (2010), p. 13307. DOI: 10.1063/1.3284524.

[91] Ohuchi, H and Yamadera, A. "Dependence of fading patterns of photo-stimulated luminescence from imaging plates on radiation, energy, and image reader". In: *Nuclear Instruments and Methods in Physics Research Section A: Accelerators, Spectrometers, Detectors and Associated Equipment* 490.3 (2002), pp. 573–582. DOI: https://doi.org/10.1016/S0168-9002(02)01074-4.

[92] Walker, P. A., Bourgeois, N., Rittershofer, W, et al. "Investigation of GeV-scale electron acceleration in a gas-filled capillary discharge waveguide". In: *New Journal of Physics* 15.4 (2013), p. 045024. DOI: 10.1088/1367-2630/15/4/045024.

[93] Pollock, B. B., Clayton, C. E., Divol, L., et al. "Two-Screen Method for Determining Electron Beam Energy and Deflection From Laser Wakefield". In: *Proceedings of PAC09* (2009), pp. 3035–3037.

[94] Soloviev, A. A., Starodubtsev, M. V., Burdonov, K. F., et al. "Two-screen single-shot electron spectrometer for laser wakefield accelerated electron beams". In: *Review of Scientific Instruments* 82.4 (2011), p. 43304. DOI: 10.1063/1.3585862.

[95] Svensson, K. "Laser-Produced Plasmas for Particle Acceleration". PhD thesis. Lund University, 2012.

[96] Schnell, M., Sävert, A., Uschmann, I., et al. "Characterization and application of hard x-ray betatron radiation generated by relativistic electrons from a laser-wakefield accelerator". In: *Journal of Plasma Physics* 81.04 (2015), p. 475810401. DOI: 10.1017/S0022377815000379. arXiv: 1503.07304.

[97] Ross, P. A. "A New Method of Spectroscopy for Faint X-Radiations". In: *Journal of the Optical Society of America* 16.6 (1928), p. 433. DOI: 10.1364/JOSA.16.000433.

[98] Tuszynski, J. *PhotonAttenuation, MATLAB File Exchange*. 2016.

[99] Hubbell, J. H. and Seltzer, S. M. DOI: 10.18434/T4D01F.

[100] Soules, J. A., Gordon, W. L., and Shaw, C. H. "Design of differential X-ray filters for low-intensity scattering experiments". In: *Review of Scientific Instruments* 27.1 (1956), pp. 12–14. DOI: 10.1063/1.1715354.

[101] Kirkpatrick, P. "On the Theory and Use of Ross Filters". In: *Review of Scientific Instruments* 10.6 (1939), pp. 186–191. DOI: 10.1063/1.1751523.

[102] Ju, J. "Electron acceleration and betatron radiation driven by laser wakefield inside dielectric capillary tubes". PhD thesis. Universitté Paris Sud, 2013.

[103] Albert, F., Pollock, B. B., Chen, Y.-H., and Alessi, D. "Betatron X-Rays from a Laser Wakefield Accelerator in the Ionization Induced Trapping Regime". In: (), pp. 3–5.

[104] Albert, F., Pollock, B. B., Shaw, J., et al. "Betatron x-ray production in mixed gases". In: 8779 (2013). Ed. by E. Esarey, C. B. Schroeder, W. P. Leemans, K. W. D. Ledingham, and D. A. Jaroszynski, 87791Q. DOI: 10.1117/12.2017187.

[105] Guo, H. "A simple algorithm for fitting a gaussian function". In: *IEEE Signal Processing Magazine* 28.5 (2011), pp. 134–137. DOI: 10.1109/MSP.2011.941846.

[106] Anthony, S. M. and Granick, S. "Image Analysis with Rapid and Accurate Two-Dimensional Gaussian Fitting". In: *Langmuir* 25.14 (2009), pp. 8152–8160. DOI: 10.1021/la900393v.

[107] Rousse, A., Ta Phuoc, K., Shah, R., Fitour, R., and Albert, F. "Scaling of betatron X-ray radiation". In: *The European Physical Journal D* 45.2 (2007), pp. 391–398. DOI: 10.1140/epjd/e2007-00249-7.

[108] Buck, A., Wenz, J, Xu, J, et al. "Shock-Front Injector for High-Quality Laser-Plasma Acceleration". In: *Physical Review Letters* 110.18 (2013), p. 185006. DOI: 10.1103/PhysRevLett.110.185006.

[109] Schmid, K., Buck, A., Sears, C. M. S., et al. "Density-transition based electron injector for laser driven wakefield accelerators". In: *Physical Review Special Topics - Accelerators and Beams* 13.9 (2010), p. 091301. DOI: 10.1103/PhysRevSTAB.13.091301.

[110] Bulanov, S. V., Pegoraro, F., Pukhov, A. M., and Sakharov, A. S. "Transverse-Wake Wave Breaking". In: *Physical Review Letters* 78.22 (1997), pp. 4205–4208. DOI: 10.1103/PhysRevLett.78.4205.

[111] Bulanov, S. V., Naumova, N., Pegoraro, F., and Sakai, J. "Particle injection into the wave acceleration phase due to nonlinear wake wave breaking". In: *Phys. Rev. E* 58.5 (1998), R5257–R5260. DOI: 10.1103/PhysRevE.58.R5257.

[112] Janesick, J., Elliott, T., Bredthauer, R., Chandler, C., and Burke, B. "Fano-noise-limited CCDs". In: *Proc. SPIE*. Ed. by L. Golub. Vol. 982. 1988, p. 70. DOI: 10.1117/12.948704.

[113] Prigozhin, G., Butler, N. R., Kissel, S. E., and Ricker, G. R. "An experimental study of charge diffusion in the undepleted silicon of X-ray CCDs". In: *IEEE Transactions on Electron Devices* 50.1 (2003), pp. 246–253. DOI: 10.1109/TED.2002.806470.

[114] Smith, A. R., McDonald, R. J., Hurley, D. L., et al. *Radiation events in astronomical CCD images*. Tech. rep. Berkeley: Lawrence Berkeley National Laboratory, 2001.

[115] Owens, A., Mineo, T., McCarthy, K. J., and Wells, A. "Event recognition in X-ray CCDs". In: *Nuclear Inst. and Methods in Physics Research, A* 346.1-2 (1994), pp. 353–365. DOI: 10.1016/0168-9002(94)90723-4.

[116] Chivers, D. H., Coffer, A., Plimley, B., and Vetter, K. "Electron-track Compton imaging using high-resolution charge-coupled devices". In: *IEEE Nuclear Science Symposium Conference Record* (2010), pp. 1512–1517. DOI: 10.1109/NSSMIC.2010.5874029.

[117] Pavlov, G. G. and Nousek, J. A. "Charge diffusion in CCD X-ray detectors". In: *Nuclear Instruments and Methods in Physics Research, Section A: Accelerators, Spectrometers, Detectors and Associated Equipment* 428.2 (1999), pp. 348–366. DOI: 10.1016/S0168-9002(99)00045-5.

[118] Miyata, E., Miki, M., Hiraga, J., et al. "Application of the mesh experiment for the back-illuminated charge-coupled device: I. Experiment and the charge cloud

shape". In: *Japanese Journal of Applied Physics, Part 1: Regular Papers and Short Notes and Review Papers* 41.9 (2002), pp. 5827–5834. DOI: 10.1143/JJAP.41.5827. arXiv: 0206021 [physics].

[119] Tsunemi, H., Hiraga, J., Miyata, E., Yoshita, K., and Ohtani, M. "Distortion of a charge cloud shape inside the CCD produced by an X-ray photon". In: *IEEE Transactions on Nuclear Science* 47.6 (2000), pp. 2014–2019. DOI: 10.1109/23.903838.

[120] Miyata, E., Miki, M., Kamiyama, D., Tsunemi, H., and Miyaguchi, K. "Measurement of the Charge Cloud Shape Generated in the Fully Depleted Back-Illuminated Charge-Coupled Device". In: *Japanese Journal of Applied Physics* 42.11R (2003), p. 7135. DOI: 10.1143/JJAP.42.7135.

[121] Hiraga, J., Tsunemi, H., and Miyata, E. "Subpixel Spatial Resolution of the X-Ray Charge-Coupled Device Based on the Charge Cloud Shape". In: *Japanese Journal of Applied Physics* 40.Part 1, No. 3A (2001), pp. 1493–1498. DOI: 10.1143/JJAP.40.1493. arXiv: 0101052 [physics].

[122] Ju, J., Svensson, K., Ferrari, H., et al. "Study of electron acceleration and x-ray radiation as a function of plasma density in capillary-guided laser wakefield accelerators". In: *Physics of Plasmas* 20.8 (2013), p. 083106. DOI: 10.1063/1.4817747.

[123] Plateau, G. R., Geddes, C. G. R., Thorn, D. B., et al. "XâĂŘray Emission from Electron Betatron Motion in a LaserâĂŘPlasma Accelerator". In: *AIP Conference Proceedings* 1299.1 (2010), pp. 139–143. DOI: 10.1063/1.3520302.

[124] Agostinelli, S., Allison, J., Amako, K., et al. "GEANT4 - A simulation toolkit". In: *Nuclear Instruments and Methods in Physics Research, Section A: Accelerators, Spectrometers, Detectors and Associated Equipment* 506.3 (2003), pp. 250–303. DOI: 10.1016/S0168-9002(03)01368-8. arXiv: 1005.0727v1.

[125] Killedar, J. S. *Dynamometer: Theory and Application to Engine Testing*. Xlibris Corporation LLC, 2012.

[126] Geant4 Collaboration. "Geant4 User's Guide for Application Developers". In: December (2016).

[127] Allison, J., Amako, K., Apostolakis, J., et al. "Recent developments in GEANT4". In: *Nuclear Instruments and Methods in Physics Research, Section A: Accelerators, Spectrometers, Detectors and Associated Equipment* 835 (2016), pp. 186–225. DOI: 10.1016/j.nima.2016.06.125.

[128] Geant4 Collaboration. "Physics Reference Manual". In: December (2016).

[129] Hall, D., Holland, A., and Turner, M. "Simulating and reproducing instrument background for X-ray CCD spectrometers in space". In: *High Energy, Optical, and Infrared Detectors for Astronomy III*. Vol. 7021. \procspie. 2008, 70211Y. DOI: 10.1117/12.790711.

[130] Esposito, M., Price, T., Anaxagoras, T., and Allinson, N. M. "Geant4-based simulations of charge collection in CMOS Active Pixel Sensors". In: *Journal of Instrumentation* 12.03 (2017), P03028–P03028. DOI: 10.1088/1748-0221/12/03/P03028.

[131] Potdevin, G., Trunk, U., and Graafsma, H. "HORUS, an HPAD X-ray detector simulation program". In: *Journal of Instrumentation* 4.09 (2009), P09010–P09010. DOI: 10.1088/1748-0221/4/09/P09010.

[132] Klein, O. and Nishina, Y. "Über die Streuung von Strahlung durch freie Elektronen nach der neuen relativistischen Quantendynamik von Dirac". In: *Zeitschrift für Physik* 52.11 (1929), pp. 853–868. DOI: 10.1007/BF01366453.

[133] Berger, M. J., Coursey, J. S., and Zucker, M. A. *ESTAR, PSTAR, and ASTAR: Computer Programs for Calculating Stopping-Power and Range Tables for Electrons, Protons, and Helium Ions (version 1.21)*. 1999.

[134] Gürler, O., Yalccin, S., Gültekin, A., and Kaynak, G. "Calculation of projected range of electrons in some elemental solids and gases". In: *Japanese Journal of Applied Physics, Part 1: Regular Papers and Short Notes and Review Papers* 44.12 (2005), pp. 8630–8634. DOI: 10.1143/JJAP.44.8630.

[135] Van Pelt, W. R. and Drzyzga, M. "Beta Radiation Shielding with Lead and Plastic: Effect on Bremsstrahlung Radiation when Switching the Shielding Order". In: *Health Physics* 92.2 (2007), pp. 13–17. DOI: 10.1097/01.HP.0000248127.71398.b1.

[136] Amato, E. and Lizio, D. "Plastic materials as a radiation shield for β- Sources: A comparative study through Monte Carlo calculation". In: *Journal of Radiological Protection* 29.2 (2009), pp. 239–250. DOI: 10.1088/0952-4746/29/2/010.